AC Zeeman Potentials for Ultracold Atom Experiments: Suppressing Potential Roughness and the Development of a Microwave Atom Chip

William Miyahira

Escondido, CA

Master of Science, William and Mary, 2021
Bachelor of Science, University of Puget Sound, 2019

A Dissertation presented to the Graduate Faculty of
The College of William and Mary in Virginia in Candidacy for the Degree of
Doctor of Philosophy

Department of Physics

The College of William and Mary in Virginia
May 2026

© Copyright by William Miyahira 2026

APPROVAL PAGE

This Dissertation is submitted in partial fulfillment of
the requirements for the degree of

Doctor of Philosophy

William Miyahira

William Miyahira

Reviewed by the Committee, May 2026

Committee Chair
Seth Aubin, Associate Professor, Physics
College of William & Mary

Eugeniy Mikhailov, Professor, Physics
College of William & Mary

Todd Averett, Professor, Physics
College of William & Mary

Gregory Bentsen, Assistant Professor, Physics
College of William & Mary

Charles A. Sackett, Professor, Physics
University of Virginia

ABSTRACT

This thesis presents the development and experimental study of chip-scale AC Zeeman (ACZ) traps for ultracold neutral atoms. These trapping potentials may enable precision atom-interferometric measurements of sub-mm gravity and Casimir-Polder forces, studies of one-dimensional gasses, and inertial measurements. This work advances the understanding and application of ACZ traps along two main directions: (1) characterization of axial potential roughness in a radio-frequency (RF) ACZ trap, and (2) development of a broadband microwave ACZ atom chip.

While atom chip traps offer the ability to sculpt complex electromagnetic fields for confinement and manipulation of ultracold atoms, they are traditionally limited in their use due to defects in the chip wires, which manifest as distortions in the trapping potential. Here, we report the first experimental demonstration of potential roughness suppression in a radio-frequency (RF) ACZ chip trap. Compared with an equivalent DC Zeeman trap operating at the same location and trap frequency, the ACZ trap exhibits a strong suppression of atom-cloud fragmentation. We further characterize the dependence of ACZ trap roughness on trap height and RF frequency.

To extend our ACZ trapping capabilities to GHz-level frequencies operating on hyperfine transitions, we present the design and simulation of a broadband microwave atom chip and discuss initial manufacturing. This chip uses a trio of parallel microstrip transmission lines for transverse ACZ trapping, with trap characteristics controlled by detuning, relative phase, and power. Axial confinement and positioning are accomplished using a microwave lattice based on the ACZ or AC Stark effect. A DC trapping scheme is proposed, which uses additional wires beneath the microstrip trap for enhanced axial confinement. To efficiently couple broadband (DC-10+ GHz) signals onto the atom chip, we develop a three-dimensional tapered microstrip wedge interface, supported by electromagnetic simulations and large-scale prototypes.

TABLE OF CONTENTS

ACKNOWLEDGMENTS

The time spent in graduate school is largely dictated by one's advisor, so I feel lucky to have worked in Seth's lab for the past six years. I attribute much of who I am as a physicist today to his endless guidance, insight, and never-ending supply of tea and chocolate, for which not enough thanks can be given. I must also thank the former PhD students of the Aubin Lab who built the apparatus and much of the equipment that I've been able to use throughout my time here. It is a testament to their work that the apparatus continues to routinely produce BECs without (that many) issues. In particular, I'd like to acknowledge Andrew Rotunno and ShuangLi Du, with whom I overlapped during my first year in the lab as they finished their dissertations. Drew has proved to be a solid friend and mentor, always happy to offer ideas or help troubleshoot equipment. The lab is now in the capable hands of Trevor and Russell, and I can't wait to see the results you achieve!

I have been lucky to have a plethora of undergraduate students come through the lab during my tenure, all of whom were incredibly gracious in allowing me to distract myself from my own work to talk about physics, life, and–surprisingly more than once–the Barbie cinematic universe. I am especially grateful to those who assisted in work related to this thesis: Sindu Shanmugadas, Morgan Logsdon, and Cate Sturner, who were pivotal in the early stages of FEKO simulations; and Paul Kelemen, Kisa Avrutina, and Pablo Tartiere-Martinez, who assisted with HFSS simulations and the characterization of atom chip substrates.

The memories of my time at W&M are highlighted by the many great friends I've made. Pat, Collin, and Nik quickly adopted me into their circle during my first year despite my horrendous Halo skills, and I now look forward to our yearly mountaineering trips. I hope we continue to conquer many summits together in the future. To the members of the William & Mary Secret Climbing Club (WMSCC for short)–Rob, Noah, Felipe, Ben, Paul, and the JLab folks–thank you for indulging me in a hobby that has featured as many bruises and lost patches of skin as it has smiles. I'm also thankful to have had great comrades in my class and have enjoyed our many game nights, DnD sessions, and late-night study marathons.

The W&M Physics staff also deserve a shout-out for their dedication to making graduate students' lives easier: Ellie, Paula, Yvette, Carol, Ann, Melinda, and Belmari. Additionally, Will Henninger was always more than happy to provide outstanding machining support and made sure I left with all my fingers still attached.

My family and friends have always been extremely supportive throughout my journey in grad school, and I count myself very lucky to have such strong backing.

Finally, not enough thanks can be given to Danaé, with whom I shared many late-night and early-morning calls across the world. She has been a source of joy and laughter and a steadfast companion during countless hours-long data-taking sessions. I am forever thankful for her unwavering and unconditional support.

To my family and Danaé.

LIST OF TABLES

LIST OF FIGURES

Chapter 1

Introduction

This thesis presents my work in furthering the use of AC Zeeman (ACZ) potentials for experiments in ultracold atom interferometry. Such an effort takes us along two paths: experiments possible with our current experimental apparatus, and the development of the tools necessary for next-generation experiments in the Aubin Lab at William & Mary. Subsequent chapters explore these two fronts, all with an eye towards interferometry. This chapter aims to set the stage for the remainder of the thesis, giving context to the presented work and framing ACZ potentials as a useful tool for atom interferometry.

1.1 Ramsey Interferometry

At the heart of our atom interferometry scheme is Ramsey interferometry. This technique, or a variant known as Ramsey-Bordé interferometry [1], has been used to perform extremely sensitive measurements using atoms, such as the acceleration due to Earth's gravity to a part in 10^{-11} precision [2, 3], atomic clocks which take longer than the age of the universe to be off by one second [4], and searches for a permanent electric dipole moment of the electron [5, 6], to name a few.

The use of trapped atoms on an atom chip offers a number of benefits to the type of physics we want to probe. Precision gravimetry measurements are often done with the atoms in free-fall, and thus the time in which the experiments can be performed is

limited by the distance the atoms can fall. To give this a scale, the Kasevich group at Stanford University makes use of an 8.7 m long drop tower interferometer to achieve a 1.4 cm arm separation for measurements of gravity to a level of $\Delta g/g = 3 \times 10^{-11}$ precision [3]. To push the realm of precision metrology further, a 100 m long baseline atom interferometer, MAGIS-100 [7], is currently under development at FermiLab. While this strict requirement can be mitigated by putting atom interferometers in micro-gravity [8] or in space [9], planetary-bound free-fall based atom interferometers are still subject to the effects of gravity. Utilizing localized atom packets in a trap, such as tractor [10] or lattice [11] atom interferometers, for example, eliminates the constraint on the interrogation time due to gravity.

The Ramsey interferometry sequence is diagrammed for a two-level system in Fig. 1.1. It begins by initializing the atoms in one of the two states, denoted $|\uparrow\rangle$ or $|\downarrow\rangle$. For this example, the atoms begin in $|\uparrow\rangle$. A $\pi/2$-pulse puts the atoms into an equal superposition of the two states. They then undergo a free evolution time (sometimes referred to as the interrogation or integration time), during which they acquire an overall phase $\phi = \Delta E \times T/\hbar$, where ΔE is the energy difference between the two states, T is the free evolution time, and $\hbar$ is the reduced Plank's constant. This energy difference can arise from an external effect on the atom, such as a gravitation potential or an electric or magnetic field. After this time, a second $\pi/2$-pulse is applied, and the relative population in each state is measured. The probability to be found in the original state is given as

$$P_{|\uparrow\rangle}(T) = \frac{1}{2}\left[1 - \cos(\phi)\right] = \frac{1}{2}\left[1 - \cos\left(\frac{\Delta E \times T}{\hbar}\right)\right] \tag{1.1}$$

Precise measurements of the energy difference, ΔE, can be obtained by measuring the frequency of the interferometer fringes.

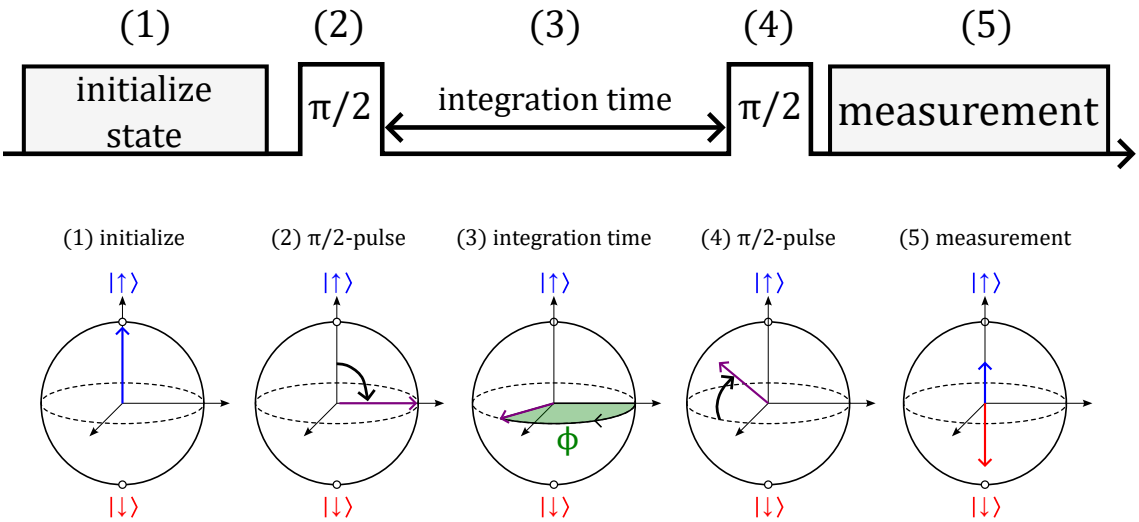

Figure 1.1: Ramsey interferometry sequence in a 2-level atom. (1) Atoms are initially prepared in a given state, $|\uparrow\rangle$. (2) A $\pi/2$-pulse puts the atoms in a superposition of the two states. (3) The atoms freely evolve, acquiring a phase, ϕ. (4) A second $\pi/2$-pulse brings the atoms off the equator of the Bloch sphere. (5) The relative population of the atoms in each state is given as the projection of the state in (4) onto the axis defining pure spin.

1.2 AC Zeeman Potentials for Atom Interferometry

The AC Zeeman (ACZ) effect describes the interaction between an atom and a time-dependent AC magnetic field. In our case, the frequencies used are in the MHz (RF) or GHz (microwave, μw) range, corresponding to atomic transitions within (RF) or between (μw) hyperfine manifolds. Atoms that interact with the AC field have their energy levels shifted, which we can leverage to confine them in a *spin-specific trap* at a minimum of the AC magnetic field. The trapping fields are generated from an atom chip [12, 13], which yield strong near-field gradients for modest RF or microwave powers.

ACZ potentials have a number of benefits, including:

- Inherent **spin-specificity**, allowing for control over a given atomic spin state by controlling the frequency and near-field polarization.
- The ability to make **any spin state a low- or high-field seeker** through the detuning of the AC field from resonance.

- **Detuning, phase, and polarization as experimental control parameters**, allowing for precise tuning of the trapping potential.

- **Operation at arbitrary background DC field**, opening the door for exploring Feshbach resonances or "magic" magnetic fields, which eliminates common-mode DC magnetic noise. Additionally, the DC field and AC frequency can be simultaneously changed to shift the atomic resonance frequency while maintaining a constant detuning, demonstrated in Sec. 5.7.

- The lifetime of the ground hyperfine states being much longer than the experiment time, such that the ACZ potential **does not suffer from spontaneous emission**.

- The ACZ potential **suppresses potential roughness**, primarily due to atomic selection rules. This is the topic of Chapter 6.

- ACZ potentials can be **sculpted with near-fields generated by a microwave atom chip**, which is the topic of Chapter 7.

We intend to use ACZ potentials to operate a Ramsey interferometry with spatially separated atomic states. Such a scheme has been used to measure DC and AC Zeeman shifts using atoms trapped on an atom chip [14, 15]; however the separation is caused by a spin-dependent gradient field from an atom chip trace on a spin independent trap, such as an optical dipole trap, rather than having full positional control over two spin-specific traps, such as an ACZ trap. Figure 1.2 shows the underlying scheme for the ACZ interferometer. Initially, two independent ACZ traps, one for $|\uparrow\rangle$ and one for $|\downarrow\rangle$, are spatially overlapped. The two states will be different $|F, m_F\rangle$ levels in the $F = 1$ or 2 hyperfine manifolds of ground state ^{87}Rb. The two traps will thus target different microwave transitions, and should not affect each other as long as the microwave frequencies are sufficiently different. The traps can then be independently moved around on the chip through power, phase, or a microwave lattice based on the ACZ or AC Stark effect [16, 17]. Numerical simulations have shown that as long as the splitting is adiabatic, the phase of the atomic wavefunction

should not be affected. As the two traps are separated, they will experience a differential external potential, for example gravity, by which a phase of $\phi = mghT/\hbar$ will be obtained (see Fig. 1.1). Having precise control over the two independent ACZ traps is key for our proposed scheme. In the case of a single spin-independent harmonic trap, such as a dipole trap, with spatial separation generated by a spin-dependent gradient, the interferometer phase, i.e., the difference in energy at the bottom of the traps, is dependent not only on gravity, but also the harmonic trap and spin-dependent force. With the spatial separation controlled via independent harmonic traps, the interferometer phase becomes dependent solely on gravity and the arm separation, provided the two traps share a common trap frequency and energy offset, and are symmetrically split in space. After holding the traps separate for a given interrogation time, they are spatially recombined and we can read out the relative population in each state, leading to the classic Ramsey interference fringes. More formally, the Ramsey phase is related to the spacetime separation of the two traps, given as the enclosed area formed by the interferometer arm paths integrated over time.

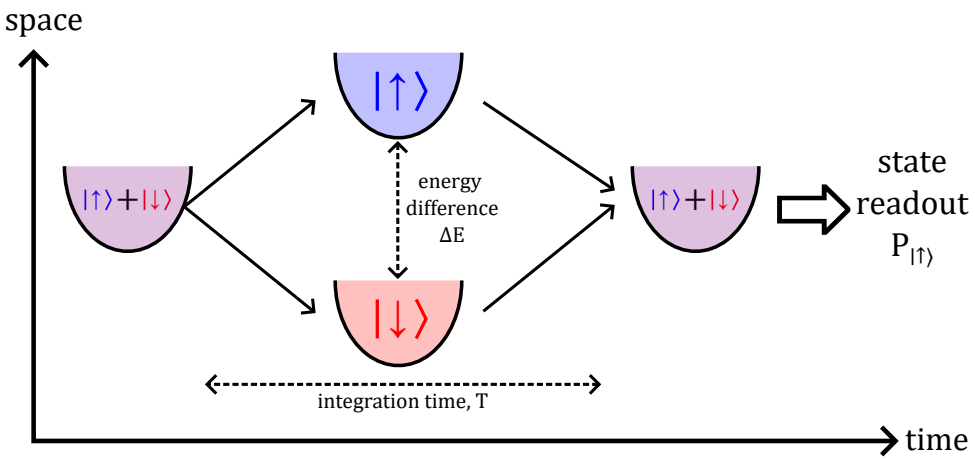

Figure 1.2: Ramsey interferometry with spatially separated ACZ potentials. Two independent traps, one for $|\uparrow\rangle$ and one for $|\downarrow\rangle$, are initially overlapped before being spatially separated. During this time, T, the two traps are subject to a differential energy, ΔE. The two traps are then recombine and the relative population in each state as a function of T form the Ramsey interference fringes.

It is important in this interferometer scheme that the two traps maintain the same trap frequency and bias, i.e., the energy at the bottom of the trap, throughout the entirety of

the sequence. Changes in trap frequency can come from jitter in the microwave power, phase, or frequency, and must be exceptionally well controlled to realize long interrogation times. Constraints on these parameters are discussed in Chapter 9. Unwanted shifts in the trap bias energy can manifest in the phase of the interferometer, potentially skewing measurements. Moreover, BECs exhibit substantial atom-atom interactions, which can dephase the interferometer. The ultimate goal of the lab is to use fermionic ^{40}K, in which the s-wave scattering length is zero, eliminating this problem. As a precursor, we can still use bosonic ^{87}Rb or ^{39,41}K at temperatures slightly above BEC formation, which should also somewhat limit these collisional effects. Additionally, common-mode DC magnetic noise between each arm of the interferometer can be eliminated by working at so called "magic" magnetic fields [14], in which the differential DC Zeeman shift between the two states in the interferometer is zero.

1.3 Measurements of Interest

While this thesis primarily focuses on the characterization of the ACZ trap and development of a novel microwave atom chip, it is important to keep in mind the future physics that can be explored with the ACZ atom interferometer. Here, I focus on two measurements of interest: gravimetry and sub-mm gravity.

1.3.1 Gravimetry

The sensitivity of the ACZ interferometer for measuring local acceleration due to Earth's gravity is given as (assuming quantum projection noise limited)

$$\Delta g/g = \frac{\hbar}{mgdT\sqrt{N}} \tag{1.2}$$

where $\hbar$ is the reduced Plank's constant, m is the atom mass, g is the acceleration due to gravity, d is the arm separation, i.e., the distance between the two paths of the interfer-

ometer, T is the integration time, and N is the atom number. I will note that $T < T_c$, the coherence time of the system.

An overview of the experimental apparatus and atom chip based interferometry scheme is shown in Fig. 1.3. Briefly, atoms prepared at sub-μK temperatures are prepared on a

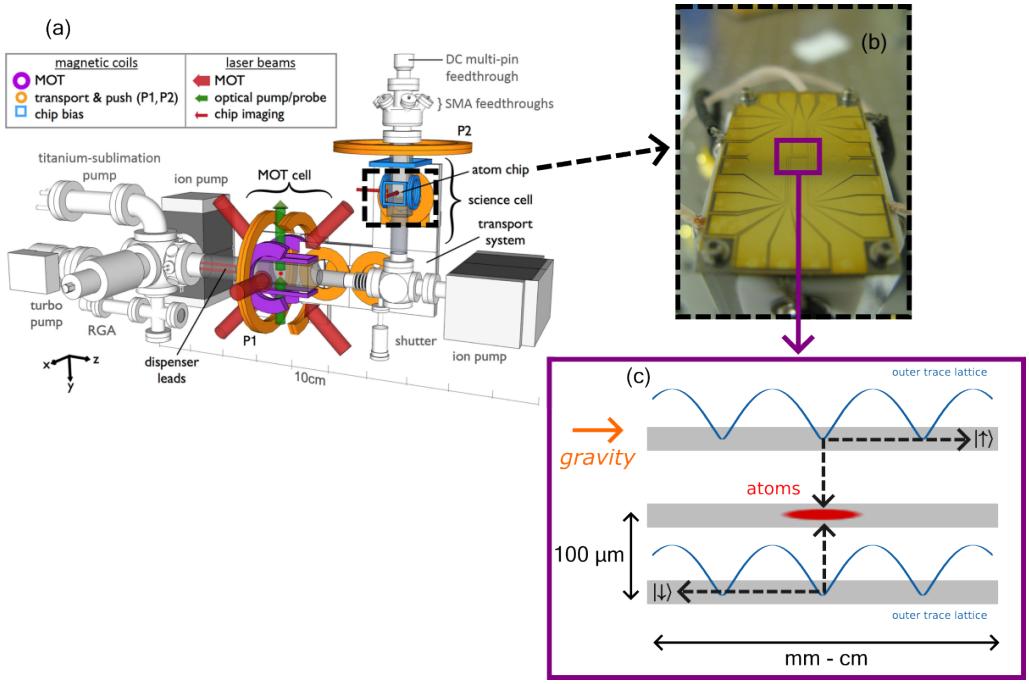

Figure 1.3: Overview of ultracold atom apparatus and atom chip based interferometry scheme. (a) CAD image of the apparatus, taken from Ref. [18]. (b) Birdseye view of the current atom chip installed in the apparatus. The purple box indicates the region featuring parallel atom chip wires where interferometry will take place. (c) Diagram of the gravimeter interferometry scheme, adapted from Ref. [17]. The atoms are split using two spin-specific AC Zeeman traps into microwave lattices for achieving larger arm separations. Gravity points along the direction of the splitting.

micro-fabricated atom chip. A $\pi/2$-pulse puts the atoms in a superposition of two spin states, $|\uparrow\rangle$ and $|\downarrow\rangle$. The different states are then split along the direction of gravity using independent ACZ traps and microwave lattices, before being recombined to complete the interferometer. Specifics on the apparatus and interferometry scheme can be found in Chapters 4 and 9, respectively. Figure 1.4 shows the sensitivity we expect to be able to achieve with the ACZ atom interferometer. Separation of the traps can be done two ways. First, using a three-microstrip configuration, the traps for different spin states can

be spatially separated transversely by changing the phase of the center trace relative to the outer traces [17]. The achievable separation is on par with the trace separation, a few tens to hundreds of μm, and so can be somewhat limiting. With coherence times of 0.5-1 s [16], we should be able to get sensitives of $\Delta g/g \simeq 10^{-9} - 10^{-8}$, on par with commercial cold atom gravimeters (Exail, [19]). Larger arm separations can be obtained via a microwave lattice, allowing for translation of the traps axially along the traces. This scheme is explained in Chapter 3. The arm separation is then limited by the length of the atom chip wires (mm-cm) rather than the inter-trace spacing. If we are able to achieve an arm separation of 1 cm with an integration times of 1 s in this scheme, we will be able to get a sensitivity of $\Delta g/g \simeq 2 \times 10^{-11}$.

1.3.2 Sub-mm Gravity

Another future measurement of interest is that of sub-mm gravity, i.e., testing Newtonian gravity at short length scales. The form of the gravitational potential is typically written as [20, 21]

$$V(r) = -\frac{Gm_1m_2}{r}\left(1 + \alpha e^{-r/\lambda}\right) \tag{1.3}$$

where the parameters α and λ characterize the strength and length scale of the modified gravitational attraction. Such modifications to gravity are motivated by efforts to merge general relativity and quantum field theory. This correction can be attributed to $n \geq 2$ compactified extra dimensions, in addition to the usual four, which get diluted in the long range, but emerge at length scales less than $\mathcal{O}(10^{-4})$ μm [21]. Experiments using torsion pendulums have been able to constrain α at length scales down to $\lambda \approx 50$ μm [22]. At shorter length scales, however, the Casimir-Polder (CP) force [23, 24, 25, 26, 27], originating from vacuum fluctuations of the atom's dipole moment interacting with a surface, cannot be ignored. Following the treatment in Ref. [28], we can calculate the acceleration of a ^{87}Rb from the CP force and compare it to that caused by gravity, plotted in Fig. 1.5. For a temperature of 300 K, the acceleration of a ^{87}Rb due to the CP force at a distance of

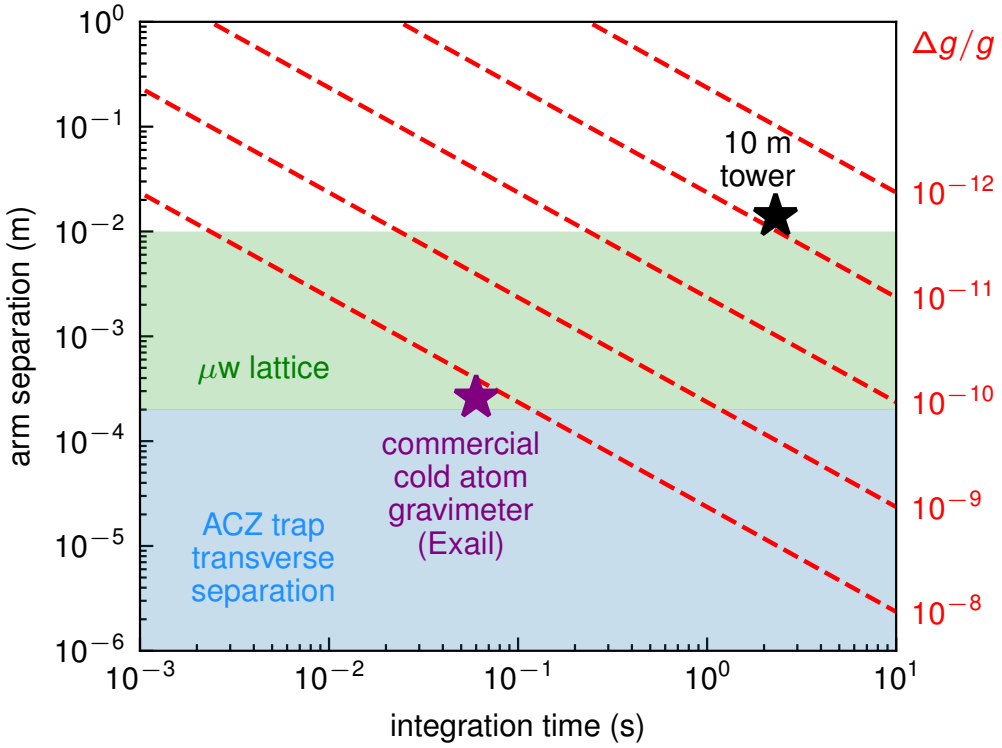

Figure 1.4: Expected per-cycle sensitivity of an ACZ chip based gravimeter with 10^5 atoms, given by Eq. 1.2. Red dashed curves indicate lines of constant sensitivity. The blue shaded region indicates the region of arm separations achievable through transverse separation of the two traps, on the order of the trace separation [17]. The green shaded region shows the sensitivities obtainable with the implementation of a microwave lattice, yielding much longer axial separations. Values for the commercial and 10 m tower gravimeters come from Refs. [19] and [3], respectively, both of which operate with the atoms in free-fall.

50 μm from the surface of a 1 mm tungsten sphere is roughly 37 times larger than the acceleration due to gravity at the same distance. Gravity only begins to dominate over the CP force at distances larger than about 125 μm. We can work around this by placing a thin, low density dielectric membrane, such as SiO_2, between the atoms and test mass, as shown in Fig. 1.6. This membrane, which could be the atom chip itself, acts as a screen for CP interactions between the atoms and test mass, so by moving the test mass around, we should be able to distinguish effects due to gravity in the atom interferometer signal from a common CP signal.

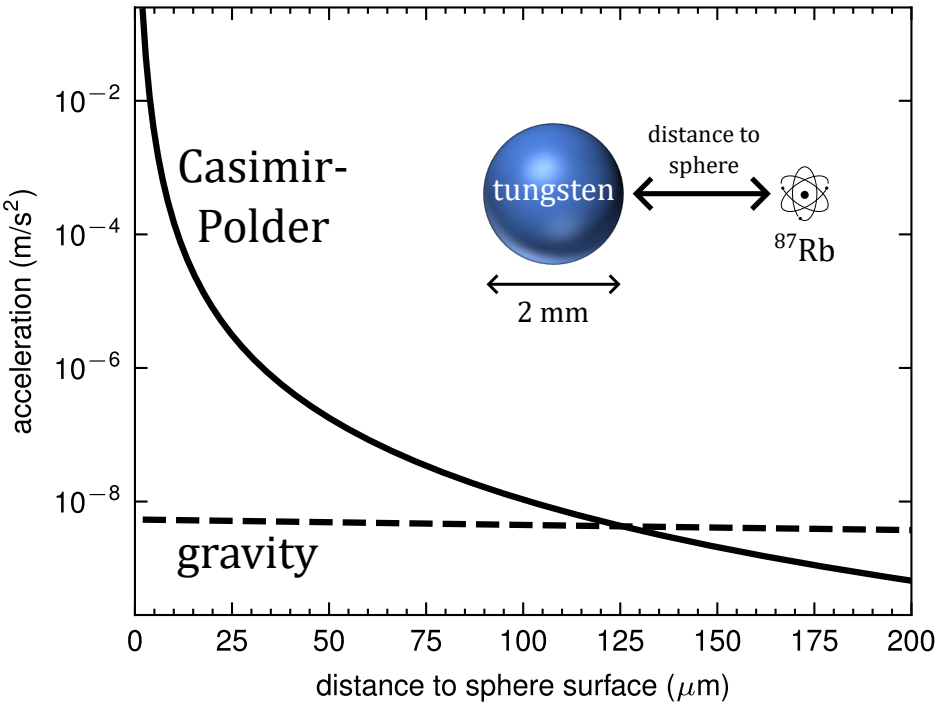

Figure 1.5: Acceleration of a ^{87}Rb atom due to gravity (dashed line) and the Casimir-Polder (solid line) forces as a function of distance to the surface of a 1 mm radius tungsten sphere.

The accumulated phase of the interferometer is given as

$$\phi = \frac{GMm_{atom}T}{\hbar}\left(\frac{1}{r+R} - \frac{1}{r+d+R}\right) \tag{1.4}$$

where $G = 6.6743$ m^3/kg/s^2 is the gravitational constant, M is the mass of the sphere of radius R, m_{atom} is the mass of the atom being used, T is the integration time, r is the distance of the atom to the sphere surface, and d is the arm separation. Figure 1.7 plots the accumulated phase as a function of integration time for arm separations up to 1 cm, achievable using the microwave lattice. Incorporating the lattice in this scheme improves the interferometer phase by roughly an order of magnitude over what is obtained using transverse separation ($\sim$100 μm). The interferometer phase noise is given by the standard quantum projection noise, $\delta\phi \approx 1/\sqrt{N}$ [29], where N is the atom number. The

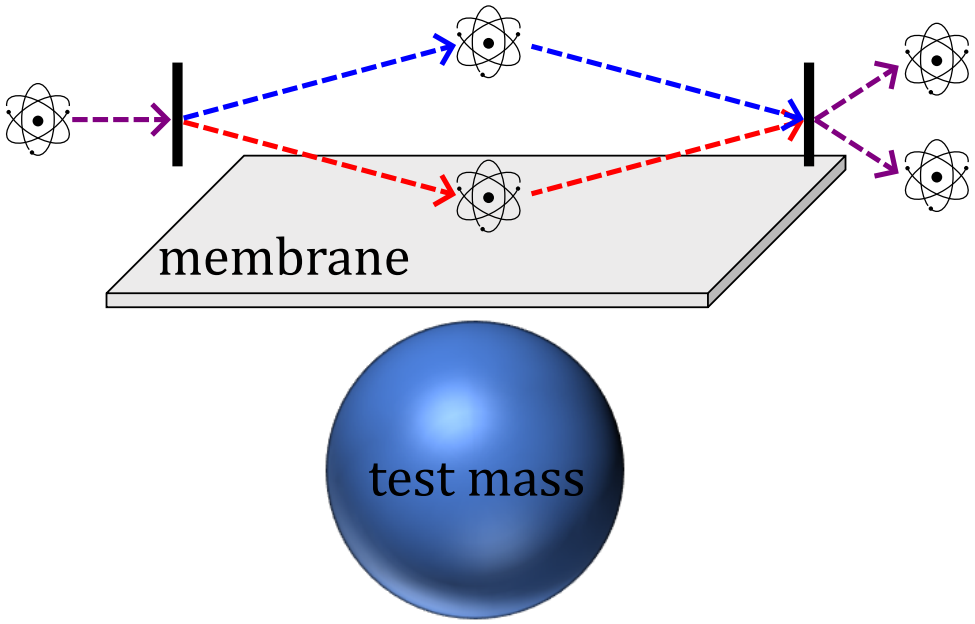

Figure 1.6: Experimental scheme for measuring sub-mm gravity. A thin dielectric membrane is placed between the interferometer (see Fig. 1.2) and test mass to help decouple Casimir-Polder effects from short range gravity measurements.

signal-to-noise ratio (SNR) of the measurement is then given as

$$SNR = \frac{\phi}{\delta\phi} = \phi\sqrt{N} \propto T \tag{1.5}$$

1.4 Structure of the Thesis

The thesis is structured in the following way: Chapters 2 and 4 set the stage for performing experiments in our lab by discussing the theory and apparatus behind the production of ultracold atoms. We give the theory of the AC Zeeman (ACZ) effect in the dressed atom framework in Chapter 3. The implementation of an ACZ trap on an atom chip is discussed in Chapter 5. Chapter 6 contains the main experimental work of this thesis: the demonstration of potential roughness suppression in a radio-frequency ACZ trap. We then move onto the design and simulation of a novel microwave atom chip in Chapter 7. Chapter 8 continues this by developing a tapered microstrip wedge coupler to efficiently transmit

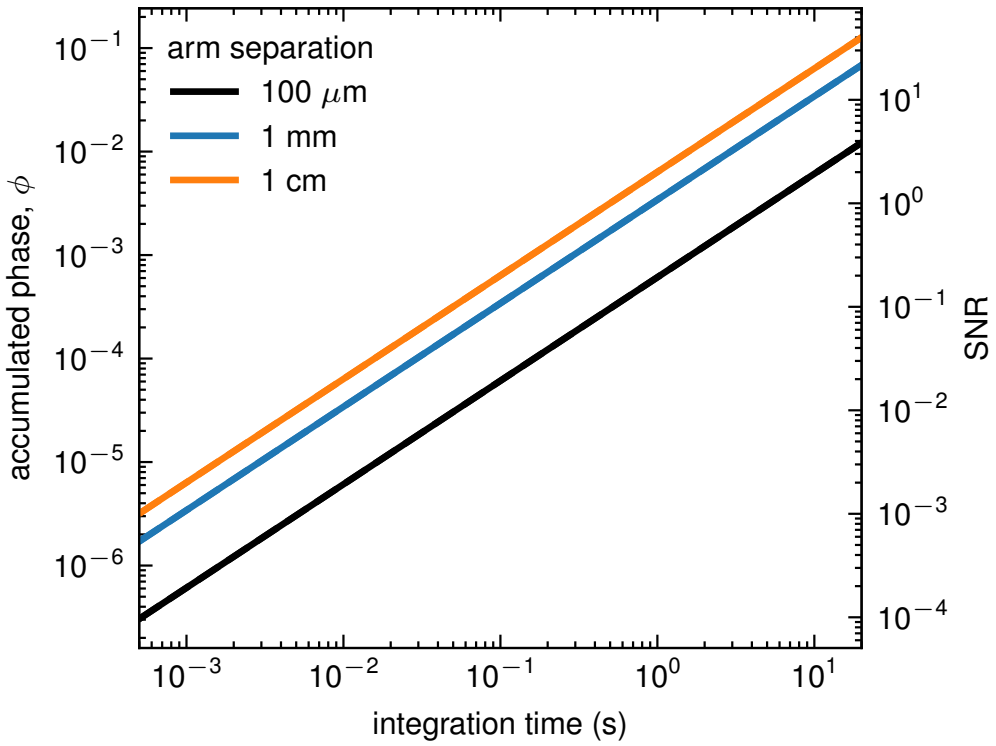

Figure 1.7: Expected signal for measuring the effect of gravity for ^{87}Rb atoms 50 μm from the surface of a 1 mm radius tungsten sphere. The accumulated phase is calculated using Eq. 1.4.

broadband AC signals onto the thin atom chip traces. Finally, Chapter 9 summarizes the work and provides an outlook for future experiments. Relevant code for this thesis can be found in Ref. [30].

Chapter 2

Ultracold Atom Theory

The idea that matter can have wavelike properties was first postulated by Louis de Broglie in his 1924 PhD thesis [31]. The typical wavelength of an atom at a given temperature is given by the thermal de Broglie wavelength [32],

$$\lambda_{dB} = \frac{h}{\sqrt{2\pi m k_B T}} \tag{2.1}$$

where h is Plank's constant, m is the mass of the atom, k_B is Boltzmann's constant, and T is the temperature of the atom. At normal temperatures, these atomic wavelengths are extremely small, as illustrated in Fig. 2.1. To realize a coherent matter wave, we need to reach a state in which the wavelength of the atoms is on the order of, or larger than, the inter-particle spacing. We can characterize this relation via a quantity known as the phase space density (PSD):

$$PSD = n\lambda_{dB}^3 \tag{2.2}$$

where n is the atom density. When $PSD \geq 2.612$, a collection of bosonic atoms undergoes a phase transition into a new state of matter called a Bose-Einstein Condensate (BEC).

First theorized in the 1920s [35], the ability to reach such a state requires atoms to be at extremely low temperatures. The notion that lasers, introduced in 1960 [36], could trap and cool atoms via radiation pressure came from Arthur Ashkin in 1978 [37]. Inspired by this

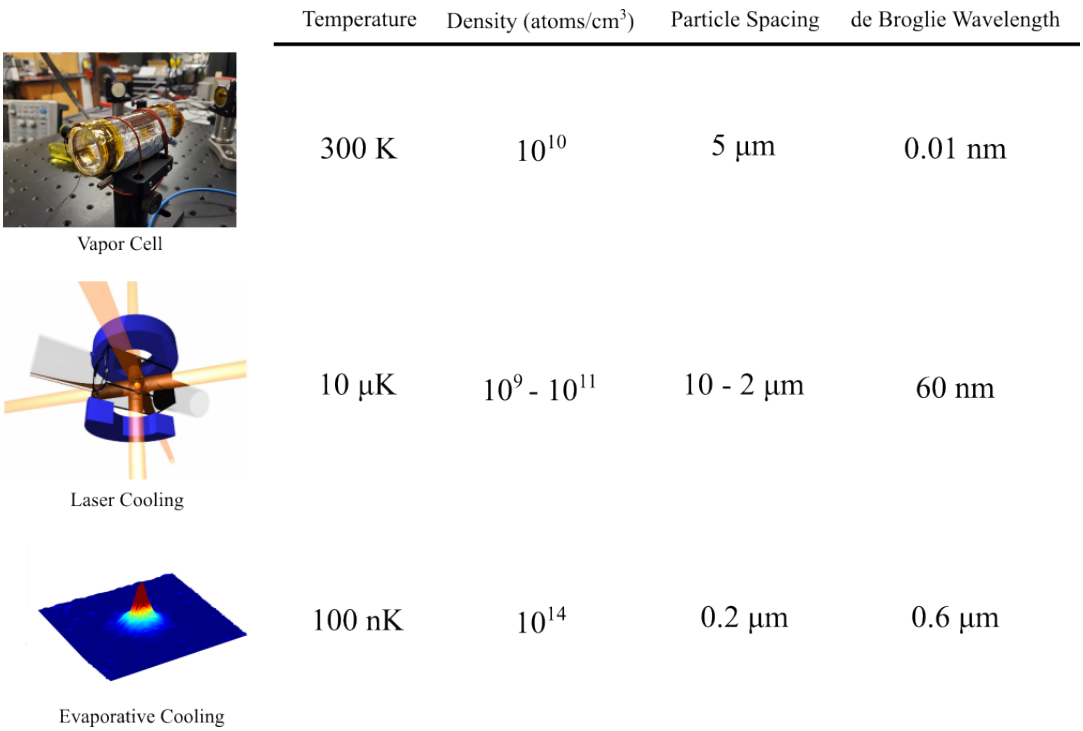

Figure 2.1: Atom density and de Broglie wavelength for different atomic systems along the journey to Bose-Einstein condensation. The particle spacing is given as $n^{-1/3}$, where n is the atom density. The de Broglie wavelength is calculated from Eq. 2.1 using rubidium-87 and the given temperature. Values for the density in the vapor cell are from [33], and density values for the laser and evaporative cooling are from [34].

work, researchers began efforts to laser cool atoms, demonstrating the cooling of a neutral sodium atomic beam in 1985 [38, 39]. The first observation of magnetically trapping cold neutral atoms was seen later that year [40], and the now-standard magneto-optical trap (MOT) was introduced in 1987 [41], which provided simultaneous cooling and trapping of neutral atoms. Experimental evidence of cooling below the so-called Doppler limit of laser cooling [42] sparked the theoretical description of sub-Doppler optical molasses cooling in 1989 [43], opening the pathway to bring atom temperatures to tens of microKelvin. It took several more years to achieve temperatures low enough to observe BEC formation, notably with the development of evaporative cooling. In 1995, groups in Boulder, CO [44] and MIT [45] achieved the first experimental observations of BEC. Atom chips [46, 47, 48, 12], introduced a few years later, allowed experimenters to generate complex electromagnetic

fields using microscopic wires for producing and manipulating ultracold atoms.

In this chapter, I go through the theoretical background of the methods used to cool and trap neutral atoms to BEC in the Aubin lab. In Sec. 2.1, I discuss how two counter-propagating laser beams can impart a cooling force on atoms. Section 2.2 introduces the concept of magnetic trapping, and Sec. 2.3 discusses the magneto-optical trap (MOT), the workhorse of laser cooling experiments. Cooling below the Doppler limit via Sisyphus cooling is the topic of Sec. 2.4, which brings the atom temperature down to tens of μK. Once there, the atoms are optically pumped and magnetically transported (Sec. 2.5) onto a micro-magnetic atom chip trap (Sec. 2.6). Finally, we cover evaporative cooling in Sec. 2.7, which takes atoms into the BEC state. More in-depth discussions on laser cooling and trapping can be found in Refs. [49, 50].

2.1 Doppler Cooling

Consider a two-level atom in the presence of a laser, as shown in Fig. 2.2. The atom reacts to the laser by scattering it through a process of absorption and re-emission of the laser light, at a rate γ_s. Each time the atom absorbs a photon of light, it receives a backwards momentum kick $\hbar k$, where $\hbar$ is the reduced Plank's constant and $k = 2\pi/\lambda$ with λ being the wavelength of the laser. For ^{87}Rb, this changes the atom's velocity by $v_{kick} = 6$ mm/s. The force exerted on the atom by the laser is then the total number of momentum kicks given by the scattered photons. In 1-D:

$$\begin{aligned} F &= \hbar k \gamma_s \\ &= \hbar k \frac{s_0}{1 + s_0 + (2\delta_l/\gamma)^2} \frac{\gamma}{2} \end{aligned} \tag{2.3}$$

where $s_0 = I/I_s$ is the saturation parameter with I_s being the saturation intensity, γ is the natural linewidth of the atomic transition ($2\pi \times 6$ MHz for the D2 line in ^{87}Rb), and δ_l is the detuning of the laser from the atomic transition. For an atom moving at velocity

v, the laser detuning will be shifted due to the Doppler effect, so that $\delta = \delta_l \pm kv$, where the $\pm$ sign refers to the direction of the applied laser with respect to the atom's motion. If we apply two counter-propagating lasers (see Fig. 2.2), the total force on the atom is

$$F_{tot} = \frac{\hbar k \gamma s_0}{2} \left\{ -\frac{1}{1 + s_0 + \left[\frac{2(\delta_l + kv)}{\gamma}\right]^2} + \frac{1}{1 + s_0 + \left[\frac{2(\delta_l - kv)}{\gamma}\right]^2} \right\} \tag{2.4}$$

We plot this force as a function of atom velocity in Fig. 2.3. If we look at small velocities (i.e. $|kv| << \delta_l$) then F_{tot} can be written in the form of a damping force as

$$F_{tot} \simeq \frac{8\hbar k^2 \delta_l s_0}{\gamma(1 + s_0 + (2\delta/\gamma)^2)} v = -\beta v \tag{2.5}$$

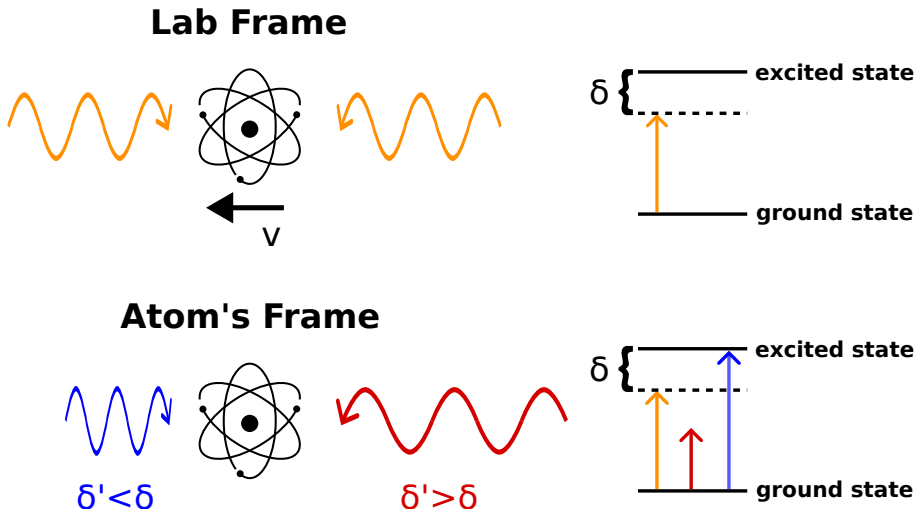

Figure 2.2: Doppler laser cooling. In the lab frame, the atom moves in some direction with velocity v, and we apply counter-propagating lasers red-detuned from the energy splitting between the ground and excited states. From the perspective of the atom, it is at rest while the lasers get red- or blue-detuned depending on the atom's direction of motion. The atom is now more likely to absorb a photon from the laser in the counter-propagating direction of its motion and receive a backwards momentum kick, ultimately slowing it down and cooling the atom.

We see that the lasers apply a restoring force to the atoms such that whichever way they move, they will absorb a photon and receive a momentum kick, pushing them backwards.

While this momentum kick imparts only about a 6 mm/s change to the atom's velocity, the atom scatters on the order of 10^7 photons/second. It is the cumulative process of these momentum kicks that acts to slow the atoms down, in turn lowering their temperature.

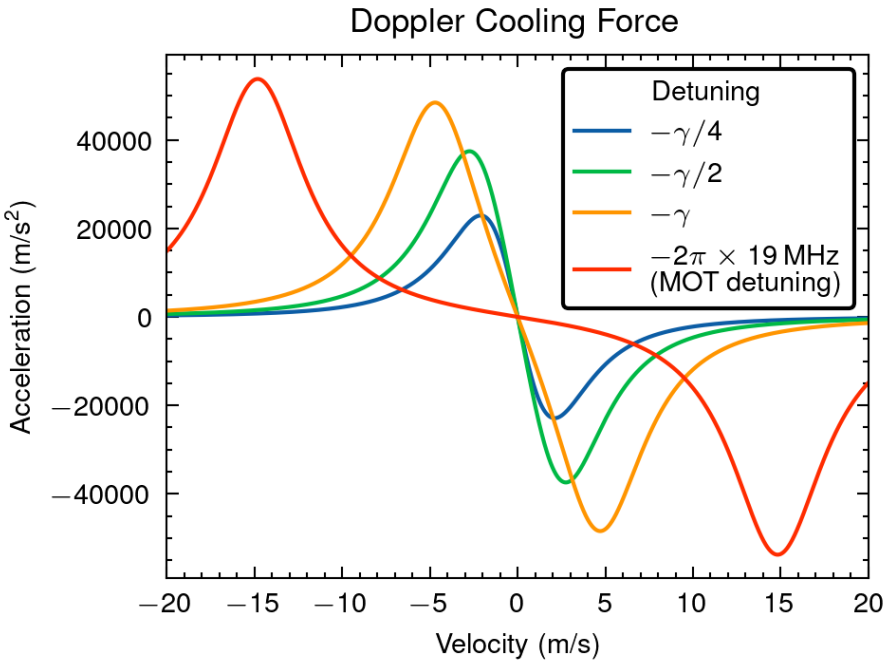

Figure 2.3: 1-dimensional Doppler cooling force on a two-level atom plotted for different laser detunings (Eq. 2.4). For low atom velocities, the acceleration depends linearly on the velocity.

2.1.1 Doppler Cooling Limit

Each time the atom in Fig. 2.2 absorbs a photon and receives a momentum kick, it eventually has to re-emit that photon. When doing this reemission, the atom receives another momentum kick in a random direction, in turn heating it up. From this argument, we can put a lower bound on how cold we can make our atomic sample through Doppler cooling. This temperature can be derived using the equilibrium condition that the cooling rate from the lasers is equal to the heating rate from reemission [51, 52]. The Doppler temperature

is set by the natural linewidth of the atomic transition, γ, and is given as (for $\delta_l = -\gamma/2$)

$$T_{Doppler} = \frac{\hbar\gamma}{2k_B}. \tag{2.6}$$

For laser cooling ^{87}Rb on the D2 line, which has a linewidth of $\gamma = 2\pi \times 6$ MHz, we get that the Doppler cooling limit is 144 μK, corresponding to a deBroglie wavelength of $\lambda_{dB} = 0.015$ μm. For typical MOT densities on the order of $10^{10} - 10^{11}$ atoms/cm^3, this temperature yields a phase space density still several orders of magnitude smaller than that necessary for BEC formation. Further cooling techniques must then be used, which will be discussed in the following sections. First, however, it is necessary to introduce the concept of magnetic trapping and control, as otherwise our laser cooled atoms would not be confined.

2.2 Magnetic Trapping

In the presence of a magnetic field, our atoms, which have a magnetic dipole moment $\vec{\mu}$, respond via the Zeeman effect. The case of an external magnetic field oscillating in time, dubbed the AC Zeeman (ACZ) effect, will be described and studied in later chapters. For now, we will focus on the DC Zeeman (DCZ) effect, in which the atom interacts with a magnetic field stationary in time. At magnetic field strengths which cause energy shifts much smaller than the hyperfine splitting, our atomic states are well described by the total angular momentum quantum numbers $F^2 = F(F+1)$ and F_z, and $|F, m_F\rangle$ are eigenstates of the atomic Hamiltonian. For reference, the ground state $5S_{1/2}$ hyperfine splitting in ^{87}Rb between the $F = 1$ and $F = 2$ levels is $\Delta_{hfs} \approx 6.834$ GHz. This low-field limit applies when $\mu_B B_{DC} << \Delta_{hfs}$, where $\mu_B \approx 1.4$ MHz/G is the Bohr magneton, and B_{DC} is the strength of the applied magnetic field. In this limit, the Zeeman sub-levels in each hyperfine manifold are split linearly as

$$U_{DCZ} = -\vec{\mu} \cdot \vec{B}_{DC} = g_{_F} m_{_F} \mu_{_B} |\vec{B}_{DC}|, \tag{2.7}$$

where g_F is the gyromagnetic factor, equal to $\{+1/2, -1, 2\}$ for the $F = \{2, 1\}$ $5S_{1/2}$ level, and m_F is the Zeeman sub-level, where $F_z |F, m_F\rangle = m_F |F, m_F\rangle$. Figure 2.4 calculates these energy shifts using the well-known Breit-Rabi formula [53]. It can be clearly seen from the figure that states with $g_F m_F > 0$ are shifted up in energy, while states with $m_F g_F < 0$ are shifted down. The $m_F = 0$ state, in theory, feels zero shift, according to Eq. 2.7, however, in reality, at high field, it does also get shifted slightly, as indicated in the figure.

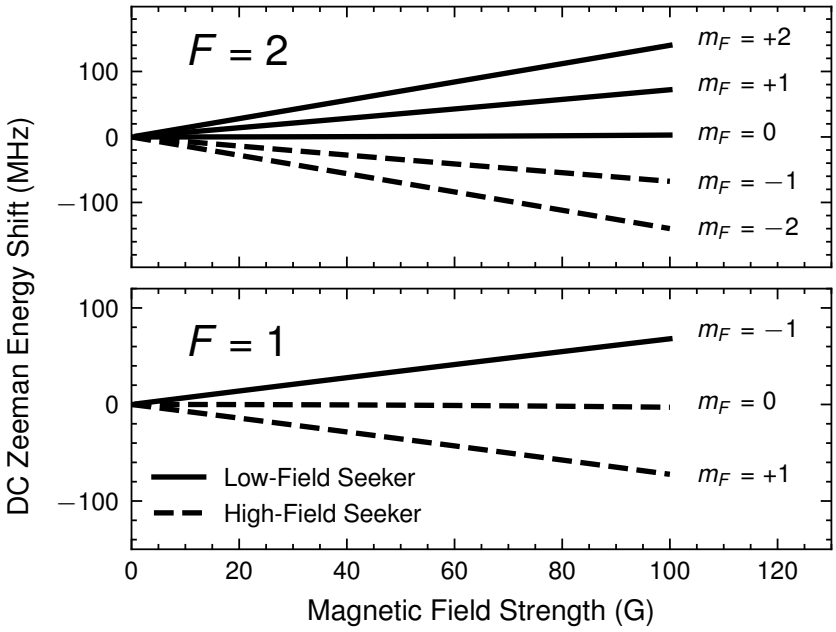

Figure 2.4: DC Zeeman energy shift for ^{87}Rb atoms in the ground state hyperfine manifolds, calculated using the Breit-Rabi formula. The shift is taken with respect to the zero-field energy. Low- and high-field seeking states are indicated by the solid and dashed lines, respectively.

Given this energy shift, we can next look at the force felt by the atoms in the presence of an external magnetic field, which is given as

$$F_{DCZ} = -\nabla U_{DCZ} = -g_F m_F \mu_B \nabla |\vec{B}_{DC}| \tag{2.8}$$

To minimize their energy, atoms with $g_F m_F > 0$ will experience a force pushing them to regions of lower magnetic field. These states are dubbed "low-field seekers". Conversely,

states with $g_F m_F < 0$ feel a force guiding them to regions of high magnetic field, giving them the name, "high-field seekers". For ^{87}Rb, these states are indicated by the solid (low-field seeker) and dashed (high-field seeker) lines in Fig. 2.4. Earnshaw's theorem for magneto-statics [54, 55] tells us that magnetic maxima cannot exist in free space. Thus, if we want to trap atoms using magnetic fields, we can only confine low-field seekers by creating a region in space containing a minimum in the magnetic field. Note that this field must also be strong enough to trap against the force of gravity, which requires a minimum gradient of 15 G/cm for ^{87}Rb in the $|2,2\rangle$ state [56]. We can use this fact to spin purify our cold atoms into this edge state, as atoms in the $|2,1\rangle$ or $|1,-1\rangle$ states need to overcome a gravitational gradient twice as strong, i.e., 30 G/cm. This was observed in our system [57], marking the first quantum signal achieved in the cold atom apparatus.

An important note about magnetic traps is the idea of adiabaticity. As the atom moves around in the magnetic trap, its magnetic moment must remain oriented such that it is a low-field seeker. If the confining magnetic field goes to zero at any point, the atom's magnetic moment no longer has a preferred direction. In this case, the atom could flip into another spin state that is a high-field seeker, being ejected from the trap in the process. This phenomenon is known as Majorana spin flip losses. To avoid these losses, the atom must move slowly enough in the trap such that its magnetic moment can smoothly respond to the inhomogeneous confining magnetic field. Put more formally,

$$\frac{U_{DCZ}}{\hbar} >> \frac{1}{B}\left|\frac{dB}{dt}\right| \tag{2.9}$$

where U_{DCZ} is given in Eq. 2.7. We can see that when $B \to 0$, this condition no longer holds.

2.3 Magneto-Optical Trapping

In the Doppler cooling scheme described in the previous section, as the atoms absorb and spontaneously emit the laser light, they undergo a random walk in phase space. Thus, there is nothing stopping the atoms from leaving the path of the cooling lasers and being lost. To be able to take advantage of the laser cooling mechanism, we need a method of trapping the cold atoms. We achieve this by cleverly adding in a spatial dependence to the optical force applied to the atoms by the laser light so that if they try to leave the trap area, the lasers apply a restoring force pushing them back towards the center of the trap. This spatial dependence is achieved by adding a magnetic field gradient produced by two coils in an anti-Helmholtz configuration. Note that the confinement comes not from a magnetic trapping force (e.g., see Sec. 2.2), but from a spatially varying atomic resonance controlled by a DC Zeeman shift. Figure 2.5 shows the operation of the MOT. If we consider an atom with ground state F=0 (so m_F can be only 0) and excited state F=1 (so $m_F = -1, 0, 1$), then we see that the presence of the magnetic gradient results in a DC Zeeman shift of the excited state m_F levels. Thus, if an atom moves to the left (i.e., towards the σ^+ polarized beam), the $m_F = 1$ state is Zeeman shifted closer to resonance with the applied laser, so the atom will preferentially absorb the σ^+ light. Conversely, when the atom moves to the right, it will preferentially absorb the σ_- polarized beam, transitioning to the $m_F = -1$ excited state. In both cases, we see that as the atom tries to move away from the center of the trap, it absorbs a photon and receives a momentum kick back towards the trap location, thus adding spatial dependence to the Doppler cooling. In our apparatus, the magnetic gradient is $\sim$9 G/cm, and we are able to trap $\sim 5 \times 10^8$ ^{87}Rb atoms. A feature of the MOT not demonstrated in Fig. 2.5 is the tendency for atoms to get optically pumped into the lowest energy ground state. For ^{87}Rb, this corresponds to the $|F = 2, m_F = -2\rangle$ state [49].

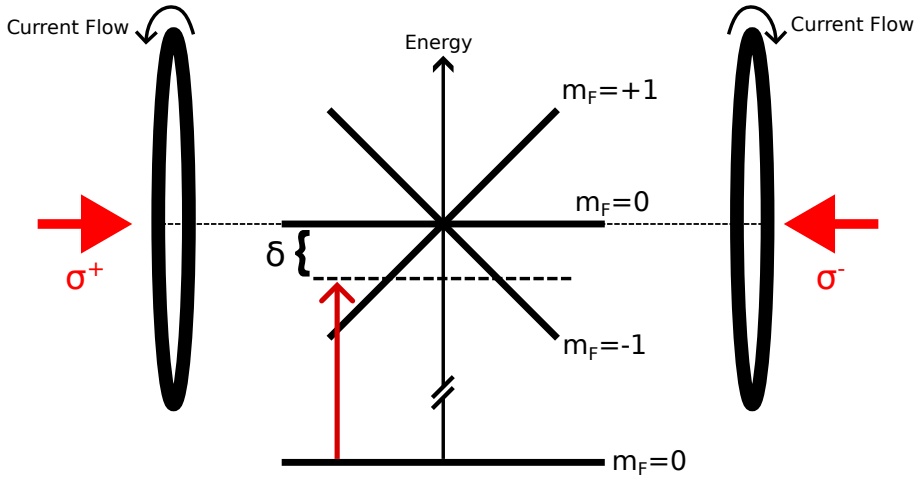

Figure 2.5: Cartoon depiction of the magneto-optical trap (MOT). Here we consider the case of an atom with ground state F=0 and excited state F=1. Two magnetic coils operated in an anti-Helmholtz configuration produce a magnetic field with a linear gradient. This gradient causes a DC Zeeman shift of the degenerate hyperfine sub-levels. Counter-propagating lasers with opposite circular polarization are red-detuned from the atomic resonance. For an atom in the ground state moving to the left (towards the σ^+ beam), the frequency of the laser gets closer to resonance with the $m_F = +1$ excited state, so it absorbs a σ^+ photon transitioning from the $m_F = 0 \Rightarrow m_F = +1$ state. When it absorbs the photon, the atom receives a momentum kick back towards the center of the magnetic field. For an atom moving towards the σ^- beam, the opposite happens, and it preferentially absorbs a photon to transition from $m_F = 0 \Rightarrow m_F = -1$. This added quadrupole magnetic field acts to add a spatial dependence to the optical force on the atoms, thus providing a mechanism for confinement.

2.4 Sub-Doppler Cooling

When the first laser cooling experiments with neutral sodium atoms were being performed in the 1980s, it was discovered that the Doppler cooling process worked better than intended, not words you often hear in an experimental setting. Specifically, experimenters found that they were able to achieve temperatures of ∼40 μK, several times lower than the theoretical Doppler temperature limit for ^{23}Na of 240 μK [42]. The origin of this extra cooling comes from the fact that our atoms are not truly two-level systems, and that these levels are degenerate without a magnetic field present.

To understand this mechanism, consider the 1D case, in which we have two counter-propagating lasers traveling along the z-direction. As in our MOT setup, we take the lasers to have perpendicular polarizations. Here, we look at the case of perpendicular

linear polarizations, dubbed the lin⊥lin configuration. The total field is then

$$E_{total} = E_1 + E_2 = E_0 \cos(kz - \omega t)\hat{x} + E_0 \cos(kz + \omega t)\hat{y} \tag{2.10}$$

where $k = 2\pi/\lambda$ with λ being the wavelength of the laser. With a bit of algebra, we can rewrite this expression as

$$E_{total} = \frac{E_0 e^{i(kz-\omega t)}}{\sqrt{2}} \underbrace{\frac{\hat{x} + e^{-i4\pi z/\lambda}\hat{y}}{\sqrt{2}}}_{\hat{\epsilon}(z)} + C.C. \tag{2.11}$$

where $C.C.$ is shorthand for complex conjugate. We see that the result is a traveling wave with a spatially dependent polarization, $\hat{\epsilon}(z)$. Mapping out this polarization, we find that it forms a standing wave with a period of $\lambda/2$, half the optical wavelength. This gives a gradient in the polarization of the light field, which is why this method is often referred to as polarization gradient cooling. We also frequently refer to this stage of cooling as optical molasses.

Consider now how this polarization gradient will affect our atoms in the absence of a magnetic field. As a simple example, take the ground state to be the state $F_g = 1/2$ (two-fold degenerate) and the excited state to be $F_e = 3/2$ (four-fold degenerate). In the presence of the combined red-detuned laser field, the ground state atomic energy levels will experience a spatially varying AC Stark shift whose strength depends on the polarization of the field and the Clebsch-Gordan (CG) coefficient for the corresponding transition [49, 50]. The CG coefficients for the different transitions are given in Fig. 2.6. When the field is pure σ_- polarization (at $z = \lambda/8$), the $m_g = -1/2$ ($m_g = +1/2$) ground state gets shifted down (up) in energy. At this point, any atoms in the $m_g = +1/2$ state will be shifted closer to resonance and get pumped into the $m_g = -1/2$ state via the polarization of the light. As the atom continues to travel along the polarization gradient, it must "climb" a potential energy hill, thereby losing kinetic energy along the way. After traveling a distance $\lambda/4$, the polarization of the light field becomes pure σ_+, and the atom in the $m_g = -1/2$ state

gets optically pumped into the lower energy $m_g = +1/2$ state. This process continues with the atom in a seemingly endless cycle of climbing the potential energy hill and reducing its kinetic energy, i.e., temperature. Inspired by the Greek myth, this mechanism is also referred to as Sisyphus cooling. In practice, we are able to achieve temperatures of around

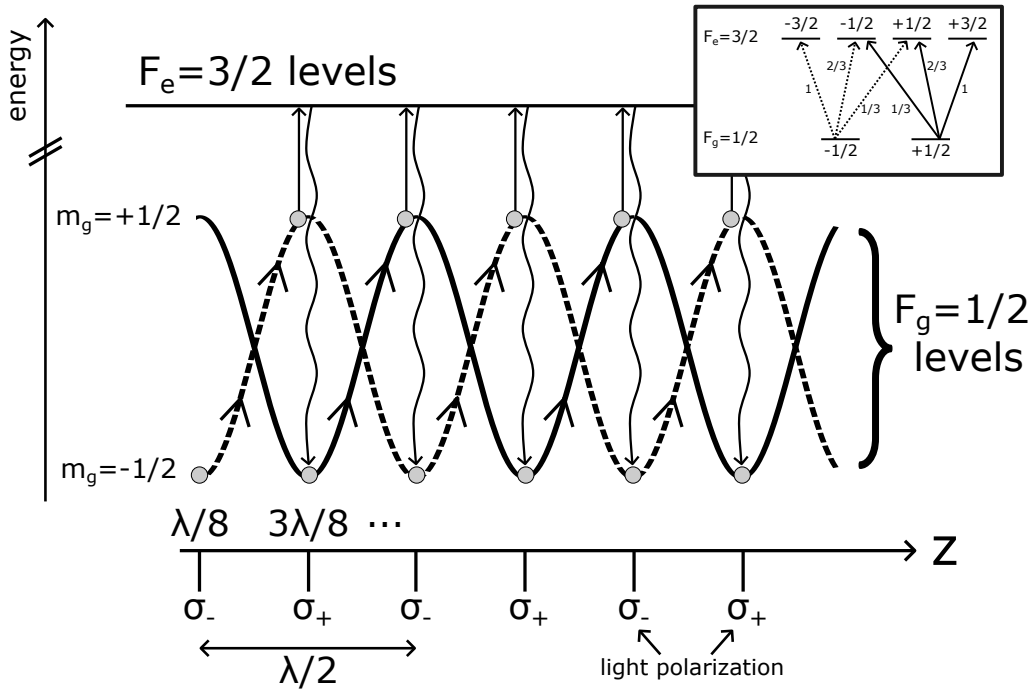

Figure 2.6: Sisyphus cooling mechanism. Counter-propagating, red-detuned lasers with orthogonal polarization (lin⊥lin) form a polarization standing wave of wavelength $\lambda/2$. Atoms in the ground state levels, $m_g = \pm 1/2$, experience a spatially varying AC Stark shift. An atom (gray circles) starting in the $m_g = -1/2$ level (dashed curve) must climb the AC Stark potential hill. After traveling a distance $\lambda/4$, the atom is pumped into the $m_g = +1/2$ level (solid curve), beginning the process over again until the atom no longer has enough kinetic energy to climb the hill. Inset: Atom energy level diagram. Coupling strengths between levels are indicated by the Clebsch-Gordan coefficients. Figure adapted from [50, 49].

15 μK after this stage of cooling [51]. In principle, this method can approach the recoil limit of 0.4 μK.

2.5 Optical Pumping and Magnetic Transport

After sub-Doppler cooling, atoms are transported into a micro-magnetic atom chip trap. This transport is done via a translating magnetic trap [18]. Since only certain m_F states

are DC magnetic field trappable, we need to be able to prepare our atoms in a specific $|F, m_F\rangle$ state. For us, this is the $|2, 2\rangle$ state in ^{87}Rb. We perform this via optical pumping, in which we take advantage of atomic selection rules to "pump" all of our atoms into this stretched state. This works by sending in σ^+ circularly polarized light acting on the $5S_{1/2}(F = 2) \longleftrightarrow 5P_{3/2}(F' = 2)$ D2 transition. Absorption of the σ^+ light by the atom changes the internal state of the atom from $|F = 2, m_F\rangle$ to $|F' = 2, m_F + 1\rangle$ due to selection rules. Once in the upper $5P_{3/2}$ manifold, the atom can decay back down to the $5S_{1/2}$ level, where the probability to end up in a given m_F state is dictated by the branching ratios [53]. After successive absorption and emission of the laser light, all of the atoms will be in the stretch state, $|F = 2, m_F = 2\rangle$. Operating on this $F = 2 \longleftrightarrow F' = 2$ transition is advantageous compared to the $F = 2 \longleftrightarrow F' = 3$ optical pumping scheme, since once in the $|2, 2\rangle$ state the atom is insensitive to σ^+ light (i.e., the atoms go "dark"), meaning the cloud will not heat due to photon recoil.

2.6 Atom Chip Trapping

After atoms are cooled in the MOT cell, they are transferred onto a "traditional" DC atom chip trap. This trap operates by creating a magnetic minimum for DC low-field seeking atomic states ($|F = 2, m_F = 2\rangle$, $|F = 2, m_F = 1\rangle$, and $|F = 1, m_F = -1\rangle$ in the ^{87}Rb ground state). Atoms in any of these states will feel a force pushing them to that magnetic minimum, thus trapping them. Conversely, DC high-field seeking states will be anti-trapped in this configuration and expelled from the trapping region. The trappable states are highlighted in Fig. 2.7(a).

To create this minimum, we send DC current through a single Z-shaped chip wire to generate a magnetic field directed azimuthally around the wire. I will note that the current supply used here must be ultra-low-noise, that is, the current jitter is several orders of magnitude smaller than the current sent through the chip. Our current supplies used for chip trapping feature fractional noise on the order of a part in 10^{-6}. Large current

fluctuations can result in heating of the atoms and limit the trap lifetime. An external bias field, known as the hold field, B_{ext}, is applied in the opposite direction as the wire field, canceling it out at some location y_{trap} below the atom chip (see Fig. 2.7(b)). Using simple infinite 1D wire theory, the distance of the trap from the chip can be calculated as

$$y_{trap} = \frac{\mu_0 I}{2\pi |B_{ext}|} \tag{2.12}$$

where μ_0 is the vacuum permeability, I is the current through the wire, and $|B_{ext}|$ is the magnitude of the external hold field.

Longitudinal (z) confinement is achieved through the Z-shaped nature of the wire, shown in Fig. 2.7(c). In this configuration, the ends of the Z, dubbed the endcaps, provide a Helmholtz-like field which contains a minimum in the magnetic field along the central section. Additionally, an external field along the z-direction (B_{Ioffe}) acts to raise the minimum of the trapping field from zero, helping get rid of spurious Majorana spin flip losses (see Sec. 2.2).

2.6.1 Realistic Chip Wires

While the use of infinitely long and infinitely thin 1D wires provides a simple way of modeling the magnetic fields generated by the atom chip wires, in reality, the wires on the atom chip are cuboids that are tens or hundreds of microns wide and a few microns thick. This necessarily changes the form of the magnetic field close to the wires, in turn modifying the trap location. The magnetic field above a rectangular wire of zero height and width w is given as [59]

$$B(y) = \frac{\mu_0 I}{\pi w}\left[\frac{\pi}{2} - \tan^{-1}\left(\frac{2y}{w}\right)\right] \tag{2.13}$$

As before, setting the above equation equal to a counter-directional uniform field, B_{hold}, we can obtain the distance of the trap above the chip. Figure 2.8 shows the distance of atoms

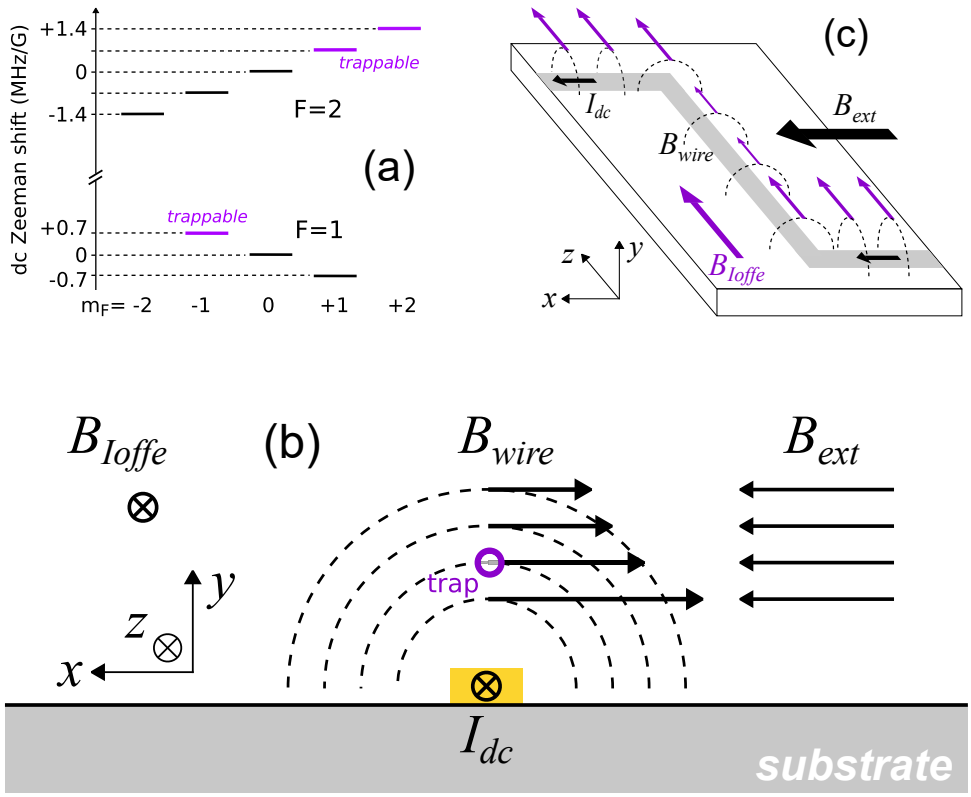

Figure 2.7: Operation of the Z-wire DC atom chip trap. (a) Splitting of the m_F Zeeman levels in the ground state hyperfine manifolds of ^{87}Rb. For low magnetic fields, the splitting is nearly linear at 0.7 MHz/G. States that experience a positive DC Zeeman shift are trappable low-field seeking states. (b) A transverse (xy) minimum in the magnetic field is generated by applying an external magnetic field, B_{ext}, which cancels out the wire field, B_{wire}, at one location. An additional magnetic field, B_{Ioffe}, is oriented along the z-direction and acts to raise the trap energy minimum to avoid spin flip losses. (c) Full 3D view of the Z-wire trace and associated magnetic fields. The ends of the wire, in addition to B_{Ioffe}, provide axial confinement along the z-direction. Figure taken from Ref. [58].

from the chip in a Z-wire chip trap measured using dark-spot imaging (see Chapter 6). For trap heights on the order of the wire width or less, we see divergence between Eqs. 2.13 and 2.12, which is reflected in the data. The finite width of the atom chip wires can also be approximated by breaking the rectangular conductor into N equally spaced, infinitely thin wires, each carrying current I/N. For $N \to \infty$, this should match the rectangular wire. This approximation can prove useful when there is no clean, closed-form expression for the magnetic field.

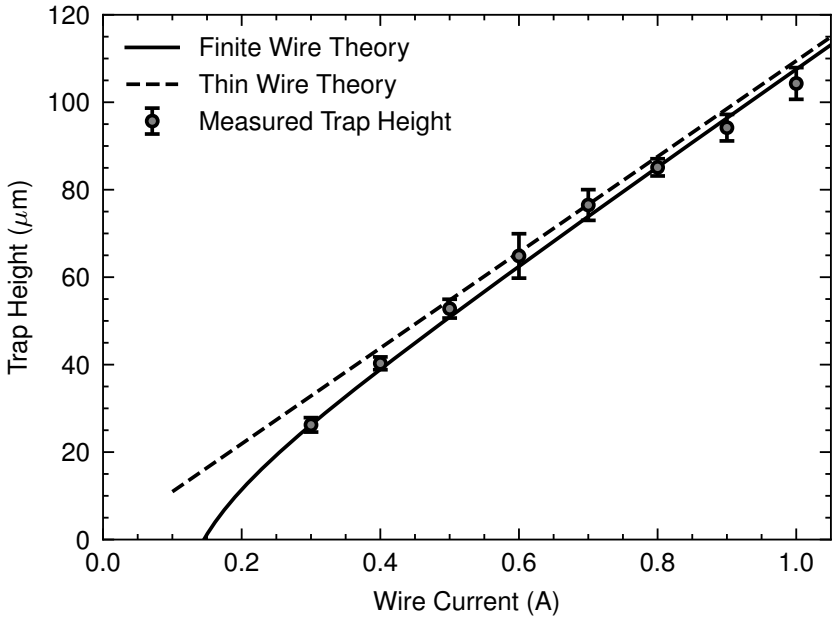

Figure 2.8: Measured trap height in the Z-wire atom chip trap for different wire currents. Data points correspond to measured values of the trap height via dark-spot imaging. The theory curves use a hold field of 18.27 G and a chip wire trace width of 50 μm. As the atoms are brought closer to the chip surface, the trap height is well described by incorporating the finite width of the wire trace. We do not include the 3 μm thickness of the wire in the model. We do not do any fitting. Data is from 28apr25.

2.7 Evaporative Cooling

We have thus far seen that laser cooling can bring the temperature of an atomic sample down from room temperature to tens of micro-Kelvin, limited by photon recoil during the process of remitting the cooling light. To reach temperatures in which the deBroglie wavelength given in Eq. 2.1 is on par with the interatomic spacing; our atoms must be brought down to hundreds of nano-Kelvin in temperature, about a factor of one hundred less than what is doable with sub-Doppler cooling. To reach temperatures necessary for BEC, we employ forced evaporative cooling, a process used in the first observations of BEC in 1995 [44, 45].

This scheme, pictured in Fig. 2.9, uses an external radio-frequency (RF) field at MHz frequencies to couple DC Zeeman trappable states to untrapped states, ejecting them

from the trap in the process. The RF "knife" starts far off-resonance with respect to the

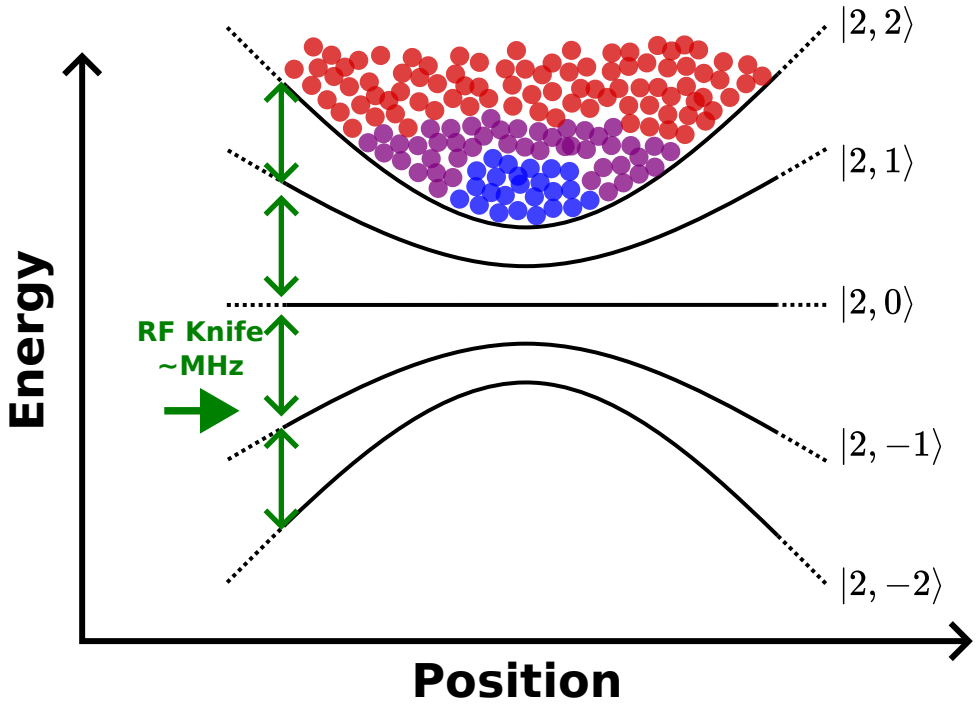

Figure 2.9: Depiction of the evaporative cooling process. Atoms trapped in the $|2,2\rangle$ state can be selectively ejected from the trap based on temperature by applying a radio-frequency (RF) "knife", which couples the $|2,2\rangle$ state to the untrapped $|2,0\rangle, |2,-1\rangle$, and $|2,-2\rangle$ states. Bringing the knife closer in keeps only the coldest atoms of the sample while ejecting hot atoms from the trap.

Larmor frequency, set by the Zeeman splitting. In this case, the hottest atoms in our trap have enough energy to traverse the potential and reach the knife frequency. When this occurs, those atoms are coupled to other atomic states, which are DC high-field seekers, namely the $|2,0\rangle, |2,-1\rangle$, and $|2,-2\rangle$ states. By slowly bringing the RF knife closer to the trap bottom, we continuously eject the hottest atoms in our trap, eventually leaving us with atoms cold enough to reach BEC. This process effectively cuts off the high velocity end of the Maxwell-Boltzmann velocity distribution describing the atom cloud, doing so slowly enough to allow for the ensemble to rethermalize. It takes an atom ~3 collisions to rethermalize [60], meaning the timescale for evaporation is set by the trap lifetime and collision rate. Typical lifetimes in the atom chip trap are on the order of 7-9 s, with collision rates of tens of collisions per second, depending on the exact trapping parameters

[18]. The collision rate is calculated as [34]:

$$CR = \frac{(8\pi a_s^2)(\sqrt{2}v)N}{(2\pi)^{3/2} s_x s_y s_z} \tag{2.14}$$

where N is the atom number, $s_i = v/\omega_i$ is the effective size of the trap in dimension i, with v the atom velocity and ω_i the trap frequency, and a_s is the s-wave scattering length. For $^{Rb}87$, $a_s = 100a_0$, where a_0 is the Bohr radius. As an example, for $N = 100,000$ atoms in a trap with $\omega_x = \omega_y = 2\pi \times 1$ kHz, $\omega_z = 2\pi \times 50$ Hz, and a velocity of 1 cm/s (corresponding to roughly 1 μK), the collision rate is 783 collisions/s per atom.

Chapter 3

AC Zeeman Theory

This chapter describes the theory behind the novel trapping scheme developed in our lab: the RF AC Zeeman (ACZ) trap, based on the ACZ effect. This effect describes the interaction between an atom with magnetic moment $\vec{\mu}$ and an oscillating magnetic field, $\vec{B}_{ac}$, typically at MHz or GHz frequencies. We utilize the ACZ effect to confine neutral atoms in a spin-specific atom chip trap potential.

The chapter is structured in the following manner: Section 3.1 takes a semi-classical approach to the ACZ effect, deriving key phenomena such as Rabi oscillations and a time-independent Hamiltonian description. Section 3.2 moves into using the dressed atom formalism and derives the eigenstates and energies of the ACZ Hamiltonian. Complimentary resources on this topic can be found in previous PhD theses [16, 51], as well as a publication by our group [17]. Section 3.3 extends the dressed atom calculation to systems of three and five levels, applicable to RF ACZ trapping within a given hyperfine manifold. The creation of a trap for neutral atoms via the ACZ is discussed in Section 3.4, in both the transverse and axial dimensions. Finally, in Section 3.5, we add an additional atomic level and electromagnetic field to the two-level model with an eye towards modeling RF/microwave evaporation and double dressing.

3.1 Two-Level Atom In an Electromagnetic Field

Much of AMO physics deals with the interaction of atoms with electromagnetic fields. The Stark effect covers interaction with an electric field, and the Zeeman effect describes the coupling of an atom to a magnetic field. I will focus here on the energy level shifts of an atom in a time-dependent magnetic field, known as the AC Zeeman (ACZ) effect.

For simplicity, we will look at the case of a two-level atom in the presence of an oscillating magnetic field, which describes the case of microwave inter-manifold hyperfine transitions, i.e., the F=1 to F=2 transition in the $5S_{1/2}$ ground state of ^{87}Rb. However, this formalism can be extended to look at systems with more than two levels, such as the intra-manifold RF transitions [16, 61] within a given manifold (see Section 3.3). The Hamiltonian describing this two-level system is

$$H_{atom} = \hbar \begin{pmatrix} \omega_g & 0 \\ 0 & \omega_e \end{pmatrix} \tag{3.1}$$

where $\hbar\omega_{g,e}$ are the energies of the ground and excited states, respectively. Now, consider applying a single-frequency oscillating magnetic field, given as

$$\vec{B}_{AC} = \vec{B}_0 \cos(\omega t) = B_0 \cos(\omega t)\hat{\epsilon}, \tag{3.2}$$

where B_0 is the strength of the field, $\hat{\epsilon}$ is a unit vector describing the polarization of the field, and ω is the frequency of the field. Our atom will couple to this field via its magnetic dipole moment, $\vec{\mu}$, through the AC Zeeman (ACZ) effect as

$$H_{ACZ} = -\vec{\mu} \cdot \vec{B}_{AC} \tag{3.3}$$

We can write this in the two-level basis as a matrix

$$H_{ACZ} = \hbar \begin{pmatrix} 0 & \Omega \\ \Omega^* & 0 \end{pmatrix} \cos(\omega t) \tag{3.4}$$

where we define the Rabi frequency, Ω, as

$$\Omega = \frac{\langle g| - \vec{\mu} \cdot \vec{B}_0 |e\rangle}{\hbar} \tag{3.5}$$

The Rabi frequency is a key parameter for many of our experiments as it describes the strength of the coupling between the atomic energy states in the presence of an AC magnetic field. If we neglect the nuclear spin, $\vec{I}$ (whose contribution is a few orders of magnitude smaller than $\vec{S}$ [53]), then the ground state ($l = 0$) magnetic moment of the atom can be written as $\vec{\mu} = -(g_s \mu_B/\hbar)\vec{S}$, where μ_B is the Bohr magneton, g_S is the electron gyromagnetic factor (which we will take to be $g_S = 2$ here), and $\vec{S}$ is the spin operator for the outermost valence electron. If we take the $\hat{z}$-direction to be the quantization axis, then the Rabi frequency can be written as

$$\Omega = \frac{\mu_B}{\hbar^2} \langle g| S_+ B_- + S_- B_+ + 2 S_z B_{0,z} |e\rangle \tag{3.6}$$

where $S_\pm = S_x \pm i S_y$ are the spin raising and lowering operators and $B_\pm = B_{0,x} \pm i B_{0,y}$ are circularly polarized magnetic fields. The full Hamiltonian for this system is then

$$H = H_{atom} + H_{ACZ} = \hbar \begin{pmatrix} \omega_g & \Omega cos(\omega t) \\ \Omega^* cos(\omega t) & \omega_e \end{pmatrix} \tag{3.7}$$

We can use the time-dependent Schrodinger equation with the above Hamiltonian to solve for the coefficients of a general wavefunction $|\Psi(t)\rangle = c_g(t) e^{-i\omega_g t}|g\rangle + c_e(t) e^{-i\omega_e t}|e\rangle$ as

$$i\hbar \frac{\partial}{\partial t} |\Psi(t)\rangle = H |\Psi(t)\rangle. \tag{3.8}$$

This leads to a system of two coupled differential equations for the coefficients $c_g(t)$ and

$c_e(t)$:

$$i\frac{\partial c_g(t)}{\partial t} = \frac{c_e(t)\Omega}{2}e^{i\delta t} \tag{3.9}$$

$$i\frac{\partial c_e(t)}{\partial t} = \frac{c_g(t)\Omega^*}{2}e^{-i\delta t}, \tag{3.10}$$

where we have introduced the detuning parameter $\delta = \omega - (\omega_e - \omega_g) = \omega - \omega_{eg}$, which tells us how far off the atomic resonant frequency the applied field is. We have also utilized the *rotating wave approximation* in which we drop fast oscillating terms that go as $e^{i(\omega+\omega_{eg})t}$ as they are typically much too fast to affect the dynamics and we keep terms that go as $e^{i(\omega-\omega_{eg})t}$. This approximation is only valid when $\omega + \omega_{eg} >> |\omega - \omega_{eg}|$, so when the applied field is near resonant with the atomic splitting. When $\omega + \omega_{eg} \approx |\omega - \omega_{eg}|$, one can no longer safely make this approximation, as is the case sometimes found in adiabatic rf dressed potentials [62]. If we start out with our atom in the ground state ($c_g = 1$, $c_e = 0$), the solutions to these differential equations are [49]

$$c_g(t) = \left[\cos\left(\frac{\Omega' t}{2}\right) - \frac{i\delta}{\Omega'}\sin\left(\frac{\Omega' t}{2}\right)\right] e^{i\delta t/2} \tag{3.11}$$

$$c_e(t) = -i\frac{\Omega}{\Omega'}\sin\left(\frac{\Omega' t}{2}\right) e^{-i\delta t/2} \tag{3.12}$$

where $\Omega' = \sqrt{|\Omega|^2 + \delta^2}$ is the generalized Rabi frequency. We can find the probability to be found in either the ground or excited states as a function of time as

$$P_{|g\rangle} = |c_g(t)|^2 = \cos^2\left(\frac{\Omega' t}{2}\right) + \left(\frac{\delta}{\Omega'}\right)^2 \sin^2\left(\frac{\Omega' t}{2}\right) \tag{3.13}$$

$$P_{|e\rangle} = |c_e(t)|^2 = \left(\frac{\Omega}{\Omega'}\right)^2 \sin^2\left(\frac{\Omega' t}{2}\right) \tag{3.14}$$

The probability to find the atom in the excited state as a function of time, $P_{|e\rangle}$, is plotted in Fig. 3.1. We see that on resonance (zero detuning), we can transfer our atom from the ground to the excited state by leaving the field on for a time $\Omega t = \pi$, colloquially known as a "π-pulse". Similarly, if we leave the field on for a time $\Omega t = \pi/2$, we create

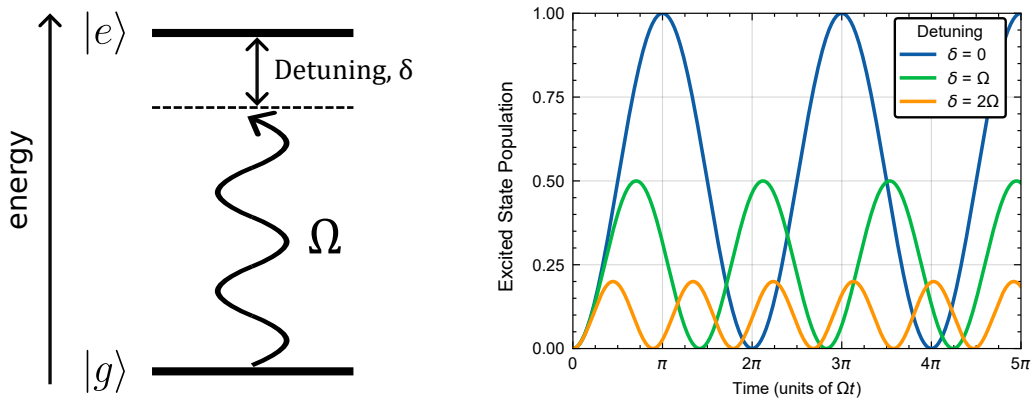

Figure 3.1: Rabi flopping of a two-level atom in the presence of an oscillating external field for different detunings as a function of time. As the detuning is increased the amplitude of the Rabi oscillations decreases while the frequency Ω' increases. The probability to be found in the ground state is $1 - P_{|e\rangle}$.

an equal superposition of the ground and excited state as their probabilities are both $P_{|g\rangle} = P_{|e\rangle} = 1/2$. This is known as a "$\pi/2$-pulse". As the detuning of the field is taken off-resonance, we are less able to fully transfer the atom between the two states, and the frequency of oscillations, given by Ω', increases.

Looking back at Eqs. 3.10, we can simplify things by making a unitary transformation to the rotating frame in which our coefficients transform as

$$\tilde{c}_g(t) = c_g(t) \tag{3.15}$$

$$\tilde{c}_e(t) = c_e(t)e^{i\delta t} \tag{3.16}$$

Under this transformation, we can write the time-dependent Schrodinger equation in the rotating frame as

$$i\hbar\frac{\partial}{\partial t}\begin{pmatrix}\tilde{c}_g(t)\\ \tilde{c}_e(t)\end{pmatrix} = \hbar\begin{pmatrix}0 & \Omega/2\\ \Omega^*/2 & -\delta\end{pmatrix}\begin{pmatrix}\tilde{c}_g(t)\\ \tilde{c}_e(t)\end{pmatrix} \tag{3.17}$$

So the Hamiltonian becomes

$$H_{rot} = \hbar\begin{pmatrix}0 & \Omega/2\\ \Omega^*/2 & -\delta\end{pmatrix} \tag{3.18}$$

Looking at the above expression, we find that by making this transformation, any time

dependence in the Hamiltonian is removed.

3.2 Dressed Atom Formalism

An equivalent method for obtaining the time-independent Hamiltonian for the two-level atom in the presence of an oscillating field is through dressed atom theory. Here we operate in the $\{|g, N\rangle, |e, N-1\rangle\}$ basis, where g and e are the two levels of the atom and N is the number of photons in the oscillating applied field. We can think of this as the atom being in the ground state with N photons present and absorbing a photon to transition to the excited state, leaving the field with $N-1$ photons. The total Hamiltonian for this system can be written as

$$H = H_{atom} + H_{field} + H_{ACZ} \tag{3.19}$$

$$= \hbar \begin{pmatrix} \omega_g & 0 \\ 0 & \omega_e \end{pmatrix} + \hbar\omega \begin{pmatrix} N & 0 \\ 0 & N-1 \end{pmatrix} + \frac{\hbar}{2} \begin{pmatrix} 0 & \Omega \\ \Omega^* & 0 \end{pmatrix} \tag{3.20}$$

where Ω is the Rabi frequency from Eq. 3.5 and ω is the frequency of the applied oscillating field. By subtracting off the energy offset $\hbar\omega_g + \hbar\omega N$ the Hamiltonian can be written as

$$H = \hbar \begin{pmatrix} 0 & \Omega/2 \\ \Omega^*/2 & -\delta \end{pmatrix} \tag{3.21}$$

which is the same as Eq. 3.18. The eigenstates of this Hamiltonian are no longer the bare states $\{|g, N\rangle, |e, N-1\rangle\}$; rather, the coupling mediated by the Rabi frequency mixes the two states. The bare state energies also receive an energy shift due to the coupling. The eigenenergies of the dressed atom Hamiltonian are

$$E_\pm = \frac{\hbar}{2}\left(-\delta \pm \sqrt{|\Omega|^2 + \delta^2}\right) \tag{3.22}$$

These energies, along with the bare state energies, are plotted in Fig. 3.2(a). We see that in the presence of a coupling between the two bare states, the eigenenergies form an avoided

level crossing where splitting on-resonance is $\hbar|\Omega|$.

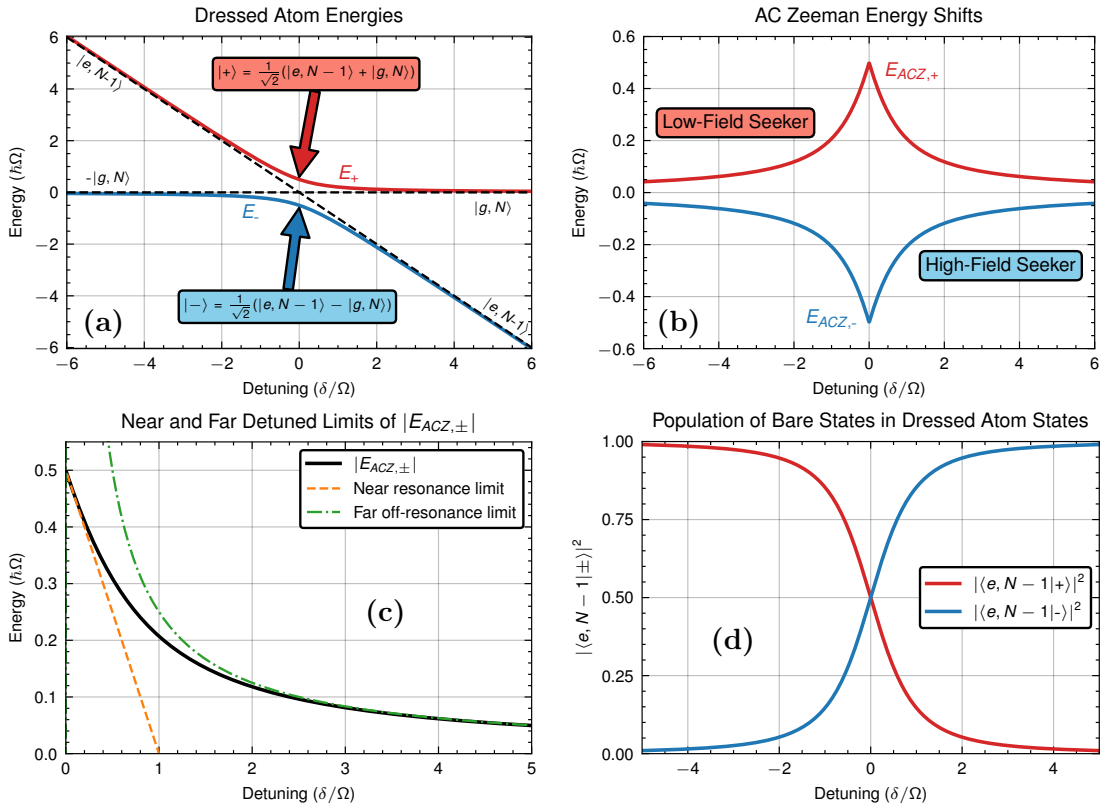

Figure 3.2: Two-level AC Zeeman theory. **(a)** Two-level AC Zeeman eigenstate (i.e., dressed state) energies. In the presence of a coupling between the bare states $|g, N\rangle$ and $|e, N-1\rangle$, the eigenenergies form an avoided level crossing. On-resonance (detuning equal to zero), the dressed states are equal superpositions of the bare states. Far off-resonance, the dressed states can be well described by one of the bare states. **(b)** AC Zeeman energy shifts for a two-level atom. The shift is maximal on-resonance, with the $|+\rangle$ state always experiencing a positive shift while the $|-\rangle$ state always experiences a negative energy shift. **(c)** Near and far off-resonance approximations of the AC Zeeman energy shifts. We see that the near-resonance limit matches well for $|\delta| \lesssim 0.25\Omega$ while the far off-resonance limit matches well for $|\delta| \gtrsim 2\Omega$. **(d)** Relative population of the bare state $|e, N-1\rangle$ in the $|\pm\rangle$ dressed states. The population in the $|g, N\rangle$ state is given by $1-|\langle e, N-1|\pm\rangle|^2$.

We can find the energy shifts by subtracting the bare state energies from $E_\pm$, shown in Fig. 3.2(b) and written as

$$E_{ACZ,\pm} = \pm\frac{\hbar}{2}\left(-|\delta| + \sqrt{|\Omega|^2 + \delta^2}\right) \tag{3.23}$$

We can see that for all detunings the $|+\rangle$ state is always shifted up in energy, while the

$|-\rangle$ gets shifted down in energy. Thus, the $|+\rangle$ state will feel a restoring force pushing it towards regions of low field so as to minimize its energy. States of this kind are colloquially known as "low-field seekers". Conversely, the $|-\rangle$ state, which has a negative energy shift, will observe a force pushing it to regions of high fields, and thus is a "high-field seeker".

In the far off-resonance limit ($|\delta| >> |\Omega|$), the two states resemble the bare states and hardly mix. The energy shift in this regime is given by $E_{g,e} \approx \pm\hbar|\Omega|^2/4\delta$, where the $\pm$ sign corresponds to the shift for the $|g, N\rangle$ and $|e, N-1\rangle$ states, respectively. This shift is the same form as for a far off-resonant optical dipole trap, and is visualized in Fig. 3.3. Near resonance ($|\delta| << |\Omega|$), the eigenstates of the dressed Hamiltonian are equal superpositions of the bare states, and the energy shift is $E_{ACZ,\pm} \approx \pm\hbar(|\Omega| - \delta)/2$. We can visualize these limits in Fig. 3.2(c). Of note is that near resonance ($|\delta| \lesssim 0.25|\Omega|$) the energy shift scales linearly with the Rabi frequency (i.e. the strength of the applied field) and becomes quadratic as we go off-resonance ($|\delta| \gtrsim 2.5|\Omega|$).

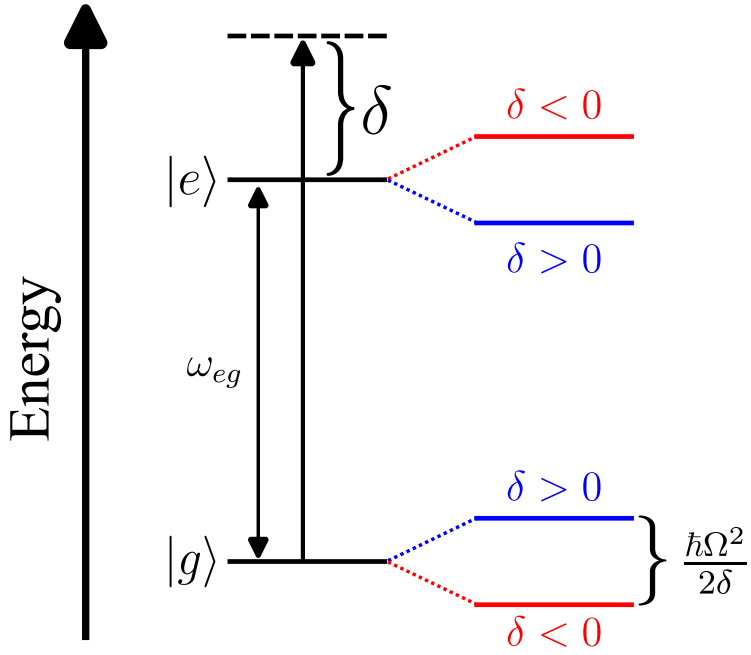

Figure 3.3: Far off-resonance ACZ shifts. For an oscillating field with frequency greater than the atomic resonance ($\delta > 0$, red-detuned), the ground (excited) state gets shifted down (up) in energy by $\hbar\Omega^2/4\delta$, making it a high (low) field seeker. For a blue-detuned field ($\delta < 0$), the opposite happens. It is clear to see in this far-detuned limit (i.e. $|\delta| >> |\Omega|$) that either state, $|e\rangle$ or $|g\rangle$, can be made a low-field seeker just by adjusting the detuning of the applied oscillating field.

The eigenstates of the dressed atom Hamiltonian are no longer the bare states but rather some linear combination of the two resulting from the interaction terms on the off-diagonals in Eq. 3.21. The eigenstates of the system are the "dressed states" given as

$$|+\rangle = \sin(\theta)|g, N\rangle + \cos(\theta)|e, N-1\rangle \tag{3.24}$$

$$|-\rangle = \cos(\theta)|g, N\rangle - \sin(\theta)|e, N-1\rangle \tag{3.25}$$

where $\sin(2\theta) \equiv \Omega/\Omega'$ and $\cos(2\theta) \equiv -\delta/\Omega'$. We can determine the relative populations of the bare states for a given dressed state as

$$|\langle e, N-1|\pm\rangle|^2 = \frac{1}{2}\left(1 \mp \frac{\delta}{\Omega'}\right) \tag{3.26}$$

$$|\langle g, N|\pm\rangle|^2 = \frac{1}{2}\left(1 \pm \frac{\delta}{\Omega'}\right) \tag{3.27}$$

Fig. 3.2(d) shows the relative population of the $|e, N-1\rangle$ bare state in the dressed states $|\pm\rangle$ as a function of detuning. We see that far off-resonance ($|\delta| >> |\Omega|$) the dressed states are well described by either of the bare states, while on-resonance ($\delta = 0$) the dressed states are equal superpositions of the two bare states. From this, we are able to see that by varying the detuning of the applied AC field, we have full control over the state of our atom.

Using an Adiabatic Rapid Passage (ARP) sweep, we can start with our AC field far off-resonance such that our dressed state is described by one of the bare states. Then, by sweeping the AC field frequency adiabatically with respect to the Rabi frequency, we can follow along one of the curves in Fig. 3.2(d) (depending on which dressed state we are in) and end up with our dressed state being described by the other bare state. Using this technique, we can make either bare state a high-field ($|-\rangle$) or a low-field ($|+\rangle$) seeker just by changing the detuning of the applied field.

3.3 Three- and Five-Level Systems

While the two-level atom treatment is nice and simple, in reality, it is very rare to have a truly two-level system. For ^{87}Rb, the atom used in this thesis, the $5S_{1/2}$ ground state is actually composed of two hyperfine levels, characterized by their total angular momentum F. In the case of ^{87}Rb, F takes the value 1 or 2. Moreover, in the presence of an external DC magnetic field, these two manifolds further split into a system of five (F=2) or three (F=1) levels, labeled by their Zeeman level, m_F, which can take the value $-F, -F+1, ..., F-1, F$. While the two-level model may be appropriate for microwave transitions between the F=1 and F=2 levels, radio-frequency (RF) transitions within a given manifold mean we have to adapt our Hamiltonian to incorporate all the states.

We decompose the $F = 2$ and $F = 1$ hyperfine manifolds into systems of five and three levels, respectively, labeled by their Zeeman sub-level, m_F, as shown in Fig. 3.4. Each system can be viewed as a ladder of coupled two-level systems with coupling strength $\Omega_{\alpha\beta}$. In the presence of a quantizing DC magnetic field, $B_{DC,z}$, the m_F levels are split by roughly 0.7 MHz/G, with small non-linearities given as the $\Delta_{\{0,1,2\}}$ shifts in our description. As per Eq. 3.6, the Rabi frequencies can be written in terms of the circularly polarized magnetic fields as

$$\Omega_{\alpha\beta} = \frac{g_s \mu_B}{2\hbar^2} \langle \alpha | S_+ B_- + S_- B_+ + 2 S_z B_{AC,z} | \beta \rangle \,, \tag{3.28}$$

where μ_B is the Bohr magneton, $\hbar$ is Plank's constant, $S_\pm = S_x \pm i S_y$ are the spin raising and lowering operators, and $B_\pm = Bx \pm i B_y$ are the circularly polarized magnetic fields. We have omitted the contribution of the nuclear spin, I, as its contribution is several orders of magnitude smaller than the electron spin, S. Additionally, we take $g_s = 2$, which is accurate to about 0.1%. Notably, in the $F = 2$ (1) manifold, only S_+ (S_-) transitions are allowed, reducing the Rabi frequency to a single term [17]. We can then pull out a common factor, dubbed the "Rabi strength", as

$$\Omega_\pm = \frac{\mu_B |B_\mp|}{\hbar} \tag{3.29}$$

where the $\pm$ sign on $\Omega_\pm$ corresponds to the F=2 or 1 system, respectively. This allows us to rewrite all the Rabi frequencies as $\Omega_\pm$ along with a scaling factor, given as the Clebsch-Gordan coefficients describing the coupling strength between adjacent m_F states [17]. For sufficiently small magnetic fields which cause a Zeeman shift much smaller than the hyperfine splitting (6.834 GHz in ground-state ^{87}Rb), the total angular momentum, $F = J + I$, is a good quantum number, and our states can be described using the $|F, m_F\rangle$ basis. The full treatment of calculating these coefficients operates using the $|S, m_S; I, m_I\rangle$ basis [16, 53]; however, at the $B_{DC}\approx$28 G field frequently used in this work, the decomposition into the $|F, m_F\rangle$ basis is accurate to better than 1%. Following the dressed state formalism in Ref. [16, 61], we can write the AC Zeeman Hamiltonian for the five- ($F = 2$) and three- ($F = 1$) level systems as

$$H_{ACZ,F=2} = \hbar \begin{pmatrix} 2\delta & \Omega_+/4 & 0 & 0 & 0 \\ \Omega_+^*/4 & \delta & \sqrt{6}\Omega_+/8 & 0 & 0 \\ 0 & \sqrt{6}\Omega_+^*/8 & -\Delta_0 & \sqrt{6}\Omega_+/8 & 0 \\ 0 & 0 & \sqrt{6}\Omega_+^*/8 & -\delta - \Delta_1 & \Omega_+/4 \\ 0 & 0 & 0 & \Omega_+^*/4 & -2\delta - \Delta_2 \end{pmatrix} \begin{matrix} |-2\rangle \\ |-1\rangle \\ |0\rangle \\ |+1\rangle \\ |+2\rangle \end{matrix} \tag{3.30}$$

$$H_{ACZ,F=1} = \hbar \begin{pmatrix} \delta & -\sqrt{2}\Omega_-/8 & 0 \\ -\sqrt{2}\Omega_-^*/8 & 0 & -\sqrt{2}\Omega_-/8 \\ 0 & -\sqrt{2}\Omega_-^*/8 & -\delta - \Delta_0 \end{pmatrix} \begin{matrix} |+1\rangle \\ |0\rangle \\ |-1\rangle \end{matrix} \tag{3.31}$$

where the ket labels indicate the organization of the m_F states within the Hamiltonian matrices. The detuning, δ, is taken to be the frequency difference between the applied RF field, ω_{rf}, and the frequency separation between the two lowest energy states, ω_0 (see Fig. 3.4), i.e., $\delta = \omega_{rf} - \omega_0$. Since the m_F states are not all shifted the same amount, we define additional detunings, $\Delta_{\{0,1,2\}}$, which act to offset the m_F states from a degenerate ladder system. The parameters ω_0 and $\Delta_{\{0,1,2\}}$ are numerically calculated using the Breit-Rabi formula across a range of DC magnetic fields in Fig. 3.4 The dressed eigenstates and eigenenergies for these systems are obtained by numerically diagonalizing the Hamiltonians. An example is given in Fig. 3.5 for $B_{dc} = 28.58$ G and $\Omega_0 = 500$ kHz.

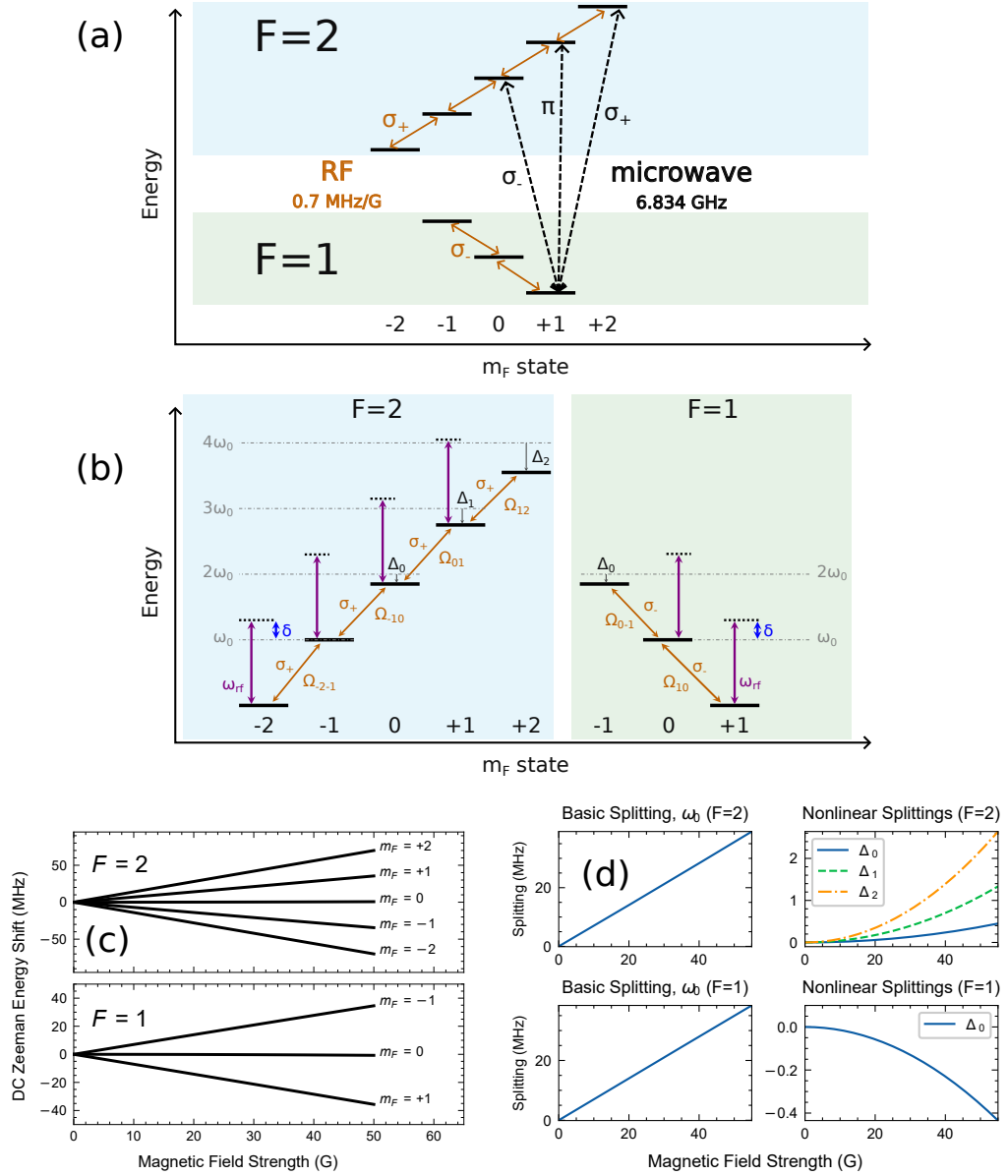

Figure 3.4: (a) Energy level diagram of the $F = 2$ and $F = 1$ hyperfine manifolds in the ground state of ^{87}Rb. A quantizing dc magnetic field splits each manifold into $2F+1$ Zeeman sub-levels by roughly 0.7 MHz/G, labeled by m_F. Transitions within a given manifold are mediated by MHz (RF) level frequencies, while GHz (microwave) frequencies allow for transitions between manifolds. (b) Zoom in of the energy diagrams for each manifold in (a), highlighting the intra-manifold transitions utilized for RF ACZ trapping. A rf field couples adjacent m_F states with coupling strength Ω_{ij}, which is a scaled $\Omega_{\pm}$ (see Eq. 3.3). (c) Zeeman sub-level splittings from the $B_{dc} = 0$ energy as a function of magnetic field strength up to 50 Gauss. (d) ω_0 and $\Delta_{\{0,1,2\}}$ parameters in Eqs. 3.30 and 3.31 as a function of magnetic field strength for the F=2 and F=1 systems.

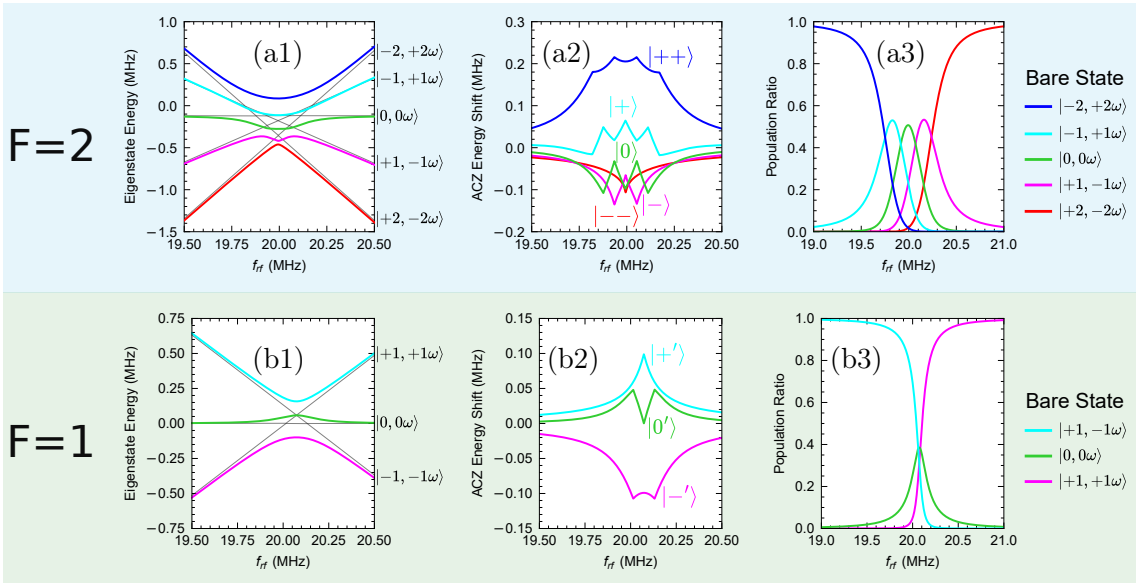

Figure 3.5: Numerically calculated ACZ eigenstates (a1, b1), shifts (a2, b2), and population ratios (a3, b3) for the F=2 (top) and F=1 (bottom) systems, using a dc field of 28.58 G and a Rabi strength of $\Omega_0 = 500$ kHz. Grey lines in (a1, b1) give the bare state energies. The population of the bare states is given for the trappable $|{+}{+}\rangle$ (a3) and $|{+}'\rangle$ (b3) states.

3.3.1 Matrix Elements

In the low-field limit, $\mu_B B_{DC} \ll \Delta_{hfs}$, where Δ_{hfs} is the ground $\ell = 0$ hyperfine splitting, $F^2 = F(F+1)$ and F_z are "good" quantum numbers, and $|F, m\rangle$ are eigenstates of the atomic Hamiltonian. We calculate the Clebsch–Gordan coefficients for the $F_\pm = I \pm S = \frac{3}{2} \pm \frac{1}{2}$ hyperfine states for the inter-manifold microwave transitions as [17]

$$\langle F_+, m|S_\pm|F_-, m'\rangle = \pm\frac{\hbar\sqrt{(F_+ \pm m)(F_+ \pm m')}}{2I+1}\delta_{m,m'\pm1}, \tag{3.32}$$

$$\langle F_+, m|S_z|F_-, m'\rangle = -\frac{\hbar\sqrt{(F_+ + m)(F_+ - m')}}{2I+1}\delta_{m,m'}. \tag{3.33}$$

For the low-frequency intra-manifold transitions, we have [17]

$$\langle F, m|S_\pm|F, m'\rangle = \eta\frac{\hbar\sqrt{(F \pm m)(F \mp m')}}{2I+1}\delta_{m,m'\pm1}, \tag{3.34}$$

$$\langle F, m|S_z|F, m'\rangle = \eta\frac{\hbar m}{2I+1}\delta_{m,m'}. \tag{3.35}$$

where ($\eta = \pm 1$ for $F = F_{\pm}$). These elements identify the transitions allowed with a Kronecker delta, give the transition amplitudes, and select a single polarization field per transition. We list explicit values for the inter-manifold values in Table 3.1 and for the intra-manifold values in Table 3.2.

$\mathbf{\Delta m}$	$\mathbf{F_+}$	$\mathbf{m}$	$\mathbf{F_-}$	$\mathbf{m'}$	$\langle \mathbf{S_+} \rangle$	$\langle \mathbf{S_-} \rangle$	$\mathbf{2}\langle \mathbf{S_z} \rangle$
	2	2	1	1	$\sqrt{12}$	0	0
$+1$	2	1	1	0	$\sqrt{6}$	0	0
	2	0	1	-1	$\sqrt{2}$	0	0
	2	0	1	1	0	$-\sqrt{2}$	0
-1	2	-1	1	0	0	$-\sqrt{6}$	0
	2	-2	1	-1	0	$-\sqrt{12}$	0
	2	1	1	1	0	0	$-\sqrt{12}$
0	2	0	1	0	0	0	-4
	2	-1	1	-1	0	0	$-\sqrt{12}$

Table 3.1: Clebsch–Gordan coefficients (factor of $\hbar/4$ pulled out) used to to determine the Rabi frequency for the inter-manifold transitions ($\Delta m = m - m'$). Note that the $\langle S_z \rangle$ coefficients have a factor of 2 included to match the form of the Rabi frequency given in Eq. 3.3.

$\mathbf{\Delta m}$	$\mathbf{F}$	$\mathbf{m}$	$\mathbf{m'}$	$\langle \mathbf{S_+} \rangle$	$\langle \mathbf{S_-} \rangle$	$\mathbf{2}\langle \mathbf{S_z} \rangle$	$\mathbf{F}$	$\mathbf{m}$	$\mathbf{m'}$	$\langle \mathbf{S_+} \rangle$	$\langle \mathbf{S_-} \rangle$	$\mathbf{2}\langle \mathbf{S_z} \rangle$
	2	2	1	2	0	0						
$+1$	2	1	0	$\sqrt{6}$	0	0	1	1	0	$-\sqrt{2}$	0	0
	2	0	-1	$\sqrt{6}$	0	0						
	2	-1	-2	2	0	0	1	0	-1	$-\sqrt{2}$	0	0
	2	1	2	0	2	0						
-1	2	0	1	0	$\sqrt{6}$	0	1	0	1	0	$-\sqrt{2}$	0
	2	-1	0	0	$\sqrt{6}$	0						
	2	-2	-1	0	2	0	1	-1	0	0	$-\sqrt{2}$	0
	2	2	2	0	0	4						
	2	1	1	0	0	2	1	1	1	0	0	-2
0	2	0	0	0	0	0	1	0	0	0	0	0
	2	-1	-1	0	0	-2						
	2	-2	-2	0	0	-4	1	-1	-1	0	0	2

Table 3.2: Clebsch–Gordan coefficients (factor of $\hbar/4$ pulled out) used to determine the Rabi frequency for the intra-manifold transitions ($\Delta m = m - m'$). Note that the $\langle S_z \rangle$ coefficients have a factor of 2 included to match the form of the Rabi frequency given in Eq. 3.3.

3.4 Trapping Using the ACZ Effect

With the internal dynamics of the atom explained, we now proceed to how to realize a trap using the ACZ effect. Such a trap offers spin-specific control, operation at arbitrary background magnetic field, use of detuning and phase as experimental control parameters, and suppression of potential roughness, which is the subject of Chapter 6. This section briefly describes the physics of generating an ACZ trap, whereas more technical details on the specifics of the trap generated in our lab can be found in Chapter 5.

3.4.1 Transverse Confinement

For simplicity, consider the two-level system of Section 3.2, in which the states interact via an AC magnetic field. Making things even simpler, we can reduce our Rabi frequency to a single term by forcing our two states to connect solely via S_+ transitions. While it may seem abstract, these assumptions can be applied to microwave inter-manifold transitions between the $F = 2$ and $F = 1$ hyperfine levels by suppressing S_- and S_z transitions via a large quantizing field. In this case, the Rabi frequency from Eq. 3.6 becomes

$$\Omega(r) = \frac{\mu_B}{\hbar^2}\langle g|S_+|e\rangle|B_-(r)| = \xi|B_-(r)| \tag{3.36}$$

where we are assuming now that we have a spatially dependent B_- field. Plugging this spatially-dependent Rabi frequency into the ACZ energy shift (Eq. 3.23), we get the ACZ energy shifts:

$$E_{ACZ,\pm}(r) = \pm\frac{\hbar}{2}\left(-|\delta| + \sqrt{|\Omega(r)|^2 + \delta^2}\right) = \pm E_{ACZ} \tag{3.37}$$

where the detuning of the AC field, δ, is constant. This, in turn, yields a spatially dependent ACZ force acting on the atom,

$$F_{ACZ,\pm}(r) = -\frac{\partial}{\partial r}E_{ACZ,\pm}(r) = \mp\frac{\partial}{\partial r}E_{ACZ}(r) \tag{3.38}$$

We can see that atoms in the $|+\rangle$ dressed state feel a restoring force trapping them in a minimum of the ACZ energy, realized through generating a minimum in the Rabi frequency via the B_- field. Conversely, atoms in the $|-\rangle$ dressed state experience the opposite force and are repelled from the minimum. Trapping atoms via the ACZ effect thus boils down to generating a minimum in the magnetic field of a given polarization.

3.4.2 Axial Confinement: Microwave Lattice

In addition to transverse trapping, we also need a method for confining the atoms axially in the ACZ trap. This can be accomplished by creating a microwave lattice based on the ACZ or AC Stark effect, which is formed by sending counter-propagating signals along the same microstrip trace and creating a standing wave due to the interference of the two fields.

We can first look at this using simple wave propagation to get at the main concept behind the lattice, ignoring details such as the AC skin effect and near-field distribution for a microstrip. The field generated by two counter-propagating waves is

$$\begin{aligned} B_{total} &= B_0 e^{-i\omega t}\left(e^{ikz} + e^{-i(kz+\phi)}\right) \\ &= B_0 e^{-i\omega t} e^{i\phi/2}\left(e^{i(kz-\phi/2)} + e^{-i(kz-\phi/2)}\right) \\ &= 2B_0 e^{-i(\omega t-\phi/2)}\cos(kz-\phi/2) \\ &= 2B_0\cos(\omega t-\phi/2)\cos(2\pi z/\lambda_{eff}-\phi/2) \end{aligned} \tag{3.39}$$

where we consider only the real part in the last step. Here, ω is the frequency of the waves, ϕ is the phase difference between the two waves, and λ_{eff} is the wavelength of the waves in the medium they are traveling through, i.e. $\lambda_{eff} = \lambda_{vacuum}/n_{eff}$ where n_{eff} is the effective index of refraction in the transmission line. In the case of the microstrip, $n_{eff} = \sqrt{\epsilon_{eff}}$ where ϵ_{eff} is the effective dielectric constant of the transmission line. For the 50 Ω microstrip on aluminum nitride (AlN, $\epsilon_r = 8.9$), $\epsilon_{eff} \approx 6$, so $n_{eff} \approx 2.5$, giving

$\lambda_{eff} \approx 1.8$ cm for a frequency of 6.8 GHz. The distance between the minima of the standing wave is given by $\lambda_{eff}/2 = 0.9$ cm, as shown in Fig. 3.6. We can also see that the position of the standing wave can be translated by changing the phase difference ϕ between the two waves generating the lattice. This ends up being a key component for the proposed atom interferometry schemes in that we can use the lattice for both axial confinement and translation, creating the arms of the interferometer.

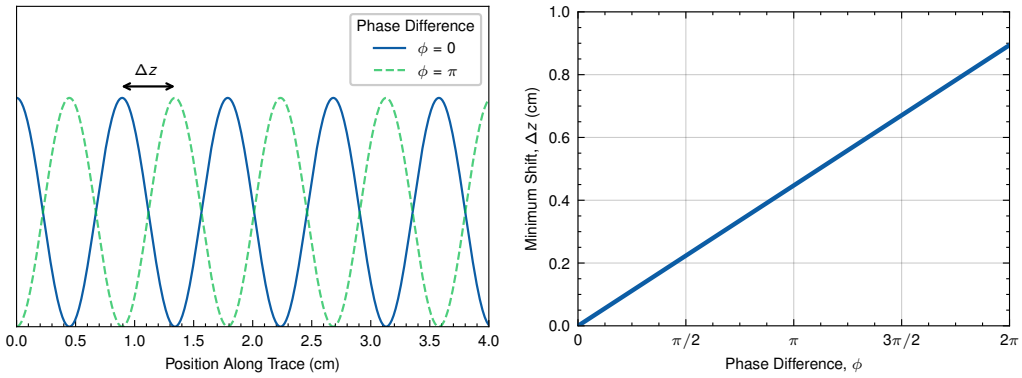

Figure 3.6: Microwave magnetic field lattice for axial AC Zeeman trapping. (Left) Standing wave formed by counter-propagating waves from Eq. 3.39. Here we plot it for two different relative phase differences between the waves. The positional difference between the lattice minima is given by the parameter Δz. (Right) Positional shift of the lattice as a function of relative phase difference between the counter-propagating waves, shown over a range of $\phi = 0 \rightarrow 2\pi$.

While this simple picture captures the core physics behind the microwave lattice, we can get an idea of the true practicality by modelling it in FEKO, a high-frequency electromagnetic computational solver. This amounts to sending counter-propagating microwave currents at 6.8 GHz down a single microstrip line and looking at the generated field, requiring two simulations in which the source and load are switched. The fields from each simulation are then added together and converted into an ACZ potential via Eq. 3.23. Figure 3.7 shows the simulated ACZ lattice potential for sending two counter-propagating 12.5 W signals at 6.8 GHz along a 50 Ω microstrip ($I = 0.5$ A) formed by a 54 μm wide trace on 50 μm thick aluminum nitride ($\epsilon_r = 8.9$). The conversion into an ACZ potential uses the $|2,2\rangle \leftrightarrow |1,1\rangle$ microwave transition in ^{87}Rb and a detuning of $\delta = 2\pi \times 1$ MHz. The potential shown is evaluated at a distance of 100 μm above the chip surface. The gen-

erated axial lattice has a trap depth of roughly 250 μK and a harmonic trapping frequency of 30.1 Hz.

We can also operate the microwave lattice using the AC Stark effect. In the microwave regime, the AC Stark effect is quasi-static and can be approximated by the DC Stark shift,

$$E_{Stark} = -\frac{1}{2}\alpha_0 |E_{rms}|^2, \tag{3.40}$$

where α_0 is the DC ground-state polarizability, and E_{rms} is the rms magnitude of the microwave electric field. For ^{87}Rb, $\alpha_0 = h \times 0.0794(16)$ Hz/(V/cm)^2, where h is Plank's constant [53]. The AC Stark lattice is useful if we need state-insensitive axial confinement or a shorter lattice spacing, as the Stark effect dominates the ACZ effect far off-resonance. We plot the AC Stark lattice generated at 6.8 GHz as the red curve in Fig. 3.7, which generates a lattice with a $\simeq$12 μK trap depth and a trap frequency of 2.8 Hz.

3.5 ACZ Physics with Two Fields

All of the ACZ theory presented thus far has dealt with the interaction of multiple atomic energy levels with a single AC magnetic field. A natural question to ask, then, is what happens when a second AC magnetic field is introduced into our system? We are interested in such a question as it applies to performing evaporative cooling in the ACZ trap. Previous work [16] has demonstrated the ability to cool via the addition of a secondary RF or microwave field to the ACZ trap, though falling short of reaching Bose-Einstein condenstation. The work presented here gives initial efforts to the theoretical description of evaporative cooling in the ACZ trap using the dressed atom framework.

Consider the system in Fig. 3.8: a 2-level RF ACZ trap coupled to a third level via a microwave field. This simple model allows us to extend the two-level dressed atom physics, and is applicable to describing microwave evaporation in an RF ACZ trap. The dressed

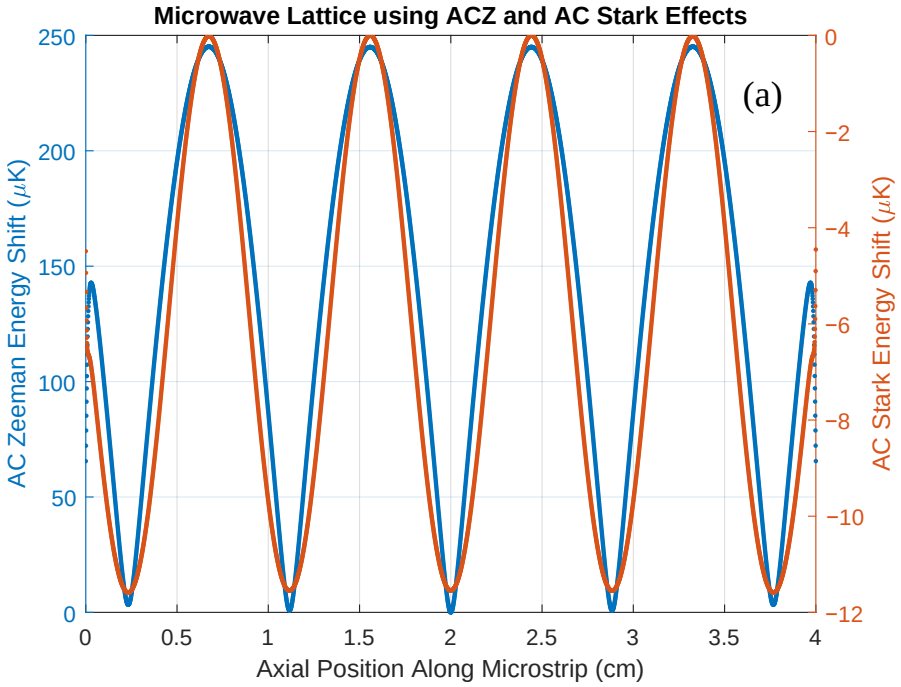

Figure 3.7: Microwave lattices for axial interferometry. Plot of the ACZ (blue) and AC Stark (orange) potentials versus axial position for a 6.8 GHz microwave standing wave produced by two counter-propagating 12.5 W traveling TEM waves directed from either end of a microstrip (each wave generates a current of 0.5 A in amplitude). The microwave frequency has a detuning of $\delta = 2\pi \times 1$ MHz on the ^{87}Rb $|1,1\rangle \leftrightarrow |2,2\rangle$ transition, and the lattice potential is evaluated 100 μm from the microstrip. Figure from Ref. [17].

atom Hamiltonian for this system is (see Appendix D)

$$H = \hbar \begin{pmatrix} \delta_{12} & \Omega_{12}/2 & 0 \\ \Omega_{12}^*/2 & 0 & \Omega_{23}e^{-i\phi}/2 \\ 0 & \Omega_{23}^*e^{-i\phi}/2 & \delta_{23} \end{pmatrix} \tag{3.41}$$

where δ_{12} and δ_{23} are the detunings of the RF and μw fields, Ω_{12} and Ω_{23} are the associated Rabi frequencies, and ϕ is the phase difference between the RF and microwave fields.

The first step to understanding this system is to see how the addition of the microwave field changes the known two-level system, namely the eigenstates and energy shifts. To set the stage, we begin by numerically diagonalizing Eq. 3.41 with $\delta_{23} = -2\pi \times 2$ MHz , varying Ω_{23} as a fraction of Ω_{12}. Figure 3.9(a) shows the dressed atom energies as a function of δ_{12}. This shows the system described as a pair of avoided level crossings formed by the state

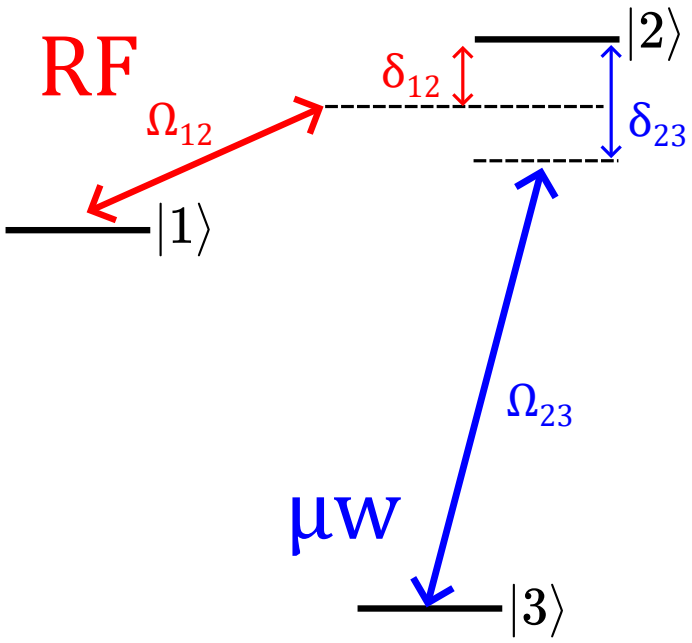

Figure 3.8: Level diagram for a three-level system in the presence of two AC magnetic fields. Here, states $|1\rangle$ and $|2\rangle$ are coupled using a strong RF field, corresponding to the ACZ trap. To perform evaporation, state $|2\rangle$ is coupled to a third level, $|3\rangle$, via a microwave field. The states $|1\rangle$ and $|3\rangle$ do not interact in this picture.

$|1\rangle$ with the $|2\rangle$ and $|3\rangle$ states. The presence of the secondary microwave field mixes in the state $|3\rangle$ with the original two-level ACZ eigenstates, $|\pm\rangle$, in turn shifting their energies.

In the context of performing evaporative cooling with the microwave field, we need to see if we can transfer population from the trapped state into the additional third level. Consider our trapping field is far below resonance, i.e., $\delta_{12} < 0$. In this case, state $|2\rangle$'s energy is shifted up, making it a trappable ACZ low-field seeker (refer to Fig. 3.3). This is akin to the RF ACZ trap, where the trappable dressed state is well described by the $|2, 2\rangle$ state far below resonance. The microwave field then drives atoms from the $|2\rangle$ state into state $|3\rangle$, which we take to be untrappable. First, we take δ_{12} to be constant and rather vary the detuning of the evaporation field, δ_{23}, solving for the eigenenergies of the system for different Ω_{23} as shown in Fig. 3.10. The dressed state energies are labeled using the same convention as Fig. 3.9. Of note is the shifting of the dressed energies from the bare states. One can see that for $\Omega_{23} = 0$, this shift is identical to the two level ACZ energy

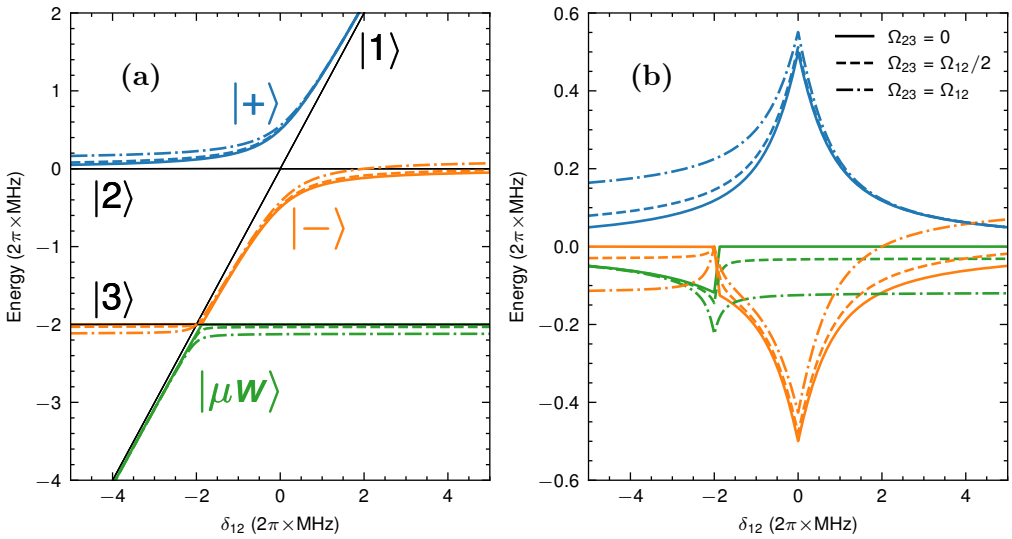

Figure 3.9: Two-level ACZ eigenenergies (a) and shifts (b) with the introduction of a third level. The eigenenergies are obtained from numerically solving Eq. 3.41, where $\delta_{23} = -2\pi \times 2$ MHz and Ω_{23} is varied as a fraction of Ω_{12}. ACZ shifts are the results of subtracting the bare state energy from the eigenenergy curves in (a). The addition of the third level forms a second avoid level crossing.

shift in Eq. 3.23. For $\Omega_{23} \neq 0$ the dressed energies receive an additional ACZ shift due to the secondary evaporation field.

We now move this pedagogical description of the system more into the framework of evaporation. In the system given in Fig. 3.8, we can take the RF field, Ω_{12}, to be the generator of an ACZ trapping potential involving the states $|1\rangle$ and $|2\rangle$. One can imagine these to be two m_F states within a ground state hyperfine manifold, for example. In order to evaporatively cool within this trap, the microwave field, Ω_{23}, must be able to transfer energetic atoms in the ACZ potential into state $|3\rangle$, which we can take to be an ACZ untrapped state. Similar to the evaporation knife described in Sec. 2.7, we want to create an escape point for the hottest atoms in the trap. To see this in our system, we can model the movement of an atom in the trap by varying Ω_{12}. For an ACZ trap, Ω_{12} is a spatially-varying Rabi frequency which is equal to zero at the trap bottom (ignoring gravity). Atoms with high thermal energy will then traverse to larger values of Ω_{12} as they move within the trap. By looking at how the relative populations in the bare states

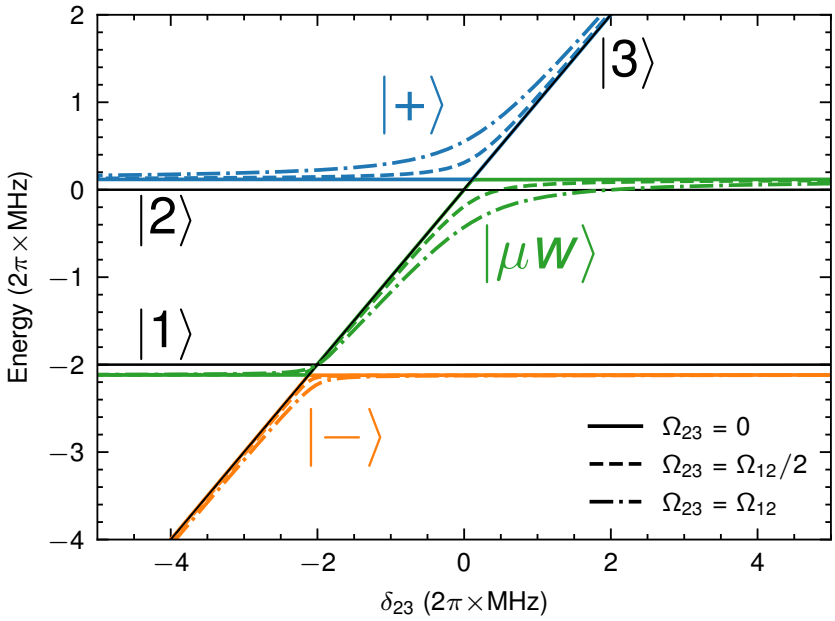

Figure 3.10: Eigenenergies from numerically solving Eq. 3.41 with $\delta_{12} = -2\pi \times 2$ MHz, $\Omega_{12} = 2\pi \times 1$ MHz, and varying Ω_{23} across a range of δ_{23}. The bare state energies ($\Omega_{12} = \Omega_{23} = 0$) are given by the black lines, with labels corresponding to the bare atomic energy levels.

change with Ω_{12} will then tell us how we can transfer atoms into state $|3\rangle$. We plot these population ratios in each of the dressed states for different values of the microwave field detuning, δ_{23}, in Fig. 3.11. In these calculations, we set the trapping RF field detuning, $\delta_{12} = -2\pi \times 0.5$ MHz, such that the $|+\rangle$ state is well described by the state $|2\rangle$ for $\Omega_{23} = \delta_{23} = 0$ (no microwave field) near the bottom of the trap, where $\delta_{12} >> \Omega_{12}$.

We see that we can get population transfer from state $|2\rangle \rightarrow |3\rangle$ when working in the $|\mu w\rangle$ dressed state. For $\delta_{23} > 0$, $\Omega_{12} = 0$, and small Ω_{23}, this state is well described by the bare state $|2\rangle$. As Ω_{12} is increased, the dressed state energies get ACZ shifted away from the bare states (see Fig. 3.10), and state $|\mu w\rangle$ becomes a mixture of all three bare states. For sufficiently large Ω_{12}, $|\mu w\rangle \simeq |3\rangle$, giving us the desired population transfer. The point at which this state transfer happens (both states are equally populated) depends on the microwave field parameters, shifting to lower Ω_{12} (i.e., lower trap depths) as $\delta_{23} \rightarrow 0$ and for increased Ω_{23}. This is precisely what we want: a microwave evaporation knife that transfers hot atoms with enough energy to reach large Ω_{12} into the anti-trapped third

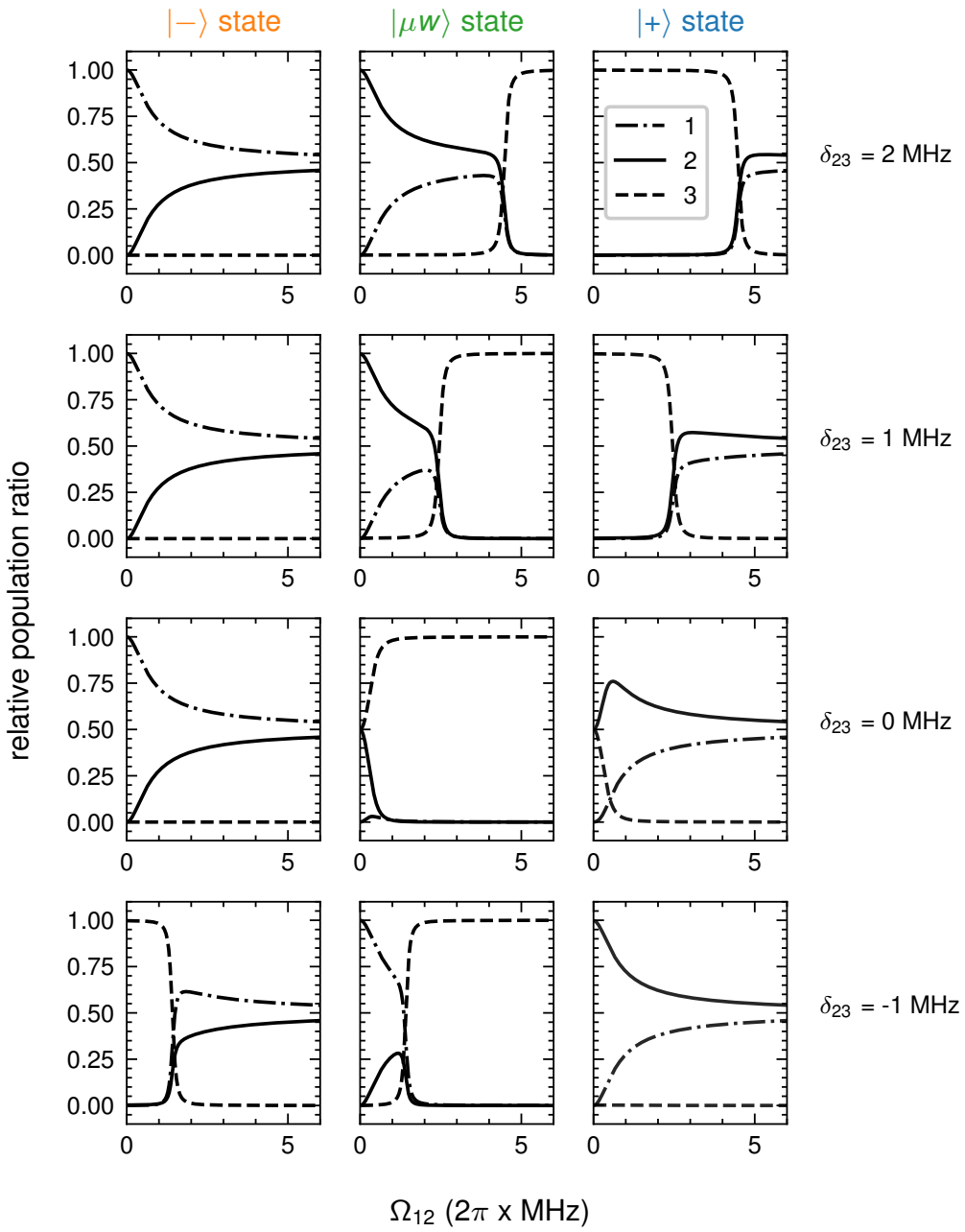

Figure 3.11: Relative population ratios of the bare atomic states in each of the dressed states across a range of Ω_{12}. Each column corresponds to a given dressed state, and the populations are evaluated at different δ_{23} values at each row. For these calculations, $\delta_{12} = -2\pi \times 0.5$ MHz and $\Omega_{23} = 2\pi \times 0.1$ MHz.

level.

3.5.1 Modeling a Trap

We now progress from the description of the three level system with two AC fields to understanding it in the context of an actual ACZ trap. In the simplest case, we can form an ACZ trap by applying an external AC magnetic field in combination with the field generated by a wire carrying AC current. This forms a minimum in the circularly polarized $B_{\pm}$ fields which in turn form the trapping potential. Following Ref. [58], we use $I_{ac} = 0.543$ A and $B_{ext,ac} = 10.86$ G. This creates a $B_{\pm}$ minimum located 100 μm from the trapping wire. For our purposes, this constitutes the RF field in Fig. 3.8, i.e., $\Omega_{12} = \mu_B|B_-|/\hbar$, where we restrict the RF trap to operate via S_+ transitions, reducing the Rabi frequency to a single term. Here, we ignore any additional scaling factors in the Rabi frequency (see Tables 3.1 and 3.2), which only adjust the trap profile slightly.

The numerically calculated trapping potentials for the three dressed atom eigenstates are shown in Fig. 3.12. These calculations use $\delta_{12} = -2\pi\times1$ MHz, and $\Omega_{23} = 2\pi\times0.1$ MHz, and are shown at different values of δ_{23}. We see that the $|\pm\rangle$ states resemble the trap energies for the standard two-level system, with an energy offset of the $|-\rangle$ state equal to the ACZ energy shift $\hbar\delta_{12}/k_B$. For $\delta_{23} > 0$, a trap is formed for the $|\mu w\rangle$ state. As we bring the microwave detuning closer to resonance, we can lower the trap depth until we reach $\delta_{23} < 0$, for which the $|\mu w\rangle$ trap is at a constant negative energy.

We have successfully developed the dressed atom formalism to begin describing evaporative cooling in an RF ACZ trap via a secondary, weak microwave field. Future efforts will focus on applying Eq. 3.41 to a realistic trapping potential formed by multiple parallel wires on an atom chip. This system has applications, in addition to evaporation, in applying a microwave ACZ force to atoms in an RF ACZ trap, double dressing, and microwave spectroscopy in the ACZ trap. We are also developing the dressed atom picture for a two-level system in the presence of two AC fields, applicable to evaporative cooling in the RF ACZ trap with a secondary RF field. This has also been shown to cool atoms

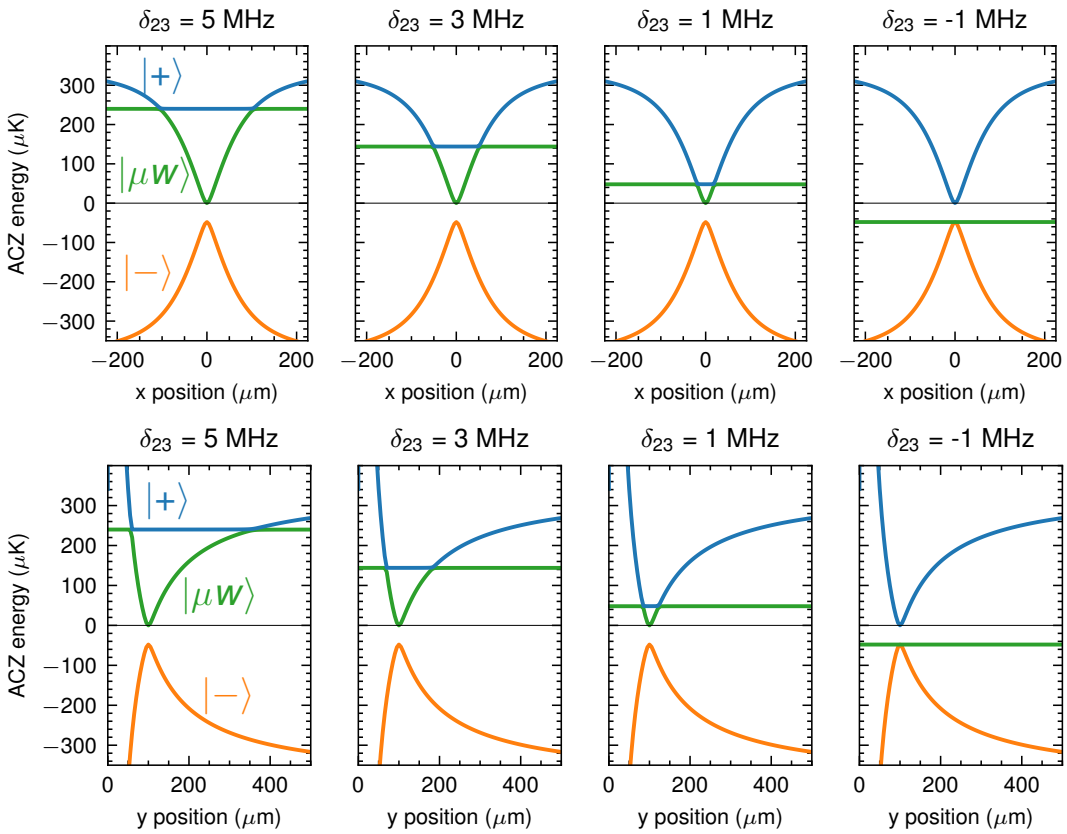

Figure 3.12: Horizontal (top row) and vertical (bottom row) trap profiles for a single wire ACZ trap with $I_{ac} = 0.543$ A and $B_{ext,ac} = 10.86$ G. The combined wire and external fields produce a spatially dependent $\Omega_{12}(x, y)$. The traps for each eigenstate are obtained by numerically solving Eq. 3.41 at each point in space. These calculations use $\delta_{12} = -2\pi \times 1$ MHz, and $\Omega_{23} = 2\pi \times 0.1$ MHz, and are shown at different values of δ_{23}. A solid black line indicates the zero energy point.

in the ACZ trap [16], and we have performed initial RF spectroscopy measurements of the RF ACZ trap (see Chapter 9).

Chapter 4

Apparatus

With the theory of reaching ultracold temperatures described in the previous chapter, I now turn to the experimental implementation of those techniques. This chapter provides an overview of the Aubin lab's ultracold atom apparatus as well as some of the theory behind the machine. The bulk of the apparatus was already built when I joined, and many detailed explanations on the different aspects of the apparatus can be found in previous theses [63, 64, 57, 14, 16, 51]. I will give a comprehensive overview of the process for making Bose-Einstein condensates (BECs) in our lab, as well as highlight some of my additions to the apparatus during my time in the lab: the addition of a second power supply for two-wire chip trapping and the construction of an IQ modulation based microwave source.

The chapter is presented as follows: Section 4.1 gives an overview of the ultracold atom apparatus, guiding the reader through the experimental process to reaching BEC. Notably, Section 4.1.8 discusses the addition of a second DC supply for two-wire trapping on the atom chip. Section 4.2 gives calibrations of the magnetic fields used in the experiments, measured using the atoms as probes. In Sec. 4.3 I go over some common measurements used throughout this thesis. Section 4.4 overviews the RF hardware and software used for ACZ trapping on the atom chip. Finally, Sec. 4.5 discusses the design, construction, and testing of a multi-channel microwave source using IQ modulation.

4.1 Ultracold Atom Apparatus

A diagram of the apparatus is shown in Fig. 4.1. Room temperature ^{87}Rb atoms in the

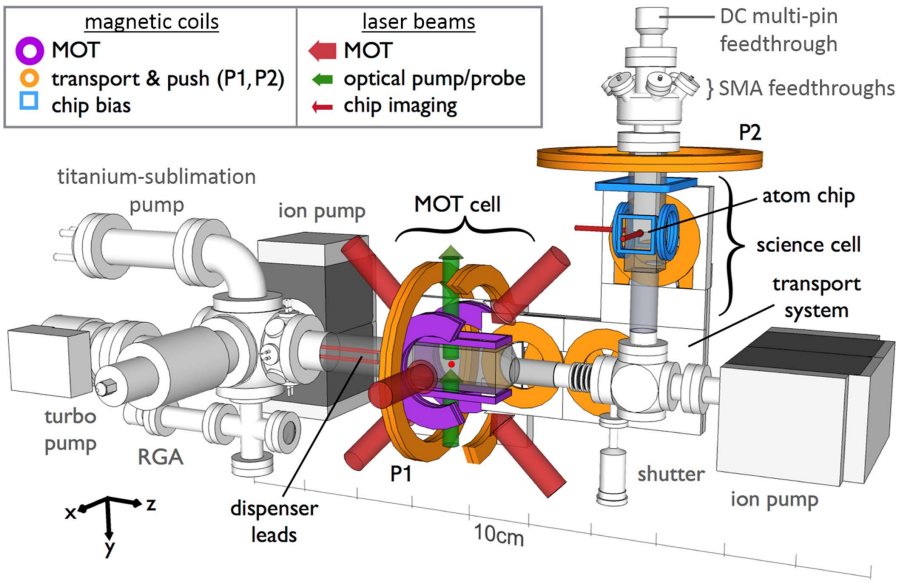

Figure 4.1: CAD image of the ultracold atom apparatus, taken from [18].

MOT (Magneto-Optical Trap) cell are first laser cooled and trapped in a three-dimensional MOT where they are reduced in temperature by a factor of 10^6. After a brief optical molasses, which provides further cooling, the atoms are optically pumped and loaded into a purely magnetic trap. This trap is transported along an L-shaped vacuum chamber and transferred onto a micro-magnetic atom chip trap. A final stage of evaporative cooling brings the atoms to the sub-μK temperatures needed for BEC. Typically, we operate slightly above the BEC threshold, which can be adjusted through the RF evaporation frequency. This cycle of producing ultracold atoms and performing experiments takes roughly 30 seconds. A typical experimental cycle is given in Table 4.1 with relevant times and atom temperatures.

Stage	Time	Temperature (μK)	Atom Number
MOT	15 s	146	5×10^8
Optical Molasses	4 ms	16	5×10^8
Optical Pumping	0.9 ms	16	5×10^8
Transport to Chip	7 s	60	3×10^8
Chip Trap	1 s	90	5×10^6
Evaporation	4 s	1-2	3×10^5
To BEC (optional)	0.2	0-0.4	2-4$\times10^4$

Table 4.1: A typical experimental cycle for producing ultracold atoms used for experiments. The temperatures and atom numbers given indicate the values at the end of each stage of the cooling process.

4.1.1 Laser Preparation

The first stage of the ultracold atom preparation is Doppler laser cooling. To perform the cooling, we need to precisely control the frequency of our lasers to access the correct cycling transition (see Fig. 4.2). Doing this is relatively straightforward; we just have the atoms tell us where the transition is! This is accomplished using a saturation spectroscopy setup [65], which allows us to resolve the hyperfine structure within the Doppler profile of the laser absorption. The saturation spectroscopy (or sat spec) signal is shown as the blue line in Fig. 4.3, scanning the laser across the D2 lines for ^{87}Rb and ^{85}Rb. Our laser cooling apparatus uses ^{87}Rb. We will narrow our focus there. The cycling transition we want to target is the $F = 2 \leftrightarrow F' = 3$ transition between the $5S_{1/2}$ and $5P_{3/2}$ states, whose hyperfine structure is shown in Fig. 4.2. This transition in the saturation spectroscopy signal is noted by the black dashed line in Fig. 4.3(b). To lock the laser to this transition, we dither the frequency of the sat spec pump laser, and then feed the sat spec signal through a lock-in amplifier which is set up to take the time derivative of the input. This signal acts as the error signal for a PI (Proportional, Integral) feedback system and is shown as the green trace in Fig. 4.3.

Looking at Fig. 4.2, we see that in addition to the $F = 2 \leftrightarrow F' = 3$ cycling transition, atoms in the $F = 2$ state can also be brought up to the $F' = 2$ level. Once there, the atoms can decay down to either the $F = 2$ state, thereby remaining in the cycling transition, or

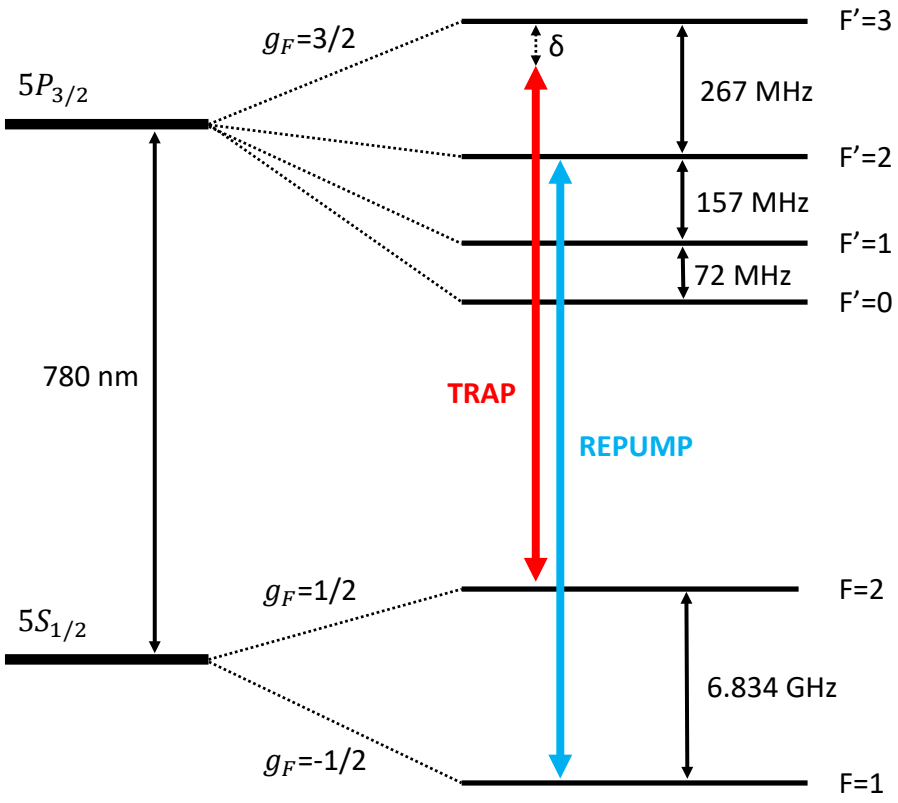

Figure 4.2: Rubidium 87 D2 hyperfine structure. Values for the hyperfine splittings are taken from [53].

the $F = 1$ state, leaving the cycling transition all together. The latter case is detrimental to the laser cooling operation, as atoms in the $F = 1$ state are practically insensitive to the trap light and will not participate in the laser cooling process. For this reason, a weak "repump" beam is added along with the trap light to repopulate atoms into the cycling transition. The process of locking the repump light is described in the PhD thesis of Megan Ivory [64]. In short, a small amount of trap and repump light are picked off and combined into an optical fiber. The beat note between these two frequencies of light is then stabilized to a known reference through a PI feedback circuit.

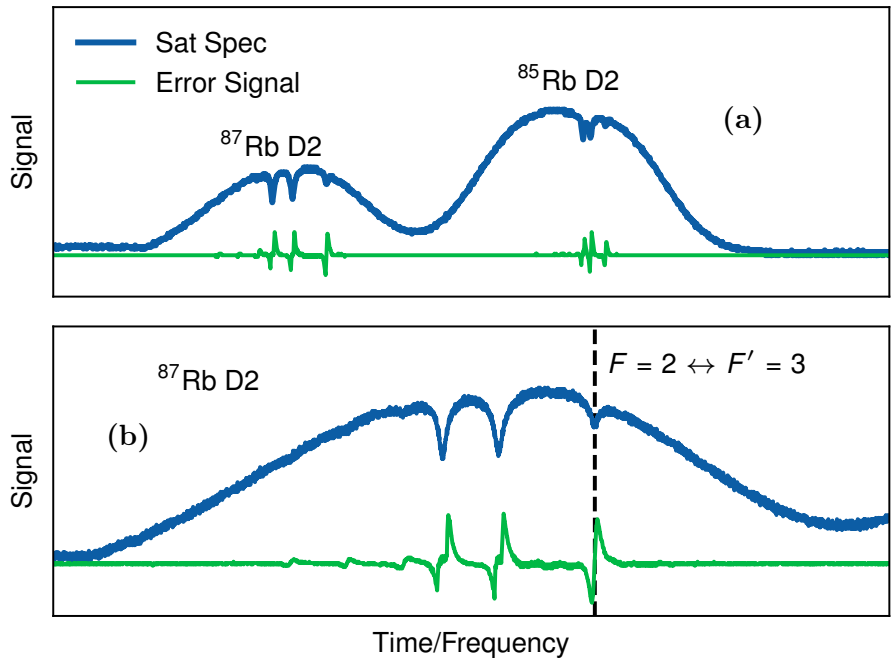

Figure 4.3: Saturation spectroscopy of the ^{87}Rb and ^{85}Rb D2 transitions (blue) and corresponding error signal (green) used for locking the trap laser. (b) Zoom in of the ^{87}Rb peaks, with the relevant $F = 2 \leftrightarrow F' = 3$ transition labeled.

4.1.2 Tale of Many Repumpers

During my time here I have used three different lasers acting as the repumper. When I first arrived, the lab was using a diode laser inside a homemade enclosure to provide humidity control when operating the laser temperature near the dew point. While this laser worked as a repumper, it often mode hopped to a different optical frequency and could take several hours to finesse back to the correct mode. Annoyed by this, I decided to swap it with a spare Toptica DLC Pro laser (same model as our trap laser) which was not being used at the time. While overqualified for the job, this laser offered notably better performance without the mode hopping issue. However, the Toptica laser was intended for other uses in the lab, and the decision was made to swap it for a third and final (at least for my time here) laser. Currently, we use a Thorlabs DBR780PN. We found that in combination with a small focus optical fiber output coupler (Thorlabs F230APC-780) the output beam diverged significantly. To solve this issue, we added a 40 cm focal length lens

approximately 10 cm from the output coupler to collimate the beam.

4.1.3 Doppler Cooling

With the trap and repump lasers locked to the correct atomic transition frequencies, each goes through a series of accousto-optic modulators (AOMs), as diagramed in Fig. 4.4. Of note is that the trap laser seeds another diode laser to injection lock it at the same

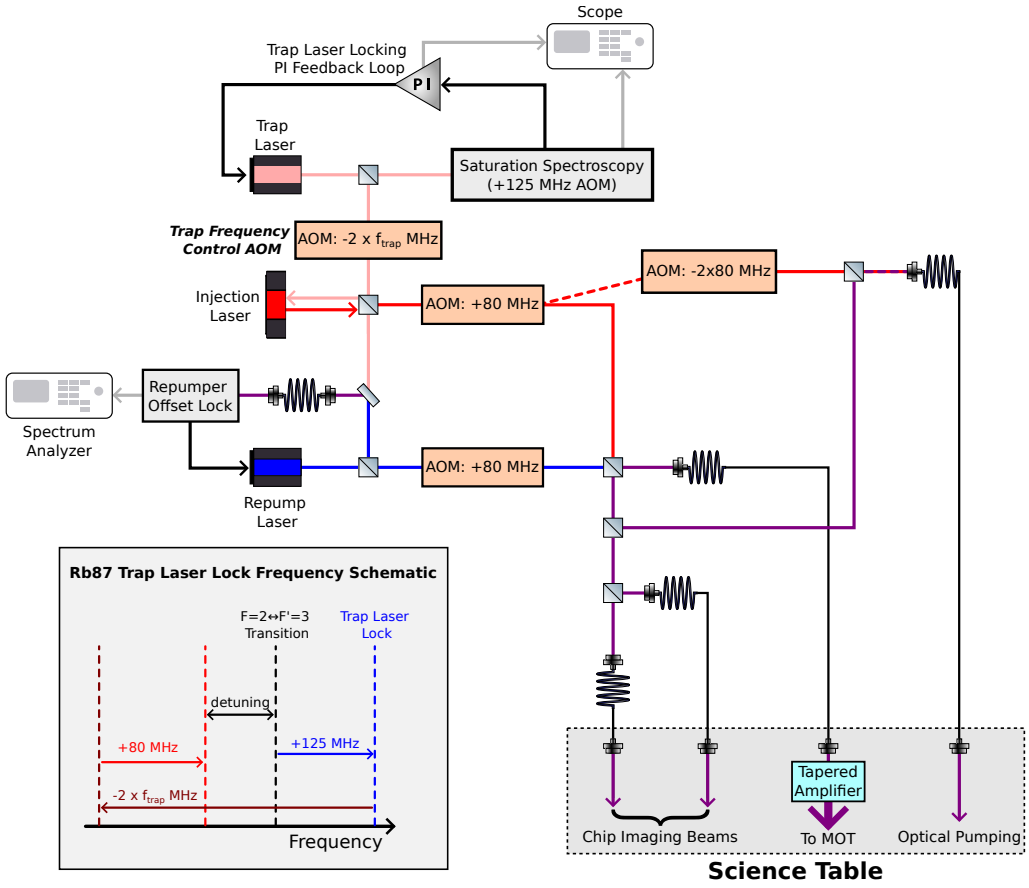

Figure 4.4: Schematic of the laser setup for generating light for the MOT, optical pumping, and imaging. Figure adapted from [18].

frequency. The injection laser outputs around 50 mW and allows us to operate the high quality Toptica trap laser at lower power, thus extending its lifespan. Trap and repump light are combined at an optical fiber and transferred to the "science" table, which contains the vacuum system housing the MOT and atom chip. Typically, we have roughly 12-15 mW

and 2-3 mW of trap and repump light coming out of the fiber, respectively. The combined light then passes through a tapered amplifier (TA) that amplifies the light. After some spatial filtering, roughly 400 mW of combined trap and repump light are sent to the MOT cell. This light is split into six beams, generating three-dimensional laser cooling for ^{87}Rb inside the MOT chamber.

4.1.4 Magneto-Optical Trapping

The magnetic confinement for the laser cooling is accomplished using a pair of coils in an anti-Helmholtz configuration which generates a gradient of ∼9 G/cm. In addition to the main MOT coils, we apply three "bias" magnetic fields to zero the environmental magnetic field for better optical molasses.

As part of the MOT, we implement a LIAD (Light Induced Atom Desorption) system to increase atom number. The LIAD system works by shining 405 nm light onto the MOT vacuum cell which acts to remove any stray ^{87}Rb atoms stuck to the glass vacuum chamber walls. One can think of this as an analog to the photoelectric effect, except we are using photons to knock the atoms free from the walls of the vacuum chamber. This process is essential to the operation of our system, increasing the size of the MOT by a few orders of magnitude, shown in Fig. 4.5. We discovered the power supply used to drive the 405 nm LEDs wore out after 10 years of operation and could only drive half the LED's current. After replacing the supply, we were able to match the previous record in the lab with a BEC of 40,000 atoms, about 1.5-2 times larger than what had become the "normal" BEC size. Additionally, the near-UV LIAD LEDs are now almost blindingly bright and I advise future students not to stare at them too long despite how mesmerizing they are.

4.1.5 Sub-Doppler Cooling

After collecting atoms in the MOT for 15 seconds, the magnetic trapping fields are quickly turned off, and the trap and repump lights are reduced in power. The trap light AOM frequency (see Fig. 4.4, "*Trap Frequency Control AOM*") is then ramped from $f_{trap} = 112 \rightarrow$

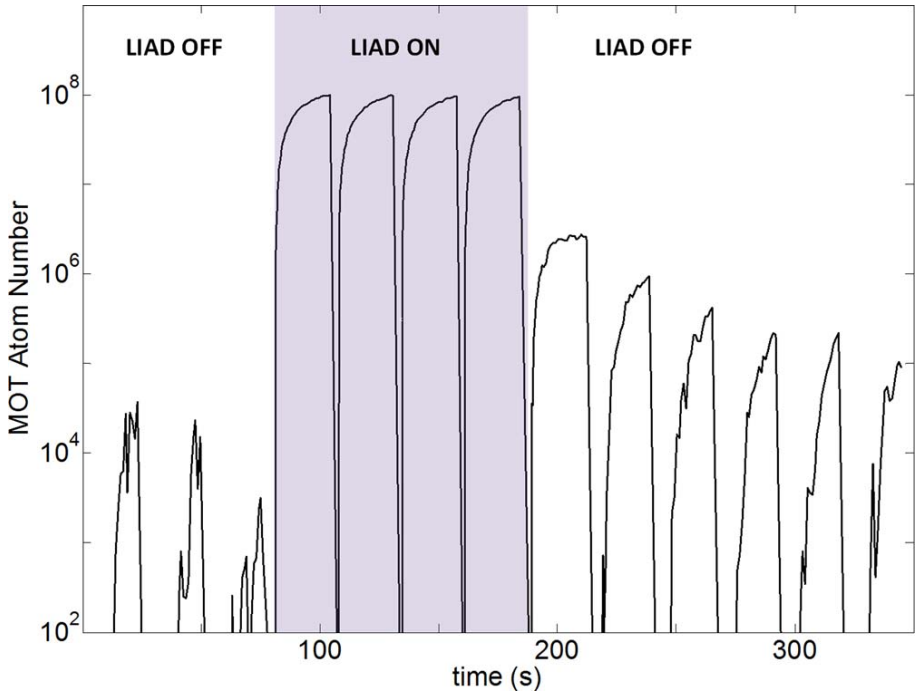

Figure 4.5: MOT loading using the light induced atom desorption (LIAD) system. The MOT was loaded for periods of 25 seconds and fluorescence imaging was used to obtain real-time atom number referenced to absorption imaging of the MOT. The ramping seen in the "LIAD ON" section is due to the loading and loss rate of the MOT, which eventually reach an equilibrium. Data from [18].

136 MHz, increasing the trap laser detuning from 19 $\rightarrow$ 67 MHz below the $F = 2 \leftrightarrow F' = 3$ transition. Moving the light farther from resonance yields more effective cooling as recoil heating from photon absorption is reduced. When everything is working perfectly, the molasses process takes 3.25 ms and reduces the temperature to around 20 μK [51].

4.1.6 Optical Pumping

To transport atoms to the atom chip we use a purely magnetic trap. These DC magnetic traps can only trap low-field seeking DC states ($|F = 2, m_F = 2\rangle$, $|F = 2, m_F = 1\rangle$, and $|F = 1, m_F = -1\rangle$ in ^{87}Rb); however in the MOT the atoms are in a mixture of all the $F = 2$ states. To transfer the population into the magnetically trappable $|F = 2, m_F = 2\rangle$ state, we apply a few hundred μW of σ^+ polarized light to pump the atoms into the desired edge state. A vertically aligned magnetic field sets the quantization axis. Previous work

[51] found that approximately 0.9 ms of optical pumping time produced the best results.

One of the diagnostics used to characterize the system performance is to monitor the number of atoms in the magnetic trap. While not providing a single answer to your problems, a low B-trap atom number can be attributed to low optical pumping power, low trap and/or repump power, or power imbalances from the waveplates, for example. There is also a "magic MOT mirror" that controls the alignment of the MOT cooling beams that occasionally must be touched up. One can also measure the lifetime of atoms in the magnetic trap as a final measure of proper operation (I say final because it can be the most time consuming option). An example of this measurement is shown in Fig. 4.6, showing a B-trap lifetime of about 40 seconds. The hold time in the B-trap is limited to approximately 30 seconds due to the heating of the trapping coils.

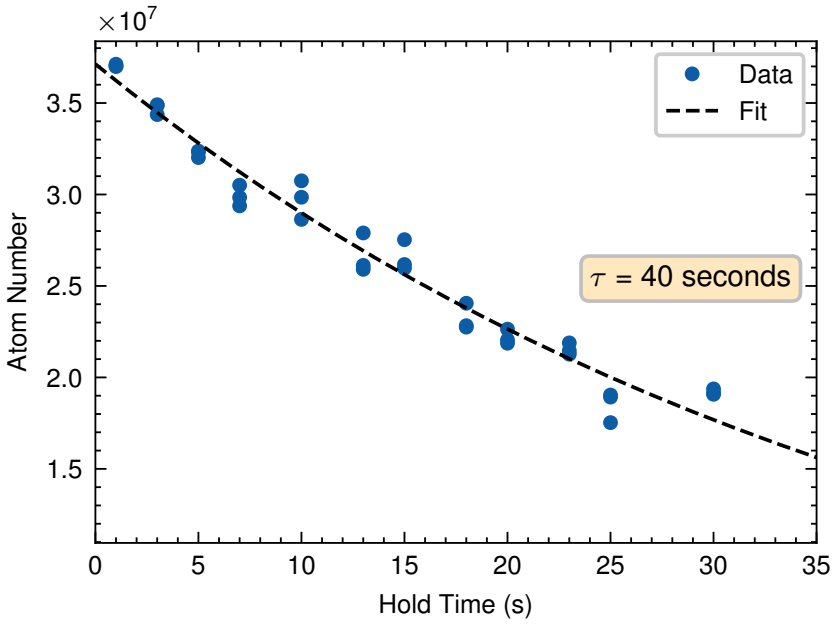

Figure 4.6: Measured lifetime in the magnetic trap. Atom numbers are obtained from fluorescence imaging after loading the MOT for 5 s and then performing optical molasses and optical pumping. The fit gives a lifetime of 40 seconds, consistent with measurements separated by multiple months. Hold times are limited to roughly 30 seconds by the heating of the magnetic trapping coils. The data here is from 07dec23. The data was fit using the function $f(t) = Ae^{-t/\tau}$.

4.1.7 Magnetic Trap and Transport

After the optical molasses, the atoms are transported along an L-shaped vacuum chamber into the science cell containing the atom chip. This transportation is accomplished by adjusting the currents in a series of magnetic coils to move the trap from the MOT chamber to the chip. This transfer process takes about 8 seconds but could potentially be made shorter through implementing machine learning algorithms [66].

4.1.8 DC Chip Trapping

Once at the chip, atoms are transferred into a DC magnetic chip trap using the Z-shaped chip wire (see Fig. 4.7). We run 1 A of current through the wire which the chip can sustain for approximately 7 s before potentially risking damage. For that reason a "kill-box" circuit was implemented to automatically disable the Z-wire current source should it run too high or for too long. The loading efficiency into the atom chip trap from the transport trap is a few percent, meaning we trap only a few million atoms on the chip. The trap lifetime in the Z-wire trap is about 7-9 seconds [18].

In addition to the Z-wire trap, I installed a second low-noise current supply (High Finesse) which attaches to a nearby U-shaped wire, spaced 100 μm center-to-center away. This allows for two-wire DC Zeeman trapping which is used for the potential roughness experiment in Chapter 6. The chip layout with relevant dimensions and orientations is given in Fig. 4.8. Of note is that the U and Z wires are naturally counter-propagating.

4.1.9 RF Evaporation to BEC

After being loaded onto the chip, the atoms are at a temperature of tens of μK. To achieve Bose-Einstein condensation, the atomic sample needs to be brought down to just a few hundred nanoKelvin in temperature while increasing the phase space density. As discussed previously, we achieve this cooling through radio-frequency evaporation. To perform evaporation, RF current starting at 19 MHz is sent through a secondary atom chip

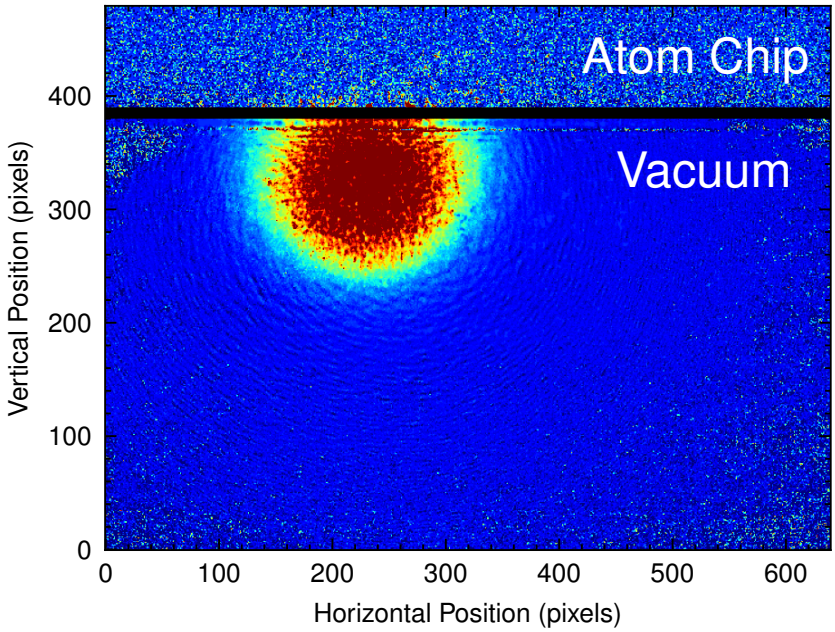

Figure 4.7: Experimental absorption image of ^{87}Rb atoms in the Z-wire DC chip trap (1 pixel = 7.4 μm).

wire. The RF frequency is then brought from 19 MHz to approximately 3.35 MHz over the course of several seconds. Fig. 4.9 shows the phase transition from a cloud of thermal atoms, indicated by an isotropic cloud, to a BEC, which has a distinct anisostropic profile.

4.1.10 Imaging and Analysis

We use two imaging methods to obtain information about the ultracold atom cloud, such as atom number, position, and cloud size: fluorescence and absorption imaging. These images are taken on a CCD camera and analyzed to obtain the cloud properties. For dense atomic clouds like those trapped on the atom chip, absorption imaging allows us to gain more accurate information about the cloud, whereas imaging photons are unable to reach the cloud center and fluoresce. All the data presented in this thesis uses absorption imaging, so I will limit the discussion to that. Information on using fluorescence imaging in our lab can be found in previous theses [64, 57].

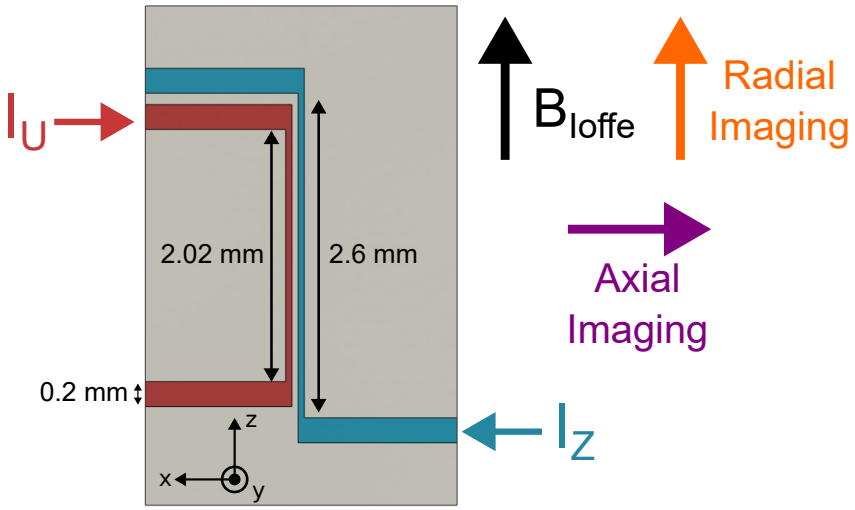

Figure 4.8: Two-wire DC atom chip layout using the Z- and U-shaped wires, with relevant dimensions and current directions labeled. The wire spacing in the central portion of the chip is 100 μm center-to-center. All other chip wires are omitted from the image. The Ioffe field and imaging beam directions are shown.

4.1.10.1 Absorption Imaging

This imaging process looks at the shadow created by the atoms in the presence of the imaging light. The attenuation of the imaging light's intensity, $I(z)$, through an atomic medium in the z direction is given by Beer's Law [49]:

$$I(z) = I_0 e^{-OD} \tag{4.1}$$

Where I_0 is the incident intensity. Explicitly, the laser intensity contains x and y coordinate information, and our image is created in the xy-plane. The optical depth, OD, is given as (for low intensity)

$$OD = \frac{\sigma_0}{1 + (2\delta/\gamma)^2} nz \tag{4.2}$$

with $\sigma_0 = 3\lambda^2/2\pi$ being the resonant cross-section, δ is the detuning of the laser from resonance, and γ is the spontaneous emission rate. We image on the ^{87}Rb D2 transition using circularly polarized light, for which $\lambda = 780$ nm and $\gamma = 2\pi \times 6.065$ MHz [53]. Generally, the imaging light is on-resonance so $\delta = 0$, which eliminates lensing effects from

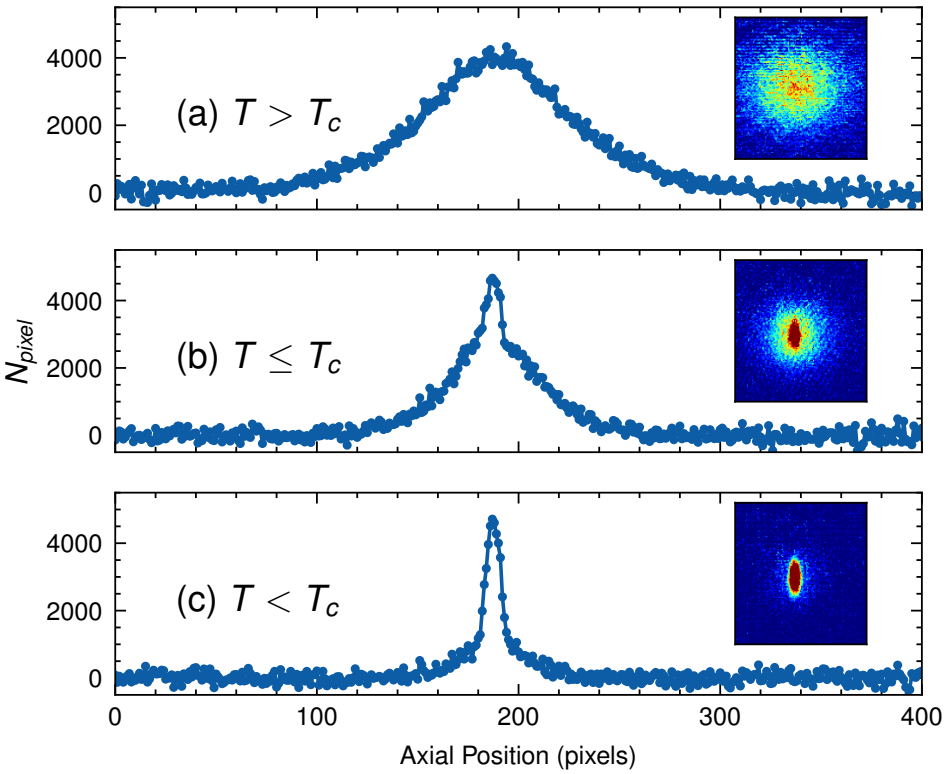

Figure 4.9: Cross-section plots of the atom cloud after 9.5 ms of free-fall and corresponding absorption images during radio-frequency evaporation to BEC. The formation of the BEC is characterized by the anisotropic density profile. For ^{87}Rb with a density of $n = 10^{14}$ atoms/cm^3, the critical temperature is $T_c \simeq 400$ nK.

the atoms. Here, n is the atom number density. For a single pixel, the atom number is given as

$$N_{pixel} = nA_{pixel}z \tag{4.3}$$

where A_{pixel} is the area of a single pixel on the CCD camera. Multiplying the optical depth by A_{pixel} we can solve for the atom number for each pixel, N_{pixel}, as

$$N_{pixel} = \frac{A_{pixel}}{\sigma_0}\left[1 + (2\delta/\gamma)^2\right] \ln\left[\frac{I_0}{I(z)}\right] \tag{4.4}$$

The intensities are given by the number of counts measured by the CCD camera with and without atoms present, so we can rewrite the above equation as (for on-resonance light)

$$N_{pixel} = \frac{2\pi}{3\lambda^2} A_{pixel} \ln\left[\frac{C_{laser}(x,y)}{C_{atoms}(x,y)}\right] \tag{4.5}$$

where C_{laser} is the number of counts without atoms present and C_{atoms} is the number of counts with atoms present.

In practice, we select a region of interest (ROI) where atoms are located and sum the pixel atom numbers along each direction to obtain projections of the 2D cloud along each spatial dimension. These projections are then fit to a Gaussian distribution $We^{-(x-b)^2/(2\sigma^2)}+d$ to obtain the amplitude (W), width (σ), and position (b) of the cloud. This fitting process is visualized in Fig. 4.10. The atom number along each spatial dimension can be obtained from the fit via

$$N_{x,y,z} = \sqrt{2\pi} W_{fit} \sigma_{x,y,z} \tag{4.6}$$

4.1.10.2 Stern-Gerlach Imaging

To distinguish atoms in different m_F spin states we apply a magnetic gradient via a Stern-Gerlach coil oriented perpendicular to the chip wires. Atoms in different m_F states will thus experience a spin-dependent force resulting in spatially separated atom clouds (see Fig. 4.11). This technique is useful for getting relative spin state populations for Rabi oscillations and diagnosing the chip trap for unwanted spin contamination, for example. As part of this imaging, we apply both trap and repump light for a short time (0.5-1 ms) as a "prepulse" to optically pump atoms into the $|2,2\rangle$ state to image on the cycling transition.

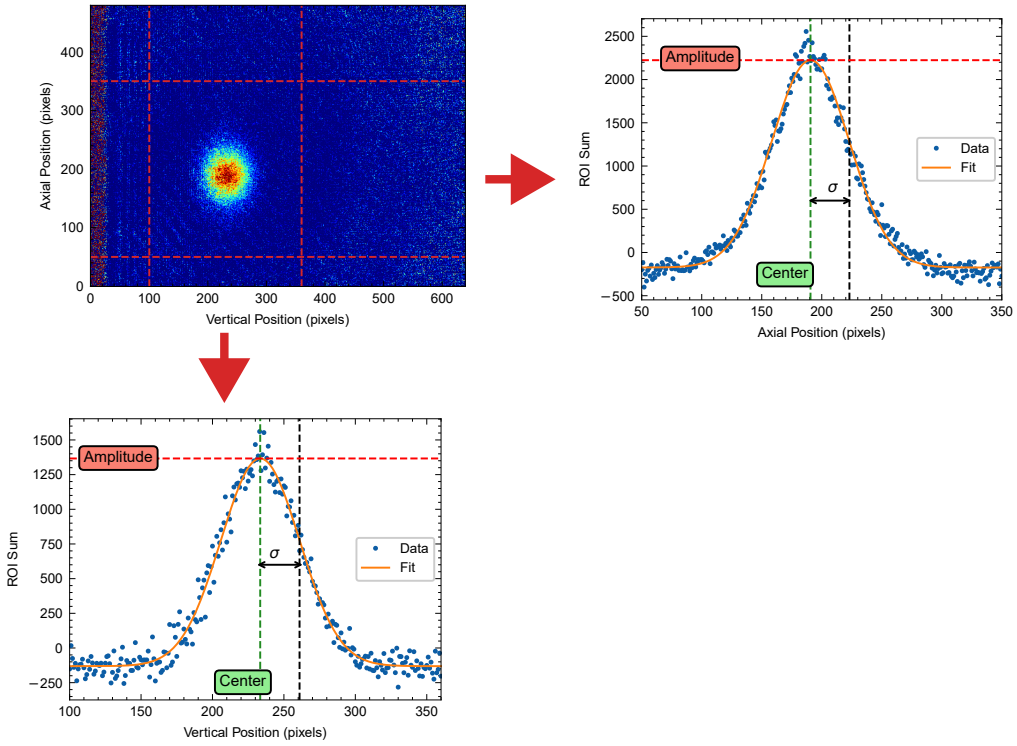

Figure 4.10: Analysis of absorption images of ultracold atoms. Using Eq. 4.5 we convert the images into an atom number for each pixel and then project the 2D image into a 1D atom distribution by summing the pixels along each spatial dimension. The 1D distributions are then fit to Gaussians from which we can obtain the atom number (through Eq. 4.6), cloud width, and center-of-mass position.

4.2 Magnetic Field Calibrations

All our methods of trapping require the use of at least one magnetic field generated by a coil or pair of coils. It is therefore helpful to know the strength of the field felt by the atoms for a given current through the coil(s). One method uses a Gauss meter to measure the magnetic field at the location of the atoms. For the coils installed within the apparatus, this is essentially impossible since the atom chip is encased inside a glass vacuum cell preventing access with a probe. Instead, we use the atoms as a probe to measure their response to an applied magnetic field via the Zeeman effect. This method is described in more detail in Chapter 6 and described briefly herein. In essence, we measure the frequency difference between the $|2,2\rangle$ and $|1,1\rangle$ states in ^{87}Rb as a function of magnetic

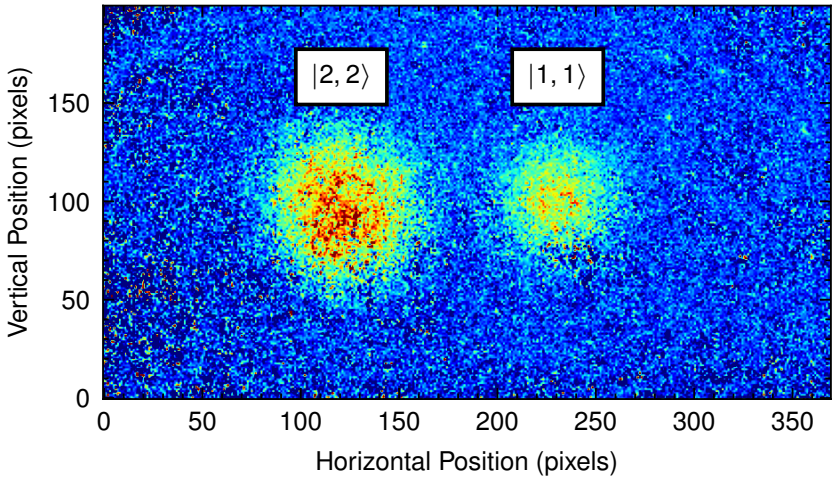

Figure 4.11: Simultaneous absorption image of two atomic spin states after Stern-Gerlach separation (1 pixel = 4.65 μm).

field strength generated by one of the coils. This gives us a plot of state splitting versus current sent through the coil(s), which we fit to a line. In the low-field regime, these states split linearly by $\sim$ 2.107 MHz/G. Equating this theoretical splitting to our fit yields the conversion from current to Gauss. I note that in some instances, the control setting in the Adwin sequencer program is in Volts rather than Amps. In these cases, you must also calibrate the Amperage output from the supply for a given Adwin voltage setting.

Coil	Power Supply	Proportionality	Offset
Ioffe	Kepco	(2.66 G/A)I_{Ioffe}	-1.29 G
Chip Vertical Trim	Kepco BOP	(1.41 G/A)I_{vert}	+0.06 G
Chip Hold Field	Kepco BOP	(5.33 G/V)V_{adwin}	-0.118 G

Table 4.2: Magnetic field calibrations for various coils in the lab.

4.3 Common Measurements

In this section, I describe some of the common measurements performed with ultracold atoms that will be used throughout this thesis.

4.3.1 Measuring Temperature

To measure the temperature of the atoms on the chip, we use a standard time-of-flight (TOF) technique. When all trapping fields are shut off (magnetic or optical), the cloud of thermal atoms expands ballistically under gravity according to their thermal characteristics. Thus, atoms at a higher temperature will expand faster than colder atoms. By imaging the atom cloud as it falls, we can fit the atom distribution with a Gaussian and extract the rms width, σ. We can then fit the width of the cloud versus the TOF to the equation

$$\sigma(t) = \sqrt{\sigma_0^2 + (vt)^2}, \tag{4.7}$$

where σ_0 is the initial size of the cloud before expanding and v is the expansion velocity (see Fig. 4.12). This velocity can be related to the atom's temperature (hotter atoms will have more energy, i.e. velocity, and will thus expand at a faster rate) through the equation

$$\frac{1}{2}mv^2 = \frac{1}{2}k_B T \Rightarrow T = \frac{mv^2}{k_B}. \tag{4.8}$$

A cool note for ^{87}Rb is that, to within $\sim 5\%$, you can obtain the temperature in μK of the atoms just by squaring the velocity in cm/s (i.e. $T_{\mu K} = v^2_{cm/s}$).

In practice we extract a temperature for each spatial dimension and take an average. This is typically done looking at the transverse (xy) direction so that we obtain two temperatures, T_x and T_y, from which we obtain the average temperature.

4.3.2 Measuring Trap Frequency

One of the main characteristics of ultracold atom traps is the trap frequency, ω, describing the curvature of the harmonic trapping potential. To measure the trap frequency, we give the atoms a kick by applying a force (usually from a magnetic coil or chip wire) and allow the atoms to undergo harmonic oscillation in the trap. By taking images of the atoms at various times, we can plot the position as a function of time. Fitting this data to a

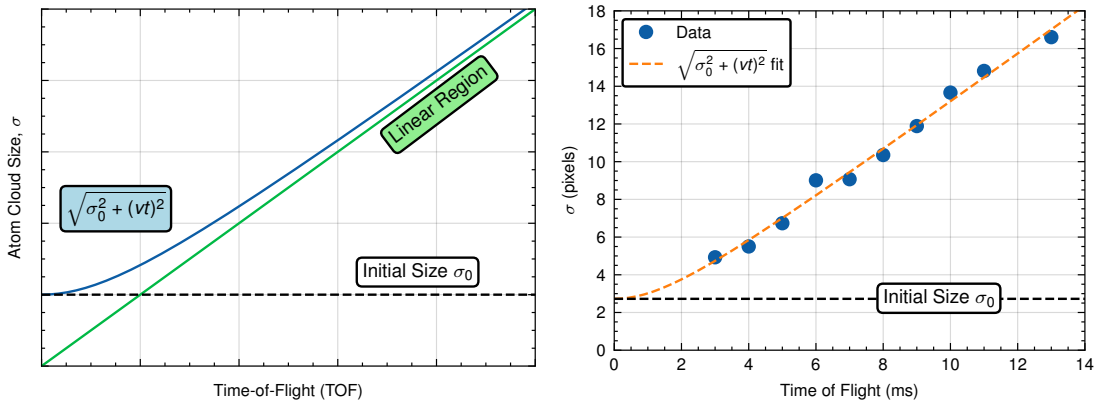

Figure 4.12: Method for determining the temperature of the ultracold atomic samples from time-of-flight measurements. (Left) Plot of the fitting function (Eq. 4.7) indicating the initial cloud size and region where the atom cloud size changes linearly with TOF. (Right) Example of experimental data measuring the temperature of atoms trapped in a two-wire DC magnetic chip trap. Each data point is the average cloud width of up to three shots. This uses the radial imaging camera, for which 1 pixel = 7.4 μm The temperature obtained from the fit is 0.96 μK.

sinusoid then yields the trap frequency. This data are generally fit to a sinusoial function with exponentially decaying amplitude:

$$f(t) = Ae^{-t/B}\sin(\omega t + C) + D, \tag{4.9}$$

where A is the amplitude of the sine wave, B is the $1/e$ decay time, C is the phase offset, and D is the vertical offset. The decay term likely comes from the atoms sampling anharmonic regions of the trapping potential. An example data set is shown in Fig. 4.13 for atoms trapped in an RF ACZ chip trap.

4.3.3 Lifetime Measurements

Another key measurement of the atom traps is the trap lifetime. This tells us how long we are able to hold atoms in the trap before they start to leave. While the exact loss mechanism is not necessarily clear from a lifetime measurement, it is a good benchmark for how well the apparatus is running and also helps put time scales on your experiments. To measure the lifetime we simply hold the atoms in the trap for varying amounts of time

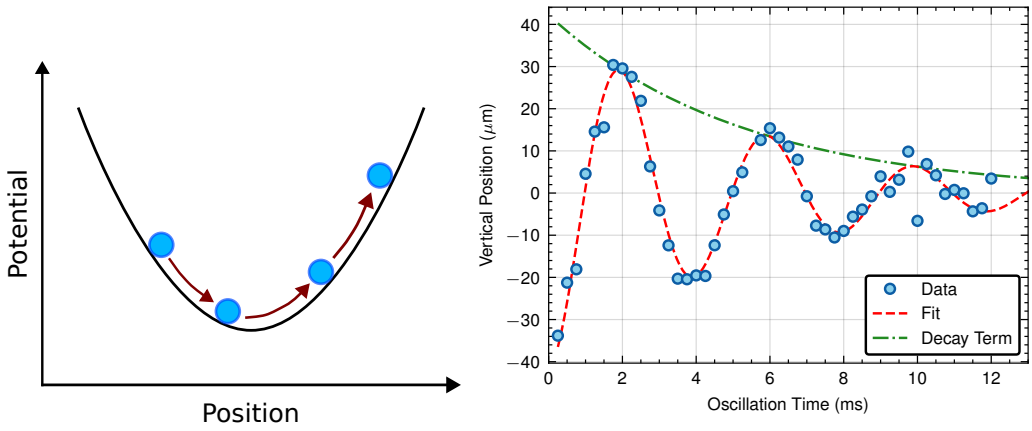

Figure 4.13: Example trap frequency measurement. Here, the atoms are trapped in an RF AC Zeeman trap and given an initial DC push using a chip wire. The dashed red line shows the fit of the data using Eq. 4.9, and the green dot-dashed line shows the exponentially decaying oscillation amplitude. Here I am only showing vertical oscillation data, but this technique can also be applied to get the horizontal trapping frequency.

and then look at the atom number, obtained through either fluorescence (for the magnetic trap) or absorption (for experiments on the chip) imaging. The data can then be fit to a decaying exponential

$$f(t) = Ae^{-t/\tau}, \tag{4.10}$$

where τ is the trap lifetime (i.e. the $1/e$ decay time). An example of this measurement is shown in Fig. 4.6. It should be noted that it is not uncommon to fit the lifetime data to two decaying exponentials, one with a fast decay and another with a slow decay. The initial fast decay can be caused by some free evaporation in the trap while the slow decay gives the trap lifetime. I will also note that one should be careful of fitting with a constant offset, as depending on how the atom number is measured and how many "lifetimes of data" you have, this addition can result in a false lifetime.

4.4 RF AC Zeeman Trapping Hardware

While the ultimate goal of the lab is to perform microwave AC Zeeman (ACZ) trapping using inter-manifold atomic transitions, this requires a new chip capable of supporting such

high frequencies (between F=1 and F=2 at ∼6.8 GHz). The atom chip currently installed in our apparatus was designed with the intention of operating as a DC trap, meaning it has poor coupling for AC signals. Luckily, we can get away with making a RF ACZ trap on our current chip using intra-manifold transitions within a given hyperfine manifold. This was first developed by Drew Rotunno [16] and is used in Chapter 6 where we demonstrate potential roughness suppression. Here I will briefly go over the hardware needed to produce these traps.

4.4.1 Source: FlexDDS

In order to operate the RF ACZ trap, we require a multi-output source with relative phase control between channels. As seen later in this thesis, relative phase between AC signals on the chip is a crucial parameter in the operation of the ACZ trap. Therefore, being able to deterministically control phase between multiple RF signals simultaneously is a strict requirement for us. We use the WieserLabs FlexDDS-NG, a multi-channel phase continuous source utilizing the AD9910 DDS (Direct Digital Synthesizer) chip. The rack can fit up to six FlexDDS slots, each containing two outputs. Commands are sent via Ethernet using a suite of commands developed by Drew Rotunno [16]. A sample of MATLAB code is given in Ref. [30].

We typically operate a two-wire RF ACZ trap in our current setup. When attempting to sweep the frequency of the two phase control channels, we found that one channel could inadvertently exhibit phase slipping, causing potential heating in the RF trap. The work-around to generate the two signals requires the use of two slots: one for frequency control and the other for phase control. In the two-slot scheme, the two outputs from one slot generate signals at 100 MHz with differential phase. A second slot outputs a signal at 100 MHz + f_{RF}, where f_{RF} is the operational frequency of the ACZ trap, which can be swept. The phase control signals are sent into mixers with the frequency control signal and mixed down to frequency f_{RF} while maintaining the differential phase. This mixing scheme allows us to sweep frequency while keeping the phase constant, thereby eliminating

possible phase slipping. Figure 4.14 outlines this scheme. Explicitly, the signals from each of the mixers are

$$\begin{aligned} \text{output1} &= \cos(\omega_0 t + \phi)\cos(\omega_0 t + \omega_{\text{RF}} t) \\ &= \frac{1}{2}\left\{\cos[(2\omega_0 + \omega_{\text{RF}})t + \phi] + \cos(\omega_{\text{RF}} t - \phi)\right\} \end{aligned} \tag{4.11}$$

and

$$\begin{aligned} \text{output2} &= \cos(\omega_0 t)\cos(\omega_0 t + \omega_{\text{RF}} t) \\ &= \frac{1}{2}\left\{\cos[(2\omega_0 + \omega_{\text{RF}})t] + \cos(\omega_{\text{RF}} t)\right\} \end{aligned} \tag{4.12}$$

where $\omega_0/2\pi = 100$ MHz, $\omega_{\text{RF}}/2\pi = f_{\text{RF}}$, and ϕ is the relative phase difference between signals. Inside the "Fluffy" amplifier system, each signal goes through a low-pass filter (MiniCircuits SLP50+), which provides more than 70 dB of attenuation to signals above 200 MHz. We can then drop the terms that go as $\cos[(2\omega_0 + \omega_{\text{RF}})t]$, so the signals delivered to the chip are:

$$\text{output1} = \cos(\omega_{\text{RF}} t - \phi) \tag{4.13}$$

$$\text{output2} = \cos(\omega_{\text{RF}} t) \tag{4.14}$$

where we have ignored changes to the overall amplitude, as both signals get amplified prior to being sent onto the chip.

4.4.2 Amplifier: Fluffy

Since the current atom chip is not 50 Ω impedance matched to the input RF signals, there will be significant reflections at the chip resulting in power losses. In order to get sufficient RF power onto the chip we utilize "Fluffy", a system containing three 10 W amplifiers which amplify the outputs from the FlexDDS [16]. The power coupled onto the chip is

controlled using analog voltage variable attenuators. Additional attenuators provide 6 dB of attenuation before getting delivered to the chip. Nominally, we send up to 400 mW to the chip, though typically we work at lower powers (∼200 mW) to avoid potentially damaging the chip wires.

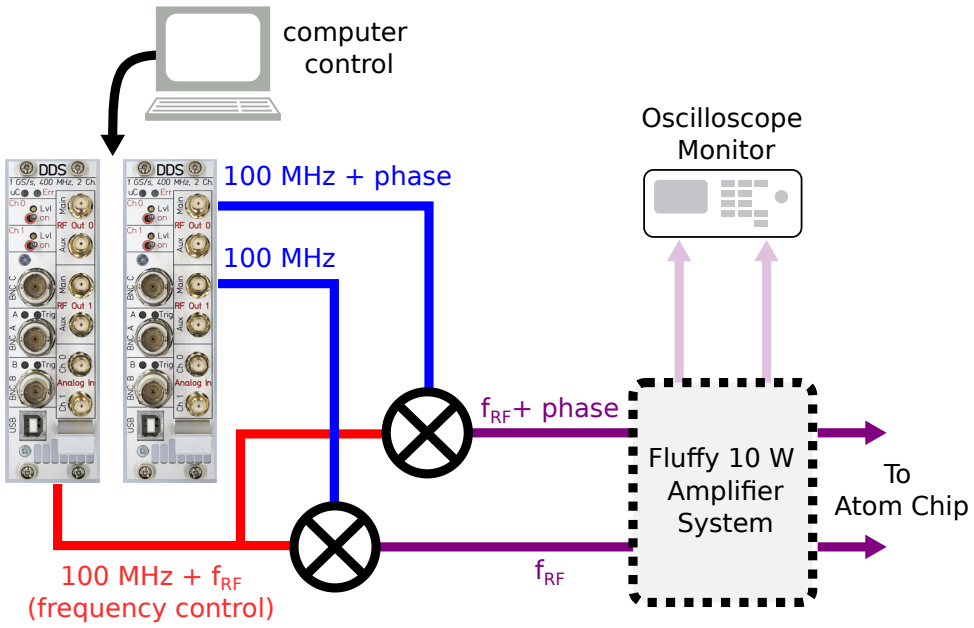

Figure 4.14: Diagram of the operation of the FlexDDS for RF ACZ chip trapping. Signals are generated using two slots for frequency and phase control. Each phase control channel at 100 MHz is sent into a mixer with the frequency control signal from a second slot at 100 MHz + f_{RF}. The outputs from the mixer at f_{RF} are then sent into a 10 W amplifier system before being sent to the atom chip. Part of the signals are picked off and sent to an oscilloscope for monitoring frequency, amplitude, and phase.

4.4.3 Bias Tee

We combine the DC and AC signals onto the same atom chip wires (U and Z in Fig. 4.8) using a bias tee (Marki Microwave BTN2-0018) on each line. This device allows for simultaneously sending DC and AC current onto the chip and lets us operate the two-wire DC Zeeman and RF AC Zeeman traps using the same wires.

4.5 Digitally Phase Controlled Microwave Source

To enter the domain of microwave ACZ trapping, two key components are required: an atom chip capable of operating at GHz frequencies, and a microwave source for enabling trapping and coherent manipulation. The former, currently under development by our group, is the subject of Chapter 7. This section focuses on the design and construction of a multi-channel, 6.8 GHz microwave source based on IQ modulation. By employing this technique, we can precisely control an ultra-low noise microwave signal using the FlexDDS RF source introduced in the previous section. IQ modulation enables phase-continuous frequency and phase sweeps at microwave frequencies, with rapid (ms-scale) sweep times accessible through straightforward software control.

4.5.1 IQ Modulation Theory

The basic diagram for IQ modulation is shown in Figure 4.15. A local oscillator (LO) at

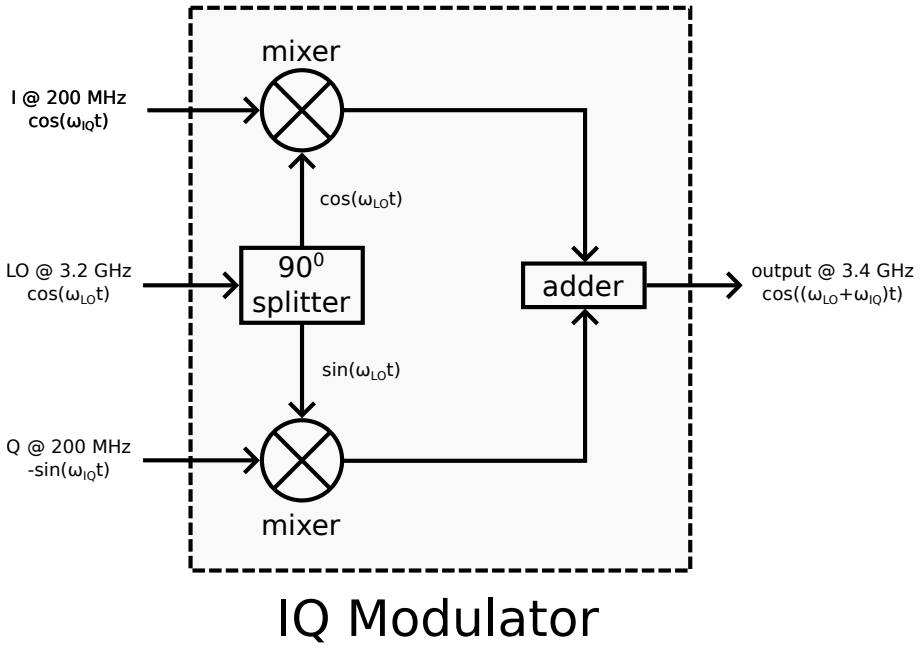

Figure 4.15: Basic block diagram of the IQ modulator.

frequency ω_{LO} goes into a 90-degree splitter where the outputs are 90° out of phase with

one another. Those LO signals are then sent into a mixer and combined with the in-phase (I) and quadrature (Q) signals at frequency ω_{IQ}. The output of the mixer is the product of the inputs, which are

$$\begin{aligned} RF_1 &= I \times LO_2 = AB\cos(\omega_{LO}t)\cos(\omega_{RF}t) \\ &= \frac{AB}{2}\left\{\cos[(\omega_{LO}+\omega_{RF})t] + \cos[(\omega_{LO}-\omega_{RF})t]\right\} \end{aligned} \tag{4.15}$$

$$\begin{aligned} RF_2 &= Q \times LO_1 = -AB\sin(\omega_{LO}t)\sin(\omega_{RF}t) \\ &= -\frac{AB}{2}\left\{\cos[(\omega_{LO}-\omega_{RF})t-\phi] - \cos[(\omega_{LO}+\omega_{RF})t+\phi]\right\} \end{aligned} \tag{4.16}$$

The mixer outputs RF_1 and RF_2 are then summed together using an adder, giving

$$\begin{aligned} Output &= RF_1 + RF_2 \\ &= AB\left\{\cos(\phi/2)\cos[(\omega_{LO}+\omega_{RF})t+\phi/2] + \sin(\phi/2)\sin[(\omega_{LO}-\omega_{RF})t+\phi/2]\right\} \end{aligned} \tag{4.17}$$

If the I and Q signals are perfectly 90° out of phase ($\phi = 0$), the output is at the frequency $\omega_{LO} + \omega_{RF}$, i.e., the LO modulated by the RF frequency. We refer to this modulated signal as the single sideband (SSB). In the ideal model described above, the only output of the IQ modulator is the SSB; however, in reality, there is also bleed-through of the LO and IQ signals. Additionally, from Eq. 4.17 we see that any deviation from perfect IQ signals (i.e. $\phi \neq 0$) results in an unwanted sideband at $\omega_{LO} - \omega_{RF}$ (see Fig. 4.16). Through sufficient filtering, these unwanted signals can be suppressed.

4.5.2 Constructed IQ System

The functional block diagram for a single channel of the IQ system is shown in Figure 4.17. The ultra-low phase-noise microwave source (Holzworth HSM 4001b) acts as the local oscillator for the IQ modulator at 3.2 GHz. This frequency was chosen as it resulted in the lowest number of unwanted spurs on the Holzworth output. The modulation is

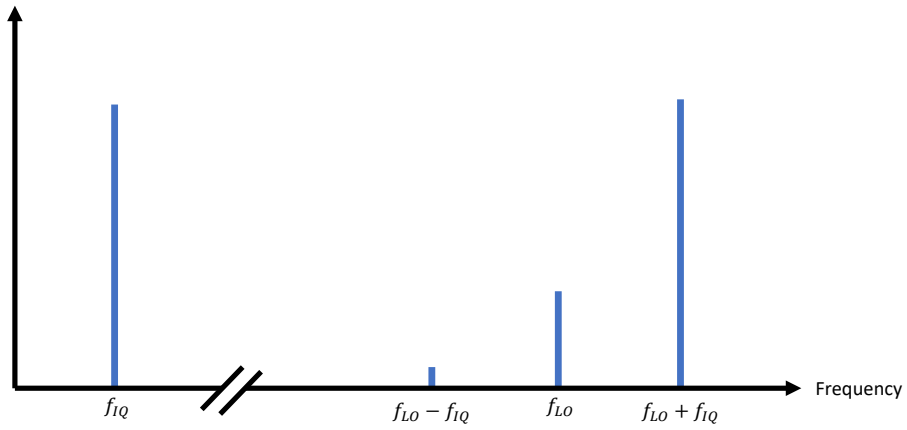

Figure 4.16: Demonstrative frequency spectrum of IQ modulation.

performed by the WieserLabs FlexDDS-NG rack module, which operates multiple AD9910 DDS chips on the same clock in expandable slot pairs. The internal timing is handled by FPGAs and can be interfaced through an Ethernet connection using a suite of MATLAB commands made by Andrew Rotunno, a former graduate student of the lab. Using a single FlexDDS slot (which has two outputs), we generate the I and Q signals at a modulation frequency of 200 MHz (with some scannable frequency range described later). Before going into the IQ modulator, the FlexDDS signals are sent through MiniCircuits SLP-300+ low-pass filters to remove any unwanted harmonics at multiples of 200 MHz. By setting the Q signal to be -90° out-of-phase with the I signal, we are able to modulate the local oscillator up in frequency to 3.4 GHz, i.e. the wanted sideband. To remove unwanted extra harmonics resulting from intermodulation distortion (spaced by the modulation frequency) the IQ modulated output is sent through a MiniCircuits ZVBP-3300+ band-pass filter, which offers a narrow pass-band (3.1-3.5 GHz) and a steep roll-off. Filtering of the local oscillator leakage is done by two microwave pipe-cap filters, described later. The signal is then amplified by a MiniCircuits ZX60-83LN-S+ low-noise amplifier. To get to 6.8 GHz, the modulated signal is sent through a doubler (MiniCircuits ZX90-2-36-S+) and two high-pass filters (MiniCircuits VHF-4600+) to remove a signal at 3.4 GHz. The doubling will be performed as a part of the 20 W amplifier system, so the IQ system will end after the

amplifier and output at 3.4 GHz (see Fig. 4.18).

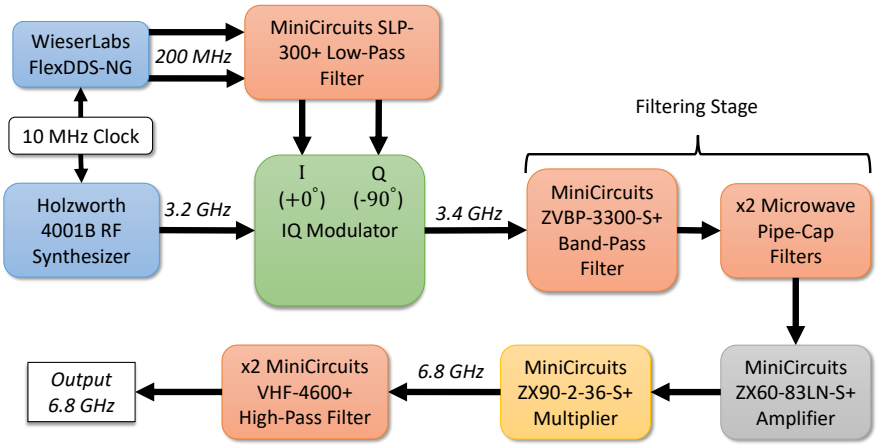

Figure 4.17: Functional block diagram of a single channel of the IQ modulation system.

4.5.3 Filtering

While in the ideal scenario the only output of the IQ modulator is the modulated output at 3.4 GHz (before being doubled to 6.8 GHz), in reality there are multiple additional sidebands spaced by the modulation frequency. These are a result of LO leakage and intermodulation distortion. If these additional harmonics are sufficiently strong, they could excite unwanted responses from the atoms that could degrade the quality of future experiments.

4.5.3.1 Notch Filter Design

One of the unwanted outputs of the IQ modulator is leakage of the local oscillator. For quality IQ modulators, this is already decently suppressed ($\leq$40 dBc), however we would like it to be at least twice as suppressed ($\leq$80 dBc). To provide this extra suppression, we utilize a microwave pipe-cap filter [67, 68] that suppresses signals within a narrow frequency band.

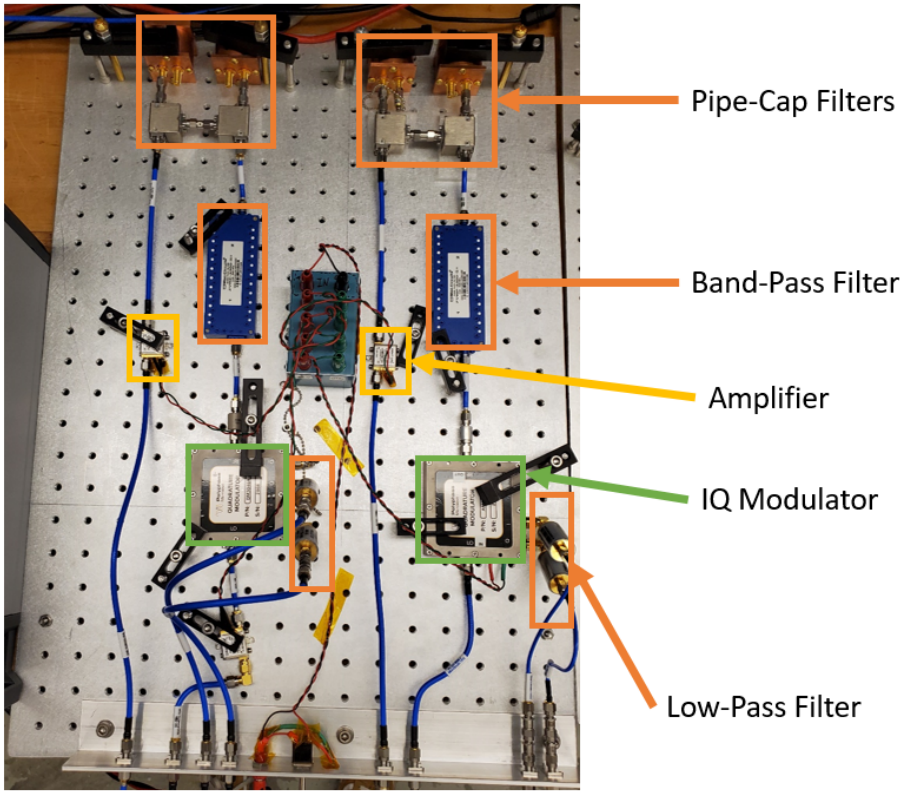

Figure 4.18: Layout of *ONDRA*, a 2-channel IQ modultion system.

The design of the filter follows that of [67], and a block diagram is shown in Figure 4.19. The cavity is formed by a 1-inch diameter copper pipe with each end plugged by a 1/4-inch copper block. A brass screw is then inserted on one end of the pipe to set the stop frequency of the filter. Putting the screw in further (taking it out more) results in a lower (higher) stop frequency. To achieve fine tuning of the resonator frequency solder was placed on the end of the brass screw and carefully filed to set the stop frequency to 3.2 GHz. This "pipe-cap filter" is combined with a microwave circulator to act in reflection mode (i.e. the output is the reflected signal from the cap filter).

Using a vector network analyzer (VNA) we can measure the suppression of the filter, as shown in Figure 4.19. From this data, we are able to see a few important details. First, the achieved suppression is not the same for each filter. While a few hang in the 15-20 dB range, filter D is around 10 dB while filter A gives more than 30 dB. Because

of this difference we choose to put two filters in series to add together their respective suppression factor, resulting in ∼40 dB of suppression for each IQ modulated channel. Secondly, the width of the resonances differs between the filters. This is not as important as the suppression factor, since the widths are on the order of a few tens of MHz while the spacing between IQ modulated peaks is a few hundred MHz (i.e. the filter is centered at 3.2 GHz and the IQ modulated signal is at 3.4 GHz), so there is no risk of the filters affecting the signal of interest at 3.4 GHz. Lastly, I found that for the majority of filters, leaving the pipe-cap filter's second SMA port non-terminated actually improved the suppression. However, for one of the filters (filter E), the opposite was true, and a 50 Ω terminator was used to achieve maximal suppression.

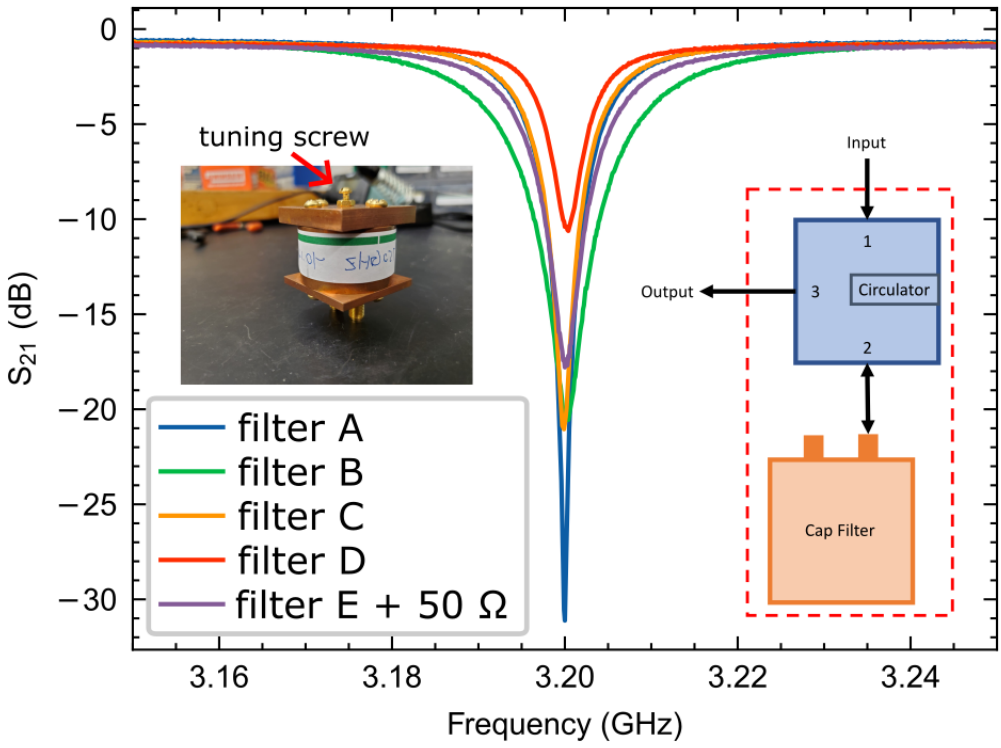

Figure 4.19: Measured response of five different pipe-cap filters. The decrease in transmission (S_{21}) corresponds to the pass-band when operating in reflection mode. Right inset: Diagram of the design showing the cap filter in combination with a circulator to act in reflection mode. Left inset: Picture of the cap filter. The circulator is not shown.

4.5.3.2 Filtering Unwanted Harmonics

In addition to the local oscillator leakage, we also found harmonics around the wanted sideband spaced by the IQ modulation frequency. These extra harmonics are dependent upon the I and Q input powers. However, even lowering the input IQ power, these harmonics were still only a few tens of dBm below the wanted sideband. We were also concerned with working at low FlexDDS powers as it may affect the bit resolution. The workaround for this issue was to include a band-pass filter (MiniCircuits ZVBP-3300-S+) on the output of the IQ modulator. This filter offers a narrow pass-band of 3.1-3.5 GHz and offers ∼70 dB of suppression to all of the unwanted harmonics. This filter also provides ∼40 dB of suppression to the unwanted lower sideband. We can then operate the FlexDDS at full power, requiring us to add 15 dB of attenuation to the outputs of the FlexDDS as to not damage the IQ modulators. Additionally, we add low-pass filters (MiniCircuits SLP-300+) to the FlexDDS I and Q inputs to remove additional harmonics in the RF that propagate through to the IQ modulator output.

4.5.4 Source Output

Example outputs of the IQ modulation system are shown in Fig. 4.20 for different scan ranges. Notably, we observe phase noise of approximately 90 dBc. We also see that the passive modulator system (QM03040A) gives a slightly narrower peak, as seen in Fig. 4.20(b) as compared to the active model (AM0260A). Since we found comparable performance between the passive and active IQ modulators, future sources were constructed using the passive modulator as it is roughly half the cost.

4.5.5 Frequency Scan Range

To perform many of the AC Zeeman experiments, we require the ability to perform adiabatic sweeps, often starting at least 10 MHz off-resonance. To characterize the scannable frequency range of the IQ system we can look at how the output power changes as a func-

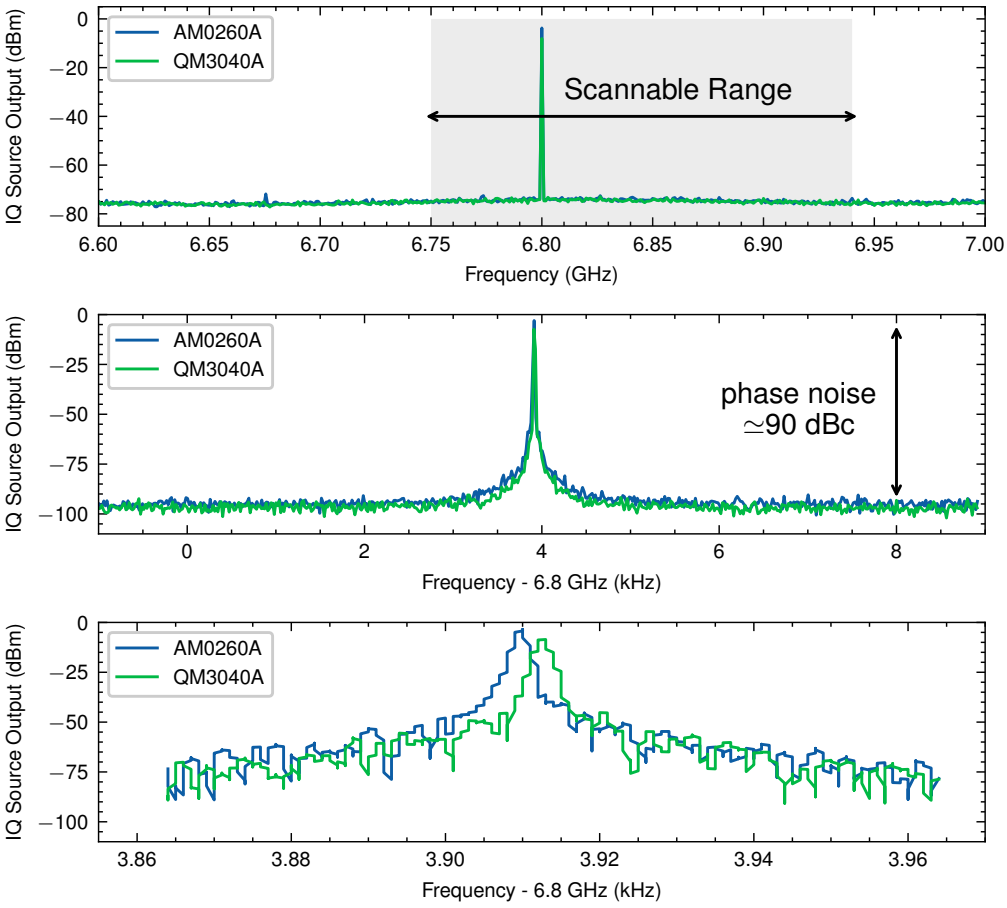

Figure 4.20: Output of the IQ source (ONDRA) doubled to 6.8 GHz. Measurements were made using the Anritsu MS2038C spectrum analyzer. (Top) 500 MHz scan range, 300 Hz RBW. (Middle) 10 kHz scan range, 3 Hz RBW. (Bottom) 100 Hz scan range, 1 Hz RBW.

tion of frequency. Ideally the output power would remain constant over the sweep range, so we can look when the amplitude of the output starts to decrease and define the scannable range.

The factor limiting our scan range are the low-pass filters on the FlexDDS. The Mini-Circuits SLP-300+ filters have a pass-band from 0-270 MHz (where the loss is less than 1 dB). The 300 in the filter name actually corresponds to the frequency where the signal's power decreases by 3 dB (a factor of 2). So we will only be able to modulate the IQ frequency to a maximum of 270 MHz without affecting the output power. The lower scan limit also ends up being decided by the filter choice, as going to too low of a frequency on

the FlexDDS results in unwanted harmonics below the cutoff frequency of the filter that can appear on the IQ modulated output. I found that the lowest modulation frequency we could work at to avoid this problem is 170 MHz. We see from Figure 4.21 that the

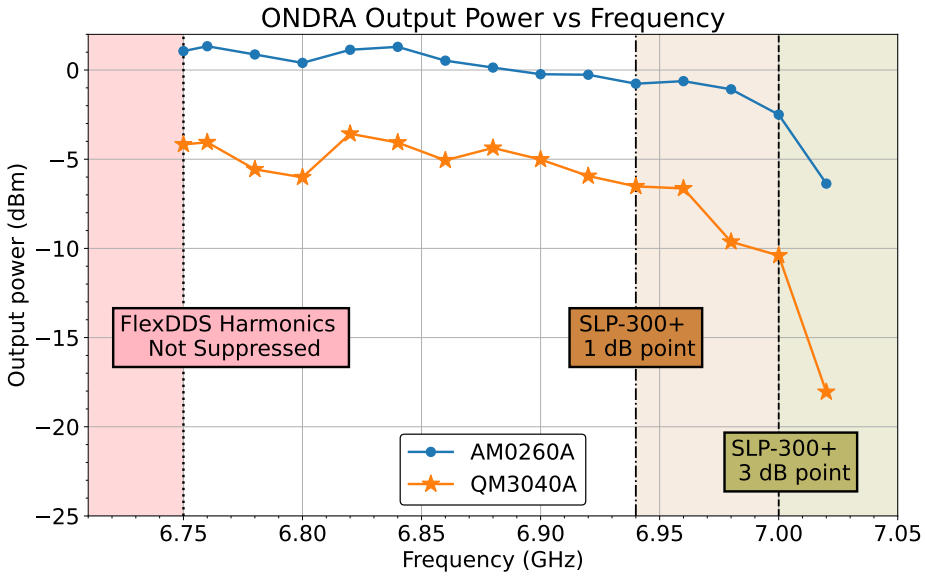

Figure 4.21: Output power versus frequency for the *ONDRA* 2-output IQ source. Important frequency labels are highlighted. Power measured using the Agilent E4407B spectrum analyzer.

available frequency sweeping range is from 6.75 - 6.94 GHz.

4.5.6 Testing Phase Control

The key selling point of this IQ modulation system is its ability to precisely digitally control the relative phase between microwave channels. We can write the IQ source 1 signal as $f(t) = A\cos(\omega t)$ and the signal from IQ source 2 as $g(t) = B\cos(\omega t + \phi)$, where ϕ is the phase difference between the two sources. When the two signals are sent into the mixer,

the output is

$$\begin{aligned} output &= f(t)g(t) \\ &= AB\cos(\omega t)\cos(\omega t + \phi) \\ &= \frac{AB}{2}\left[\cos(2\omega t) + \cos(\phi)\right]. \end{aligned}$$

The first term is a high-frequency signal at twice the signal frequency (i.e. 6.8 GHz $\times$ 2 = 13.6 GHz). The second term is a DC signal that is proportional to $\cos(\phi)$. To test the relative phase control, we can measure this DC output across a range of phase differences and map out the cosine behaviour. Important in this setup is that both sources are referenced to the same clock so that the phase-locked loops are in sync. For our system this corresponds to using the lab's 10 MHz rubidium standard as the clock input for the Holzworth and FlexDDS.

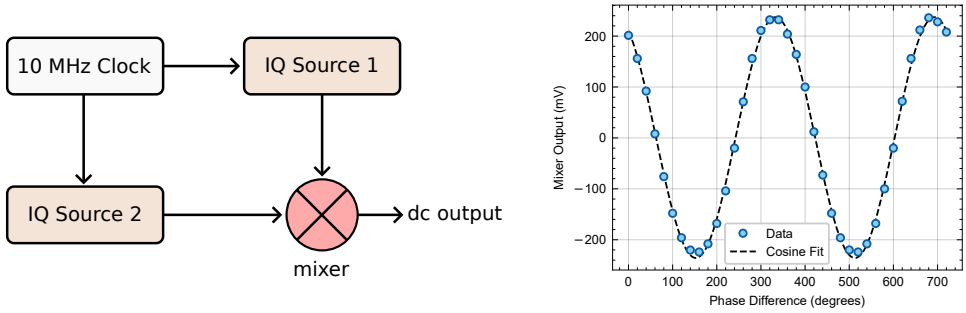

Figure 4.22: Setup for testing relative phase control between IQ modulated sources. (Right) Data from 11jan23 showing the ability to control the phase between multiple IQ modulated outputs.

Next steps for this system involve measuring the phase stability of the IQ modulated outputs, key to achieving long integration times in the atom interferometer (see Sec. 9.1). This can be done by constructing an interferometer for the microwave signals similar to Fig. 4.22, parking the mixer output at zero and looking for variations over time.

Chapter 5

AC Zeeman Trapping

With the atomic physics theory behind the ACZ trap developed in Chapter 3, we now consider how to implement such a trap on an atom chip. Previous work on microwave traps for neutral atoms utilized cavities with tens [69] or hundreds [70] of Watts of microwave power. With an atom chip, we can take advantage of strong near-field gradients to produce ACZ traps with tens of μK trap depths using only a few hundred mW of RF power [16].

This chapter is organized as follows. Section 5.1 introduces the method for generating the magnetic field landscape—specifically, a minimum in $B_{\pm}$ (one of the circular polarization components of the RF near field—using a pair of parallel atom chip wires. Section 5.2 then describes the implementation of this approach in our apparatus, including both transverse and axial confinement, along with the experimental timing sequence for loading atoms into the ACZ trap. Subsequent sections present additional experimental considerations related to the RF ACZ trap. Section 5.3 demonstrates the use of microwave spectroscopy to probe the m_F state splitting to elucidate the resonance frequency of the ACZ trap. Section 5.4 then describes measurements of the atom-chip distance in the ACZ trap, which shows excellent agreement with simple two-wire theory. In Sec. 5.5, we discuss ACZ traps observed more than 0.5 MHz below resonance, a regime not previously explored. Section 5.6 highlights a software error in the RF source's phase sweep and explains how correcting it improved vertical positioning of the trap. In Sec. 5.7, we demonstrate simul-

taneous ramping of the trapping RF frequency and quantization magnetic field strength, enabling trap generation over a 30 MHz frequency window, from 13 MHz to 40 MHz. Finally, Sec. 5.8 provides a brief exploration of incorporating a secondary RF field into the ACZ trap, investigated via spectroscopy.

5.1 Sculpting the Near-Field

The scheme for generating a circularly polarized magnetic field minimum from two point-like wires is shown in Fig. 5.1. In this model, the wires, located at $(x, y) = (\pm d, 0)$, have equal current magnitudes and are offset in phase by ϕ =90°. As we cycle through time in steps of $\omega t = \pi/2$, we can map out points at which the currents in the wires are of equal magnitude and equal or opposite sign (Fig. 5.1(a)). At the location $(x, y) = (0, \pm d)$, we observe the total magnetic field rotating in time at frequency ω (Fig. 5.1(b)). Notably, the rotation directions are opposite at $\pm d$. Taking a slice of the magnitudes of the circularly polarized fields, $B_\pm = B_x \pm iB_y$, along the y-axis at $x = 0$, we find a zero in $B_\pm$ at $y = \mp d$ (Fig. 5.1(c)). From this wire configuration, we are able to form the circularly polarized magnetic field landscape for generating an ACZ trap. A more complete derivation of the circularly polarized magnetic fields formed by multiple parallel wires can be found in Appendix B and Ref. [17, 16].

This simple model also highlights the ability to sculpt the trapping potential using the relative phase difference between the trapping wires. For example, the y position of the $B_\pm$ minima can be shifted simply by changing the phase. In the two-wire case shown here, this changes as $y_{min,\pm} = \pm d \tan(\phi/2)$ (Fig. 5.1(d)) [17] . Additionally, one can swap the location of the minima by flipping the phase by π. This feature is key in being able to trap atoms in both the $F = 1$ manifold, which responds to the B_+ field, and the $F = 2$ manifold, which uses the B_- field [16]. Moreover, the x position of the trap can be adjusted by changing the current ratio in the wires [16, 17]. While the use of infinitely thin wires fails to capture more complex details such as finite wire sizes or the AC skin and proximity

effects, it is a useful model for examining the essential physics of the ACZ atom chip trap. A full 2D ACZ potential model including such features can be found in Ref. [16]. Though we only consider two wires here, a discussion of three-wire and multi-microstrip systems can be found in Ref. [17].

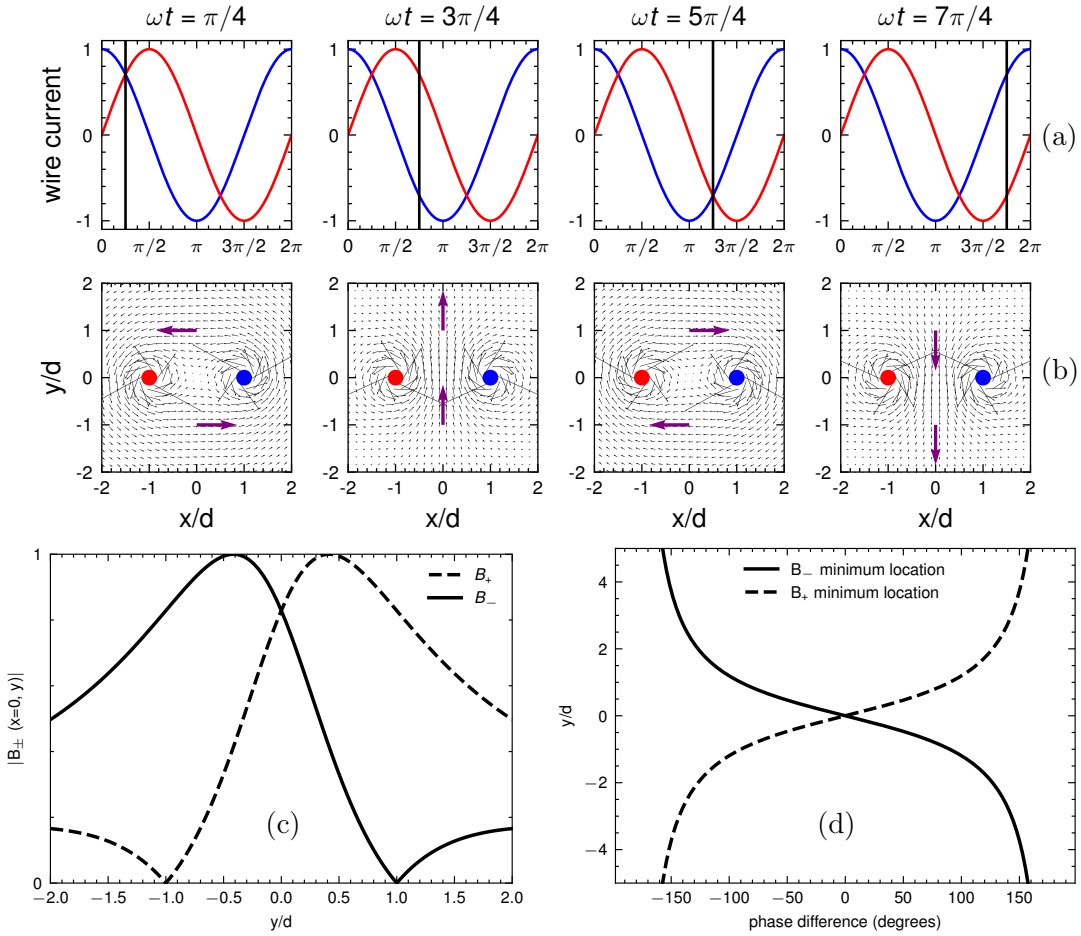

Figure 5.1: Circularly polarized magnetic field generated by a pair of wires. Currents (a) and magnetic field vector plots (b) for a pair of point-like wires. The red wire is offset in phase from the blue wire by -90°. Both wires have equal current and are separated by a distance $2d$. The vertical lines in (a) indicate the value of ωt at which we evaluate the magnetic field shown by the vector plots in (b). The purple arrows in (b) show the total magnetic field at $(x, y) = (0, \pm d)$. (c) Magnitude of the $B_\pm$ fields along the y-direction for $x = 0$, normalized to it maximum. At the location of pure polarization in one circular field, there is a zero in the opposite handedness. (d) Vertical location of the $B_\pm$ minimum as a function of relative phase between the two wires, ϕ, given as $y_{min,\pm} = \pm d \tan(\phi/2)$.

5.2 Experimental Implementation

We generate a minimum in B_- and B_+ by driving ≈20 MHz RF currents through two parallel wires on an atom chip at a fixed phase difference. Figure 5.2(a) shows a sketch of the central portion of the atom chip with the middle segments of the two wires directed along the z-axis: a Z-shaped wire on the left (L) with current $I_L \cos(\omega t)$ and a U-shaped wire on the right (R) with current $I_R \cos(\omega t + \phi_{RL})$ and phase ϕ_{RL}. In Fig. 5.2(b), we show the B_- near field generated for the case of $\phi_{RL} = -90°$ as in Fig. 5.1. This model incorporates both the finite size of the wire and the AC skin effect. These act to shift the B_- minimum closer to the chip, yielding a trap height location of 44 μm compared to 50 μm using 1-D wire theory [17]. Changing the phase to $\phi_{RL} = +90°$ we can realize the B_+ field to look identical to Fig. 5.2(b), whereas it is flipped about the chip axis for $\phi_{RL} = -90°$.

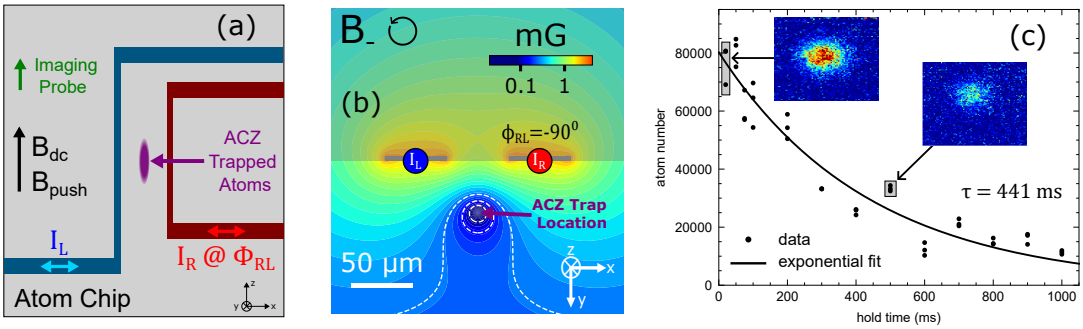

Figure 5.2: Experimental implementation of the ACZ atom chip trap. (a) Sketch of the atom chip wires used for the ACZ trap (not to scale). (b) Map of the B_- component of the rf near field for realistic traces, with the trap located ≈ 44 μm below the chip (shaded region). The wire traces are 50 μm wide and separated by 100 μm (center-to-center), and the rf current amplitude is $I_{R,L} = 250$ mA. (c) Lifetime of atoms in the "canonical" ACZ trap, at a detuning of ∼0.5 MHz and trap height ∼90 μm. The zero hold time begins after stage 4 in Fig. 5.5. Atom number data is fit to a decaying exponential, $N(t) = N_0 e^{-t/\tau}$, giving a lifetime $\tau = 441$ ms. Figure adapted from [71].

5.2.1 Axial Confinement

In its current implementation, the RF ACZ trap only provides trapping in the transverse (xy) plane. We do see some confinement from the endcaps in the Z and U-wires in modeling,

however, this is only on the level of one Hz. Originally [16], a weak optical dipole trap was used for axial endcapping. However, early in my PhD tenure, the 40-year-old dipole trapping laser finally kicked the bucket. Fortunately, the Ioffe field (B_{dc} in Fig. 5.2) is not truly constant in space, instead featuring some natural curvature (see inset of Fig. 5.3) that we can exploit for axial confinement. This forms a minimum in the field between the coils, trapping DC Zeeman low-field seeking states. Far below resonance, the $|{+}{+}\rangle$ ACZ eigenstate is well described by the $|2,+2\rangle$ bare atomic state. In this limit, we are able to provide axial confinement for the $|{+}{+}\rangle$ state. Our experimental capabilities are then somewhat limited as the $|{+}{+}\rangle$ state is anti-trapped above resonance, where it is described by the DCZ high-field seeking $|2,-2\rangle$ state. A dipole laser will be needed to provide axial confinement for this state.

In order to accurately model the system, we need to know the physical parameters of the Ioffe coil pair (see Table 5.1), as well as the spacing between the coils. To elucidate

Coil	D_{outer}	D_{inner}	$D_{average}$	# of turns	Distance from Atoms
Ioffe	7.2 cm	4.5 cm	5.85 cm	23	± 3.455 cm
Gradient Push	8 cm	4.6 cm	6.3 cm	31	8.27 cm

Table 5.1: Parameters for the Ioffe and gradient push coils.

the position of the coils in relation to the atoms, we compare the simulated and measured ratio between the magnetic field strength felt by the atoms and the current through the coils. This ratio is measured in experiment through microwave spectroscopy (see Sec. 5.3), yielding a ratio of 2.66 G/A. The model uses a closed-form expression for the magnetic field of a circular coil [72] and the average diameter of the coil, $D_{average} = 5.85$ cm. With the spacing between the coils as the only free parameter, we found a distance of 6.91 cm gave the same field-to-current ratio. With this in hand, we convert the magnetic field into a DC Zeeman potential to extract the trap frequency as a function of Ioffe coil current, plotted in Fig. 5.3. At the 11.29 A current used in the 20 MHz RF ACZ trap, this yields an expected axial trap frequency of 3.67 Hz.

In our first ACZ traps using the Ioffe field for axial confinement, it was found that the

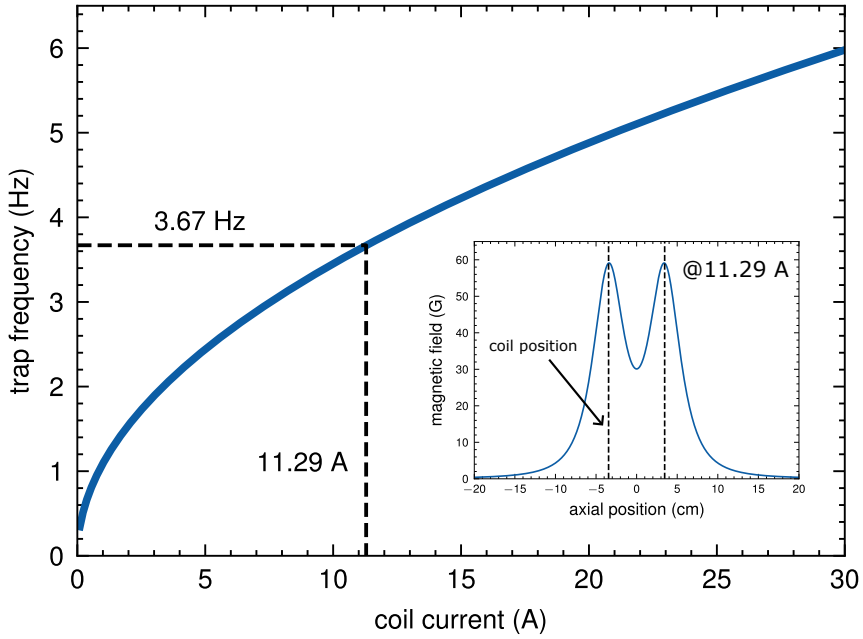

Figure 5.3: Simulated trap frequencies from the natural Ioffe field curvature. The coils use 23 turns each, a diameter of 5.85 cm, and are separated by a distance of 6.91 cm. The magnetic field generated by the coil pair is converted into a DC Zeeman energy for the $|2,2\rangle$ state and fit to a polynomial to extract the trap frequency. Inset: the magnetic field generated using a current of 11.29 A, as used in the 20 MHz RF ACZ trapping. The position of the coils is indicated by the vertical dashed lines.

position of the atoms in the Z-wire DCZ trap did not naturally overlap with the ACZ trap location. To remedy this, we installed an additional gradient magnetic field coil along the axial direction (see Fig. 5.2) [63, 64]. One of the transport coil power supplies (PSC) acts as the current source for this coil, with digital control via a high-speed, high-current switch built by A.J. Pyle [63], operated in parallel with the coil and supply. I performed a slight modification to this device to allow for longer on times (∼1 s) at currents of around 20 A. This field allows us to spatially position the ACZ trap, helping overlap it with the two-wire DCZ trap in the roughness experiment and reduce residual oscillations from transferring from the Z-wire trap, as shown in Fig. 5.4. Similar to the Ioffe field, we can compare the total magnetic field from the Ioffe and push coils to measurements made using microwave spectroscopy of the atoms. For $I_{Ioffe} = 11.29$ A, we measured the push coil to shift the field by 0.27 G/A$_{push}$. Using the parameters in Table 5.1, the position of the push coil

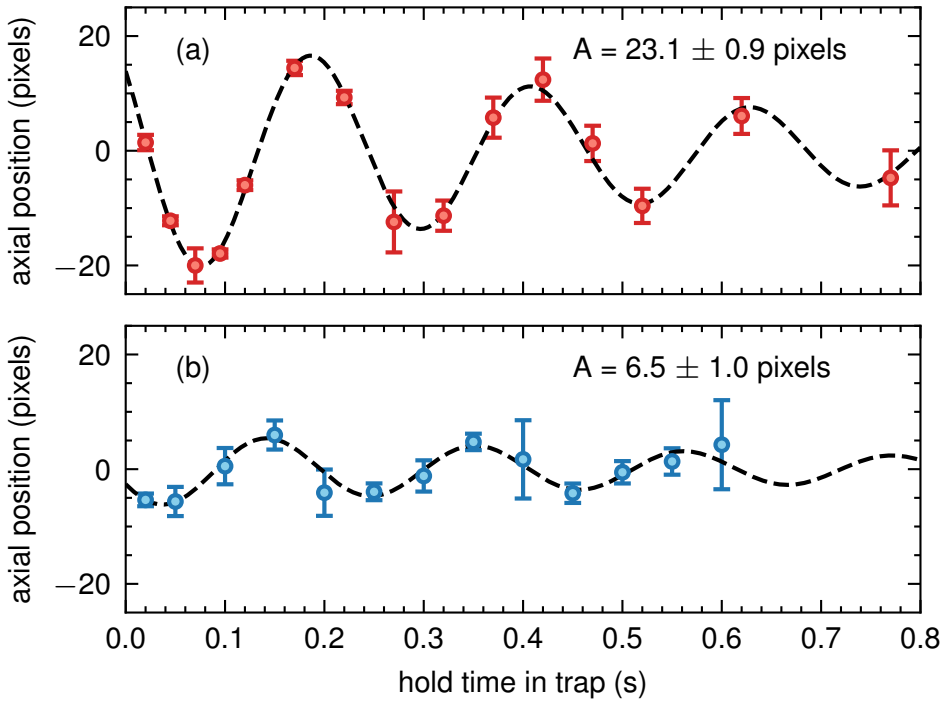

Figure 5.4: Residual axial oscillations in the RF ACZ trap after loading from the Z-wire trap (1 pixel = 4.65 μm). (a) Oscillations after loading using the original loading sequence. (b) Reduced oscillations using a more optimized sequence with the push coil. Data points and error bars come from the average and standard deviation of several images. The data is fit to an exponentially decaying sinusoid: $f(t) = Ae^{-t/b} * \sin(2\pi ft + c) + d$, given by the black dashed line. Using the improved loading method, we reduced the oscillation amplitude by a factor of 4. The cloud is fit to a Gaussian and has a width of $\sigma = 60$ pixels, yielding a full width at half max of $2{*}2.35\sigma = 282$ pixels. The improved method in (b) gives an amplitude of 4% of the total cloud size.

was adjusted until the model and measured slopes agreed. Doing this, we found that the push coil is located a distance of 8.27 cm from the atoms. The linear gradient from the coil felt by the atoms goes as 0.088 (G/cm)/A$_{push}$. This gradient has little effect on the axial trapping frequency, changing it by 0.01 Hz/A$_{push}$ for $I_{Ioffe} = 11.29$ A.

5.2.2 Timing Diagram

A timing diagram for loading atoms into the RF ACZ trap is given in Fig. 5.5. This sequence is the same as that used to characterize potential roughness in the ACZ trap. We begin by cooling atoms in the MOT and transferring them into the standard Z-wire trap,

where they are evaporatively cooled down to roughly 1 μK. We then adjust the chip wire current, hold field, and a vertical bias field to shift the position of the Z-wire trap between the Z and neighboring U wires (i.e., roughly 50 μm in both the horizontal and vertical direction). During this time, the Ioffe field is ramped to a value of 28.74 G, and the RF frequency is initialized at 11 MHz (stage 1). It is important to start the frequency far off-resonance such that the trappable $|{+}{+}\rangle$ state is well described by the bare state $|2,2\rangle$, but also above half the resonance frequency to avoid encountering potential harmonics during the sweep. Once the atoms are between the two wires, the Z-wire trap (wire current, hold field, and vertical bias field) is ramped off while the RF ACZ trap power is ramped on (stage 2). It was found that having the RF frequency ramp in a shorter time than the power gave a much better atom number. For the RF power ramp time of 150 ms used here, a frequency sweep time of 85 ms was used. After the atoms are transferred into the ACZ trap, they are held for 50 ms (stage 3) before the push coil current is increased over 300 ms to its final value, chosen to overlap with the two-wire DC trap (stage 4). Since the push coil field contributes to the quantizing field strength, we also adjust the RF frequency to account for the larger m_F state splitting. Microwave spectroscopy measurements found the push coil shifts the m_F states by about 0.19 MHz/A, in addition to the $\sim$20 MHz splitting induced by the Ioffe field. We then hold the atoms for 400 ms to allow the cloud to thermalize (stage 5).

5.3 Measuring the RF Resonance

One of the main experimental parameters when using the ACZ trap is the detuning of the RF trapping field from the atomic resonance. This controls features such as the trap frequency and depth, as well as lifetime [16]. To measure the resonance, we move from the RF, where all the m_F states of a given manifold are coupled together, to the microwave, in which we can isolate a pseudo 2-level system. By applying an external microwave field, we induce Rabi oscillations between the $|F=2,m_F=2\rangle$ and $|F=1,m_F=1\rangle$ states (see

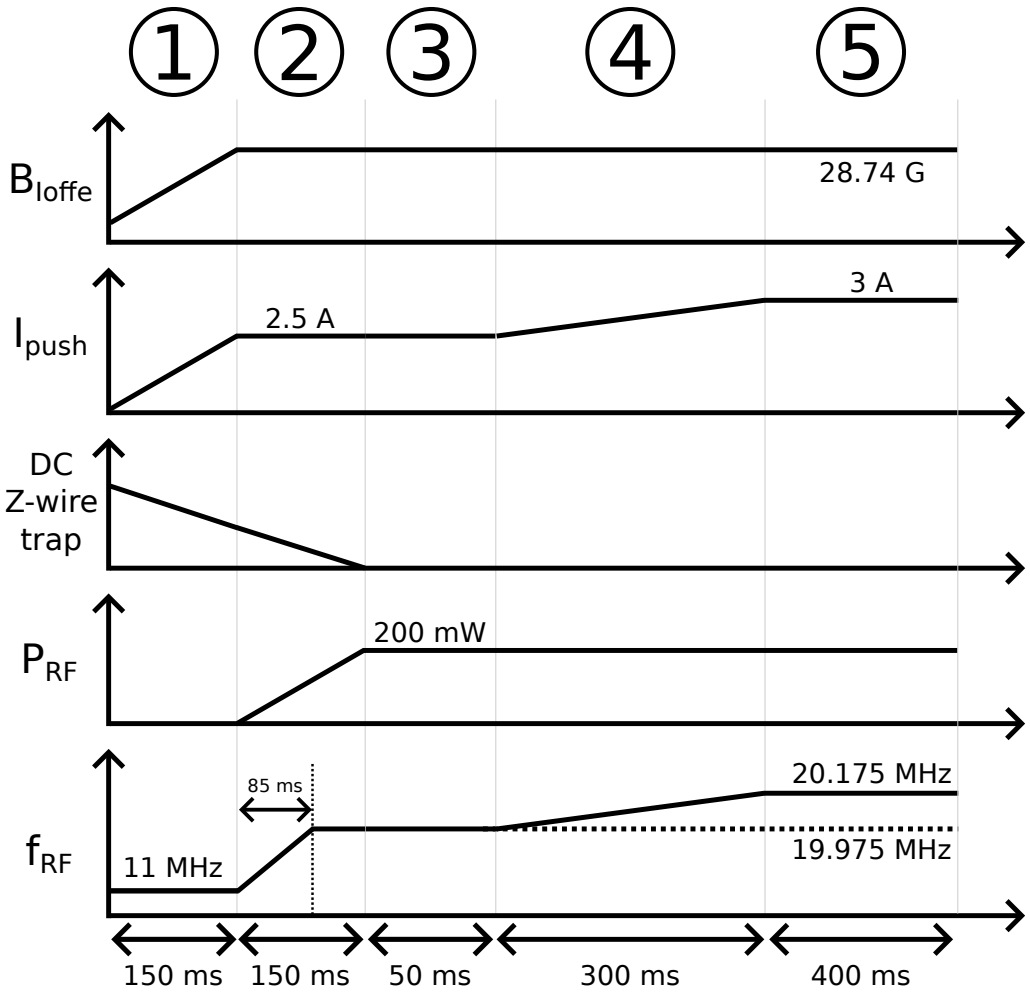

Figure 5.5: Experimental timing diagram for loading atoms into the 20 MHz RF ACZ trap. 1) After evaporative cooling to $\approx$1 μK in the DC Z-wire trap, the DC fields are adjusted to shift the trap between the U and Z wires. The Ioffe field is also ramped to its final value of 28.74 G. A gradient push coil (I_{push}) is also turned on during this time to reposition the atoms axially. 2) As the DC trap is ramped off, the RF trap is ramped on. Notably, the RF frequency is ramped in a shorter time (85 ms) than the power (150 ms). 3) Atoms are held in this trap for 50 ms. 4) The RF frequency is then ramped to its final value in 300 ms. Simultaneously, the push coil current is also increased. 5) Atoms are held in the trap for 400 ms to thermalize. The relative phase between the two trapping wires stays constant throughout this entire sequence.

Fig. 5.6(a-b)), which decay after several tens of μs. On resonance, these oscillations settle at equal population in both states. Going off-resonance shifts the settling point preferentially into the initial state. We can then scan the microwave frequency and measure when the populations settle to 50%.

In practice, we trap atoms in the $|2,2\rangle$ state in the Z-wire trap, stopping just shy of BEC creation. The trap is then shut off and the atoms are allowed to free-fall for 3 ms, allowing enough time for eddy currents in the chip wires to dissipate [51]. During that time, the DC magnetic fields are ramped to a given value. Microwaves are applied via a dipole antenna located near the atoms on the outside of the vacuum cell. Since the atoms are prepared in the $|2,2\rangle$ state, we can only drive Rabi oscillations between the $|2,2\rangle$ and $|1,1\rangle$ states. The microwaves come from an ultra-low phase noise Holzworth HSM-4001b source sent through a 20 W amplifier (Amaterasu) built by ShuangLi Du [14]. We apply the microwaves for long enough to allow the Rabi oscillations to settle, typically on the order of 0.5-1.5 ms. The population ratio between the two states is measured using Stern-Gerlach imaging (see Chapter 4). A sample resonance measurement is shown in Fig. 5.6(c). We additionally use this technique as a method for calibrating magnetic fields at the chip (see Table 4.2 and Appendix A).

5.4 Measuring the Trap Height

Another of the previously mentioned control parameters of the ACZ trap is the relative phase between currents in the atom chip wires. This controls the vertical position of the trap relative to the chip, i.e., the trap height, and can also flip the polarization of the circularly polarized magnetic near field to trap atoms in either ^{87}Rb ground-state hyperfine manifolds. Control of the phase is relatively simple in an experiment, providing precise control over the trap height. This trap height had previously only been estimated using the inserted phase difference and a natural $\approx 175^\circ$ offset at 20 MHz (see Fig. 5.11(b)). Without any way of directly measuring the relative phase on the chip, uncertainty in the trap height

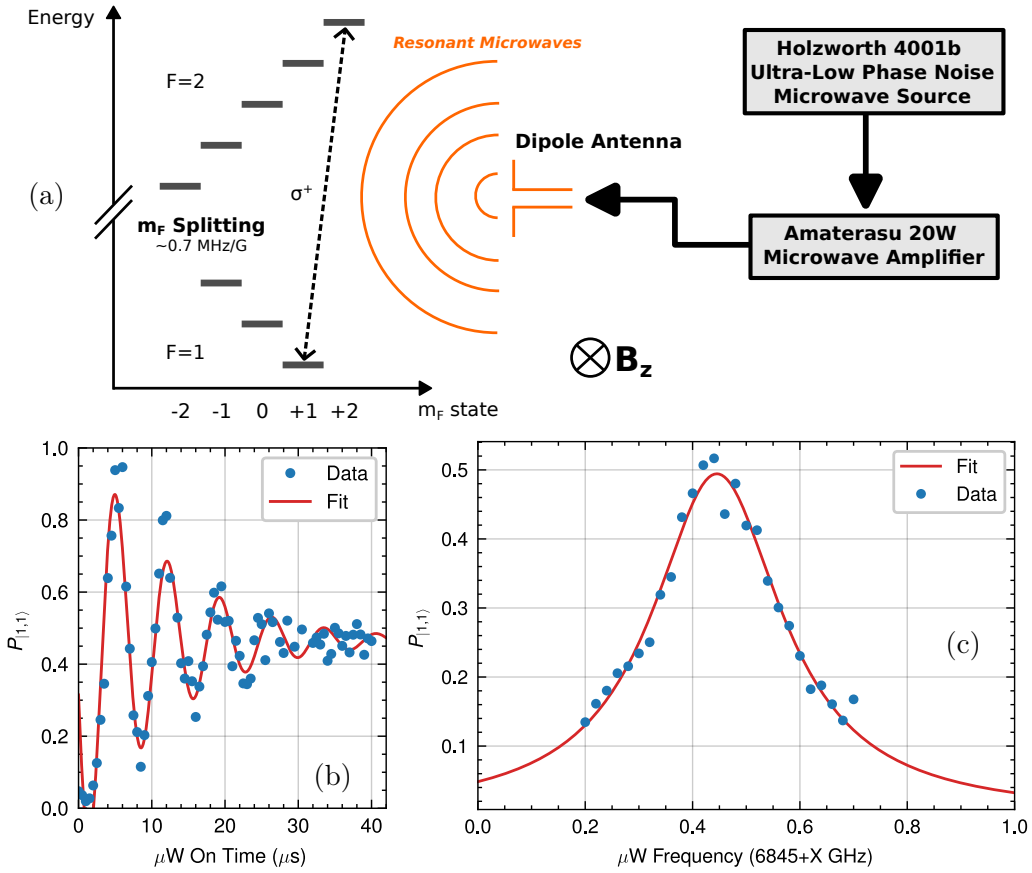

Figure 5.6: Example of finding the m_F splitting using microwave Rabi spectroscopy. (a) Experimental setup. An ultra-low phase noise microwave source (Holzworth HSM-4001b) is sent into the "Amaterasu" amplifier system, which contains a 20 W amplifier for 6.8 GHz signals. The output of the amplifier is sent to a dipole antenna located outside the science cell, roughly 10 cm from the atoms. This resonant microwave radiation hits the atoms in the $|2,2\rangle$ state, driving Rabi oscillations between the $|2,2\rangle$ and $|1,1\rangle$ states. The Zeeman splitting between m_F levels comes from a quantizing $B_z\hat{z}$ magnetic field. (b) Relative atom population in the $|1,1\rangle$ state versus time, showing decaying Rabi oscillations. The oscillations de-phase after about 50 μs. The data is fit to a decaying sine wave. (c) Microwave Rabi spectroscopy of the relative population in the $|1,1\rangle$ state versus the applied microwave frequency. The microwaves are left on for several hundred ms, allowing the population in each state to settle at 50% on resonance. The data is fit to a Lorentzian to extract the resonance frequency for the $|2,2\rangle \leftrightarrow |1,1\rangle$ transition, which in turn tells us the magnetic field strength and m_F splitting.

constituted one of the larger error bars when modeling the ACZ trap [16]. Measurement of the ACZ trap height would then aid in modeling efforts, and is also essential to spatially align the ACZ and DC Zeeman traps in the potential roughness experiment in Chapter 6.

We employ a method we dub, "dark-spot imaging", since it is related to but distinct from a method of that name [73], to measure the trap height in the RF ACZ trap, diagrammed in Fig. 5.7. In this scheme, imaging probe light gets diffracted by the atom cloud, which then reflects off the chip surface before passing through a lens and onto the CCD camera. This diffracted light results in a bright atom image "inside" the chip, located a distance $2h$ from the real atoms, where h is the atom-chip separation. When subtracted from the image with no atoms, this shows up as a dark spot in the absorption image (see inset of Fig. 5.8). This method assumes the imaging beam comes in at a small angle with respect to the atoms, so care must be taken to properly align the beam. With minimal optimization, however, we were able to calibrate this method by measuring the trap height in the Z-wire trap (see Fig. 2.8), yielding excellent agreement with the finite-sized wire theory.

Measured trap heights in the RF ACZ trap as a function of phase are shown in Fig. 5.8. We average ten shots for improved dark-spot signal-to-noise. The signal is then integrated along the axial position and fit to the sum of two Gaussians (see lower inset of Fig. 5.8). Noise in the chip ($\lesssim 70$ pixels) stems from reduced imaging light intensity in this region. The difference between the locations of the two Gaussians gives twice the trap height. The error in the measurements is given as the quadrature sum of the positional errors of the fit, i.e., $\sigma_h = \sqrt{\sigma_{atom}^2 + \sigma_{dark}^2}$. Larger error bars at the farther away traps stem from a decreased dark-spot signal. We were able to resolve the trap height for $h \geq 35$ μm using this method. At lower heights, the atom cloud becomes sufficiently cut off by the chip to reliably image.

Assuming equal currents in the wires, we can calculate the trap height of the ACZ trap using 1D wires. From Ref. [17], this gives $h = d\tan(\phi/2)$, where $d = 50$ μm is half the wire separation, and ϕ is the relative phase difference between wire currents. This theory is shown as the black dashed line in Fig. 5.8, where we incorporate the 175° phase offset.

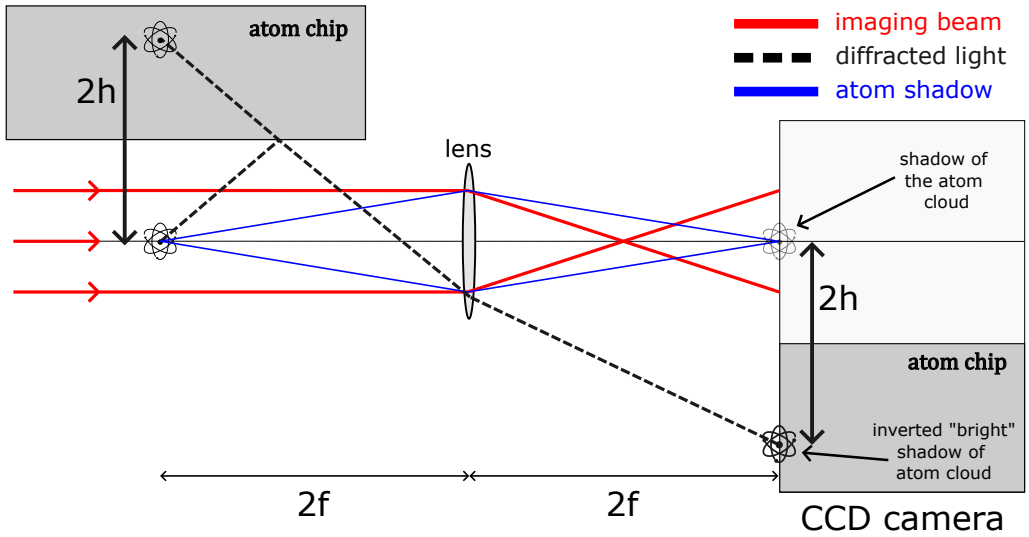

Figure 5.7: Optical setup for dark-spot imaging atoms in the chip trap. Imaging light (red solid lines) is shone onto the atoms before going through a lens (Thorlabs MAP10100100-B 1:1 achromatic doublet pair imaging system) of focal length $f = 100$ mm and diameter 30.5 mm, placed a distance $2f$ from the atoms and the CCD camera. The atom cloud acts to block some of the imaging light, generating a shadow (blue solid lines) in the CCD image. Some of the imaging light gets diffracted by the atoms (black dashed lines) and gets reflected off the chip before passing through the lens and onto the CCD. The diffracted light results in a bright atom image "inside" the chip, which is turned into a dark spot when subtracted from the image without atoms.

The data and theory yield excellent agreement, indicating the validity of our method as well as the assumed phase offset. Fitting the data to the two-wire theory with the phase offset as a free parameter yields an offset of 175.11 ± 0.21 degrees.

5.5 Further Red-Detuned Trapping

The first RF ACZ trapping experiments [16] were unable to realize a trap below about 0.5 MHz detuned below resonance. For the trap formed with a resonance frequency of 20 MHz, this set the bottom range of trapping to $f_{rf} = 19.5$ MHz. It was odd, however, that there were no issues with trapping above resonance, going up to $f_{rf} = 25$ MHz. When rebooting the ACZ trap (after Dr. Drew Rotunno graduated), I decided to do a quick exploration to see if I could resolve this issue. On the first day of this attempt, I found that these red-detuned traps could be made using a different relative phase between the

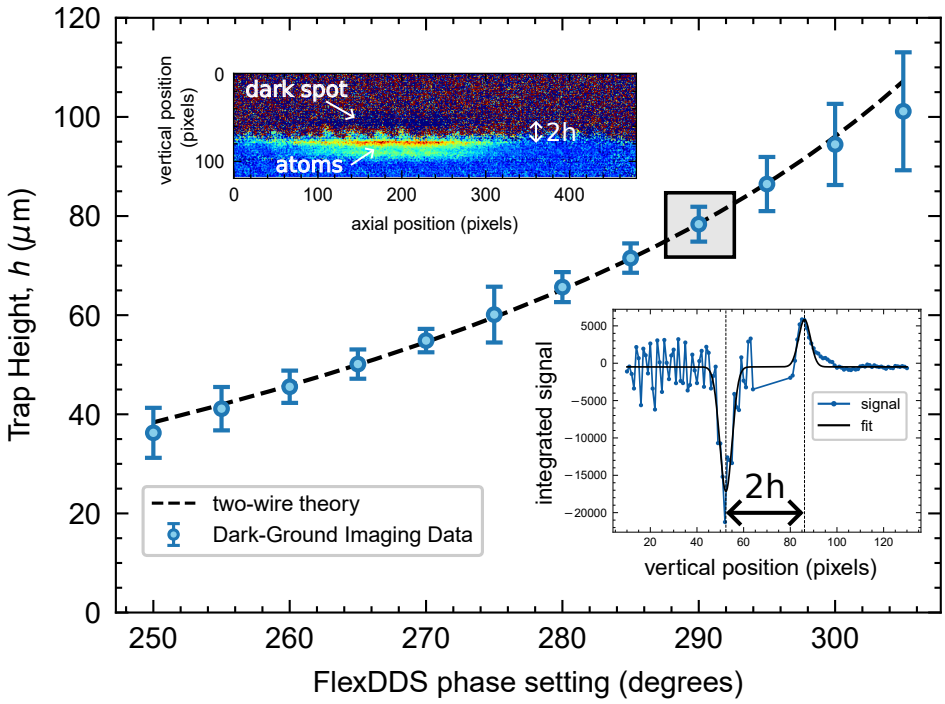

Figure 5.8: Trap height measurements of atoms in the RF ACZ (f_{RF} = 20.175 MHz) trap as a function of phase. Measurements were made using the dark-spot imaging method on the axial camera. Data points reflect the average of ten shots. Error bars are the sum of the Gaussian cloud fit error on the position of the atom and dark spot signals. The black dashed line uses simple two-wire theory for the trap height [17], i.e., $h = d\tan(\phi/2)$, where d = 50 μm. Upper inset: average of ten absorption images of the atoms and dark spot at a phase setting of 290°. Lower inset: Fitting the absorption image signal to a sum of two Gaussians (1 pixel = 4.65 μm). The difference between the locations of the peaks is twice the trap height, h.

atom chip wires. In this scheme, I ramped the RF frequency from 11 MHz to the final frequency, f_{rf}, with a set relative phase difference. Where my original trap had used a set phase of 300° from the FlexDDS source, I was able to form traps at f_{rf} = 17 and 18 MHz using phase settings of 240° and 261°, respectively. While not optimized, these gave trap lifetimes of τ_{17} = 400 ms and τ_{18} = 246 ms (see Fig. 5.9), in a range consistent with lifetime measurements at similar detuning values above resonance using 200 mW of power [16].

While not fully explained yet, we hypothesize that it may be due to the Ioffe field not being truly constant, instead featuring some curvature in the longitudinal and transverse

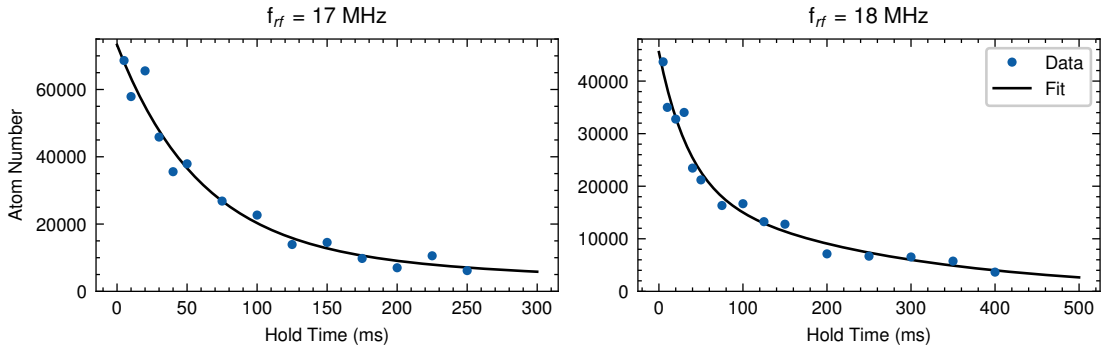

Figure 5.9: Trap lifetime data for RF ACZ traps at 17 and 18 MHz. The resonance is at roughly 20 MHz. Data is fit to a sum of two decaying exponentials, giving lifetimes of $\tau_{17} = 400$ ms and $\tau_{18} = 246$ ms, respectively.

directions. Above resonance, when atoms in the $|{+}{+}\rangle$ project into the $|2, -2\rangle$ bare state, the transverse Ioffe curvature provides trapping, while the axial does not. Below resonance, when $|{+}{+}\rangle \approx |2, +2\rangle$, the opposite is true, and the Ioffe field anti-traps in the transverse direction. To overcome this, we need a stronger ACZ potential, which can be achieved by lowering the relative phase and bringing the atoms closer to the chip. From trap height measurements (see Fig. 5.8), such phases used for the 17 and 18 MHz traps would put the atoms ≈30-45 μm from the chip.

5.6 Improved Phase Movement

The distance of the ACZ trap from the chip can be controlled using the relative phase difference between the RF currents in the trapping wires [16]. When first attempting to change the trap height, I discovered that asking the FlexDDS RF source to sweep to a lower final phase difference (i.e., closer to the chip) caused the signals to "snap" into the final phase rather than smoothly sweeping in the prescribed time. This snapping effect, a feature of the AD9910 DDS [74], leads to a smearing out of the atom cloud in the vertical direction. Sweeping up in phase difference (i.e., further away from the chip) did not show this effect.

To address this issue, we use two different MATLAB control scripts for moving closer

or farther from the chip. During loading into the ACZ trap, the phase difference is held constant on one FlexDDS output channel (call it channel A), with the other (call it channel B) set to zero phase offset. To move the trap farther from the chip, we can simply adjust the phase of channel A while keeping channel B at zero phase. To move closer to the chip, we instead keep channel A constant at the loading phase and sweep channel B up in phase to achieve the desired phase difference. Figure 5.10 shows the measured cloud width after a 9 ms time-of-flight for the different phase sweeping methods. Using the original phase sweeping method (a), the snapping effect causes the vertical cloud width to sharply increase when lowering the phase difference, while the horizontal width follows a steady increase. By switching to using two different FlexDDS command scripts (b), the horizontal and vertical widths are equal as the phase is shifted, both following a steady increase. The increase in cloud width is expected and is a result of the trap getting tighter as we bring the atoms closer to the chip, inducing some heating of the atoms.

5.7 Ramping Frequency and Magnetic Field

A previously unexplored benefit of the ACZ trap is the ability to dynamically change the resonance, i.e., the m_F level splitting. This could find use in exploring ACZ physics near Feshbach resonances [75], for example. In this thesis, I use it to compare the potential roughness in an ACZ trap at different resonance frequencies to look for frequency-dependent features (see Chapter 6). After loading into a "canonical" ACZ trap with a resonance frequency of roughly 20 MHz, we simultaneously ramp the RF frequency of the currents in the chip wires, f_{RF}, and the strength of the quantizing DC field, B_{DC}, which sets the m_F splittings. A relatively constant detuning can be kept using the magnetic field calibration for the Ioffe field in Table 4.2 to determine the m_F splitting at the end of the ramp. An elementary timing diagram for this procedure is given in Fig. 5.11(a). It is important to note when using this technique that the two chip wires used to generate the ACZ trap have a natural, frequency-dependent phase difference [16], as shown

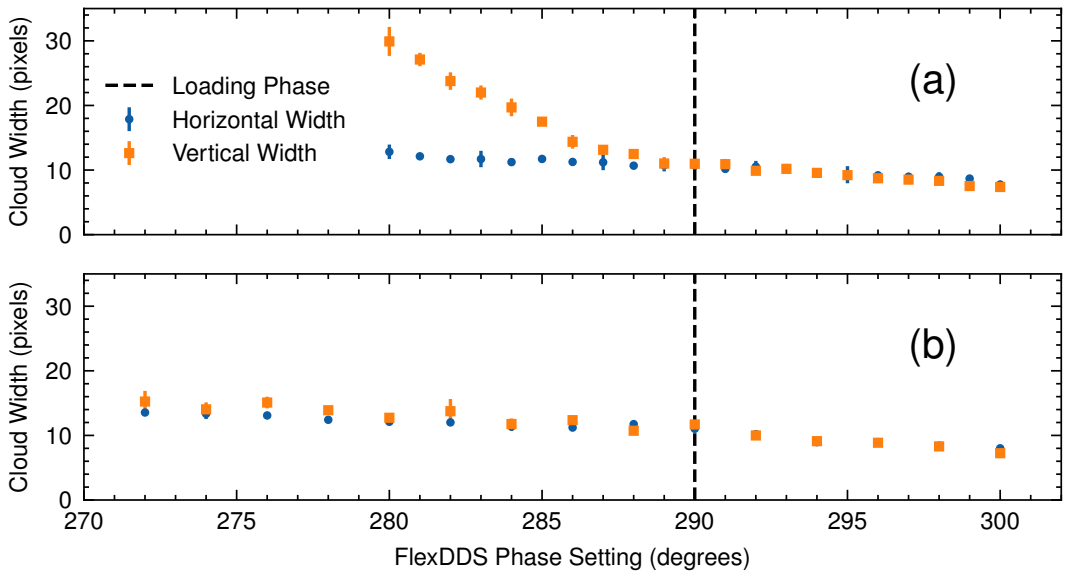

Figure 5.10: Atom cloud size in the RF ACZ trap after a linear phase sweep starting at 290° and sweeping to the given phase in 25 ms (1 pixel = 7.4 μm). (a) Cloud width using the initial phase sweep method. When the phase of the FlexDDS is swept from high to low, the AC signals "snap" to the final phase setting, resulting in a smearing out of the atom cloud in the vertical direction. (b) Cloud width using two different FlexDDS command scripts to sweep either up or down in phase from 290° (see text for details). With this implementation, the horizontal and vertical cloud widths remain identical as the atoms are brought closer to the chip. The data and error bars reflect the mean and standard deviation of up to three shots.

in Fig. 5.11(b). This acts to shift the trap height during the ramp, and so care must be taken if one is trying to overlap the original and final traps in space, either by presetting the original trap's phase or through shifting the phase after the ramp. In addition, the U and Z wires on the atom chip (see Fig. 5.2), are already set up to be 180° out-of-phase. At a frequency of 20 MHz, then, the total natural phase difference between the chip wires is 175°. Both methods were shown to produce an ACZ trap, though further studies are needed for full optimization.

Using this technique, we were able to form traps at resonant frequencies of roughly 13 MHz and 40 MHz. Figures 5.11(c) and (d) show lifetime measurements in these traps. We observed a significant drop in atom number when trying to trap at lower frequencies, i.e., below 13 MHz. This may be attributed to the natural phase difference between the wires, which begins to sharply spike around 10 MHz, or a possible problem when doing

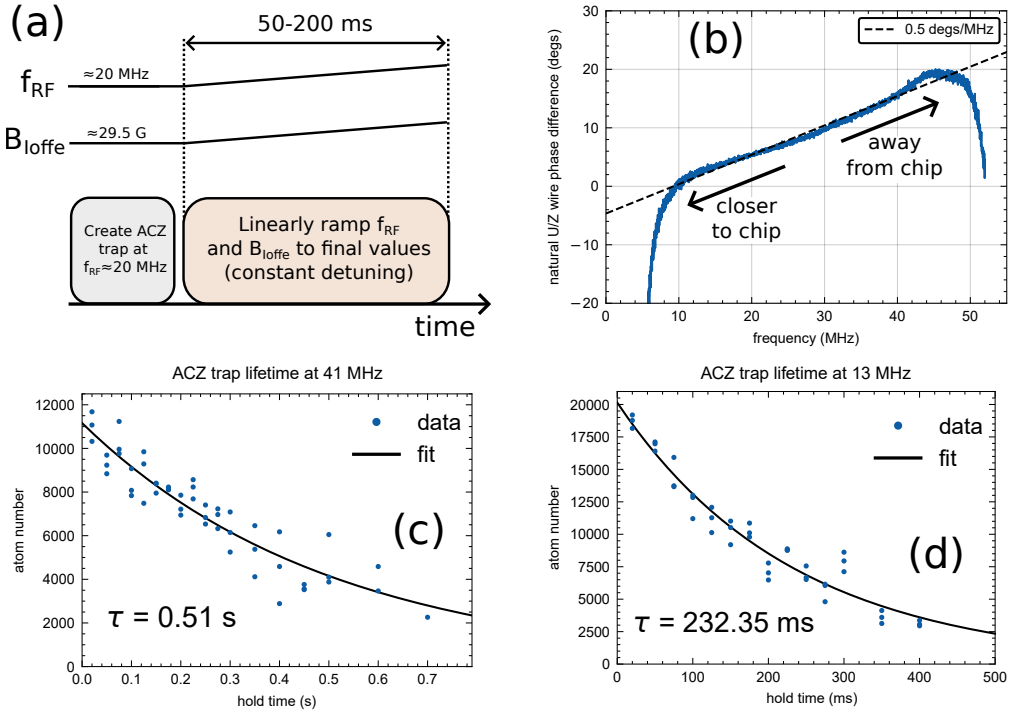

Figure 5.11: RF ACZ trapping at different atomic resonances. (a) Simple timing diagram for simultaneously ramping the RF frequency and quantizing Ioffe field from the 20 MHz trap. The sweep time was not optimized and was performed in the 50-200 ms range, depending on the final resonance frequency. (b) Frequency-dependent phase difference between the U and Z wires on the atom chip [16]. In the 10-45 MHz range, this phase changes roughly linearly with a slope of 0.5 degrees/MHz. (c) Lifetime measurement in the ACZ trap with a resonance set around 41 MHz. (d) Lifetime measurement in the ACZ trap with a resonance set around 13 MHz.

sweeps to below half the starting RF frequency. I did not attempt to fully characterize the ramping method here, but rather demonstrate its proof-of-principle operation for use in the roughness experiment.

5.8 Spectroscopy in the RF ACZ Trap

An area of future interest in both theory and experiment is the addition of a secondary RF or microwave field to the ACZ trap. Such a system was explored in Sec. 3.5 of Chapter 3 in the context of microwave evaporation, and here we demonstrate the ability to probe the RF ACZ trap with an additional RF field. In this case, the probing field was scanned around the atomic resonance, and the trapping field was kept in the far-detuned limit.

On resonance, atoms in the $|{+}{+}\rangle \simeq |2,2\rangle$ ACZ dressed state (see Sec. 3.3) will absorb a photon, transitioning to a different m_F state. Since the trapping RF field is far-detuned from resonance, each of the bare states, $|2, m_F\rangle$, is well described by one of the ACZ dressed atom states. These other dressed states are un-trapped by the ACZ potential (or very weakly trapped in the case of the $|+\rangle$ state), and will be ejected. We expect, then, to see a drop in atom number as we scan across this resonance.

For experimental ease, we employed the evaporation wire on the atom chip as the probing field source. In the current setup, the RF source for this field can only go up to 19 MHz, so we utilize the technique of Sec. 5.7 to shift the trap resonance, i.e., m_F splitting, to around 13 MHz, with the trapping RF frequency set to 12.6 MHz. With the atoms held in this trap, the probing RF field was switched on at a VVA voltage setting of 0.25 V for 100 ms before being switched off. After, the atoms were held in the trap with the probe field off for 20 ms before being released and imaged after an 8 ms time-of-flight.

Figure 5.12 shows the number of atoms left in the trap after the application of the probing RF field. A Lorenztian fit to the data gives a resonance at 13.079 ± 0.003 MHz, demonstrated by the loss of atoms. This value is close to the expected $|2,2\rangle \leftrightarrow |2,1\rangle$ transition at 13.062 ± 0.006 MHz, calculated from the Breit-Rabi formula for a magnetic field of $B = 18.779 \pm 0.009$ G. The magnetic field value is obtained using the calibrations for the given Ioffe (7.29 A) and push coil (2.5 A) currents. Multi-photon transitions to other m_F states are larger by intervals of roughly 25 kHz, and act to broaden the resonance.

Focusing on the dominant $|2,2\rangle \leftrightarrow |2,1\rangle$ transition, we expect the probe field resonance to be larger than the expected state splitting. If we consider the two-level dressed atom picture, when the trapping AC field is set below the resonance frequency, the dressed states are shifted apart from each other (see Fig. 3.3). In this experiment, the trapping RF field was set to 12.6 MHz, roughly 0.5 MHz detuned below the resonance. We thus expect the resonance between dressed states to be larger than that of the bare atomic states, which is observed in the data. We can use our model of the five-level ACZ system developed in Sec. 3.3 to estimate the Rabi frequency needed for a 15 kHz resonance shift.

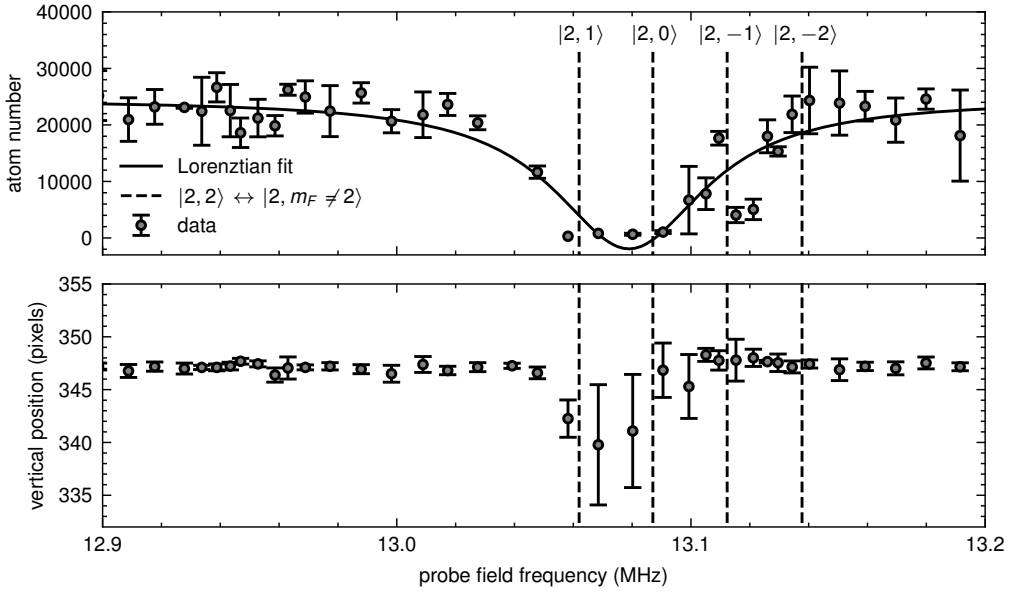

Figure 5.12: RF spectroscopy in an RF ACZ trap. Atoms are trapped in an ACZ trap with a resonance frequency of roughly 13.1453 MHz. A secondary, weak RF field is added via the evaporation wire to probe the m_F state splittings via the dips in atom number. The RF probe field VVA is set to 0.25 V and the field is pulsed on at a given frequency for 100 ms. The atoms were then held in the trap with the probe field off for 20 ms before being dropped for 8 ms before imaging. The data and error bar correspond to the atom number (a) or vertical position (b) and standard deviation from three absorption images at each probe frequency. The atom number data is fit to a Lorenztian: $N(f) = \frac{A}{\pi}\frac{C/2}{(f-f_0)^2+(C/2)^2} + D$. The fit (solid line) yielded a resonance at $f_0 = 13.079 \pm 0.003$ MHz. Transition frequencies from $|2,2\rangle \leftrightarrow |2, m_F \neq 2\rangle$ are given via the vertical dashed lines. Transitions to these states from $|2, m_F = 2\rangle$ require Δm_F photons at the given frequency.

Due to the nonlinearity of the DC Zeeman effect, the ACZ shifts experienced by the $|{+}{+}\rangle$ and $|{+}\rangle$ states are not equal; however we find that a difference in the energy shifts of $E_{ACZ,++} - E_{ACZ,+} = 15$ kHz at a frequency of 12.6 MHz is obtained using a Rabi frequency of roughly $\Omega = 2\pi \times 0.42$ MHz. We can also try to characterize this as a Bloch-Siegert shift [76], which for the two-level system is $\Delta_{BS} = \Omega^2/4\omega_0$, where Ω is the Rabi frequency and ω_0 is the bare state energy difference. This shift comes from including the counter-rotating terms that normally get ignored in the dressed atom picture via the rotating wave approximation. A Bloch-Siegert shift of 15 kHz would require $\Omega = 2\pi \times 0.89$ MHz. Typically, we consider $\Omega = 0$ at the bottom of the ACZ trap, however, gravitational sag and movement of atoms around the trap could account for these $\Omega \neq 0$ type shifts.

A full theoretical or experimental exploration into this topic is beyond the scope of this thesis; rather, we demonstrate the ability to add a secondary RF field to atoms in the RF ACZ trap. With this in place, a future area of interest is trying to probe splittings between the $|{+}{+}\rangle$ and other dressed states, previously investigated experimentally in the context of evaporative cooling [16]. At the bottom of the trap, where $\Omega \to 0$, these are multiples of the detuning of the trapping RF field frequency, modified by the nonlinear m_F splittings (see Sec. 3.3 on 3- and 5-level ACZ physics). We have begun looking into this process theoretically, which will be discussed in future theses and publications by the group. We also observed from this data a shift in the vertical position of several pixels (1 pixel = 7.4 μm) of the atoms with the same resonant behavior (Fig. 5.12(b)), as seen previously by our group for atoms in an optical dipole trap [61]. One could imagine using this effect to shift the trap minimum off of the $\Omega = 0$ point, where possible transitions to other dressed states could limit the lifetime in the trap [16].

Chapter 6

Potential Roughness Suppression in a Radio-Frequency AC Zeeman Trap

This chapter covers the main experimental work of the thesis: demonstration of potential roughness suppression in an RF AC Zeeman (ACZ) trap. The work presented here builds on the theoretical description of the roughness suppression developed by Austin Ziltz [57] and ShuangLi Du [14], and can be found in a paper by our group [58].

6.1 Introduction

Atom chips [12, 13] offer many benefits for ultracold atom experiments. Most obviously, they are compact, being just a few centimeters in length and width, which reduces the SWaP-C (Size, Weight, Power, and Cost) of the experiment and allows for integration into portable devices and even aboard the International Space Station [77]. Secondly, with modern micro-fabrication techniques, users can design complex wire layouts to precisely sculpt the electromagnetic fields experienced by the atoms and even incorporate optical elements onto the chip [78]. With this technology, the atom chip community has been able to produce Bose-Einstein condensates [48] and degenerate Fermi gasses [79], as well as study unique potentials via RF adiabatic potentials [80].

To make use of the versatility and potential of these devices, it is favorable to confine trapped atoms at short distances from the chip surface. However, proximity to the chip wires results in increased sensitivity to potential roughness effects, in which the trapping potential deviates from a smooth harmonic trap due to defects in the chip wires [81, 82, 83, 84]. This roughness can cause fragmentation of the atom cloud [85, 86] and limit experimental capabilities [81, 87]. Modern lithographic techniques can reduce chip wire defects [88], and materials such as graphene [89] and videotape [90] have been investigated to reduce roughness effects. Modulating the DC current through the chip wires by tens of kHz was also found to reduce roughness effects by time-averaging out irregularities in the trapping potential [91]. In some applications, researchers actually leverage the ultracold atomic density fluctuations caused by roughness to probe the current distribution in 2D materials [92].

Atom chips that generate traps via the AC Zeeman (ACZ) effect, recently demonstrated in our lab [16], have been theoretically shown to suppress potential roughness effects by a few orders of magnitude [58]. This suppression stems primarily from atomic selection rules for inter- and intra-manifold transitions, which make contributions to the trapping potential from additional axial magnetic fields resulting from defects in the atom chip wires negligible. In the case of the radio-frequency (RF) ACZ trap used in this work, only $\sigma_{\pm}$ transitions are allowed, depending on the hyperfine manifold, so extra axial fields corresponding to π-transitions do not contribute to the trapping potential. Additional suppression can come via the ac skin effect at sufficiently high frequencies; however, this suppression mechanism is a substantially smaller at MHz frequencies than the selection rule suppression and is dependent on the defect geometry [58]. For our 50 μm wide gold atom chip wires, the skin depth at 20 MHz, the working AC frequency in our experiments, is 16.8 μm, so the roughness suppression presented here is primarily due to selection rules.

In this work, we demonstrate potential roughness suppression in a radio-frequency (RF) AC Zeeman (ACZ) chip trap and compare to an identical DCZ trap at the same trap location and radial trapping frequency. The chapter is outlined in the following way:

In Sec. 6.2, we describe the origins of potential roughness in an atom chip magnetic trap. Section 6.3 then goes through the theory behind roughness suppression in an ACZ trap. Following that, Sec. 6.4 looks at the expected behavior of the roughness features in identical ACZ and DC Zeeman (DCZ) traps. Sections 6.5 and 6.6 discuss the experimental setup and analysis techniques for investigating the roughness suppression. In Sec. 6.7, we compare the potential roughness in identical ACZ and DCZ traps, demonstrating the anticipated suppression. We then characterize the longitudinal behavior of the ACZ trap at different heights (Sec. 6.8), detunings (Sec. 6.9), and resonance frequencies (Sec. 6.10). We end with concluding thoughts in Sec. 6.11.

6.2 Potential Roughness Origins

In fabricating atom chips for ultracold atom experiments, it is practically impossible to realize wire traces with perfectly rectangular cross sections. Even with modern fabrication techniques [88, 81, 93] defects in the chip wires are still present. These can manifest as bumps in the edges of the trace or, more commonly, local variations in the wire conductivity. Any such defect will cause the current traveling through the wire to deviate from a straight path, leading to the generation of unwanted variations in the magnetic fields transverse and parallel to the wire (see Fig. 6.1).

The main culprit causing the potential roughness is the creation of additional magnetic fields with components along the chip wire axis, which form local magnetic minima in addition to the overall magnetic trapping potential. For large enough defects, this can fragment the atom cloud. We can demonstrate this using simple 1D wires to form a Z-wire trap, shown in Fig. 6.2. In the ideal case, i.e., no defects in the wire, the trapping potential is a smooth harmonic trap. Modeling the defects as triangular deviations in the wire current [58], we see that the trap becomes "rough". The effects of the roughness become larger at closer distances to the chip [86, 81, 83].

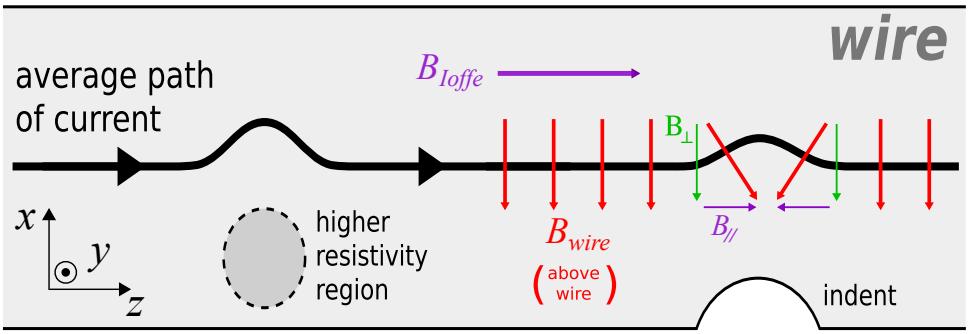

Figure 6.1: Deviation in the current path in an atom chip wire due to manufacturing imperfections. Defects such as non-uniform conductivity or an indent in the edge of the wire, causes the current in the trace (black line) to deviate from its straight line path. When the current in the chip wire strays from its path due to a defect, forming an angle θ with the z-axis, magnetic fields are generated along the longitudinal (z) direction that add linearly to the external B_{ioffe} field, forming a local minimum in the trapping field resulting in regions of local axial confinement in the trapping potential. Adapted from [58].

6.3 AC Zeeman Roughness Suppression Theory

The ACZ trapping potential is characterized by the spatially-varying Rabi frequency, given as (see Chapter 3)

$$\Omega = \frac{\mu_B}{\hbar^2}\langle m_F|S_+B_- + \underbrace{S_-B_+ + 2S_zB_z}_{0 \text{ for } F=2 \text{ system in } {}^{87}\text{Rb}}|m'_F\rangle = \frac{\mu_B}{\hbar^2}|B_-|\,\langle m_F|S_+|m'_F\rangle \tag{6.1}$$

In our experiment, we trap using intra-manifold RF transitions between m_F states in the $F = 2$ ^{87}Rb $5S_{1/2}$ ground state hyperfine manifold. This reduces the Rabi frequency to a single magnetic field term, dependent on $B_- = B_x - iB_y$, as absorption of RF photon energy raises alters Δm_F by $+1$ [16, 94]. The other magnetic field terms, B_+ and B_z, do not contribute to the ACZ potential, then, since they correspond to σ^- (B_+) and π (B_z) transitions, which are not allowed within the $F = 2$ system (see Fig. 6.3).

As shown in Fig. 6.1, defects generate additional magnetic field components perpendicular ($\perp$) and parallel ($||$) to the wire. These fields go as $B_{||} \propto \sin(\theta) \approx \theta$ and $B_\perp \propto \cos(\theta) \approx 1 - \theta^2/2$, where θ is the angle made between the current path and z-axis around the defect [58]. Since θ is typically small, on the order of $10^{-4} - 10^{-2}$ rads,

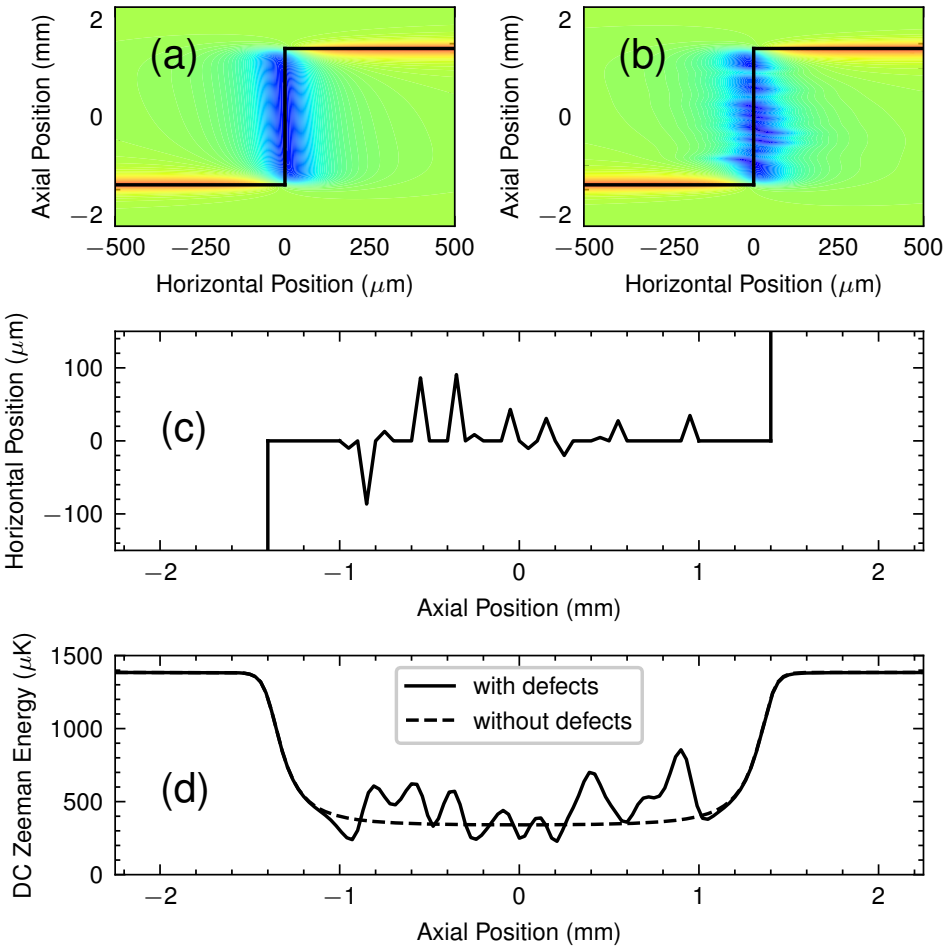

Figure 6.2: Modeled potential roughness in a z-wire DC trap. (a) Trapping potential formed using a z-wire trap with 1 A of current, a 20 G hold field, and a 5 G Ioffe field, putting the trap at $y \simeq 100$ μm. (b) The same trap with 20 random bumps in the central portion of the wire, each 100 μm long and at most 100 μm in width. In both top plots, the shape of the z-wire (without defects) is shown by the black lines. (c) Bump geometry in the Z-wire. (d) The axial trapping potential with and without the defects, evaluated at the trap location.

the parallel field component will dominate. However, from Eq. 6.1, we see that only $B_\perp$ will factor into the ACZ trapping potential, since $B_{z,tot} = B_z + B_{||}$ does not contribute. Meanwhile, for the DC Zeeman (DCZ) trap, both additionally generated field components add to the potential, since $U_{DCZ} \propto |\mathbf{B}|$. It is this difference that is at the root of the ACZ roughness suppression: selection rules allow the ACZ potential to be insensitive to the stronger parallel fields generated by atom chip wire defects. For realistic atom chip defect sizes, it was found that the ACZ trap should provide up to a few orders of magnitude in suppression, though this is very dependent on the defect geometry [58].

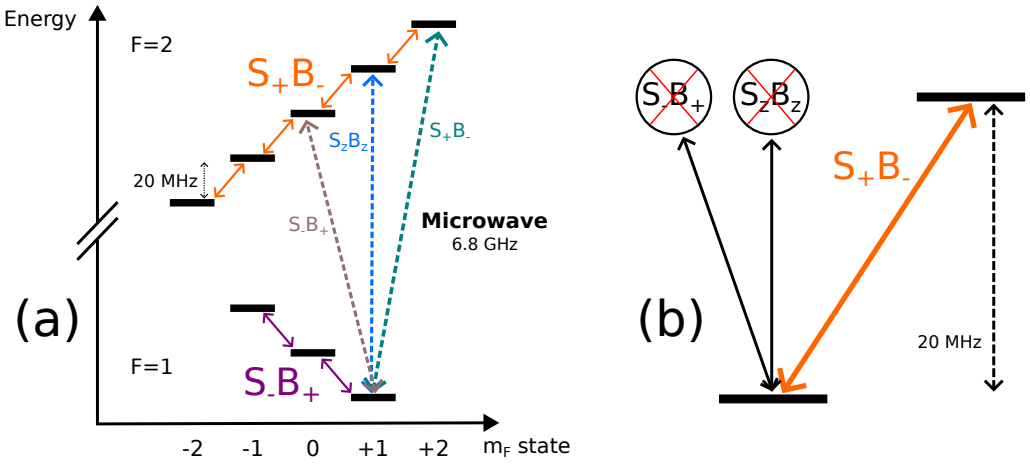

Figure 6.3: (a) Energy levels for the $F = 1$ and $F = 2$ hyperfine manifolds of ground state ^{87}Rb. When a quantizing DC field is applied along the wire axis, the Zeeman levels, labeled by m_F, break degeneracy and are split by ≈0.7 MHz/G. The states can be coupled together by an RF (intra-manifold transitions) or microwave (inter-manifold transitions) magnetic field. Within a given manifold, we can only drive transitions using a given magnetic field polarization. Between manifolds, we can drive transitions using any polarization, but the resonance condition must be met. (b) The $F = 2$ levels can be decomposed into a ladder of two-level systems, coupled together via a circularly polarized magnetic field, B_-. Transitions via B_+ or B_z fields are not allowed.

The same suppression scheme can be realized by driving microwave inter-manifold transitions between the $F = 1$ and $F = 2$ levels. In this case, applying a sufficiently large background DC field can effectively suppress π-transitions by making them far off-resonance. Additionally, at sufficiently high frequencies, the AC skin effect causes the current to hug the edges of the wire [95]. This makes the currents much less sensitive to conductivity defects and can provide further roughness suppression [58, 96].

6.4 Potential Roughness Features

To extract what kind of roughness features we expect in the DCZ and ACZ trap, we can model the roughness due to a wire defect by simplifying Fig. 6.1 to an infinitely thin wire. We focus on two bump models: a triangular bump (Fig. 6.4(a)), and a step bump (Fig. 6.4(b)). Both models use a bump length of 100 μm and a width of 5 nm, giving an angle of $\theta = 0.1$ mrad with respect to the z-axis. These values reflect representative defect sizes for atom chips fabricated using evaporative deposition [58]. In each case, we calculate the magnetic field generated by the wire with and without the bump present, the difference of which gives the distortion of the trapping potential, plotted in Fig. 6.4. The trap parameters are taken from Ref. [58] to ensure a common trap height of 100 μm and transverse trap frequency of 1 kHz. While these values are not necessarily what is used in the experiment (trap height of 90 μm, transverse trap frequency of $\simeq$250 Hz), we use these models to qualitatively probe the shape of the expected roughness.

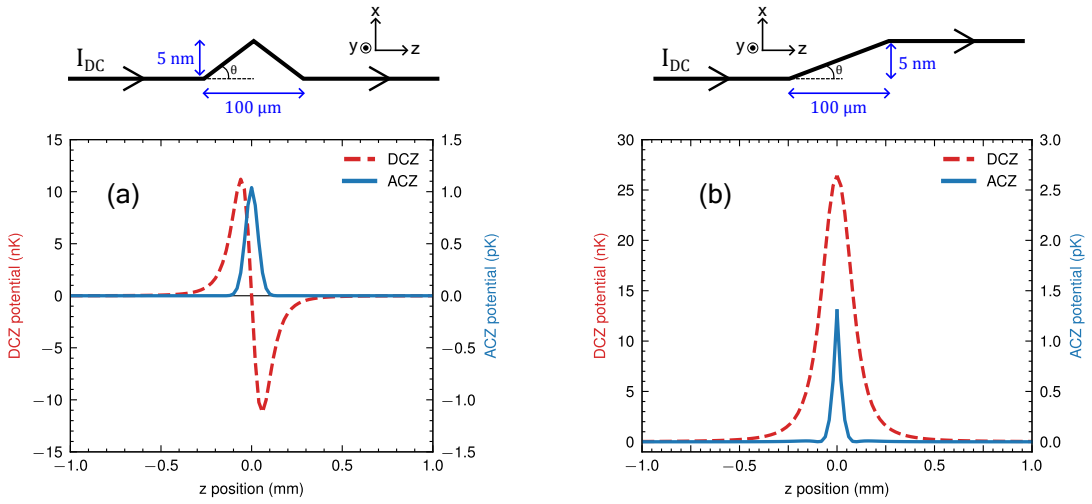

Figure 6.4: Distortion in the ACZ and DCZ trap due to a triangular (a) and step (b) bump. The DC trap is formed using $I_{DC} = 0.8796$ A with a hold field of $B_{hold} = 17.592$ G and an Ioffe field $B_{Ioffe} = 5$ G. The AC trap uses an $I_{AC} = 0.543$ A and a hold field $B_{ext,AC} = 10.86$ G. The model uses bump parameters $l = 100$ μm, $w = 5$ nm, and $\theta = 0.1$ mrad. The ACZ potential is computed using the $|2,2\rangle \leftrightarrow |1,1\rangle$ transition in ground state ^{87}Rb with a detuning of $\delta = 2\pi \times 1$ MHz.

For the triangular bump model, we find that the DCZ distortion is bipolar about

$z = 0$, while in the ACZ case it only causes a positive bump in the potential. This difference stems from the fact that the current bump results in a longitudinal and transverse magnetic field component, which depend on the bump angle as $B_{||} \propto \sin(\theta) \approx \theta$ and $B_{\perp} \propto \cos(\theta) \approx 1 - \theta^2/2$. For the DCZ trap, both components add vectorally into the potential, with $B_{||} > B_{\perp}$ since $\theta << 1$. This causes the distortion to flip directions at $z = 0$, where the bump angle flips sign. The ACZ potential, however, has zero dependence on $B_{||}$, only sensitive to the smaller $B_{\perp}$ component. This this goes as θ^2, the distortion does not go negative. A similar analysis can be applied to the step bump model, however, since the sign of θ never changes, both distortion bumps remain positive. In both models, we see a suppression in the ACZ trap by a few orders of magnitude. Moreover, in the triangular bump model, it was found that for the case of multiple bumps, the spatial frequency in the ACZ trap is twice that in the DCZ trap [58]. The bump also causes a positional change in the traps; however, this is expected to be much smaller than the pixel size of our camera (4.65 μm), so this cannot be used as a metric for comparison in the experiment.

6.5 Experiment

Our apparatus, described in Ref. [18] and Chapter 4, produces ultracold samples of roughly 3×10^5 ^{87}Rb atoms in the $|F = 2, m_F = 2\rangle$ state at a few μK temperature using a Z-wire Ioffe-Pritchard micro-magnetic atom chip trap. The DC trapping fields, i.e. the Z-wire current and horizontal and vertical bias fields, are then adjusted to shift the trap location between the Z and neighboring U-shaped chip wire. The wires, both 50 μm wide, are spaced 100 μm center-to-center. During this time, the Ioffe field is raised to $B_{\text{Ioffe}} = 28.74$ G, which splits the m_F states by roughly 20 MHz. A secondary gradient magnetic field oriented along the $\hat{z}$-direction, B_{push} is ramped to a value of 2.5 A. This field is primarily used to positionally overlap the different traps axially (along $\hat{z}$). The linear gradient felt by the atoms by this field is 0.088 (G/cm)/A$_{push}$, with an offset of 0.27 G/A$_{push}$, further splitting the m_F states by roughly 0.19 MHz/A$_{push}$. Once at this stage, the atoms are

adiabatically transferred into either a two-wire ACZ or DCZ trap. Schematics of the atom chip are shown in Fig. 6.5.

The process of loading atoms into the ACZ trap is described in Chapter 5, and briefly described here. The ACZ trap is loaded by ramping on RF power at $f_{RF} = 11$ MHz to the U and Z wires at a set relative phase difference of 120° while simultaneously ramping off the DC trapping fields. The RF frequency is then swept in two stages, first to 19.975 MHz, then to 20.175 MHz. The push coil current is also increased to 3 A during the second frequency sweep, giving an RF detuning of roughly 0.5 MHz. This two-step process helps reduce residual axial oscillations in the ACZ trap originating from a positional mismatch with the Z-wire trap. These oscillations were found to be roughly 4% of the full cloud size (FWHM $\approx 2.35\sigma$). The atoms are then held in the trap for 400 ms to thermalize, leaving 2.4×10^4 atoms at a temperature of 0.75 μK and trap height of 86.5 $\pm$ 5.5 μm from the chip. The radial trap frequency of this trap was measured to be 248.7 $\pm$ 4.6 Hz.

The two-wire DCZ trap is loaded by simultaneously ramping DC current through the U and Z wires to 0.325 A and 0.4 A, respectively, set to be counter-propagating from one another. This current difference shifts the trap roughly 10 μm in the $\hat{x}$-direction, giving transverse overlap with the ACZ trap. At the same time, the horizontal bias field is ramped to zero while the vertical bias field is ramped to $B_{bias} = 6.7$ G, canceling the wire field at a vertical position of 92.4 $\pm$ 6.5 μm. The push coil is simultaneously increased to 18 A, which tilts the axial potential enough to overcome the global trap minimum formed by the anti-aligned endcap currents. The atoms are then held in the trap for 400 ms to thermalize, leaving 6×10^4 atoms at a temperature of 0.99 μK and radial trap frequency 263.7 $\pm$ 1.4 Hz.

The axial potential is obtained through absorption images of the atoms, taken after a 1.5 ms time-of-flight (TOF) to allow the atoms to fall enough to not be obstructed by the chip. To enhance the signal-to-noise of the measurements, we average over 150 and 300 shots of the DCZ and ACZ trap, respectively. Temperature measurements (see Sec. 4.3) were taken before and after the data sets and averaged.

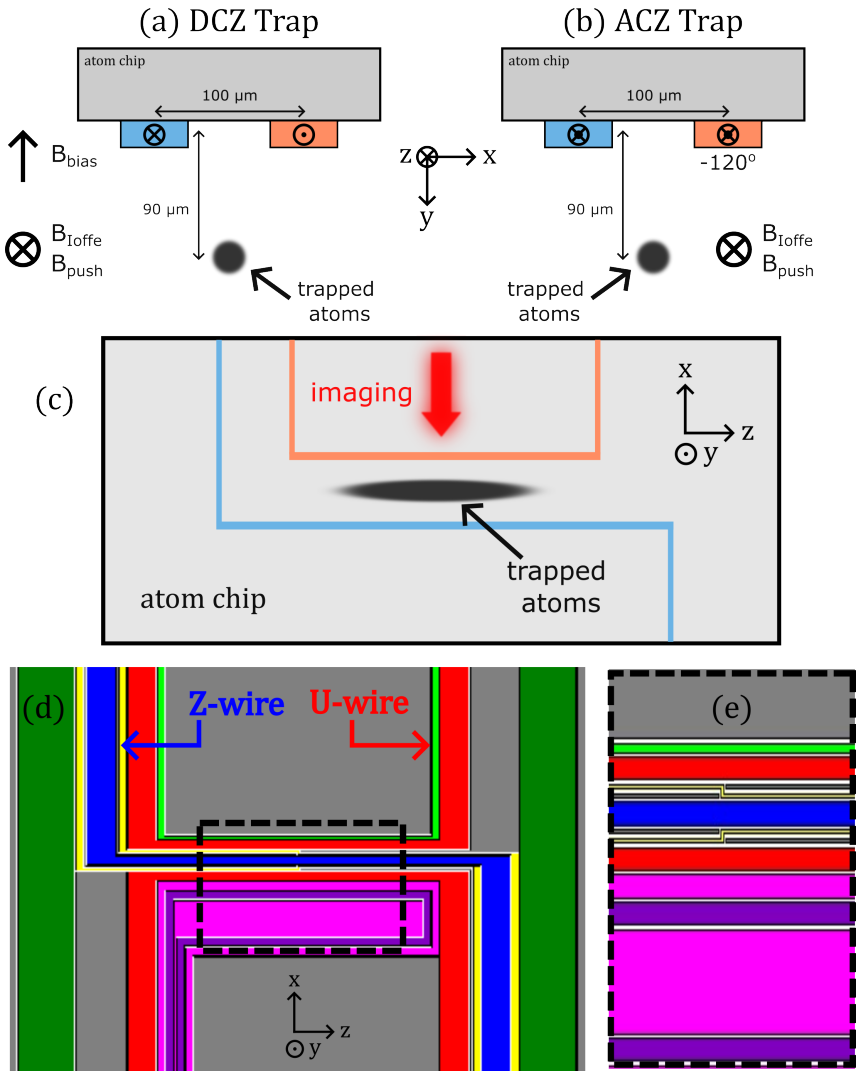

Figure 6.5: Schematic for the DCZ (a) and ACZ (b) two-wire atom chip traps. (c) Top view of the atom chip. The endcap wires forming the U and Z shapes are 200 μm wide. Dimensions are not to scale. (d) Full atom chip wire configuration. The central blue Z-wire is 2.6 mm long, as measured to the inside edge of the endcap wires. The red U-wire is 2.02 mm long, as measured to the inside edge of the endcap wires. Both the U- and Z-wires are 50 μm wide in the central region. The endcaps are 0.2 mm wide. The yellow wires are 10 μm wide. The light green wire is 20 μm wide. (e) Zoom in on the central region of the chip. The gaps between wires are 10 μm.

6.5.1 Extracting the Potential from Absorption Images

The density of a Bose gas in an external potential along the axial z-direction is [97]

$$n(z) = \frac{1}{\Lambda^3} \sum_{j=1}^{\infty} \exp\left\{j[\mu - U(z)]/k_B T\right\} / j^{3/2} \tag{6.2}$$

where $\Lambda = \hbar/\sqrt{2\pi M k_B T}$ is the thermal de Broglie wavelength, μ is the chemical potential, and $U(\mathbf{r})$ is the trapping potential. At low temperatures, $\mu \sim 0$, and only the first term in this infinite sum significantly contributes. For a harmonic trapping potential at 1 μK the second term contributes at most 3% to the atom density. For this reason we neglect everything except the first term, allowing us to write the atom density as

$$n(z) = \frac{1}{\Lambda^3} \exp\left[-U(z)/k_B T\right] \tag{6.3}$$

We can solve the above equation for the trapping potential, U(z), to obtain

$$U(z) = -k_B T \ln(n(z)) \tag{6.4}$$

where we ignore the additional term $-k_B T \ln(\Lambda^3)$ which acts as an energy offset to the potential but does not affect the roughness features of the trapping potential.

Thus, to obtain the trapping potential for the atoms in the trap, we only need to know the atom number density, $n(z)$, and the temperature, T. The temperature of the atoms can be easily measured through standard ballistic expansion (see Sec. 4.3). Atom number density can be obtained by absorption imaging of the atoms. Taking a narrow region of interest (ROI) covering only the atom cloud we integrate along the vertical direction to obtain the ROI sum of the atom number at every pixel along the axial direction, given as (see Chapter 4 for on-resonance absorption imaging)

$$\text{ROI sum} = \sum_y N_{pixel}(y,z) = \sum_y \ln\left(\frac{C_{laser}(y,z)}{C_{atoms}(y,z)}\right) \frac{2\pi}{3\lambda^2} A_{pixel} \tag{6.5}$$

where C_{laser} and C_{atoms} are the CCD are the number of CCD camera counts without and with the atoms present, respectively. We then divide the ROI sum by the pixel size of our camera, which for the axial camera is 4.65 μm/pixel, to yield the atom density $n(z)$.

To average out the shot-to-shot noise in our measurement we average over many absorption images of the atoms. To calculate the potential from these many shots we first average the atom densities, then adjust the minimum to one so that the natural log of that point returns zero. We then convert the averaged atom density to a potential via Eq. 6.4. The extracted potential is then fit with a second order polynomial, $U_{harm}(z) = az^2 + bz + c$, which gives the axial trapping potential in the absence of roughness. This can be subtracted out from the experimentally obtained trapping potential to give the roughness, i.e., $u(z) = U(z) - U_{harm}(z)$.

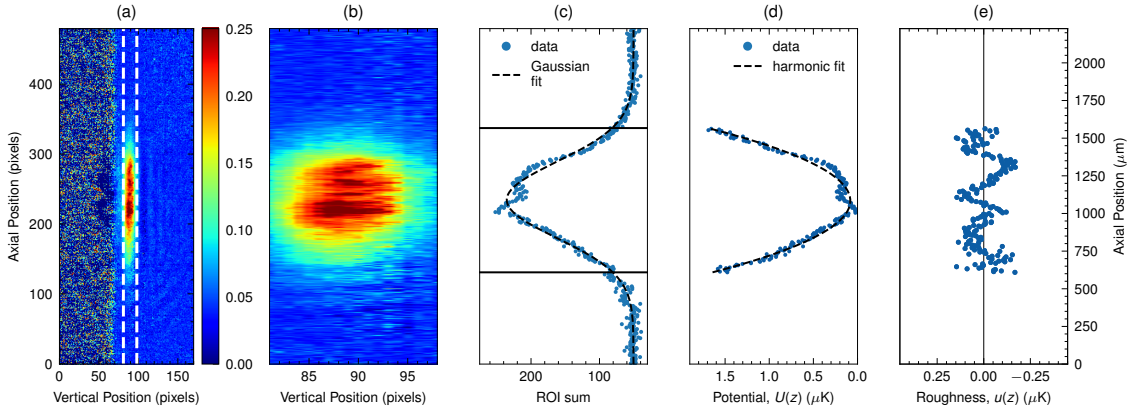

Figure 6.6: Extracting the axial trapping potential from absorption images. (a) Absorption image of atoms in the RF ACZ trap taken after a 1.5 ms TOF. Shown is the optical depth averaged over 300 shots. White dashed lines indicate the bounds of the region-of-interest (ROI) for analyzing the potential. (b) Absorption image of the atoms zoomed into the ROI region. (c) ROI sum from Eq. 6.5. The dashed line shows a Gaussian fit to the data. The solid lines indicate the axial bounds for evaluating the potential. (d) Extracted axial trapping potential from Eq. 6.4 with a temperature of 0.99 μK. The dashed line shows a harmonic fit to the data. (e) Roughness extracted from subtracting the harmonic fit from the data in (d). The solid line indicates zero. Data from 20jul25.

6.5.2 Time-of-Flight Effects

In our experiments, we release the atoms from the trap and allow them to fall for a short time before imaging. During this time-of-flight, the atoms move a distance related to their temperature. This has the effect of partially washing out some of the roughness features, depending on their axial size. It is in our best interest, then, to select the shortest possible time-of-flight; however, it must also be long enough for the atoms not to be obscured by the chip when imaging. We found that a time-of-flight of 1.5 ms gave the atoms this proper time.

Following Refs. [98, 91], we can estimate by how much certain roughness features will get washed out by modeling the atom density distribution as $n(z, t = 0) = \sin(2\pi z/\lambda)$, where λ is the length scale of the roughness features. After expanding for a time t, the atom density is (see Appendix C)

$$n(z,t) = \sin\left(\frac{2\pi z}{\lambda}\right) \underbrace{e^{-2\pi^2(\delta(t)^2+\sigma_{res}^2)/\lambda^2}}_{A(\lambda,T,t)} \tag{6.6}$$

where $\delta(t) = t\sqrt{k_B T/m}$ is the distance traveled by an atom with mass m and temperature T after a time t. The above equation also includes a convolution with a Gaussian of rms width of $\sigma_{res} = 6.1$ μm, indicating the smallest feature we can image with our system (Thorlabs MAP10100100-B 1:1 achromatic doublet pair) [18]. We can see that the amplitude of the roughness, $A(\lambda, T, t)$ goes to zero as $t \to \infty$. The fractional reduction of this amplitude is given as

$$\alpha(\lambda, T, t) = \frac{A(\lambda, T, t)}{A(\lambda, T, 0)} = e^{-2\pi^2\delta(t)^2/\lambda^2} \tag{6.7}$$

This quantity tells us by how much the amplitude of the roughness feature of length scale λ has changed at a given temperature, T, and expansion time, t. If $\alpha = 1$, then the amplitude of the roughness has not changed at all from its original value at $t = 0$. However, when $\alpha \to 0$, the roughness gets completely washed out by thermal expansion of the cloud. From Eq. 6.7, we can see that the amplitude for smaller length scales, go to zero much faster

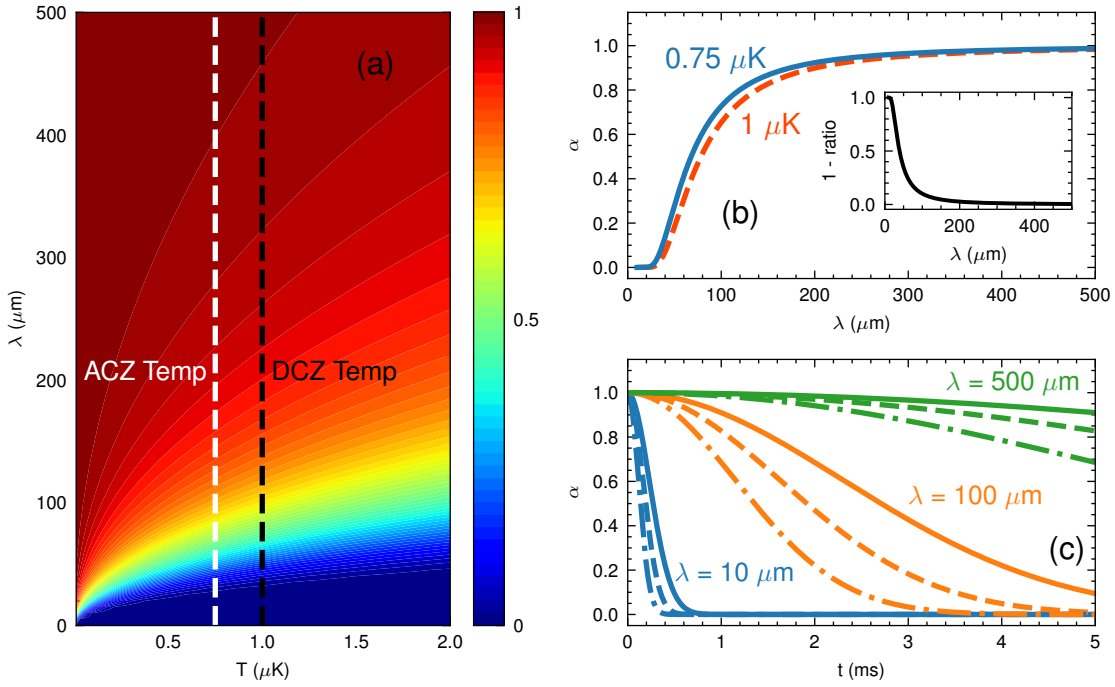

Figure 6.7: Effect of expansion time on roughness amplitude. (a) α (Eq. 6.7) evaluated across a range of λ and T for an expansion time of $t = 1.5$ ms. Vertical lines indicate the temperatures of the ACZ and DCZ traps in Fig. 6.11. (b) Slices of α at the ACZ and DCZ trap temperatures in (a) across λ for $t = 1.5$ ms. Inset: ratio between the 1 μK and 0.75 μK curves. (c) α as a function of expansion time, t, evaluated at different λ, indicated by the different colors, at $T = 0.5$ μK (solid line), $T = 1$ μK (dashed line), and $T = 2$ μK (dot-dashed line).

than larger ones, demonstrated in Fig. 6.7.

We plot $\alpha(T, \lambda, t = 1.5 \text{ ms})$ for $T = 0.75$ μK and $T = 1$ μK, the temperatures of the ACZ and DCZ traps in Fig. 6.11, respectively, as a function of λ in Fig. 6.7(b). As expected, the DCZ trap features are more suppressed than in the ACZ trap due to the larger temperature, with the difference peaking at 0.1 at 61 μm. The DCZ trap measurement will therefore appear a little smoother than the ACZ trap. Features below $\lambda \approx 19$ μm and $\lambda \approx 22$ μm get completely washed out in the ACZ and DCZ traps, respectively. The ratio between the two curves (shown in the inset) will tell us how the two traps having different temperatures will affect the suppression factor. For example, at a length scale $\lambda = 100$ μm and an expansion time $t = 1.5$ ms, $\alpha_{DCZ} = 0.65$ and $\alpha_{ACZ} = 0.73$. The suppression factor at this feature length will then be reduced by $1 - \frac{\alpha_{DCZ}}{\alpha_{ACZ}} = 10\%$. At a

length scale $\lambda = 200$ μm, the suppression factor is reduced by 2.6%.

6.5.3 Modeling the Trap Potentials

We can create a three-dimensional model of the trapping potentials using infinitely thin wires of finite length. An expression for the magnetic field generated by such a wire can be found in Ref. [58]. Figure 6.8 shows the magnetic field generated by the U and Z wires, along with the orientations of the external magnetic fields used for forming the trap. The

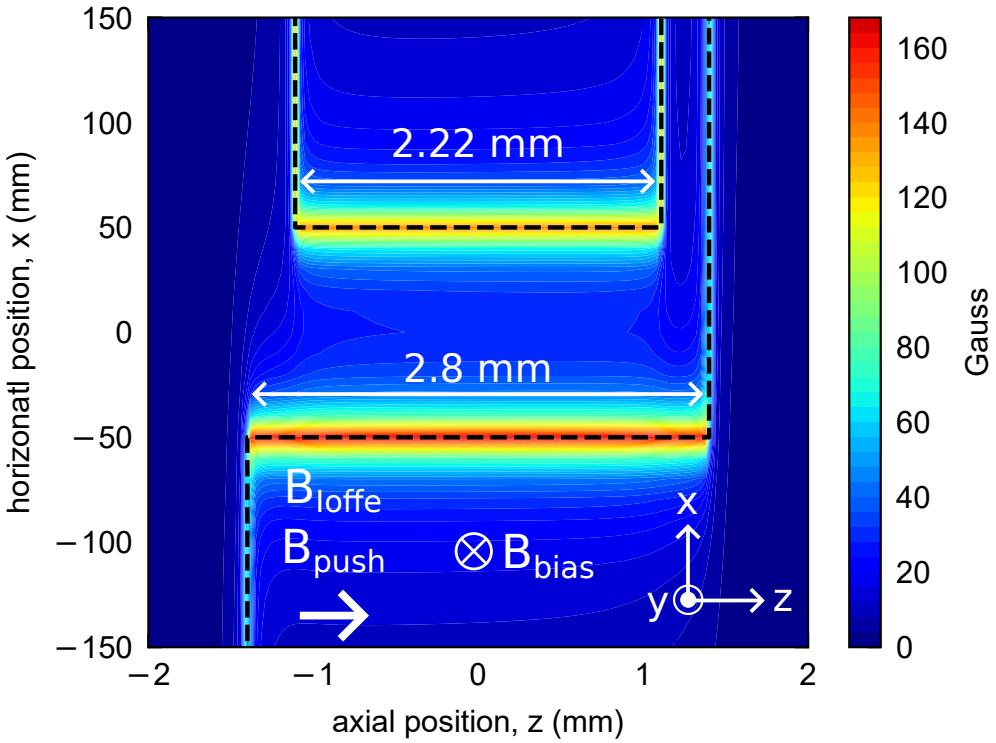

Figure 6.8: Magnetic field generated by the U- and Z-shaped atom chip wires, using infinitely thin wires with relevant lengths, evaluated at $y = 5$ μm. The length of the central section of each wire incorporates half the width of each endcap, which in reality are 200 μm wide. The endcaps have a length of 10 mm. The wire locations are indicated by the black dashed lines. Other field involved with the trap, i.e., B_{bias}, B_{Ioffe} and B_{push}, are shown with their respective orientations, however, they are not included in the contour plot.

Ioffe and push coil fields incorporate their non-uniformity (see Sec. 5.2); the Ioffe field uses a harmonic fit to the magnetic field generated by the coil pair at $I_{Ioffe} = 11.29$ A ($B_{Ioffe} \simeq 28.74$ G), which produces an axial harmonic potential of 3.67 Hz. The lab's

natural offset of 1.29 G is subtracted off of this field. The push coil is known to shift the magnetic field felt by the atoms by $b_{push} = 0.27$ G/A and have a gradient of $m_{push} = 0.088$ (G/cm)/A. The push coil field is then given as $B_{push} = m_{push}z + b_{push}$. Neither field incorporates any curvature in the transverse xy-directions. Gravity is also included, which acts to shift the vertical position of the trap slightly as well as lower the vertical trap frequency.

The DCZ potential is calculated using the standard DC Zeeman energy: $E_{DCZ} = m_F g_F \mu_B |\vec{B}|$ for the $|F, m_F\rangle = |2, 2\rangle$ state. The ACZ potential uses the five-level dressed atom Hamiltonian from Sec. 3.3 for the $|{+}{+}\rangle$ state with $f_{RF} = 20.175$ MHz. We calculate the Rabi frequency at each point in space and diagonalize the Hamiltonian incorporating the spatially varying Ioffe and push coil fields as the quantization field strength. Parameters for the canonical ACZ and DCZ traps are given in Table 6.1, which produce the trapping potentials shown in Fig. 6.9.

Trap	I_Z	I_U	ϕ	B_{bias}	I_{push}	f_x	f_y	f_z
DCZ	400 mA	325 mA	N/A	6.7 G	18 A	277.4 Hz	265.8 Hz	8.9 Hz
ACZ	158 mA	$158e^{i\phi}$ mA	-120°	N/A	3 A	271.5 Hz	238.4 Hz	4.9 Hz

Table 6.1: Relevant model parameters and calculated trap frequencies for the DCZ and ACZ trap potentials in Fig. 6.9.

The currents and magnetic fields are well known from calibrations, with the largest uncertainty being the current magnitudes for the ACZ trap. We nominally send 200 mW of RF power onto the chip, which gives a current of 158 mA using an effective impedance of 8 Ω [16]. It is very likely, however, for the currents in the traces to be unequal due to the wires having a different impedance. In practice, we found that we had to adjust the DCZ wire currents in order to spatially overlap it with the ACZ trap. The DCZ trap using these currents is found to be located at $x \simeq 10$ μm. By changing the current magnitudes in the model for the ACZ trap to $I_U = 148$ mA and $I_Z = 163.5$ mA, respectively, we were able to overlap the trap minima in the x-direction while having minimal effect (≤ 1 Hz) on the trap frequencies. This model agrees well with experimentally measured trap positions

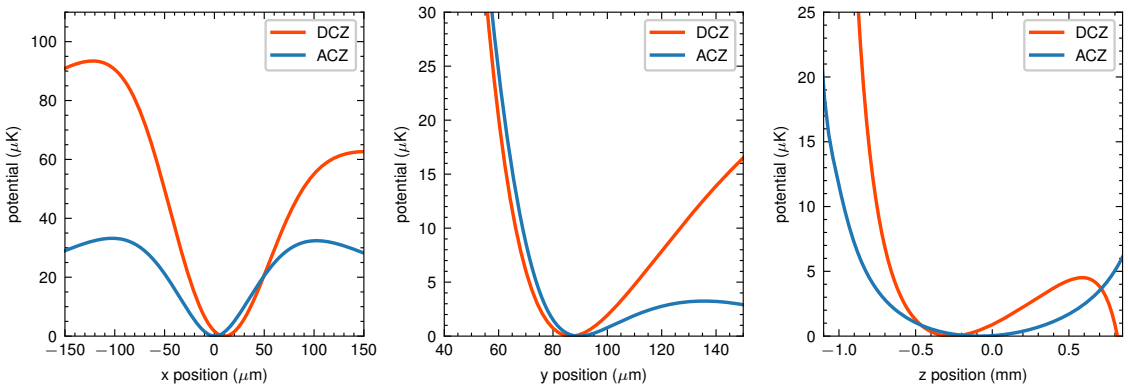

Figure 6.9: Modeled ACZ (blue) and DCZ (red) potentials generated by the UZ wire configuration in Fig. 6.8, evaluated at the trap minimum. Energy offsets are subtracted to set the potential minima at zero. Parameters used in the model are given in Table 6.1. Both traps incorporate the curvature of the Ioffe field generated using 11.29 A of current (see Fig. 5.3). The trap frequencies from the model are $\{f_x, f_y, f_z\}_{DCZ} = \{277.4, 265.8, 8.9\}$ Hz and $\{f_x, f_y, f_z\}_{ACZ} = \{271.5, 238.4, 4.9\}$ Hz, respectively.

and trap frequencies, differing by at most about 6% in the transverse direction. Axially, the ACZ trap frequency, measured via oscillations (see Fig. 5.4), differs from the model by 2%. Given the significant roughness in the DCZ trap, which fragments the cloud, we extract the axial trap frequency by fitting the outer edges of the trapping potential to a second order quadratic polynomial. From this, we get an axial trap frequency of 8.5 Hz for the DCZ two-wire trap, 4.5% different from the model.

6.6 Roughness Analysis Techniques

This section goes over the techniques used to analyze the potential roughness obtained from experiment, including predictions for the behavior of certain roughness features in real space and spatial Fourier space.

6.6.1 Spectral Analysis

We can infer the size of the roughness features by performing a spectral decomposition of the roughness into its Fourier components. We define the Fourier transform of the

roughness, $u(z)$, as [83]

$$\tilde{u}(k) = \frac{1}{\sqrt{2\pi L}} \int u(z) e^{-ikz} dz \tag{6.8}$$

where L is the axial size of the potential. The units of $\tilde{u}(k)$ are $\mu\text{K}\cdot\sqrt{\mu\text{m}}$. The Fourier transform can tell us the dominant spatial frequencies of the potential roughness. For example, if our potential had a bump of size l then we would see a spike in the Fourier transform at length l.

A common figure of merit when analyzing potential roughness is the power spectral density (PSD, not to be confused with phase space density). Using our definition of the Fourier transform, the PSD is simply the square of the Fourier transform

$$PSD(\lambda) = |\tilde{u}(k)|^2 \tag{6.9}$$

The PSD has units of $\mu\text{K}^2 \cdot \mu\text{m}$, and is typically plotted as a function of length scale, λ. To better understand this metric, we can generate a fictitious trapping potential to see how certain defects manifest in the PSD. In Fig. 6.10, we calculate the PSD for the roughness with three kinds of defects: random noise, a sinusoid, and a Gaussian bump. Including random noise into the trapping potential simply adds an offset into the PSD, being more or less flat across λ. Adding in a sinusoid, $\sin(2\pi z/\lambda_0)$, generates a sharp peak in the PSD at length $\lambda = \lambda_0$. Including a Gaussian bump, $Ae^{-(x-x_0)^2/(2\sigma^2)}$, increases the PSD, with the rise starting at roughly twice the width of the Gaussian, i.e., 2σ. We can also see that in the case of the Gaussian bump, the harmonic fit to the potential gets shifted, giving the falsity that the roughness goes both positive and negative of the ideal potential.

6.6.2 Spatial Filtering

To account for imaging noise in the potentials, which occurs on the pixel-to-pixel (1 pixel = 4.65 μm) level, we apply a spatial filter to remove high frequency fluctuations. Motivated by the thermal expansion effect described in Sec. 6.5.2, we set a wavelength cutoff for which the amplitude of roughness features below the cutoff are essentially zero. This cutoff is

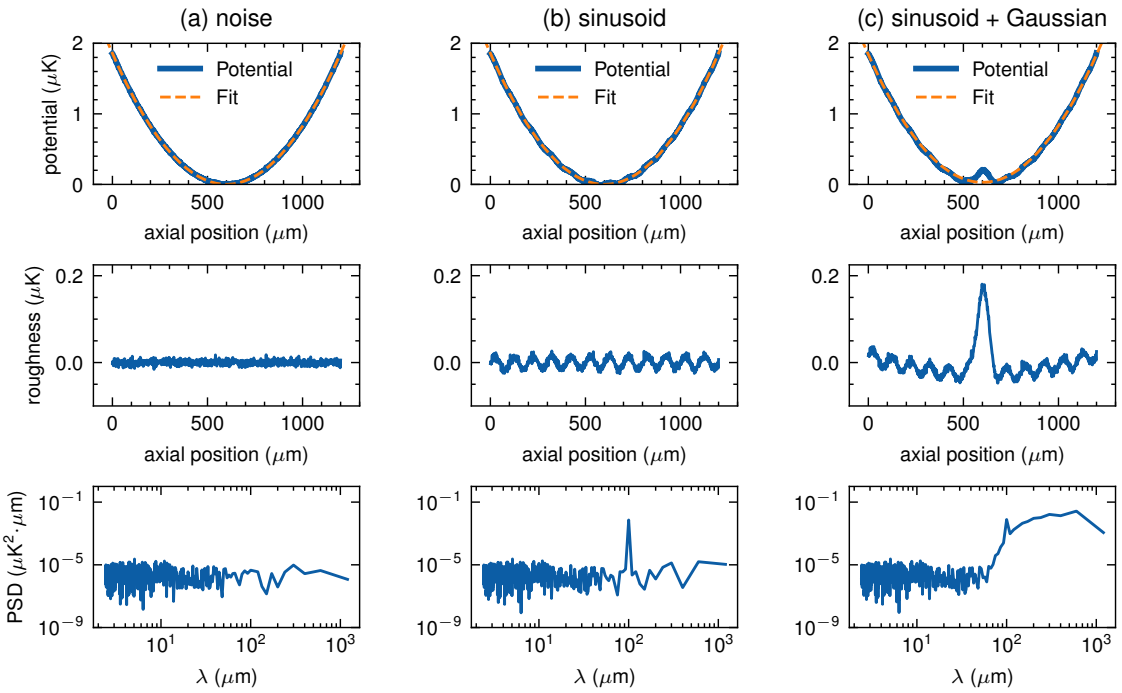

Figure 6.10: Example PSD calculated from fictitious trapping potentials. The base potential is a harmonic trap with a trap frequency of $2\pi \times 5$ Hz. The potentials (top row) are fit to a second order polynomial and subtracted off the "data" to obtain the roughness (second row). The PSD are then calculated from Eq. 6.9 and plotted on the bottom row. In each column we add a new kind of defect: (a) random noise, (b) a sinusoid, $\sin(2\pi z/\lambda_0)$, where z is the axial position and $\lambda_0 = 100$ μm, and (c) a Gaussian bump centered at 600 μm with an amplitude of 0.2 μK and a width of $\sigma = 30$ μm.

$\lambda_{ACZ} = 19$ μm and $\lambda_{DCZ} = 22$ μm for the ACZ and DCZ traps, respectively. The filtering process, in practice, is:

1. Extract the raw potential, $U(z)$, from the absorption images via Eq. 6.4.

2. Fit the potential to a harmonic to get the "ideal" trapping potential, $U_{harm}(z)$.

3. Subtract the two to get the raw roughness, $u(z) = U(z) - U_{harm}(z)$.

4. Take the Fourier transform (FFT) of $u(z)$ and set it equal to zero for all wavelengths past the thermal cutoff.

5. Take the inverse Fourier transform of the modified FFT and add $U_{harm}(z)$ to get the spatially filtered trapping potential, $U_{filtered}(z)$.

The filtered trapping potential, $U_{filtered}(z)$, is then used for all further analysis.

6.6.3 RMS Roughness Calculation

In our experiments, we typically observe roughness features in the RF ACZ trap that are too small to confidently compare individual bumps between the DCZ and ACZ traps. We can then use the root mean squared (RMS) value of the potential roughness for characterization. The RMS roughness is given as

$$u_{RMS} = \sqrt{\frac{1}{N}\sum_{i=0}^{N} u(z_i)^2} \tag{6.10}$$

where N is the total number of data points, and $u(z_i)$ is the value of the roughness at axial pixel position z_i.

6.7 ACZ and DCZ Trap Roughness Comparison

Figure. 6.11 shows the main results of our experimental efforts: potential roughness suppression in an ACZ chip trap. The atom cloud in the DCZ trap features clear fragmentation into three distinct potential wells, with smaller features also visible. This fragmentation goes away completely in the ACZ trap, and we are left with a smooth, continuous cloud of atoms. A harmonic fit to each potential gives axial trap frequencies of $f_{DCZ} = 7.9$ Hz and $f_{ACZ} = 5$ Hz, consistent with the 1D wire model. Subtracting out this harmonic gives the potential roughness in each trap, plotted in Fig. 6.11(d). Notably, the roughness for each trap is shown on scales differing by a factor of 10, indicating the approximate scale of the suppression in the ACZ trap.

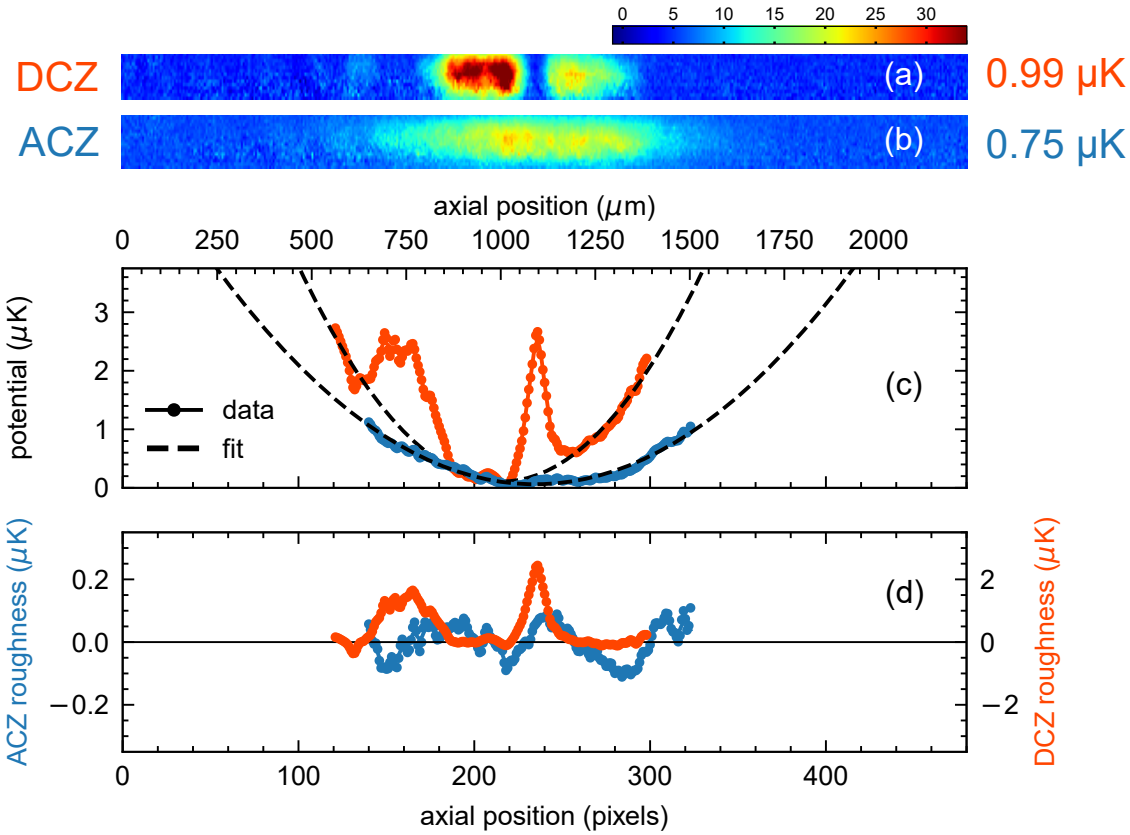

Figure 6.11: Demonstration of potential roughness suppression in an RF ACZ atom chip trap. Absorption images of atoms in a two-wire DC Zeeman (a) and AC Zeeman (b) potential. The images are a sum of 150 and 300 shots for the DCZ and ACZ trap, respectively. Plotted is the number of atoms per pixel (1 pixel=4.65 μm). (c) Extracted trapping potential from Eq. 6.4. Dots correspond to the potential sampled every pixel, with a 5-point moving average added for visualization. The data is fit to a harmonic to give the "ideal" trapping potential in the absence of roughness. (d) ACZ and DCZ trap roughness, given as the residuals between the data and the harmonic fit. The vertical scales differ by a factor of ten.

6.7.1 Overlay with Z-wire Trap

Our atom chip is known to have defects, the most notable of which is a dimple used to aid in BEC production [18]. We can then see if any of the defects present in the Z-wire trap are also visible in the two-wire ACZ or DCZ trap profiles. While this will not necessarily tell us the exact type of defect (i.e., conductivity or edge defect), common features between the traps indicate their origin from the Z-wire.

The axial atom profiles for the different traps are overlayed in Fig. 6.12. The profiles

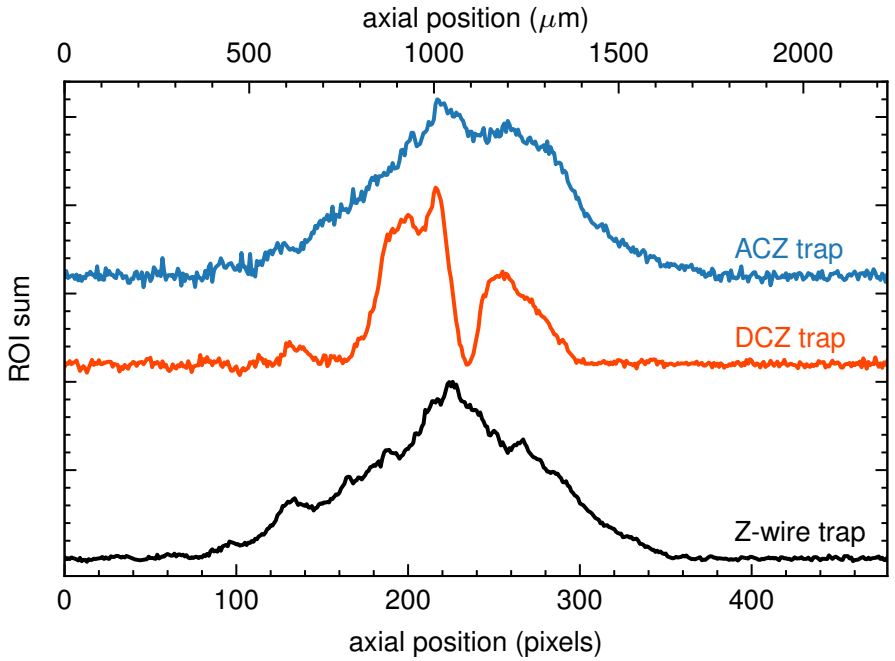

Figure 6.12: Comparison of the axial profiles of the ACZ (blue), DCZ (red), and Z-wire (black) traps. The Z-wire trap stops before BEC (after RF5 in the Adwin panel). The profiles are the sums of the atom number at each pixel (1 pixel = 4.65 μm) along the vertical direction for a given region of interest (ROI). Each profile is scaled and has an added offset.

correspond to the sum of the atom number along the vertical direction for a narrow region of interest containing the atoms. Looking at the profiles we can see a feature at roughly 130 pixels that appears to be common among all three traps. The main Z-wire trap dimple at ≈225 pixels does not overlap with the main bump in the ACZ trap, however. It is otherwise more difficult to make conclusive arguments on common features shared between the Z-wire and two-wire traps.

6.7.2 RMS Analysis

As a simple measure of the roughness, we can calculate its rms value via Eq. 6.10. The DCZ rms roughness is dominated by two large bumps at $z \simeq 160$ pixels and $z \simeq 240$ pixels. Including the full data set, the rms roughness for the DCZ and ACZ traps are 0.758 and 0.055 μK, respectively, yielding a suppression factor of 13.8. To get a sense of how much

these features affect the rms value, we can cut them out of the data prior to doing the harmonic fit. This is shown in Fig. 6.13 for the case of removing either or both of the bumps, and summarized in Table 6.2. From this, we can set a lower bound on the expected ACZ suppression factor, as we can compare regions of the potentials that are both relatively smooth. Removing either of the bumps decreases the DCZ rms roughness by 20%, showing that both features contribute roughly equally to the rms value. Cutting out the two cloud fragmenting features, the rms roughness of the DCZ trap is reduced to 0.106 μK, 7.2 times less than with them included. In each case, the ACZ rms roughness only changes by $\lesssim$5%. With both of the primary roughness features in the DCZ trap removed, the suppression factor is reduced from 13.8 to 1.8.

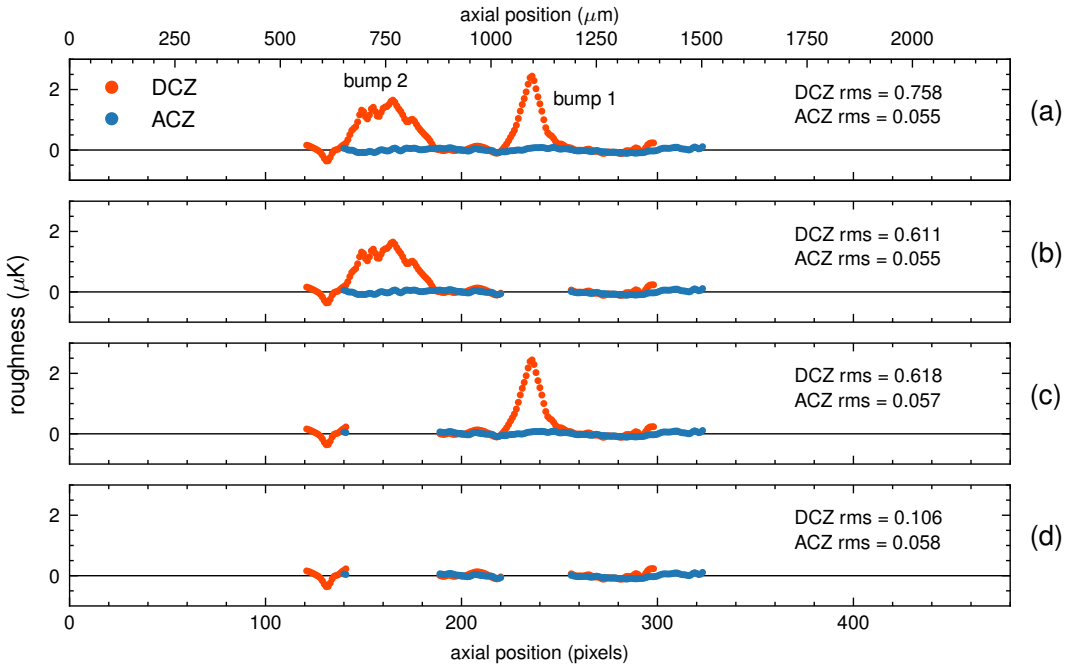

Figure 6.13: Evaluating the rms roughness for the canonical DCZ (red) and ACZ (blue) potentials (see Fig. 6.11) without the inclusion of the main roughness features. We consider four cases: (a) no cuts to the data, (b) removing bump 1 at $\simeq$240 pixels, (c) removing bump 2 at $\simeq$160 pixels, and (d) removing both bumps 1 and 2. We calculate the rms values for the roughness using Eq. 6.10.

	DCZ rms (μK)	ACZ rms (μK)	Suppression Factor
(a) No Cuts	0.758	0.055	13.8
(b) Bump 1 Removed	0.611	0.055	11.1
(c) Bump 2 Removed	0.618	0.057	10.8
(d) Both Bumps Removed	0.106	0.058	1.8

Table 6.2: Comparison of the DCZ and ACZ rms roughness with different sections of data removed (see Fig. 6.13). For each row, the data is removed using the same axial cuts for both traps, corresponding to the two main bumps in the DCZ trap at axial positions $z \simeq 160$ pixels (bump 2) and $z \simeq 240$ pixels (bump 1).

6.7.3 Bump Analysis

Each cloud features a noticeable bump at roughly 240 pixels (bump 1 in Fig. 6.13), making it a natural choice to study its suppression. Since in the DCZ trap this bump is large enough to fragment the cloud, this will give a lower bound on the suppression. Restricting the area of interest around the bump, we can fit the potential to the sum of a second-order polynomial and a Gaussian,

$$U_{fit}(z) = \left[p_1 z^2 + p_2 z + p_3\right] + \left[A e^{-(z-b)^2/(2\sigma^2)}\right], \tag{6.11}$$

giving the fit shown in Fig. 6.14. From this, we find that the prominent bump at 240 pixels is suppressed by a factor of at least 14.52 ± 0.04 in the ACZ trap. We also see the center position of the bump shift by about 40 μm between the two traps, as well as a widening by a factor of two in the ACZ trap.

	Amplitude (μK)	Suppression Factor	Position (μm)	Width (μm)
DCZ trap	2.26 ± 0.04	14.17 ± 0.05	1095.3 ± 0.1	24.8 ± 0.1
ACZ trap	0.16 ± 0.03		1145.5 ± 0.7	58.7 ± 1.6

Table 6.3: Bump 1 comparison between the ACZ and DCZ traps, using Eq. 6.11 to fit the potential. Fits are shown in Fig. 6.14.

We also observe a distinct bimodal feature in the DCZ roughness similar to the expected distortion shape for the single wire theory of Ref. [58]. This feature is located at roughly $z = 212$ pixels, and is shown in Fig. 6.15. Fitting this to the sum of two Gaussians with

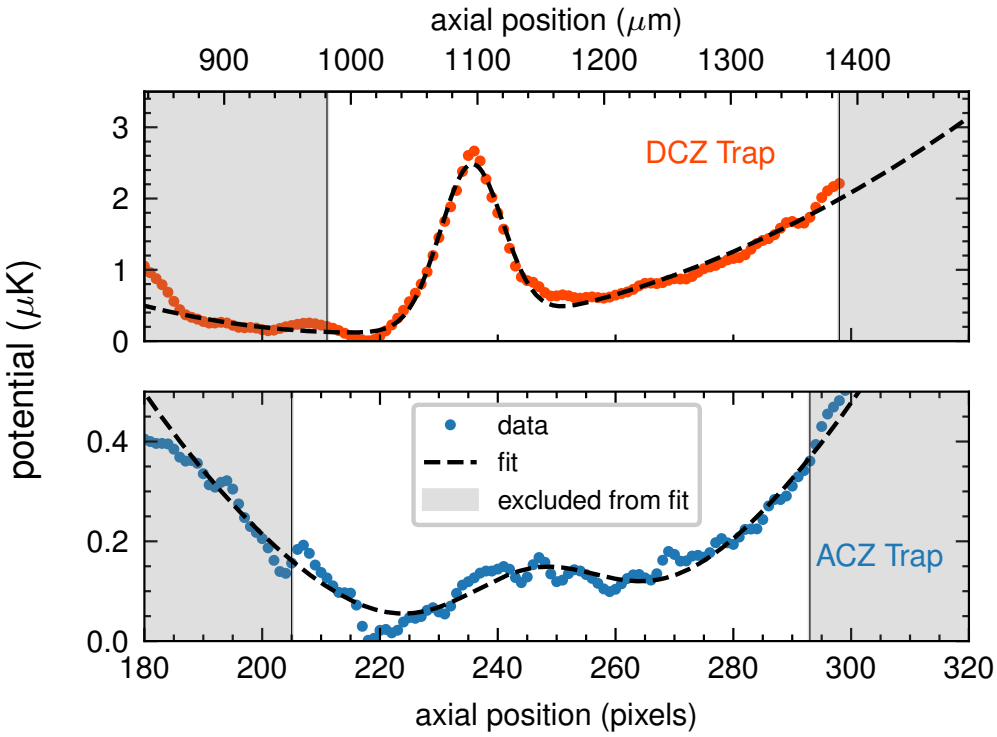

Figure 6.14: Bump comparison between the DCZ (top) and ACZ (bottom) potentials from Fig. 6.11. The data is fit using Eq. 6.11, with the fit bounds indicated by the grayed out regions. Results from the fits are given in Table 6.3.

no offset reveals three pieces of information. First, the bump is equal and opposite in amplitude about zero, reaching $A_+ = 0.134 \pm 0.014$ μK and $A_- = 0.114 \pm 0.019$ μK, respectively. Second, the distance between the peaks is $\simeq$43 μm. Thirdly, the widths of each peak are not equal, differing by a factor of about 1.9. This difference could be caused by the presence of the large, cloud fragmenting potential bump at $z \simeq 240$ pixels, which might act to squish the right side of the bipolar roughness feature, changing the respective widths and peak separation. There was no clear corresponding feature observable in the ACZ roughness. We can use the 1D-wire model developed in Ref. [58] to get an idea of the expected suppression in the ACZ trap, as well as the size of the defect causing the bump. To better match the experimental parameters, namely a trap height of 90 μm and transverse trap frequency of 260 Hz, we use $\{I_{DC}, B_{ext,DC}, B_{Ioffe}\} = \{0.4367 \text{ A}, 9.705 \text{ G}, 28 \text{ G}\}$ and $\{I_{AC}, B_{ext,AC}, \delta\} = \{0.0807 \text{ A}, 1.793 \text{ G}, 0.5 \text{ MHz}\}$. For a bump length of 50 μm and a

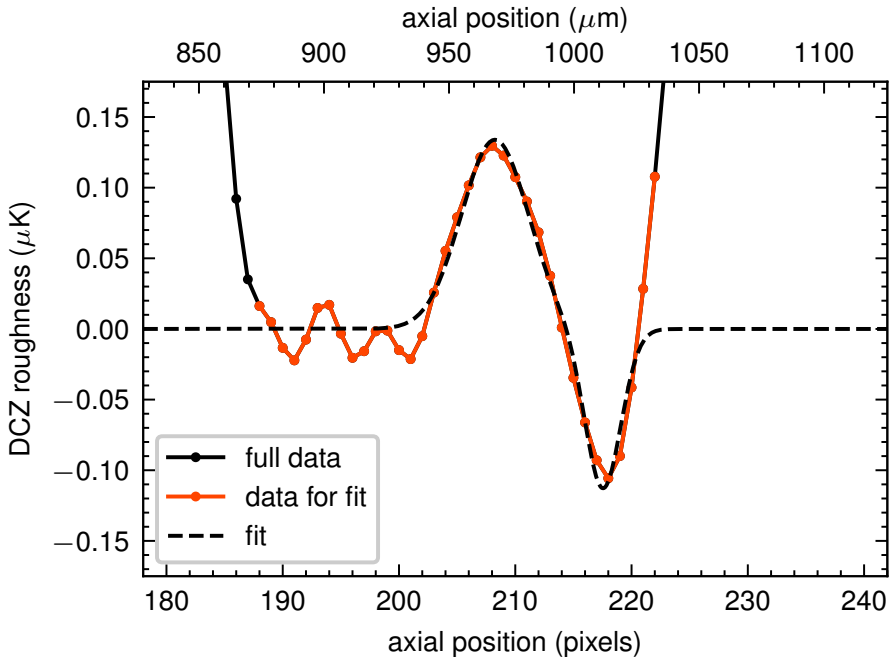

Figure 6.15: Bipolar roughness feature in the DCZ trap. The data is fit to the sum of two Gaussians with no offset.

width of 153 nm, the suppression factor is several 10^3.

6.7.4 PSD Analysis

Using Eq. 6.9, we can calculate the power spectral density (PSD) of the DCZ and ACZ roughness. These are plotted in Fig. 6.16(a), where features below the thermal motion cutoff wavelengths have already been filtered out. The square root of the ratio, $\sqrt{PSD_{DCZ}/PSD_{ACZ}}$, gives a suppression factor as a function of spatial feature size, which we plot in Fig. 6.16(b). Applying a 3-point moving average helps visualize the trends in the suppression ratio, which we give as the dashed line in Fig. 6.16(b). Using the inset plot of Fig. 6.7(b), we can adjust the suppression factor to account for the amplitude suppression from thermal motion. We do this by multiplying the suppression factor data at each wavelength by $2 - \alpha_{DCZ}(T_{DCZ}, \lambda)/\alpha_{ACZ}(T_{ACZ}, \lambda)$, where $\alpha(T, \lambda)$ is the decrease in roughness amplitude for a given wavelength and temperature, where we fix the time-of-flight to 1.5 ms. The result of this adjustment is shown in Fig. 6.16(c) and summarized in

Table 6.4. As expected, the suppression factor is improved for shorter wavelengths where the roughness amplitudes are the most suppressed. For wavelengths above 200 μm, where the adjustment is only 2.6% or less, the suppression factor is not significantly changed.

Wavelength	Raw Suppression Factor	Time-of-Flight Adjusted Suppression Factor
$\lambda < 40$ μm	$2.6 - 9.1$	$4.6 - 16.5$
40 μm $< \lambda <$ 60 μm	$5 - 12.5$	$6.7 - 17.9$
60 μm $< \lambda <$ 200 μm	$20.6 - 34.3$	$23 - 37.8$
$\lambda > 200$ μm	$14.5 - 21.9$	$14.6 - 22.2$

Table 6.4: Comparison of the suppression factor for different wavelengths, with (Fig. 6.16(c)) and without (Fig. 6.16(b)) the time-of-flight amplitude adjustment. The values shown here are taken from the 3-point moving average of the suppression factor data.

6.7.5 Comparison with Other Groups

Given the lifespan of atom chip technology [12], there has been much progress in the use of modern micro-fabrication techniques which decrease the size of chip wire defects. Other materials, such as graphene [89] or videotape [90], have also been investigated for their role in reducing potential roughness effects. These mechanisms are purely based on the quality or material of the atom chip, and are still subject to the physics behind roughness, as described in Sec. 6.2. The ACZ trap, on the other hand, relies on atomic selection rules to suppress potential roughness, and should therefore enhance the suppression achieved with improved manufacturing.

Time-Averaging Out the Roughness via kHz Current Modulation

The work in Ref. [91] built on the proposal in Ref. [99] which found the roughness maxima and minima flipped when reversing the direction of the wire current and bias magnetic field. By modulating these fields at frequencies of tens of kHz, the roughness features would get time-averaged away, leaving a smooth magnetic trap. With this mechanism, they observed a RMS suppression factor of 4-7 with respect to the static DC trap. By modeling the center-of-mass oscillations for atoms in a rough potential, an upper bound of 14 was estimated for the suppression factor in the modulated trap [98].

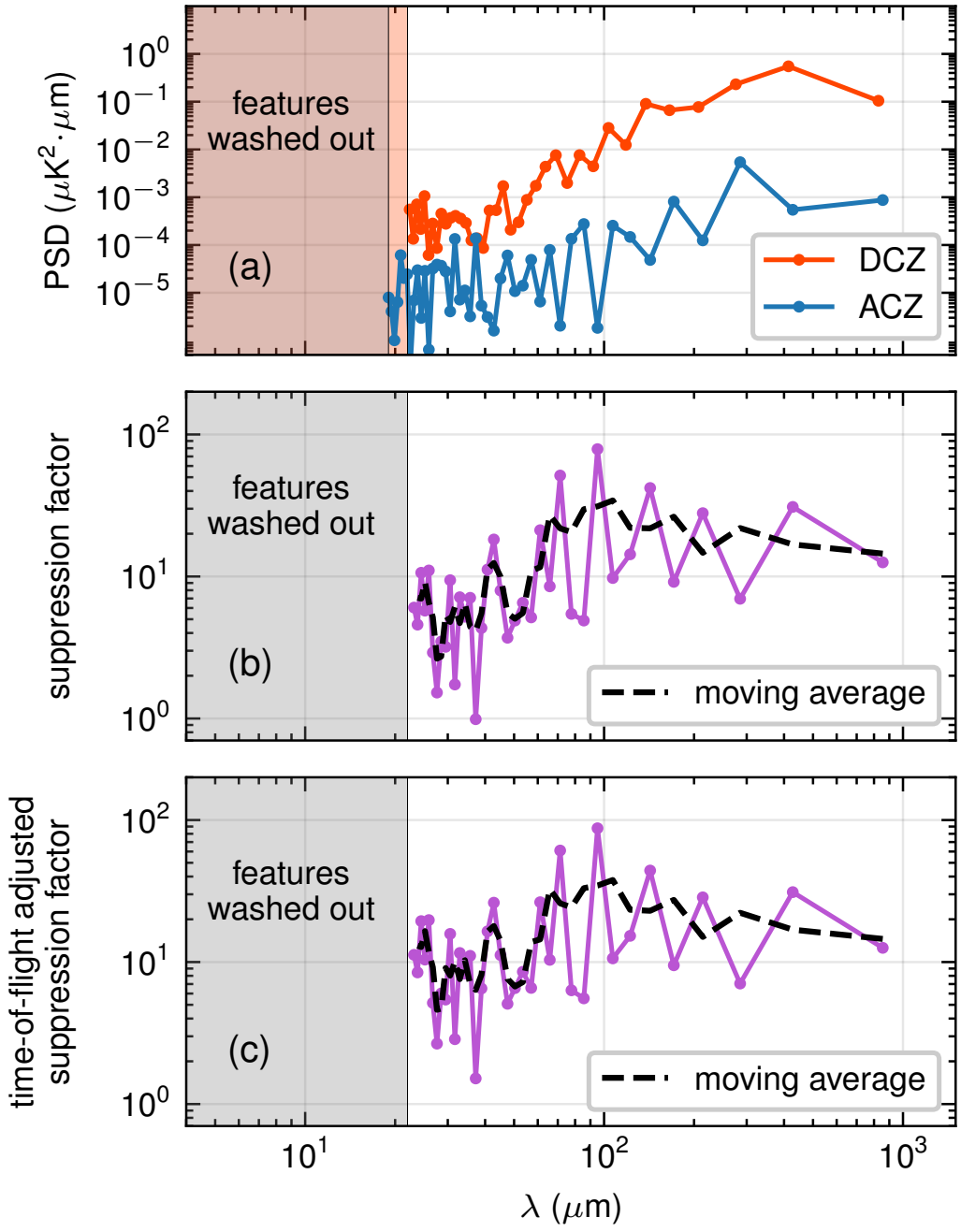

Figure 6.16: (a) Power spectral density of the ACZ and DCZ potential roughness, calculated using Eq. 6.9. The shaded region corresponds to length scales below the wavelengths for which roughness features get washed out due to thermal motion. (b) Suppression factor in the ACZ trap as a function of wavelength, given as the square root of the ratio of the DCZ and ACZ FFTs. A 3-point moving average is added for visualization. (c) Suppression factor in (b) adjusted to account for time-of-flight effects (see text for details). A 3-point moving average is added for visualization.

Adiabatic RF Potentials

Ref. [100] characterizes the longitudinal behavior of an adiabatic RF potential, formed using the DC magnetic field from a Z-shaped wire with RF fields produced by neighboring chip wires. Past a certain critical frequency, the adiabatic trap splits into two wells, and the dressed states become a superposition of the bare m_F states. This effectively averages out the roughness caused by defects in the Z-wire, as bare states with opposite m_F inversely react to the changing longitudinal DC magnetic field. By working at larger dressing frequencies, the sensitivity to the roughness in the DC current carrying wire goes to zero. In practice, they were able to observe a suppression factor of 10, limited by trap loss at high dressing frequencies.

AC Zeeman Suppression

Distinct from the previous two mechanisms, the RF AC Zeeman (ACZ) potential is formed using the gradient in the RF field produced by a pair of atom chip wires carrying MHz frequency currents. The detuning in this case is constant, set by the strength of the quantizing DC magnetic field. For the $F = 2$ ground-state hyperfine manifold of ^{87}Rb, the ACZ potential only responds to the transverse (xy) fields via the circularly polarized $B_- = B_{RF,x} - iB_{RF,y}$. Defects in the atom chip wire results in the generation of additional $B_{RF,z}$ components, which to not contribute to the trapping potential due to selection rules. The defects act to modify the transverse RF magnetic field; however, this effect is substantially smaller than the longitudinal (z) field component.

In Table 6.5, we compare the suppression measured in the ACZ trap to other physics-based suppression techniques. Both other methods [91, 100] also highlight prolonged axial oscillations made possible by the smoother trap. In the ACZ trap roughness experiment presented here, we use the gradient push coil to limit axial motion, but note that we have observed $1/e$ decay times of a few seconds in the RF ACZ trap when no compensation is done.

Group	Trap	Suppression Mechanism	Measured Suppression Factor
Ref. [91]	kHz modulated DC trap	Time-averaging via current modulation	4-7
Ref. [100]	Adiabatic RF potential	Internal state averaging	10
This work	AC Zeeman potential	Atomic selection rules	RMS: 1.8 - 13.8 Pk-Pk: 2.6 - 14.2 PSD: 2.6 - 34

Table 6.5: Comparison of the AC Zeeman potential roughness suppression and other physics-based suppression mechanisms.

6.8 Vary Trap Height

We investigate how the roughness scales with distance to the chip by changing the relative phase difference between the trapping wires, ϕ, which shifts vertical position of the atoms as $h_{trap} = d\tan(\phi/2)$, where $d = 100$ μm is the center-to-center wire separation (see Sec. 5.4) [17], as well as changes the trap frequency. After loading into the canonical trap at ≈90 μm (see Fig. 6.11), the phase is linearly ramped from $\phi = 120°$ to a final value over 50 ms. The atoms are then held in the new trap for 200 ms to thermalize. As before, the trap is then shut off and the atoms drop for 1.5 ms before imaging. Absorption images of the atoms at the different trap heights are shown in Fig. 6.17. We only report roughness down to a trap height of 50 μm, as the cloud begins to get significantly cut off by the chip as the trap height is decreased. This should not alter the roughness, except to decrease signal-to-noise, since imaging a fraction of the atoms will only add an offset to the potential via Eq. 6.4.

The images are given a custom vertical region-of-interest and are converted into potentials via Eq. 6.4, with a spatial filter applied to each potential using a wavelength cutoff according to the atom temperature (see Sec. 6.6). The resulting trap potentials and roughness are shown in Fig. 6.18. As expected, bringing the atoms closer to the chip enhances the roughness effects, allowing us to more clearly resolve the shape of the roughness

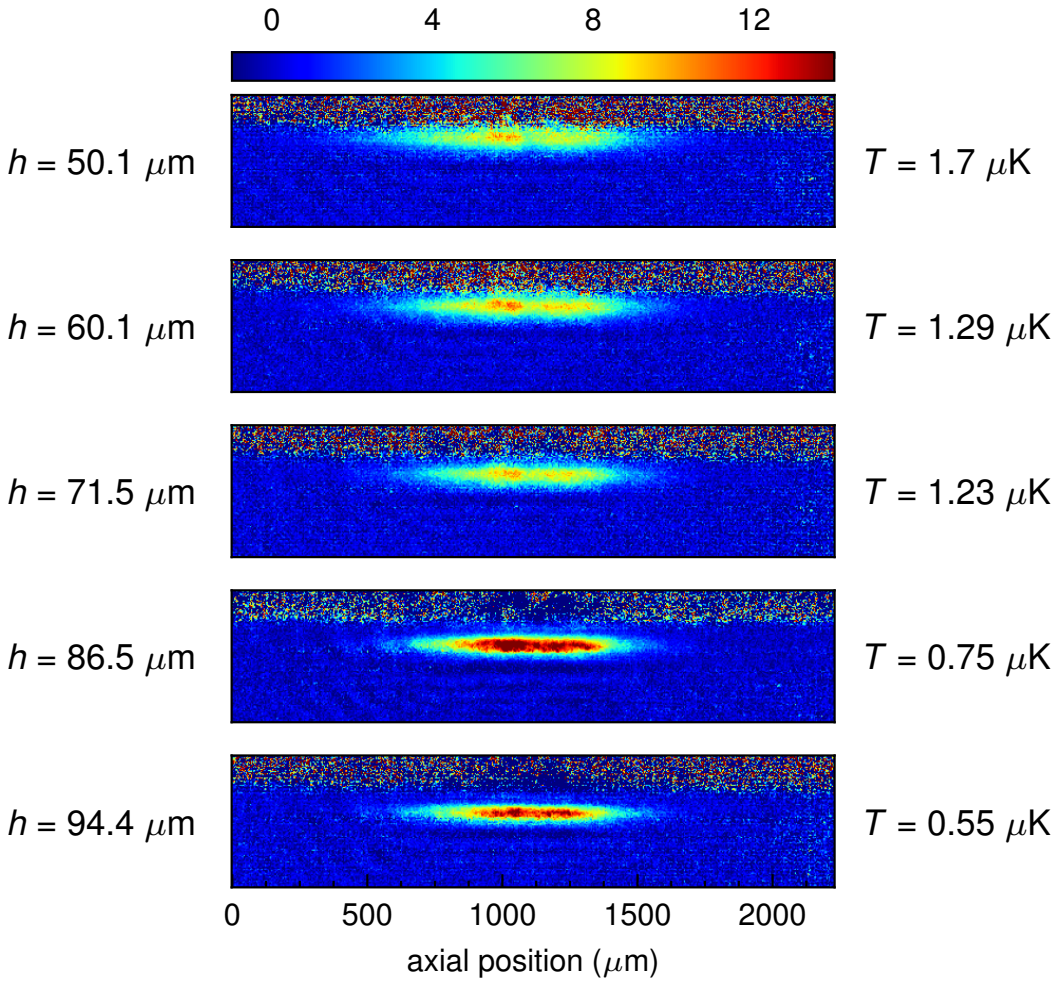

Figure 6.17: Absorption images of atoms in the RF ACZ trap at different distances from the chip. Plotted is the number of atoms per pixel (1 pixel = 4.65 μm). The atoms are released from the trap and drop for 1.5 ms before the image is taken. Each picture is an average of 150 shots, except for the image at $h = 86.5$ μm, which is taken from Fig. 6.11 with 300 shots.

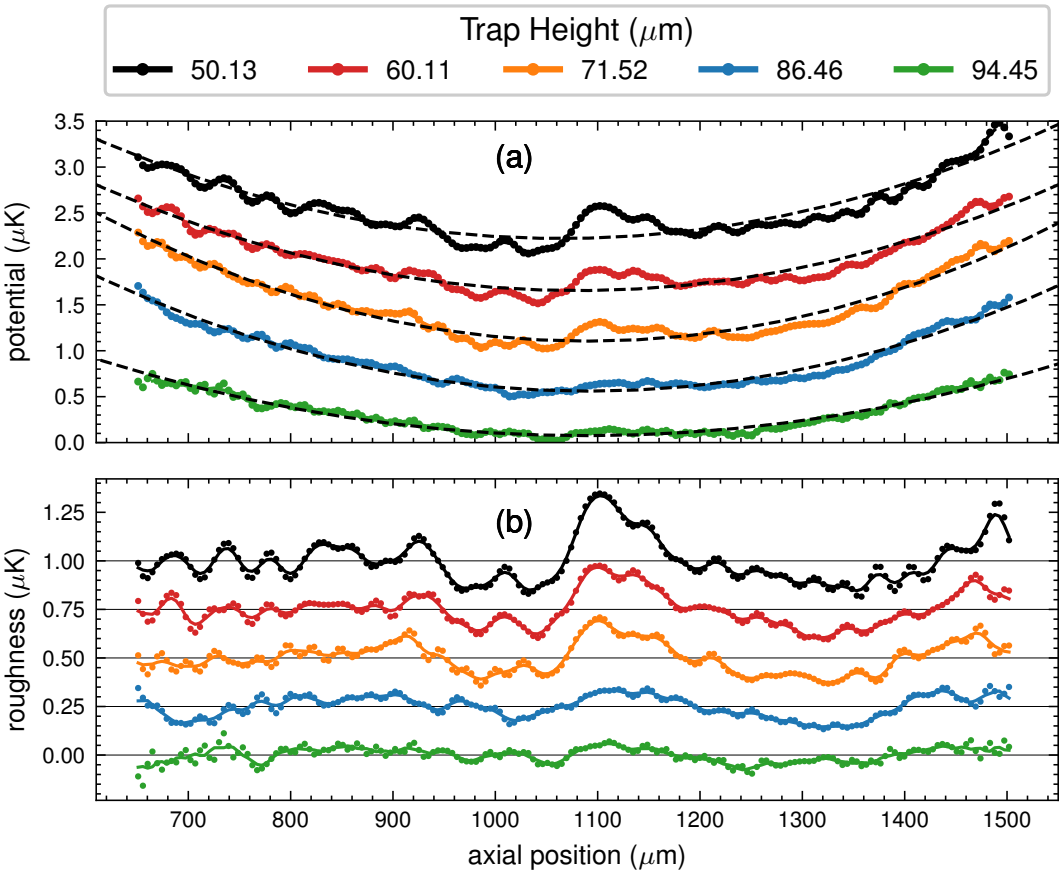

Figure 6.18: (a) RF ACZ axial trap potentials measured at different trap heights. The RF frequency is kept constant at 20.175 MHz for all traps. A harmonic fit (black dashed lines) is applied to each potential. A 0.5 μK offset is added to each set of data for easier visualization. (b) Extracted potential roughness obtained by subtracting the harmonic fit from the data. A 0.25 μK offset is added to each set of data for easier visualization.

features. For example, the main feature in the canonical trap at ≈1,100 μm, which we evaluated in Fig. 6.14, is actually made up of two bumps, the leftmost of which is located more closely with the DCZ bump at 1095 μm. The rms and peak-to-peak roughness scale linearly with trap height (see Fig. 6.19), increasing by a factor of 2.9 and 3.6, respectively, as the trap height is decreased by roughly half. Linear fits give slopes of -1.6 ± 0.2 nK/μm and -7.7 ± 0.6 nK/μm for the rms and peak-to-peak data, respectively. Extrapolating to closer atom-surface distances, we find these values remain below 0.2 μK (rms) and 0.86 μK (peak-to-peak). Since our atom chip is known to contain defects [18], these values should improve with better manufactured chips, as the ACZ suppression improves for smaller defect sizes [58]. Using the bump model in Fig. 6.4(a), we find that the amplitude of the

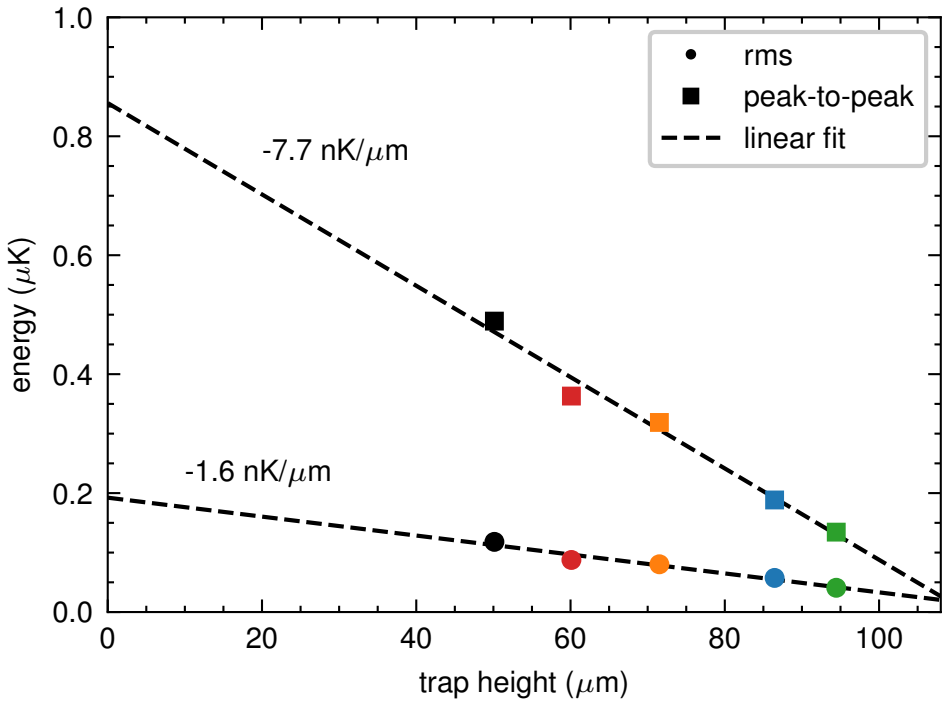

Figure 6.19: RMS and peak-to-peak roughness in the ACZ trap at different trap heights. Linear fits give slopes of -1.6 ± 0.2 nK/μm and -7.7 ± 0.6 nK/μm for the rms and peak-to-peak data, respectively.

ACZ roughness bump increases like $h^{-3.2}$, where h is the trap height. Doing a similar fit to the data in Fig. 6.19, we get that the rms and peak-to-peak roughness scale as $h^{-1.4}$

and $h^{-1.7}$, respectively.

We plot the spectral densities of the roughness in Fig. 6.20. As the atoms are brought closer to the chip, we find that, in general, the PSD for all wavelengths is increased. Moreover, we observe more strongly spiked features in the PSD at lower spatial wavelengths for closer atom-surface distances. For a given trap height, h_{trap}, we expect roughness features with wavelengths much smaller than h_{trap} tend to get averaged out, making most of the contributions to the PSD from length scales $\lambda \gtrsim h_{trap}$ [83, 86, 84, 81, 90]. In the models presented in Sec. 6.4 and Ref. [58], however, we see that the ACZ trap distortion is less wide than in the DCZ case, which may make features at $\lambda < h_{trap}$ visible in the potential.

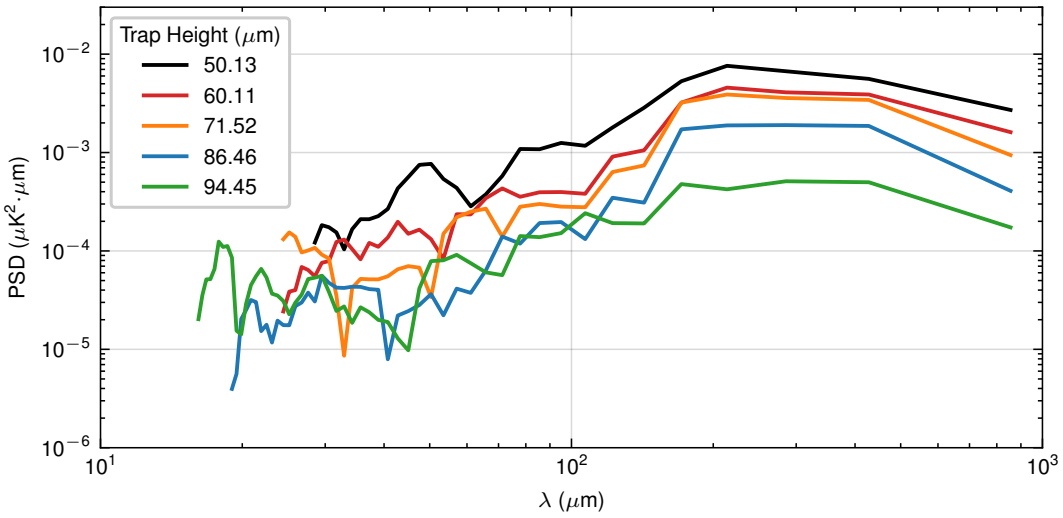

Figure 6.20: Power spectral density (PSD) of the ACZ potential roughness for different distances to the chip, evaluated using Eq. 6.9. Shown is a 4-point moving average of the PSD. Features below the thermal cutoff wavelength are omitted.

6.9 Vary RF Frequency

The other parameter we can play with is the RF frequency, f_{RF}. This primarily affects the ACZ trap frequency [16], as well as mixes the different bare states. Using the triangular bump model in Ref. [58], we found that the detuning has little to no effect on the ACZ trap

distortion for the same trap height and transverse trap frequency. The results presented here stem, then, solely from the change in trap frequency, which is expected to enhance the roughness. For the range of RF frequencies we explore here, atoms at the bottom of the trap are in the far-detuned limit of the ACZ potential, i.e., $|\delta| >> |\Omega|$, and so the trapped $|{+}{+}\rangle$ is primarily made up of the $|2, +2\rangle$ bare state. For example, with a 1 μK trap depth and detuning $\delta = 2\pi \times 0.5$ MHz, the maximum Rabi frequency is $|\Omega| \simeq 2\pi \times 0.2$ MHz. At 20.4 MHz, the highest RF frequency used here, the $|2, +2\rangle$ state makes up about 90% of the $|{+}{+}\rangle$ state. We observed a drop in atom number when attempting to go closer to resonance, as the other bare states get more mixed into the $|{+}{+}\rangle$ state. While still trapped transversely by the ACZ potential, the other bare states are more weakly trapped ($m_F = +1, 0$) or completely anti-trapped ($m_F < 0$) longitudinally by the natural Ioffe field curvature. This consequently limits the range of RF frequencies we can look at to 20-20.4 MHz. To look at roughness in other m_F states, such as the DC untrappable $m_F = -2$, we would need the use of a microwave lattice or optical dipole trap, as in Ref. [16]. Unfortunately, the previous dipole trapping laser broke relatively early on in this experiment, making the $m_F = -2$ state roughness a future study.

To investigate the role of RF frequency on the roughness, we linearly ramp f_{RF} from the canonical value of 20.175 MHz to a final frequency value over 50 ms. The set phase between trapping wires is held constant at $\phi = 120°$, corresponding to a trap height of 86.5 $\pm$ 5.5 μm. Fig. 6.21 shows absorption images of the atoms across detuning after a 1.5 ms time-of-flight. We expect the height to change by less than 0.5 μm due to the natural variation in the phase offset between the U and Z wires as the RF frequency is changed (see Sec. 5.7). Our model of the ACZ trap predicts the atoms are brought $\sim$5 μm closer to the chip as the RF frequency is brought from 20-20.4 MHz, as the tighter trap becomes less affected by gravitational sag. Analyzing the vertical profiles of the absorption images of the atoms after the 1.5 ms time-of-flight, we found the vertical separation to be twice that predicted by the model, resulting in a $\sim$10 μm trap height change over the frequency range (see Fig. 6.22), though it is unclear whether this manifests itself while the atoms

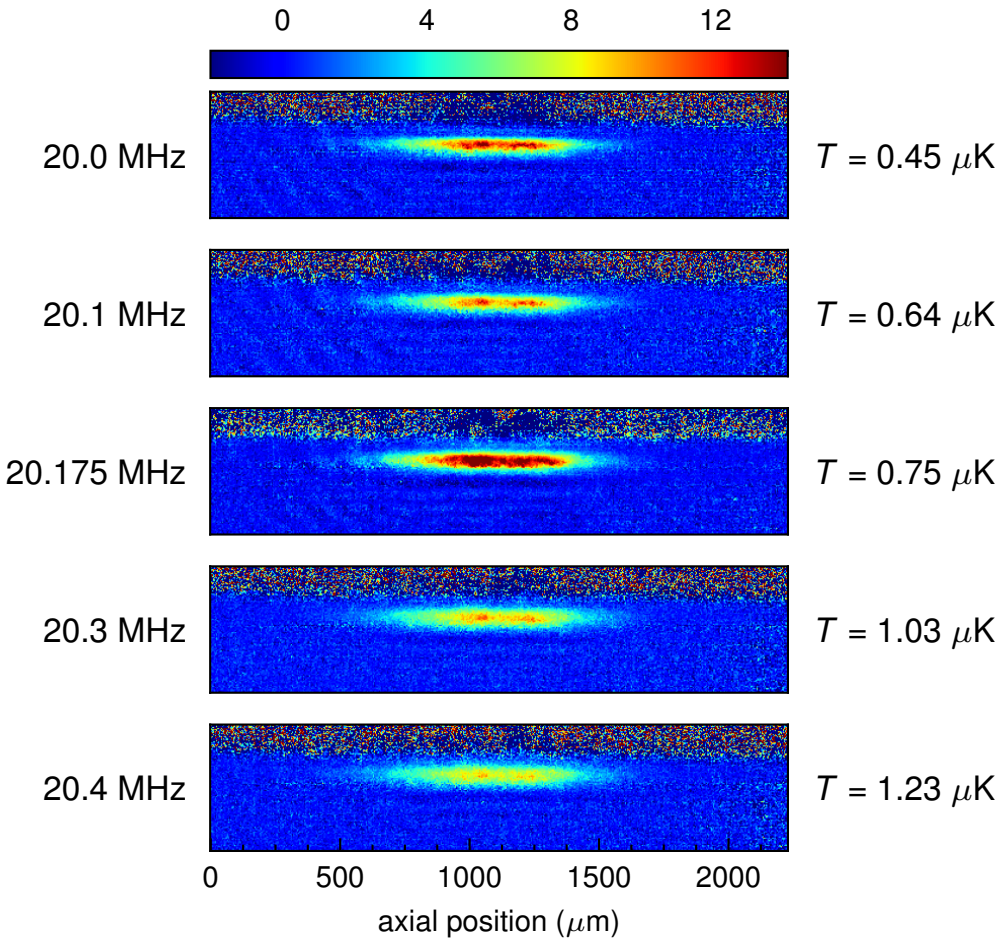

Figure 6.21: Absorption images of atoms in the RF ACZ trap at different detunings from resonance. The atoms are released from the trap and drop for 1.5 ms before the image is taken. Each picture is an average of 150 shots, except for the image at 20.175 MHz, which is taken from Fig. 6.11 with 300 shots. Temperature measurements were obtained using the time-of-flight technique.

are in the trap or in free-fall. A possible explanation for this discrepancy could come

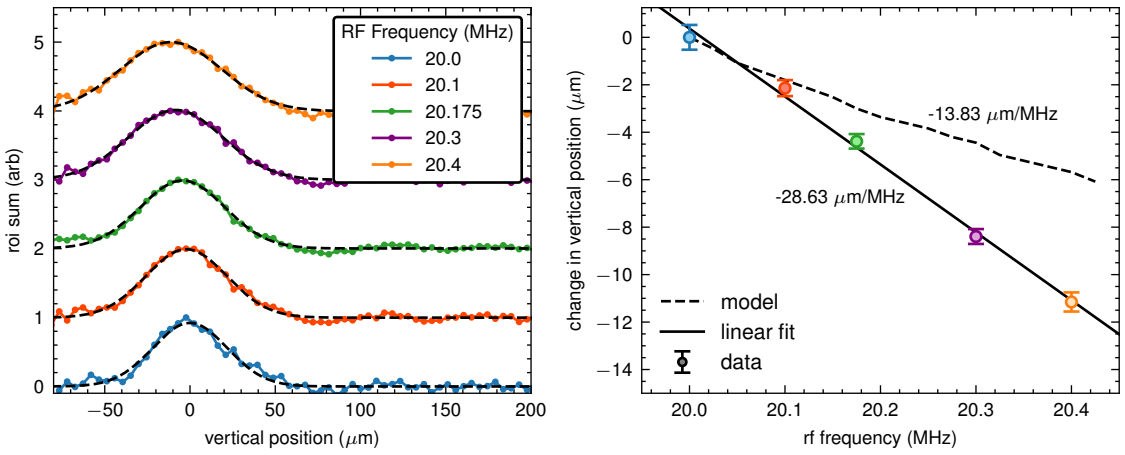

Figure 6.22: Shift in the vertical position of the ACZ potential at different RF frequencies. (Left) ROI sums of the data in Fig. 6.21 along the axial direction fit to a Gaussian, given by the dashed black lines. The data are normalized to their maxima and given an offset for visualization. (Right) Measured shift in vertical position compared to the two-wire model. The shift is referenced to the position at 20 MHz. The model uses $|I_U| = 148$ mA, $|I_Z| = 163.5$ mA, and a phase difference of 120°. Error bars for the data points are the 1-σ errors from the fits.

from the known transverse field gradient from the Ioffe coil pair, previously observed when measuring the RF ACZ force [16]. This gradient, measured to be 141.5 (mG/cm)/I_{Ioffe}, pushes the $m_F > 0$ states away from the chip while pulling the $m_F < 0$ states closer. Since atoms in the trap are primarily in the $|2,2\rangle$ state, we expect them to all be affected the same amount during the time-of-flight, where $I_{Ioffe} = 2.5$ A, by which the gradient only pushes the atoms by $\simeq$0.25 μm during the 1.5 ms free-fall. The gradient is similarly too weak to significantly shift the trap position, only altering it by $\simeq$ 0.4 μm for the 260 Hz trap frequency and $I_{Ioffe} = 11.29$ A. As the trap gets tighter closer to resonance, this shift is even less. Other culprits for this may be the gradient push coil, which certainly has transverse, but unmeasured, curvature, or something happening during the free-fall. While we do not provide a full explanation for this, we note that the study on detuning features a $\approx$5-10 μm change in trap height; however, this does not appear to be the dominant effect in the observed roughness.

The absorption images of the atoms are converted into a potential via Eq. 6.4 and

a spatial filter is applied to remove high-frequency spatial noise and ignore features that are washed out due to thermal motion (see Sec. 6.6). We plot the potentials at different detunings in Fig. 6.23(a). The potentials are then fit with a harmonic, the residuals of which give the trap roughness (Fig. 6.23(b)). As the trap is brought closer to resonance,

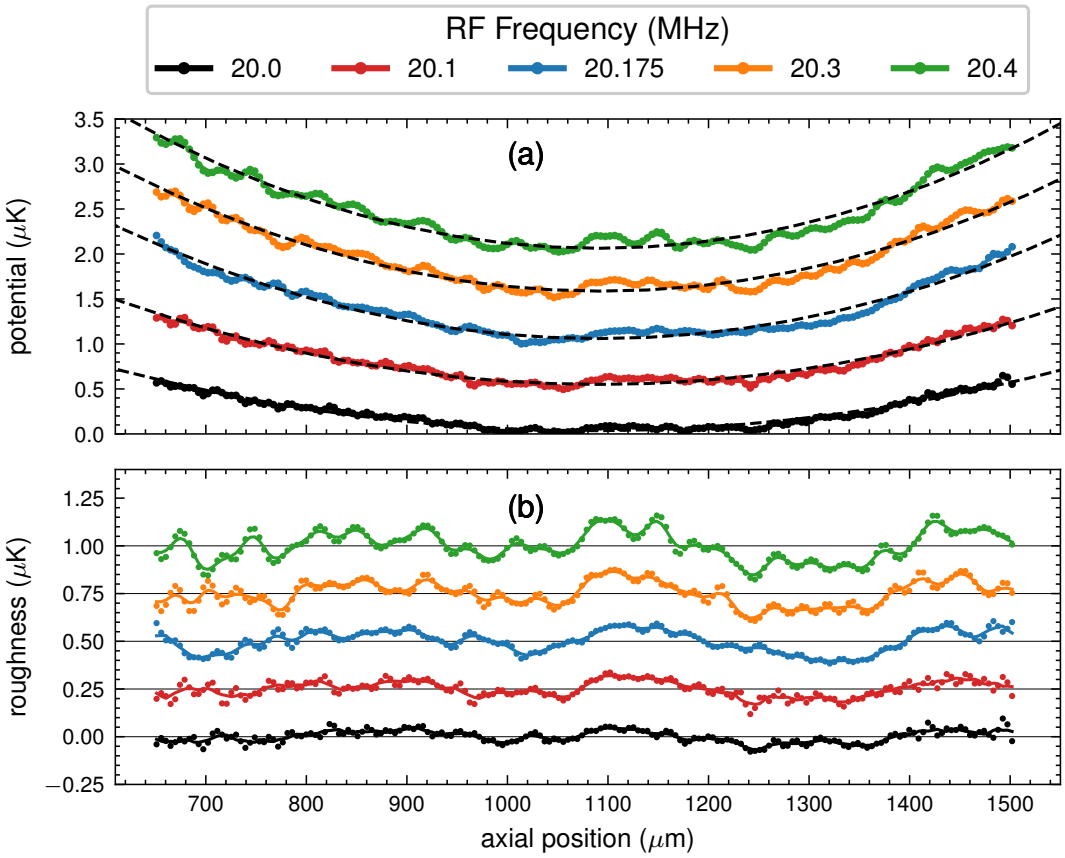

Figure 6.23: (a) RF ACZ axial trap potentials measured at different RF frequencies. A harmonic fit (black dashed lines) is applied to each potential. A 0.5 μK offset is added to each set of data for easier visualization. (b) Extracted potential roughness obtained by subtracting the harmonic fit from the data. A 0.25 μK offset is added to each set of data for easier visualization.

we observe an enhancement of the potential roughness effects. As with the trap height study, the feature at 1,100 μm splits into two distinct bumps. The rms and peak-to-peak values of the roughness are plotted in Fig. 6.24. Both values display a linear trend with RF frequency, with slopes of 0.11 μK/μm (rms) and 0.43 μK/μm (peak-to-peak). For a quantizing field strength of $B_{DC} = 29.6$ G, resonance is at ≈20.72 MHz. A clear definition

of resonance here is a little tricky, as the splitting between m_F states is not equal, differing by roughly 125 kHz. Extrapolating these values to resonance, we see they stay under $\simeq 0.425$ μK (peak-to-peak) and $\simeq 0.1$ μK (rms).

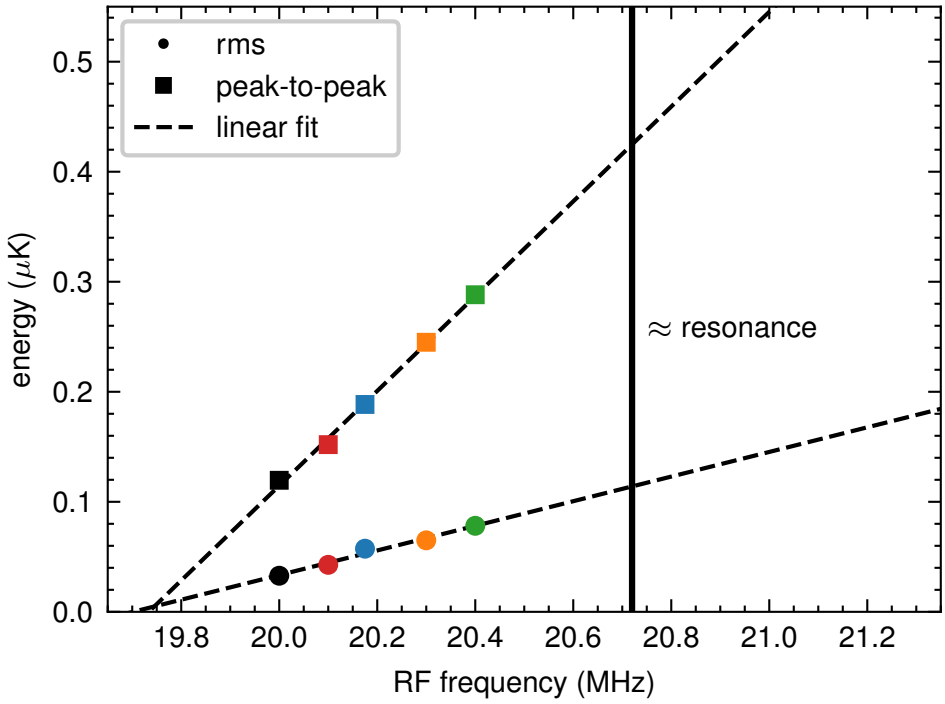

Figure 6.24: RMS and peak-to-peak roughness in the ACZ trap at different RF frequencies. Linear fits give slopes of 0.11 μK/μm and 0.43 μK/μm for the rms and peak-to-peak data, respectively. The vertical line gives the approximate resonance frequency of $B_{DC} \times 0.7$ MHz/G = 29.6 G $\times$ 0.7 MHz/G = 20.72 MHz.

The spectral density of the roughness at different RF frequencies is plotted in Fig. 6.25. Two peaks emerge in the PSD at $\lambda \approx 35$ μm and $\lambda \approx 55$ μm when the RF frequency is brought to $f_{RF} \geq 20.3$ MHz. Similar spikes at these wavelengths were also seen as the trap was brought closer to the chip (see Fig. 6.20), albeit at $\simeq$35 μm closer, indicating that the predicted 5-10 μm height change with frequency is not the dominant roughness mechanism here. For $\lambda \gtrsim 100$, the PSD at these frequencies is roughly the same as at $f_{RF} = 20.175$ MHz.

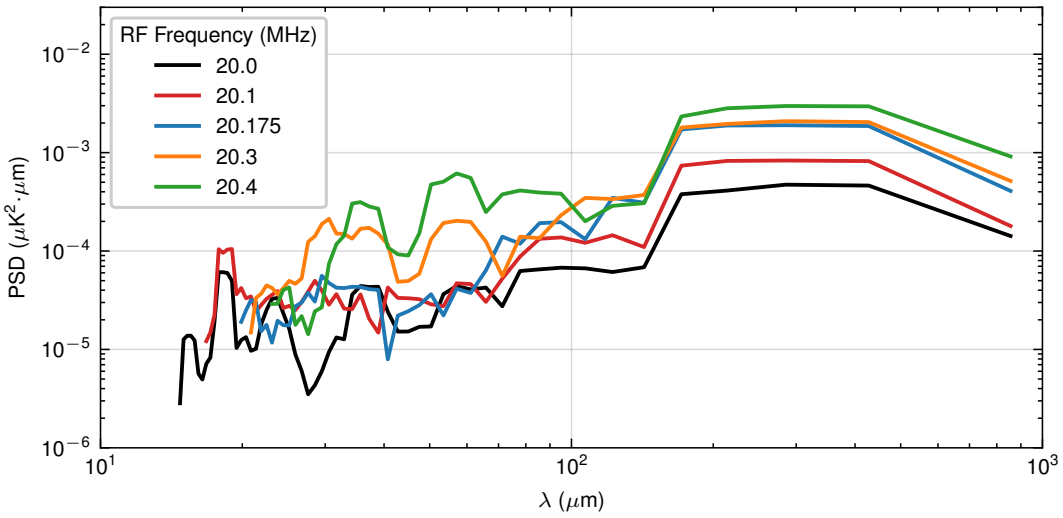

Figure 6.25: Power spectral density (PSD) of the ACZ potential roughness for different RF frequencies, evaluated using Eq. 6.9. Shown is a 4-point moving average of the PSD. Features below the thermal cutoff wavelengths are omitted.

6.10 ACZ Roughness at Different Resonance Frequencies

As demonstrated in Chapter 5, we can vary the resonance frequency, i.e., the spacing between m_F levels, while maintaining a constant detuning in the ACZ trap by simultaneously sweeping the quantizing field strength and RF frequency. This procedure should produce identical ACZ traps (same detuning, trap frequency, trap height), albeit at different resonant frequencies. This allows us to look for any frequency dependent effects on the roughness caused by, for example, AC currents coupling to chip wires besides the two used for trapping, an effect seen in both simulation and prototype circuits in our lab [17, 101].

After trapping in the canonical ACZ trap with resonance frequency of roughly 20 MHz, we shift into a trap with resonance of either 13 or 41 MHz. We then average over 200 absorption images and extract the potentials using Eq. 6.4. The atom temperatures are $T_{\{13,20,41\}} = \{0.78, 0.75, 0.56\}$ μK. The temperature of the 41 MHz trap is lower due to the loading sequence, in which atoms get pushed away from the trap when increasing the RF frequency (see Fig. 5.11(b)) before the relative phase is shifted to bring the atoms back to the same height as the 20 MHz trap. Meanwhile, for the 13 MHz trap, we load the

20 MHz trap slightly farther from the chip, such that it reaches the canonical trap height when brought to 13 MHz.

Figure 6.26 shows the measured trapping potentials and roughness for each trap, along with their spectral densities. Looking at the RMS and peak-to-peak roughness (see Table 6.6), we see no significant differences between the three traps, and there are no new significant roughness features that appear as the resonance frequency is changed. Similarly, the PSDs show similar behavior between the different traps. This gives confidence that we are not seeing significant effects from any extraneous coupling of the AC currents to other atom chip elements, so the roughness we observe is due to the U and Z trapping wires.

	13 MHz Trap	20 MHz Trap	41 MHz Trap
RMS Roughness (nK)	45.5	57.49	42.0
Pk-Pk Roughness (μK)	0.16	0.19	0.15

Table 6.6: RMS and peak-to-peak (Pk-Pk) roughness for the RF ACZ trap at different resonance frequencies (see Fig. 6.26).

6.11 Conclusions

This chapter contains the primary experimental work of this thesis: the demonstration of atom chip potential roughness suppression using an AC Zeeman (ACZ) trap. Compared to an identical DC Zeeman trap using the same atom chip wires, the ACZ trap was no longer fragmented. We furthermore found a linear scaling in the roughness as the trap was brought closer to the chip or closer to the atomic resonance while the cloud remained unfragmented. The chapter concluded by looking at the ACZ trap roughness at different atomic resonance frequencies, spanning nearly 30 MHz. The reduced potential roughness in the ACZ trap will enable experiments in which the atoms are brought close to the chip, such as sub-mm gravity and the Casimir-Polder force, as well as tighter traps for 1D confinement. Using a weak optical dipole laser for axial endcapping [16] would allow investigation into potential roughness for atoms in DC untrappable states, i.e. $|F = 2, m_F = -2\rangle$ and $|F = 1, m_F = 1\rangle$, and is an area of future experiments.

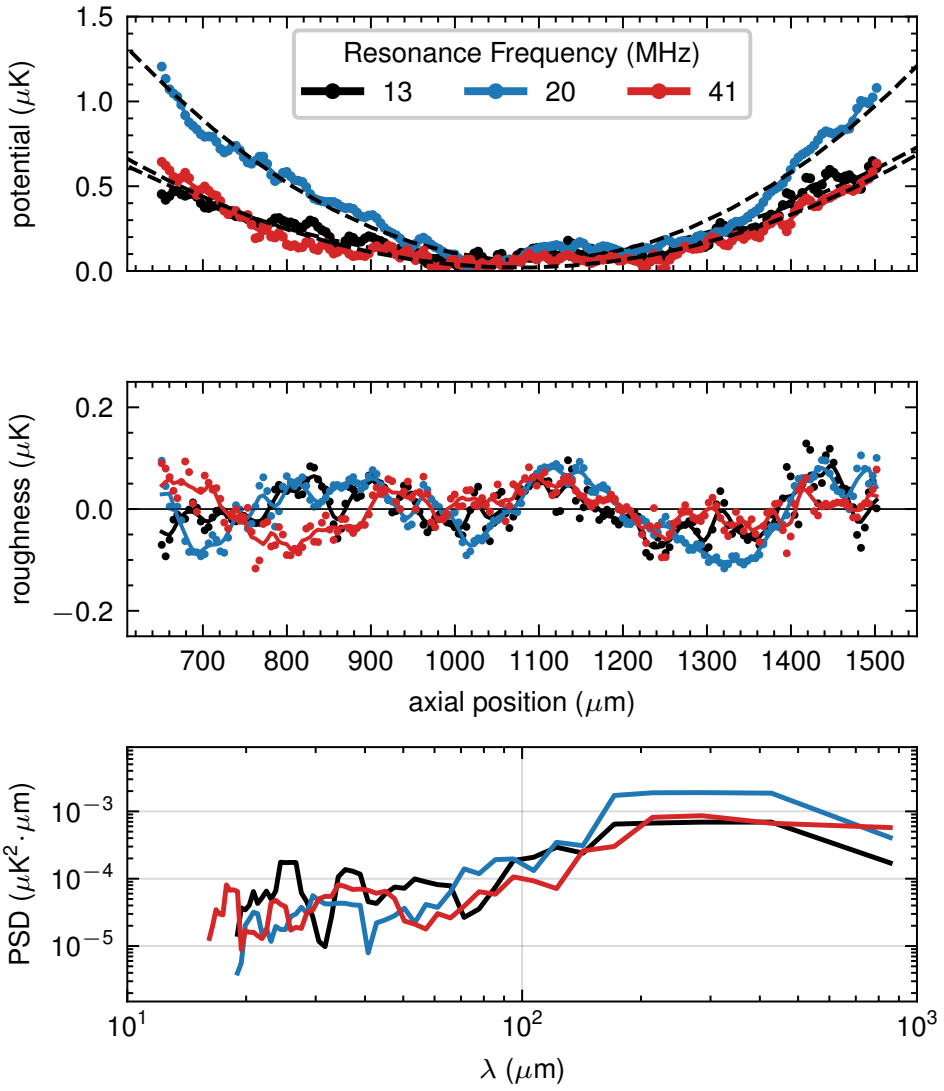

Figure 6.26: Potentials (top row), roughness (middle row), and spectral density (bottom row) for atoms trapped in an RF ACZ trap with different resonance frequencies, averaged over 200 absorption images. The potentials are fit to a second degree polynomial (black dashed line). The fit is subtracted from the data in the fitting region to obtain the roughness. The solid lines in the roughness data are five point moving averages added for easier visualization.

Chapter 7

Microwave Atom Chip

While the lab's existing atom chip can support ACZ trapping using tens of MHz RF currents, this approach uses intra-manifold transitions forming a system of five or three levels. The ultimate goal of the lab is to generate spin-specific traps using an effective two-level system, which requires accessing inter-manifold hyperfine transitions in the microwave (several GHz) regime. Previous work [102] found that the existing chip has poor microwave coupling, only transmitting 37 mA rms from a 3.3 W amplifier at 6.8 GHz, yielding an effective impedance of 2400 Ω [16]. Most of the power sent to the chip gets reflected due to the impedance mismatch between the chip and the 50 Ω cable connecting it to the source and amplifier. This greatly limits our ability to perform μw ACZ trapping, requiring massive amounts of power for even minimally acceptable trap depths. Moreover, reflections can result in the formation of a "natural" ACZ lattice on the atom chip wires, limiting atom interferometry. In order to advance the lab's ACZ trapping capabilities, a new atom chip has to be made.

This chapter covers the work done to develop such a novel microwave atom chip based on parallel microstrip transmission lines. Section 7.2 introduces the microstrip as the building block of the atom chip, with discussions on material considerations and the skin and proximity effects. We then move onto the design and simulation of the atom chip in Sec. 7.3, covering ACZ traps formed using two- and three-microstrip models. The final

chip design, the UZU chip, is also covered in this section. Section 7.4 covers the design and simulation of how to operate the new chip in "DC mode". After the simulation stage, we proceed to the initial stages of manufacturing. Section 7.5 covers experiments done to determine the decay time of eddy currents in conductors of different thicknesses and conductivities, which helped select the backing structure/ground plane of the atom chip. With that selected, we had the samples diamond turned before the substrate deposition, which is the topic of Sec. 7.6. We then move on in Sec. 7.7 to methods of characterizing the dielectric constant of the atom chip substrate, using three distinct methods. Finally, we end with a brief discussion of generating a microwave ACZ trap with the lab's current chip in Sec. 7.8.

7.1 Design Goals for the New Atom Chip

The primary purpose of a microwave atom chip is to generate microwave and RF near fields with strong enough gradients to generate a substantial ACZ trapping force. In designing such a novel atom chip, we must do our best to meet some physics and engineering design goals:

- In the near-field, the spatial scale for field variations is determined by the chip's wire spacings and wire widths (not the wavelength), so the chip's basic architectural building blocks should have small wire widths and be compatible with small inter-wire spacings.

- The building block of the chip must be able to support broadband signals (DC–>10 GHz) for ACZ trapping of different atomic species, namely Rb and K, as well as the operation of an AC Stark microwave lattice for axial confinement and translation. This will require the chip to maintain a 50 Ω impedance in this frequency regime as to be compatible with standard microwave components.

- We intend on sending large amounts (up to 20 W) of microwave power onto the chip

to generate strong ACZ traps. As such, the atom chip material must have good thermal conductivity to dissipate heat effectively.

7.2 Microstrip Transmission Line Building Block

In this thesis, we present chip trap designs based on microstrip transmission [103] because they have two key features: (1) microstrips can have relatively small trace widths and spacings, and (2) their simple and extended microwave field mode is well suited to engineering and generating trapping potentials. In contrast, while co-planar waveguide (CPW) transmission lines have been used in microwave atom chips [104, 105], their compact and double-lobed field structure makes trap design more challenging. Alternatively, the negative index of refraction metamaterial lenses represent a tantalizing prospect for generating compact microwave trapping structures but are beyond the scope of this thesis [106].

Microstrip transmission lines consist of a conducting trace on a planar dielectric substrate with a conducting ground plane on the opposite side. Figure 7.1 shows the layout and dimensions of the 50 Ω microstrip that is the basic building block for the chip trap designs in this thesis. We choose a 50 Ω impedance in order to facilitate impedance matching with the 50 Ω standard used in microwave cables, amplifiers, and sources. In order to achieve both a 50 Ω impedance and a narrow trace width, a thin substrate with a high dielectric constant is required [107, 108]. Aluminum nitride (AlN, dielectric constant $\epsilon_r = 8.9$) additionally has a high thermal conductivity to facilitate heat dissipation at high microwave power. To realize the desired impedance at 6.8 GHz with a 50 μm thick AlN substrate, we find that a 54 μm wide copper trace optimizes the transmission of microwaves through the microstrip [14]. This microstrip was simulated to be 50 Ω past 20 GHz [17].

The microwave field mode propagating through the microstrip is quasi-TEM (transverse electro-magnetic), where the "quasi" is due to a small longitudinal electric component (generally negligible) that arises from the vacuum–substrate interface. Transverse here refers to the field in the xy-plane in Fig. 7.1. The thin-substrate microstrip of Figure 7.1

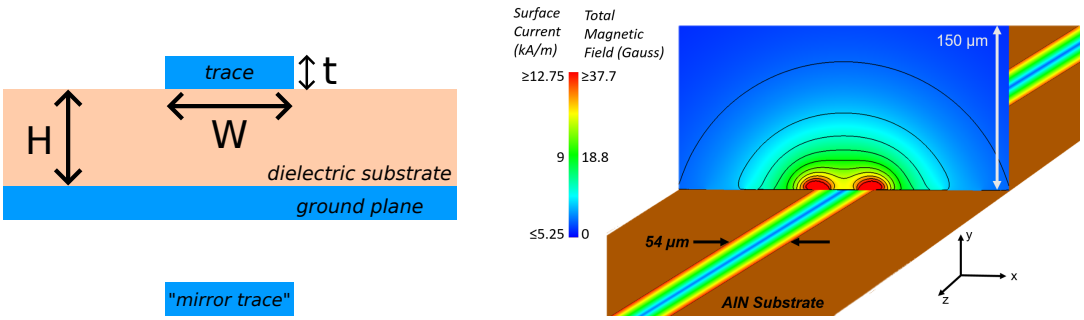

Figure 7.1: Single microstrip with 50 Ω impedance. (Left) Cross-sectional view of a single microstrip. Due to the ground plane, we can utilize image theory, in which a "mirror" trace carries equal but opposite current to the microstrip. (Right) FEKO simulation of the microstrip (left) showing the current and magnetic near field for 12.5 W at 6.8 GHz, corresponding to a microwave current of roughly 0.35 A_{rms}. The 50 Ω line is made from a $w = 54$ μw wide trace on $H = 50$ μm of aluminum nitride ($\epsilon_r = 8.9$). Due to the AC skin effect, the current density is largest along the edges of the trace. The microstrip was meshed to the width of the trace divided by 4 to show this effect. Figure adapted from [17].

has good broadband performance (i.e., largely frequency independent), which extends past 20 GHz according to our numerical simulations. Furthermore, a single microstrip can support multiple, simultaneous, independent microwave near fields at different frequencies, with each one targeted to a different spin state.

The basic structure of the microstrip's field mode can be understood to arise from the current and charge on the trace and from the opposing current and charge on the "mirror trace" expected from the method of images (see Figure 7.1): a static analysis yields a decent estimate of the magnetic and electric near fields (for distances much smaller than the wavelength) and can be converted to a time-dependent field by multiplying by $e^{i\omega_{\mu w}t}$, i.e. $B_{\mu w} = Be^{i\omega_{\mu w}t}$ and $E_{\mu w} = Ee^{i\omega_{\mu w}t}$, where $\omega_{\mu w}$ is the microwave frequency.

Numerical simulations are needed to obtain accurate estimates of the microstrip's near-field mode. In particular, at high frequencies, the current tends to hug the trace edges due to the AC skin effect [95], which in turn tends to modify the near field at distances within the trace width. Furthermore, the proximity effect tends to modify the current distribution in neighboring traces (and image traces): in a single microstrip, the current hugs the bottom of the trace (it is attracted to the ground plane); for neighboring mi-

crostrips, in-phase currents tend to repel each other, while 180° currents tend to attract. Furthermore, inductive and capacitive coupling between neighboring microstrips can also modify their currents and phases significantly (the current can "tunnel" from one trace to another via a Maxwell displacement current [101]). Here, we use commercial electromagnetic simulation software (FEKO by Altair, HFSS by Ansys, and Sonnet) to model the microstrip currents and near fields.

Even with these additional factors, there exist closed-form approximations for the impedance and effective dielectric constant of the transmission line. The impedance of the line, Z_0, is dictated by the ratio of the microstrip trace width, W, to the thickness, H, of the dielectric substrate, i.e., W/H. Typically, we omit the thickness of the signal trace, t, which is valid when $t << H$. A simple formula exists for including the trace thickness, t [109], which matches Eq. 7.1 for $H = 50$ μm, $W = 54$ μm, $\epsilon_r = 8.9$, and $t = 5$ μm. Changing the trace thickness yields impedance changes of $\sim$0.5 Ω/μm. The impedance of the microstrip line (ignoring the trace thickness) is given as [108, 110]

$$Z_0 = \begin{cases} \frac{60}{\sqrt{\epsilon_{eff}}} \ln\left(\frac{8H}{W} + \frac{W}{4H}\right) & \frac{W}{H} \leq 1 \\ \frac{120\pi}{\sqrt{\epsilon_{eff}}\left[\frac{W}{H} + 1.393 + 0.667 \ln\left(\frac{W}{H} + 1.444\right)\right]} & \frac{W}{H} \geq 1 \end{cases} \tag{7.1}$$

where ϵ_{eff} is the effective dielectric constant of the microstrip, and also depends on the dimensions of the line:

$$\epsilon_{eff} = \begin{cases} \frac{\epsilon_r + 1}{2} + \frac{\epsilon_r - 1}{2}\left[\frac{1}{\sqrt{1 + 12\left(\frac{H}{W}\right)}} + 0.04\left(1 - \frac{W}{H}\right)^2\right] & \frac{W}{H} \leq 1 \\ \frac{\epsilon_r + 1}{2} + \left[\frac{\epsilon_r - 1}{2\sqrt{1 + 12\left(\frac{H}{W}\right)}}\right] & \frac{W}{H} \geq 1 \end{cases} \tag{7.2}$$

where ϵ_r is the relative dielectric constant of the dielectric substrate. The above equations hold independent of frequency as long as the dimensions of the microstrip are much smaller than the wavelength of the microwave signal [108, 110]. We plot Eq. 7.1 for a few different ϵ_r values in Fig. 7.2, highlighting the W/H ratio required to achieve 50 Ω impedance using

different substrate materials.

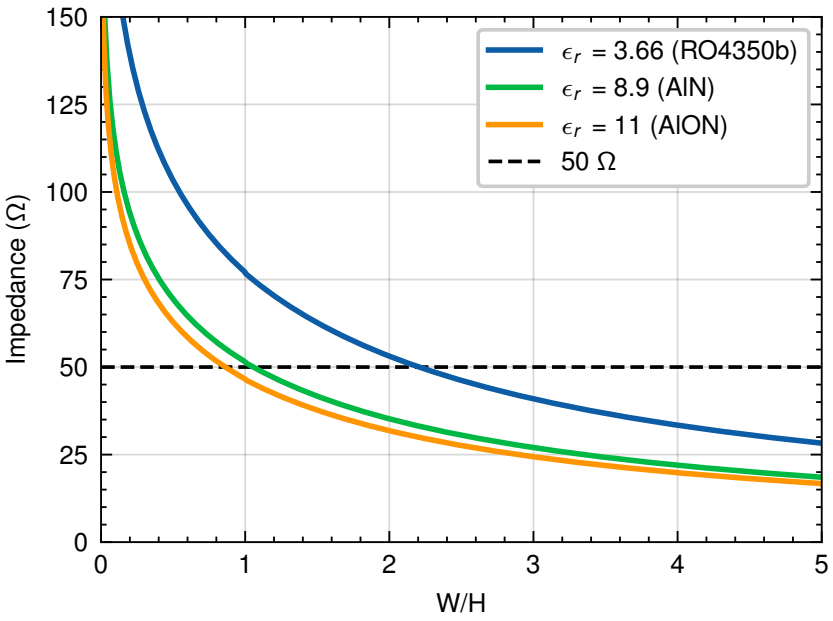

Figure 7.2: Impedance of the microstrip transmission line using Eq. 7.1 for different material dielectric constants, ϵ_r.

7.2.1 Material Choice

When designing the microwave atom chip, a key consideration is the choice of material (i.e., dielectric substrate and trace conductor) used for the microstrip transmission lines. In our chip, we intend on sending substantial microwave power (up to 20 W), so the substrate needs to have a high thermal conductivity to dissipate the heat generated in the microstrip, which could damage the transmission line and chip. Additionally, tighter AC Zeeman traps can be made by having narrow parallel microstrips closely spaced to one another. This can be achieved by using a substrate with a relatively high dielectric constant. Table 7.1 lists the dielectric constant and thermal conductivity of common dielectrics used in atom chips and microwave electronics. It should be noted that these values can often depend on how the material is made, and measurements must be done to find the true value for a given sample.

Material	Bulk Thermal Conductance (W/m·K)	Dielectric Constant	Loss Tangent
AlN [111]	285	8.9 (1 GHz)	0.001 (1 GHz)
AlON [Sec. 7.7] (Nitride Global Inc.)	unknown (estimated 2–30)	11.7 (DC)	0.006 (DC)
Silicon [111]	100–150	11.7 (1 GHz)	0.0006 (1 GHz)
GaAs [111]	50–59	12.9 (1 GHz)	0.0001 (10 GHz)
GaN [112, 113]	130	8.9 9.3 (15 GHz)	0.002 (1 GHz)
SiC [111]	350–490, 120–200	10.8	< 0.0001 (1 GHz)
Diamond [111]	1000–2000	5.7 (1 GHz)	0.0001 (1 GHz)
Alumina (99.5%) [111]	27–30	9.8 (1 GHz)	0.0001–0.0002 (1 GHz)
Sapphire [111]	31–35	9.4–11.6 (1 GHz)	0.00004–0.00007 (1 GHz)
Rogers 4350b [114]	0.69	3.66 (8–40 GHz)	0.0031 (2.5 GHz) 0.0037 (10 GHz)

Table 7.1: Dielectric constant and bulk thermal conductivity for various atom chip and microwave electronic substrates.

We opt to use aluminum nitride (AlN) as the dielectric substrate for the microstrip transmission lines on the microwave atom chip. While it does not provide the highest dielectric constant of the materials listed, a dielectric constant of 8.9 yields a height to width ratio of W/H $\simeq$1, providing narrow traces for thin substrates. Primarily, the thermal conductivity of AlN is several times better than other materials, making it more conducive for high microwave powers producing tighter AC Zeeman traps.

7.2.2 Skin and Proximity Effects

When sending AC currents through a microstrip, the currents tend to hug the edges of the trace, known as the skin effect. This has been observed in simulation and in experiment by our group [17, 95, 58]. The key parameter determining the importance of the skin effect

is the skin depth, given as

$$\delta(f) = \sqrt{\frac{\rho}{\pi \mu_0 \mu_r} \frac{1}{f}} \tag{7.3}$$

where ρ is the resistivity of the conductor, μ_r is its relative magnetic permeability, μ_0 is the permeability of free space, and f is the frequency of the AC current. This quantity defines the distance inside the conductor at which the current density reaches its $1/e$ value. For large skin depths, then, the current is more or less uniform across the trace, while at high frequencies the skin depth is several times smaller than the trace width, restricting the current primarily to the edges of the trace. At even higher frequencies, the current is located along the transverse perimeter of the trace. For a microstrip transmission line, this manifests as the current being attracted to the ground plane, living primarily on the bottom of the trace. Figure 7.3 shows the skin depth versus frequency for a few different conductors commonly used on atom chips. At the ≈20 MHz frequencies used in this thesis

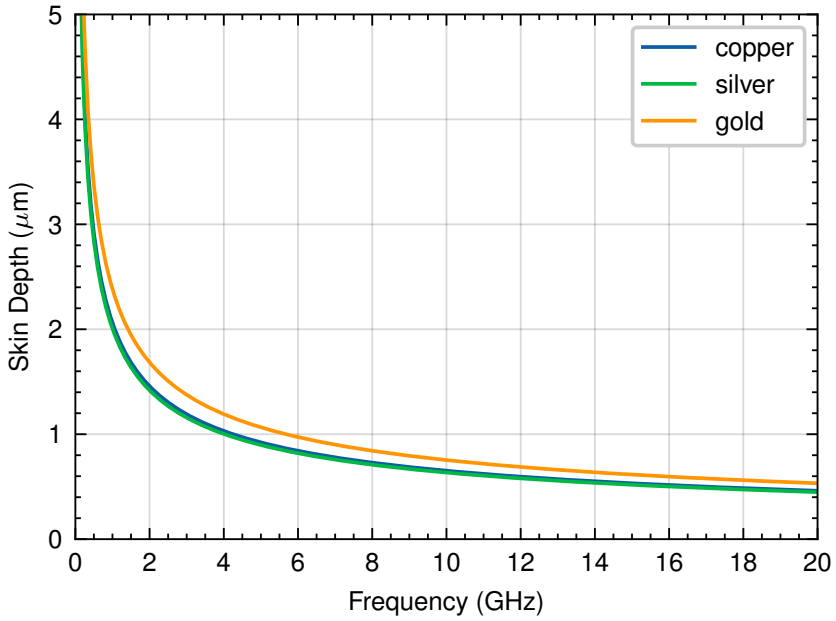

Figure 7.3: Plot of the skin depth versus frequency using Eq. 7.3 for a few different conductors.

for RF ACZ trapping, the skin depths are around 15 μm. However, at 6.8 GHz, the skin depth in copper is ≈0.8 μm, meaning most of the current in the 50 μm wide atom chip trace hugs the outermost edges of the trace (even the transverse perimeter). Additionally,

for microstrip transmission lines, the presence of the ground plane causes the current to be drawn to the bottom of the trace.

When more than one microstrip transmission lines are close together, the fields from one microstrip can affect the other, and vice versa. This is known as the proximity effect, seen in Fig. 7.4. We first observed this effect in simulations of a two-wire ACZ trap, where different relative phases between the traces affected their current densities. The preferred eigenmodes of the two-trace system are to have the currents either 0 or 180 degrees out of phase. For the 0 degree case, this causes the currents in the traces to repel one another to the outer edges of the traces. For the 180 degree case, the opposite happens, and the currents are attracted to the inner edges of the traces. For in between phases (i.e., 90 or 270 degrees), the current distribution in the traces is some linear combination of the eigenmodes and can result in the current being preferentially in one of the microstrips. While we are still able to produce ACZ traps with each of these phase configurations, the natural power imbalance caused by the proximity effect will act to displace the trap minimum in the transverse plane and warp the 3D trap.

7.3 Atom Chip Simulations

While one can write closed-form expressions for the trap location [17] and model the magnetic fields using 1-dimensional wires [58], there are many features of microwave engineering that are not obvious using the simple wire approach. Phenomena such as the skin [95] and proximity [17] effects affect the current distribution within the rectangular microstrip traces. Moreover, surface roughness or non-planar substrates can affect current propagation. Given these possibilities, we utilize commercial numerical solvers that specialize in high-frequency electromagnetic simulations. This thesis uses three software: HFSS, FEKO, and Sonnet. The simulations require a fairly high-density discretization (i.e., mesh) of the chip model traces in order to obtain reliable currents and fields (i.e., converged values). As such, these simulations must frequently be run on a supercomputer

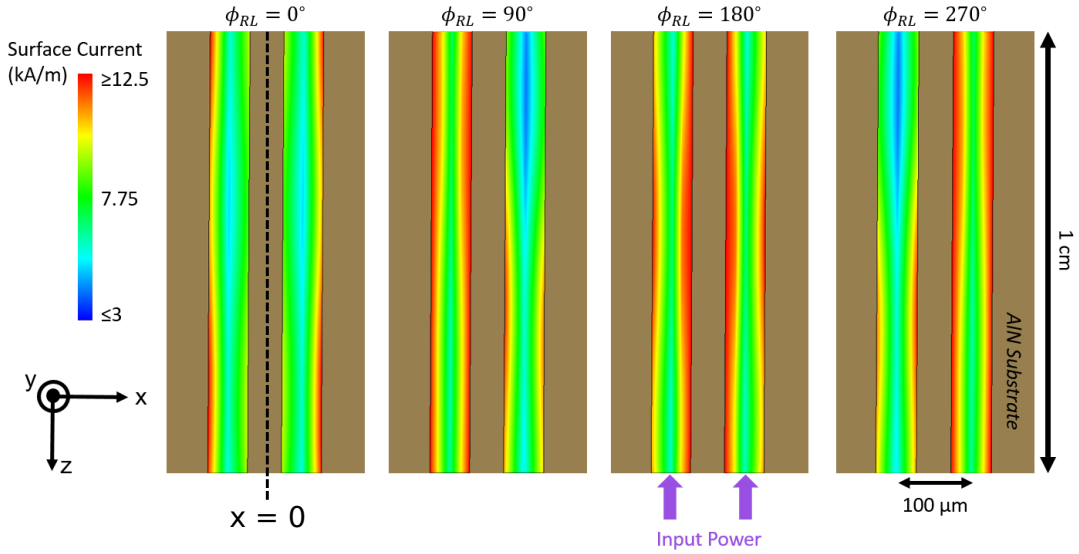

Figure 7.4: Simulation of the two-microstrip "double-s" model (Figure 7.5) at 6.8 GHz fed with 12.5 W at the inputs. The diagrams show the surface current magnitudes in the trapping region for different inter-trace phases, ϕ_{RL}. When the input phase difference is 0° or 180°, the currents are symmetric about the center ($x = 0$) and the proximity effect pushes the current in each trace towards the outer or inner edges of the microstrip, respectively. For other input phase differences (90° and 270° shown), we observe non-symmetric currents. Figure from [17].

cluster with terabyte-scale RAM memory.

7.3.1 Converting Simulations into Potentials

When simulating different atom chip structures in FEKO, the output from the software is a magnetic (or electric) near-field. To realize the ACZ trapping potential generated by this field, we must perform a bit of post-processing. Since we are considering the microwave regime, we can form an effective two-level system between the $F = 1$ and $F = 2$ ^{87}Rb ground-state hyperfine manifolds and calculate the ACZ potential from (see Chapter 3)

$$E_{ACZ} = \frac{\hbar}{2}\left(-\delta + \sqrt{|\Omega|^2 + \delta^2}\right) \tag{7.4}$$

where the Rabi frequency, Ω, is given as

$$\Omega = \frac{\mu_B}{\hbar^2}\langle g|S_+B_- + S_-B_+ + 2S_zB_z|e\rangle \tag{7.5}$$

If we take our system to be such that $|g\rangle = |1,1\rangle$ and $|e\rangle = |2,2\rangle$, the Rabi frequency reduces to a single term:

$$\Omega_{|2,2\rangle \longleftrightarrow |1,1\rangle} = \frac{\sqrt{3}\mu_B}{2\hbar}|B_-| \tag{7.6}$$

where we have used the matrix element for $\langle 1,1|S_+|2,2\rangle$ from Table 3.1. To convert the near-field from FEKO into an ACZ potential, we thus need to isolate the transverse field components to form $B_- = B_x - iB_y$, as well as choose the detuning, δ. Typically, the ACZ energy is converted into a temperature in μK through E_{ACZ}/k_B, where k_B is Boltzmann's constant. A sample of PYTHON code for this post-processing is given in [30].

7.3.2 Original 2- and 3-Microstrip Designs

The original design of the microwave atom chip was developed by ShaungLi Du [14], which I used as a base for studying the feasibility of ACZ traps generated by a pair or trio of parallel microstrip transmission lines. This is explored in a paper by our group [17], from which this subsection is taken.

7.3.2.1 Two Microstrip Traces: Standard Configuration

The combination of magnetic near fields from multiple microstrip currents can result in a trapping potential for atoms in a given magnetic hyperfine state. This section examines an accurate 3-D model for a two-microstrip trap in order to determine the current distribution in the traces and the resulting trapping potential, as well as how these depend on phase.

To overlap microwave near fields from multiple microstrips, we separate the traces by a distance of 100 μm center-to-center. Due to the 54 μm width of the microstrips, a scheme must be developed to transfer the microwaves from conventional connectorized cables (BNC, SMA, or SMP/SMPM/SMPS) down to the micron scale while maintaining a 50 Ω impedance. Accommodating for such a device, we separate the input ports of the chip by 10 mm and similarly separate the output ports. To fulfill these requirements, we adopt the "double-s" configuration shown in Figure 7.5. Here, the chip is divided into two

regions. The trapping region comprises two parallel 1 cm long microstrips spaced 100 μm center-to-center. The input (output) region consists of two microstrips that begin (end) at 10 mm separation, connected to two curved traces into (out of) the trapping region. In order to minimize the reflections for a curved microstrip, we employ a generous 1 mm turn radius, though the rule of thumb is to use a bend radius of at least three times the trace width [115].

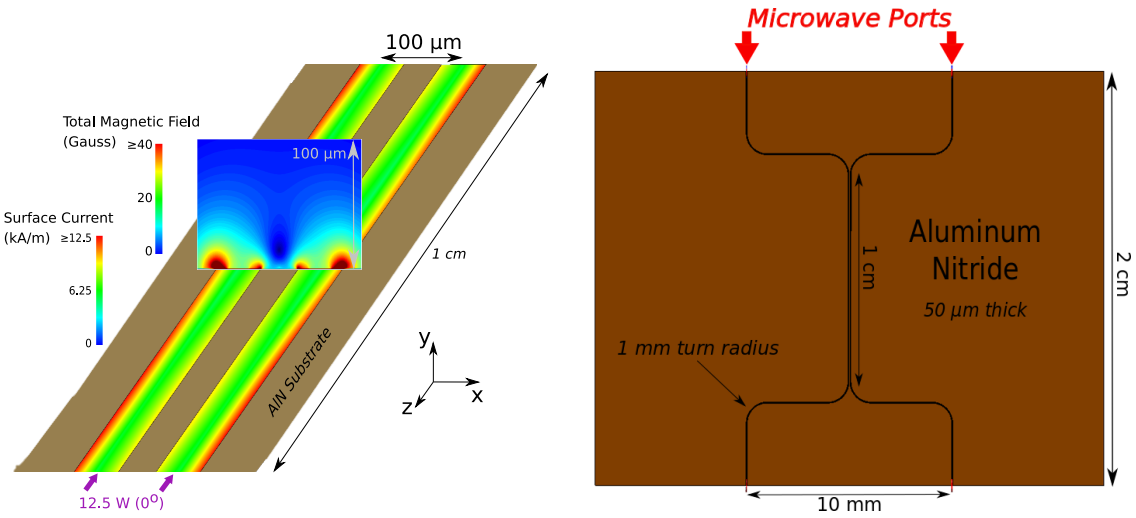

Figure 7.5: Simulation of the in-phase two-microstrip model. **Left:** Current density and magnetic near field magnitude for the model (right) with 12.5 W of power in each trace at 6.8 GHz and zero relative phase. **Right:** Geometry of the two-microstrip trap configuration. The 54 μm wide, 5 μm thick copper traces lie on a 2 $\times$ 2.5 cm, 50 μm thick AlN substrate. A 500 μm thick copper ground plane is placed below the substrate on the opposite side of the figure. A 1 mm turn radius is chosen to minimize the reflections. The traces are separated by 100 μm center-to-center in the trapping region of the chip. Microwaves are fed in through the microwave ports. Figure from [17].

A benefit to using parallel microstrips is that the presence of the ground plane lifts the minimum of the combined magnetic field from the traces out of the plane of the chip [17]. For currents in phase with one another, this results in co-located B_+ and B_- traps. Using the model of Figure 7.5 (right), we direct 12.5 W into each input at 6.8 GHz with 50 Ω impedance and zero phase difference between the left and right ports. The resulting $B_\pm$ field components and corresponding ACZ potential for $\phi_{RL} = 0°$ are shown in Figure 7.6. The substrate is shown in gray, and the black rectangles indicate the traces. Using Equation 3.22 for the $|2,2\rangle \leftrightarrow |1,1\rangle$ magnetic hyperfine transition, we can convert

the B_- field into an ACZ potential. The conversion to μK uses E_{ACZ+}/k_B, where k_B is Boltzmann's constant.

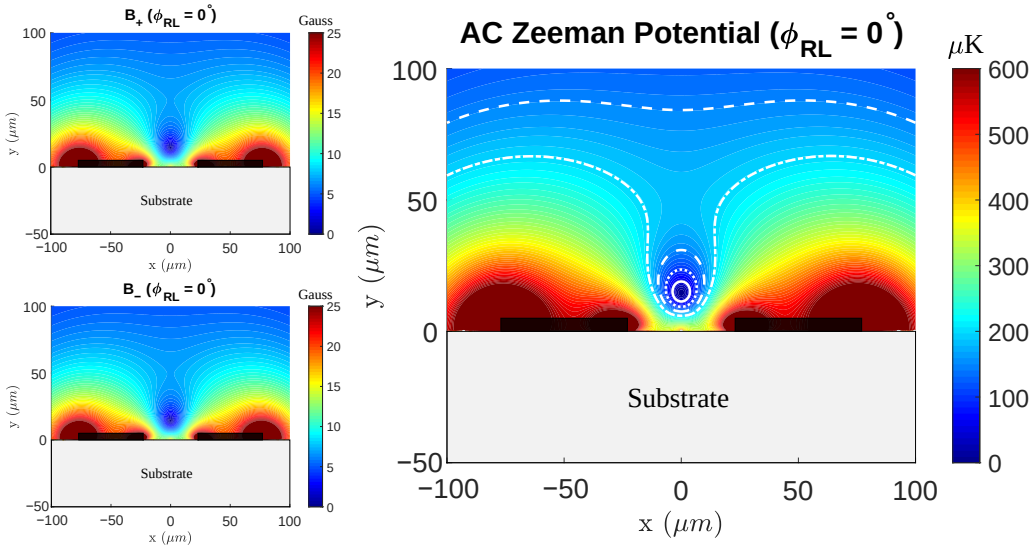

Figure 7.6: Near field $B_\pm$ components and resulting ACZ potential for the in-phase two-microstrip model for 12.5 W (in each trace) at 6.8 GHz with $\delta = 2\pi \times 1$ MHz detuning. The 50 μm thick AlN substrate is shown in gray, and the traces are indicated by 5 μm thick black rectangles. The marked white contours correspond to lines of constant potential at 50 (solid), 100 (dotted), 150 (dashed), and 200 (dot-dash) μK. The ground plane ($y = -50$ μm, not shown) moves the near field minimum (zero) out of the substrate and above the traces. Figure from [17].

The simulation results in collocated $B_\pm$ traps above the microstrips, consistent with simple theory [17]. However, as previously mentioned, the ideal theory does not account for the skin effect, which is present in our model at microwave frequencies. This effect can be seen in the current distribution of Figure 7.5, which shows higher current density near the edges of the traces. The proximity effect also has a strong effect on the current distribution and the resulting magnetic near field. As seen in Figures 7.5 and 7.6, the in-phase currents in neighboring traces effectively repel each other, leading to larger current density and near field strength on the outer edges of the two traces. This effect is most easily visualized by looking at the current density in the traces for the in- and out-of-phase cases, shown in Figure 7.4. At equal phase, the coupling causes currents in each microstrip to be pushed away from each other, resulting in a larger current density on the outside edge of the microstrips. When the currents are set to be 180° out-of-phase, we observe the

opposite effect and the currents are attracted to each other.

7.3.2.2 Two Microstrip Traces: Phase Control

To show how controlling the relative phase of the inputs affects the trapping fields, we simulate the same two-microstrip model but now put the right trace ahead by 270° with respect to the left. The results of this simulation are shown in Figure 7.7.

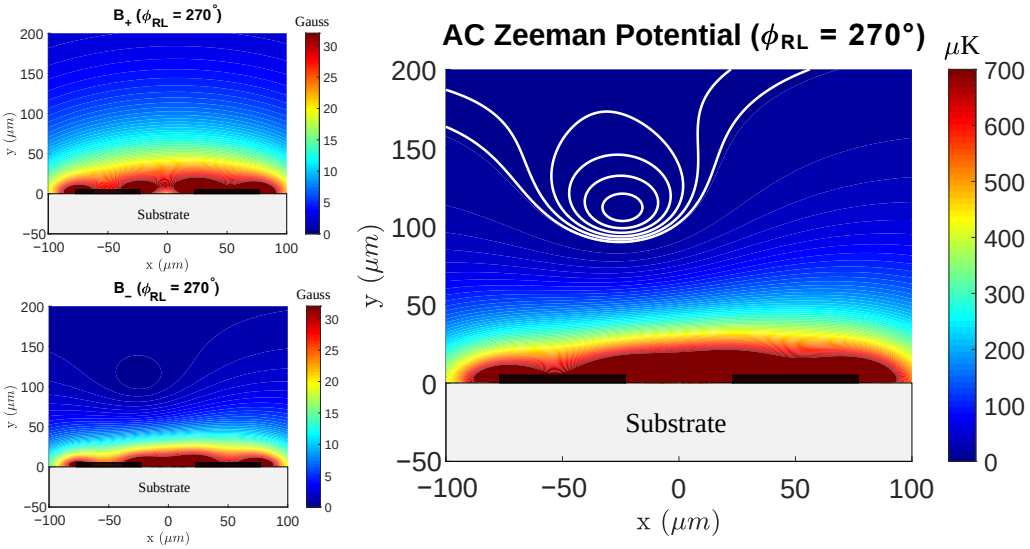

Figure 7.7: Near field $B_{\pm}$ components and resulting ACZ potential with $\phi_{RL} = 270°$ in the two-microstrip model for 12.5 W (in each trace) at 6.8 GHz with $\delta = 2\pi \times 1$ MHz detuning. The marked white contour lines correspond to lines of constant potential at 1, 3, 5, 7, 9, and 11 μK. The 50 μm thick AlN substrate is shown in gray, and the traces are indicated by 5 μm thick black rectangles. Figure from [17].

An interesting result is that, unlike the in- and out-of-phase cases, the currents in the microstrips in the trapping region are not symmetric. Instead, we observe a current imbalance, resulting in the location of the trapping field shifting horizontally. We note that, for these non-symmetric cases, the trace that initially "lags behind" in phase at the inputs gains relative current magnitude and loses relative phase in the trapping region, shown in Figure 7.4. The symmetry in the currents can be viewed by considering the traveling modes of the parallel microstrip configuration. In this system, the eigenmodes are given by the currents being completely in- or out-of-phase (0° and 180°) [108, 107]. In

these cases, we expect the currents in the microstrips to be well-behaved, modulo skin and proximity effects. For other phase differences, the traveling mode is a linear superposition of the eigenmodes, resulting in possible non-symmetry between the traces. The proximity of the microstrips may also cause the current to move between the traces via a displacement current induced by coupling. In designing a microwave atom chip, one must be aware of such effects on the microstrip's current and phase in the trapping region. Possible schemes to minimize these effects are to increase the trace separation in the trapping region and to adjust the input power and phases to account for the current differential.

7.3.2.3 Three-Microstrip Traces

Similar to the two-microstrip model, the three-microstrip design consists of two "s-curves" with an additional straight trace running between them (Figure 7.8). The addition of a third microstrip trace offers a couple of avenues for interferometry. Altering the phase of the center trace relative to the outer traces spatially separates the $B_{\pm}$ trap minima horizontally along the x-direction above the chip surface. This single-frequency trap splitting has been observed in simulation; however, it is not the primary means of interferometry intended with this chip. Using multiple frequencies, one could realize overlapping independent spin-specific traps that could subsequently be translated horizontally onto microwave lattices generated on each of the outer traces.

To achieve the 180° phase difference for the center trace current in the central section of the chip (see Ref. [17]), we note that the different travel distances of the microwaves for the center and side traces must be accounted for (in units of wavelength). For instance, at 6.8 GHz, a trap is formed for a center input phase of 80° (Figure 7.8), while at 10 GHz, the input phase is 5°. Additionally, an unintentional lattice is formed on the center microstrip due to possible couplings or reflections, affecting how the current propagates along the center trace.

The skin and proximity effects described in previous sections are present. Examining the two outer traces in Figure 7.8, the current density is seemingly larger on the inner part

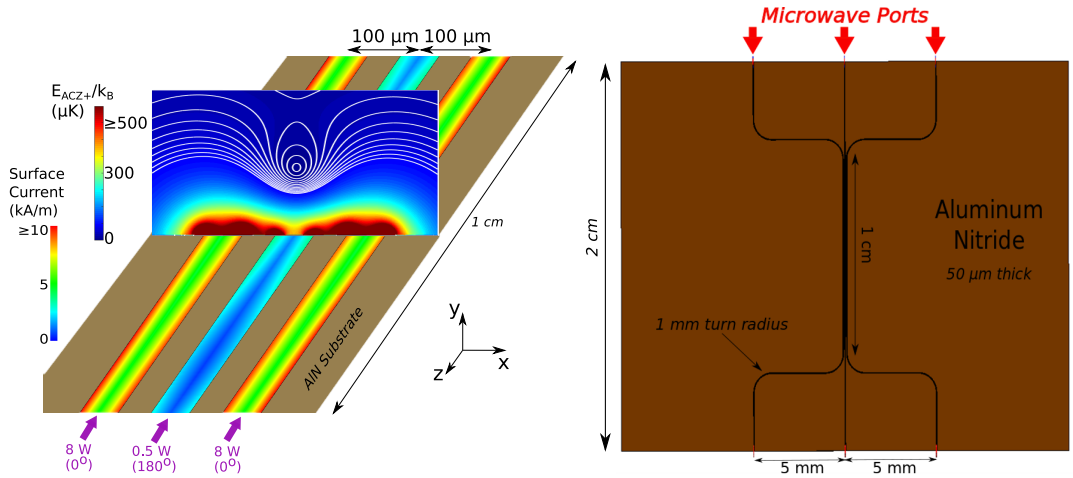

Figure 7.8: **Left:** Simulation of the three-microstrip model at 6.8 GHz. The input power and relative phases of the currents in this region are indicated in purple. The surface current magnitudes and ACZ potential ($2\pi \times 1$ MHz detuning) up to 200 μm above the chip surface are shown in the trapping region of the chip. The contours indicate lines of constant potential at 1, 5, 10, 15, ..., 60 μK. The trap is located at a distance of $\simeq$93 μm above the chip surface. **Right:** Geometry of the three-microstrip trap configuration. The traces are separated by 100 μm center-to-center in the trapping region of the chip. The power and phase directed into the center microstrip are chosen such that the relative phase between the currents in the center trace and the two outer traces at the location of the trap is 180°. Figure from [17].

of the trace than the outer trace, corresponding to a deeper red coloring. This behavior agrees with what we encountered previously from the proximity effect. Since in this region the outer currents are roughly 180° out of phase with the center, the currents in the two outer traces tend to be attracted towards the inner trace.

By lowering the power and current in the center trace, the trap is pulled closer to the chip while also reducing crosstalk to outer traces. For 8 W of input on the side microstrips and 0.5 W on the center trace, as shown in Figure 7.8, the trap is located 93 μm above the chip and has a depth of $\sim$15 μK.

7.3.3 Modified Design: the UZU Chip

The major limitation of the presented atom chip designs is the lack of optical access for imaging the ultracold atom cloud. In practice, we need to be able to image the atoms along perpendicular directions, capturing the xy and yz planes, to fully characterize our

cold atom cloud. In the previous designs, the xy-plane would be obstructed by microwave connectors at each end of the microstrip traces. To provide room for imaging light while accommodating the connectors, a new microstrip layout had to be created. This new design, dubbed the UZU chip, is shown in Fig. 7.9.

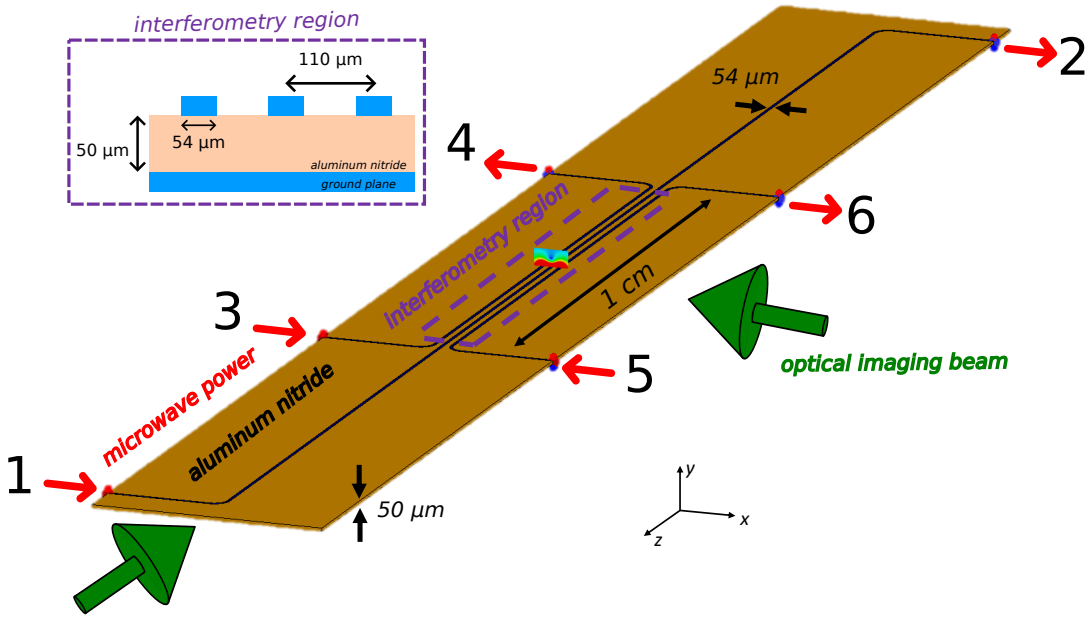

Figure 7.9: Design of the UZU microwave atom chip. Three parallel, 50 Ω microstrips formed by 54 μm wide traces on 50 μm thick aluminum nitride ($\epsilon_r = 8.9$) for the central 1 cm long interferometry region (see inset). A slice of the magnetic field generated by the traces is shown, which in reality extends throughout the entire region. See Fig. 7.10 for a larger view of the trapping potential. The trap is located at $y = 109$ μm. The traces in this region are spaced 110 μm center-to-center. Each trace features a 0.5 mm turning radius, forming the UZU shape. This design offers optical access (green arrows) for imaging atoms in the ACZ trap. The chip is 35 mm long (in the z-direction). Each port is labeled for S-parameter analysis.

Inspired by the wire layout of our existing atom chip, this design features a central Z-shaped microstrip flanked on either side by a U-shaped trace. Each curve of the microstrips uses a 0.5 mm turning radius, allowing for smooth flow of current around the bends. The interferometry region in the middle of the chip remains the same, made up of three parallel microstrip traces. We decided to space the traces slightly further away, increasing the center-to-center separation from 100 μm to 110 μm. There is a challenging interplay in this region between microstrip spacing and the crosstalk between the traces. While keeping the

traces close together yields stronger ACZ traps, the proximity effect is stronger, changing the current and phase relation in the traces. We opt to lean more into generating strong microwave ACZ traps in the first iteration of this chip, keeping in mind the possibility of a natural ACZ lattice formed on the microstrip due to reflections.

The simulated ACZ trapping potential formed in the interferometry region of this new chip design is shown in Fig. 7.10. With the current in the center trace set to be about

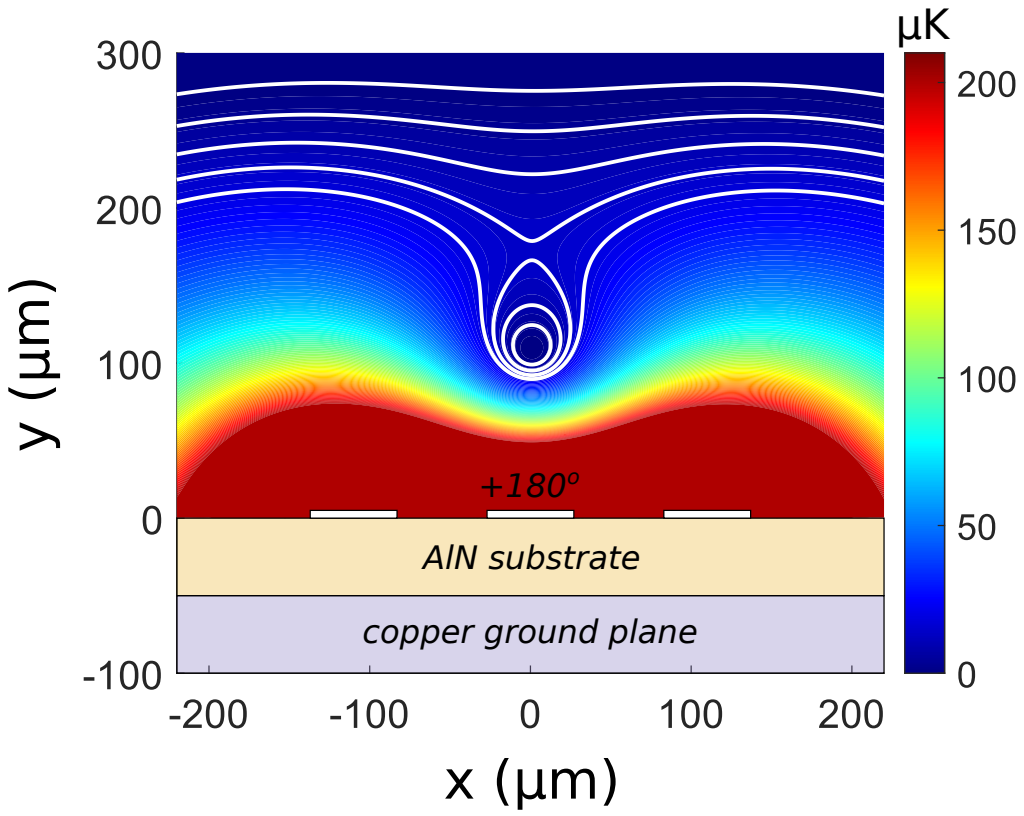

Figure 7.10: Simulated AC Zeeman potential for the UZU chip (see Fig. 7.9) at 6.8 GHz. The simulation uses 18 W of power through each U-shaped microstrip and 912 mW through the central Z-shaped microstrip. The current in the center trace is 180° out of phase with the outer traces (shown by white rectangles). Using the $|2,2\rangle \leftrightarrow |1,1\rangle$ ^{87}Rb ground state transition and a $\delta = 2\pi \times 1$ MHz detuning, this gives a trap depth of 15 μK, trap frequency of 426 Hz at a distance of 109 μm from the chip surface. White contour lines show lines of constant temperature every 5 μK up to 20 μK.

180° out-of-phase with the outer traces, the trap is located 109 μm above the chip surface. The outer traces each have 18 W of microwave power at 6.8 GHz sent through them, and

the center trace uses 0.912 W. Using the $|2,2\rangle \leftrightarrow |1,1\rangle$ inter-manifold ^{87}Rb ground state transition and a $2\pi \times 1$ MHz detuning, we get a trap depth of 15 μK and transverse trap frequency of 426 Hz.

7.3.3.1 Bandwidth of the Chip

We plot the S-parameters, simulated using HFSS, for the microwave atom chip (Fig. 7.9) in Fig. 7.11. The input reflections, S_{ii}, remain below 5% across the DC-20 GHz frequency range. It should be noted that the simulations presented here do not incorporate a realistic connector design, instead using a standard HFSS 50 Ω wave port. The transmission coefficient of the Z-wire (S_{12}) is noticeably lower than in the U-wires since it is roughly three times as long, so we expect larger losses. We can do a quick calculation of power loss in each of the microstrips, given as one minus the square of the transmission coefficients. At 6.8 GHz, the power loss in the Z-shaped trace is ≃21%, while in the U-wires it is ≃12%. It should be noted that in the trapping scheme, we intend on running much less power through the Z-trace, so the higher power loss should be less detrimental. However, sufficiently large power losses in the chip could create a thermal gradient, leading to a blackbody AC Stark shift [116] on the atoms. The lab is currently working on measuring the thermal conductivity of the microwave atom chip substrate, which will help assess the significance of the possible thermal gradient.

The operational bandwidth of the atom chip is found to be limited by the cross-talk between neighboring microstrip traces. Between the U-wires, S_{36} and S_{45}, the cross-talk increases roughly linearly with frequency by ≃0.0068 %/GHz. The most significant cross-talk comes from the coupling between the Z and either of the U wires, stemming from their closer proximity. This increases with frequency by ≃0.0188 %/GHz, about 2.5 larger than the U-wire coupling. The inter-trace cross-talk will result in a natural AC Zeeman lattice, which will compete with the controlled microwave lattice if sufficiently strong. In Fig. 7.12, we show FEKO simulations of the three-microstrip chip design from Fig. 7.8 at 6.8 GHz (left) and 10 GHz (right), highlighting the natural lattice formed due to cross-talk between

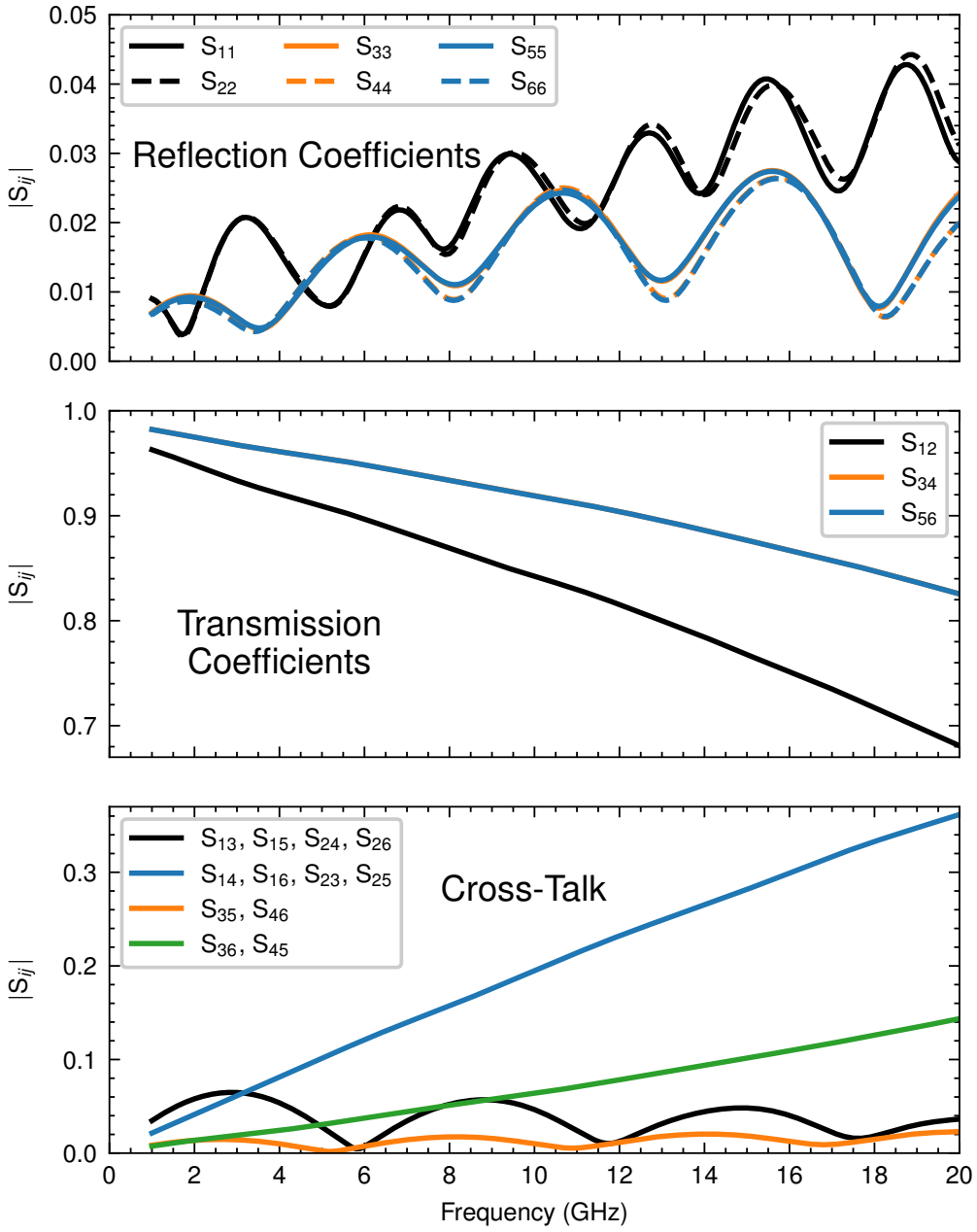

Figure 7.11: UZU microwave atom chip S-parameters. Labels correspond to the ports in Fig. 7.9.

neighboring microstrips. Increasing the wire spacing or reducing the inserted power will

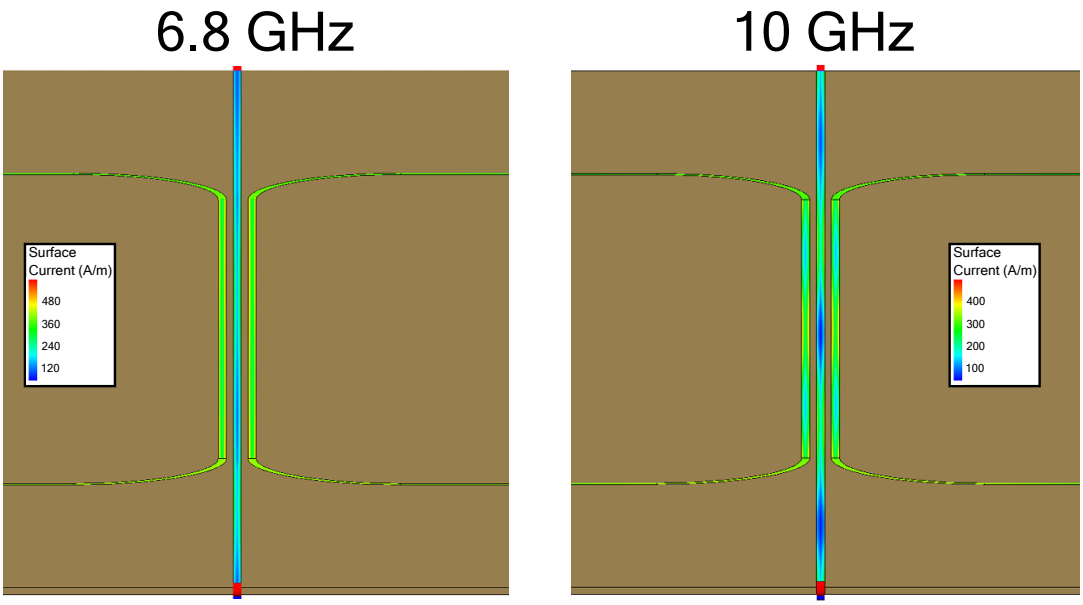

Figure 7.12: FEKO simulations of the three-microstrip chip design from Fig. 7.8 at 6.8 GHz (left) and 10 GHz (right). Shown is the current magnitude in the traces, highlighting the natural lattice formed due to cross-talk between neighboring microstrips.

reduce this cross-talk [117] at the cost weaker ACZ trap. We still expect a trap to be formed across the broad frequency range; however, as the natural lattice depth increases it may become large enough to fragment the cloud, an effect akin to the potential roughness discussed in Chapter 6. At 6.8 GHz, the coupling between the U and Z traces is $\simeq$13.6%, reaching nearly 20% at 10 GHz.

As an initial demonstration of microwave ACZ trapping and interferometry on an atom chip this should be manageable, but may be limited in the interferometer integration time. This further motivates the use of potassium [57, 14], which has hyperfine splittings of hundreds of MHz up to $\sim$1 GHz [17], reducing some of the complexity involved with microwave engineering. With there being interest in designing microwave atom chips with even closer trace spacings, it will be critical to find ways to reduce cross-talk, perhaps by putting a fence of metal vias between the traces, similar to that used in a grounded coplanar waveguide [118, 119].

7.4 DC Atom Chip Design

In addition to the microstrip transmission lines used for AC Zeeman trapping, we want to include a DC trapping scheme in the atom chip. This allows us to perform traditional DC chip trapping and initial evaporative cooling before transferring into the AC trap.

Transverse trapping can be done in the same way as our current atom chip trap by sending DC current through the Z-shaped microstrip transmission line on the microwave atom chip. The addition of a uniform bias field in the opposite direction to the field produced by the wire produces a magnetic minimum that traps DC low-field seeking states. Axial confinement along the microstrip, however, is not as simple. The lab's current atom chip features a 2.6 mm long central section of the Z-wire, with endcap wires on either side. These endcaps are close enough to the atoms (roughly 1.4 mm) to provide strong axial confinement of about 1 mK. The microwave atom chip, on the other hand, has a much longer straight central section for the Z-shaped microstrip, on the order of 2 cm. This places the endcaps about 1 cm away from the atoms, diminishing their effects on axial confinement. Figure 7.14 shows the DC Zeeman trapping potential for the Z-shaped microstrip putting 1 A of current through the wire. Notably, the axial trapping frequency is $\sim$0.5 Hz, significantly weaker than that found in our current atom chip, which operates with an axial trapping frequency of tens of Hz.

The design we have come up with incorporates a DC "carrier" chip upon which the microwave atom chip will sit. This carrier chip will contain three wires serving as the primary endcap wires for the DC operation of the new atom chip. A model of this design is shown in Fig. 7.13. Here, the two outer endcap wires supply confinement in a traditional Ioffe-Pritchard configuration, albeit at a distance H below the main Z-wire. A third central endcap is added with counter-propagating current relative to the outer endcaps and acts to lower the magnetic minimum, thereby increasing trap depth and frequency. While the figure shows the wires as rectangular, in simulation, we model everything as an infinitely thin, finite-length wire, which is sufficient when the wires are thinner than the trap height.

Here, the Z-wire microstrip is roughly 50 μm wide, so this approximation will guide us the majority of the way since our target trap height is 100 μm. The PYTHON code used for these simulations is given in [30].

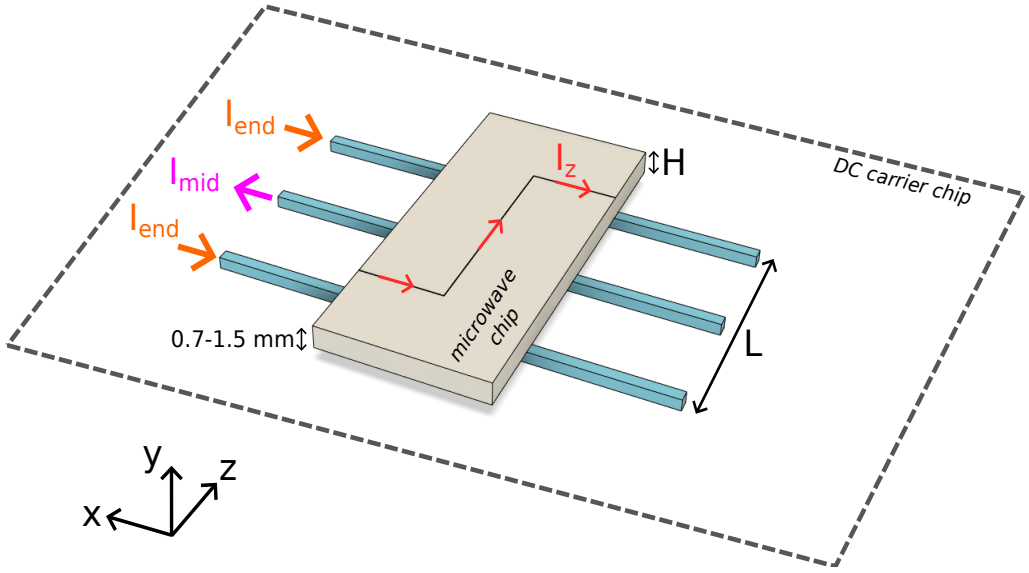

Figure 7.13: DC trapping scheme on the microwave atom chip. Transverse trapping is accomplished using the Z-shaped microstrip transmission line on the chip. Flexible axial endcapping comes from three wires located a distance H below the microwave chip, given by the 50 μm thick AlON substrate deposited on a backing structure. Not shown are the hold ($+x$ direction) and Ioffe ($+z$ direction) fields.

With this design in hand, we can do some modeling to determine an optimal configuration. The Cu-AlN-Cu sandwich used as the baseplate in the first iteration of the microwave atom chip (see Sec. 7.5) has a total thickness of 800 μm (380 μm AlN, 2×210 μm Cu). We also have roughly 50 μm of dielectric substrate deposited onto the baseplate, bringing the total thickness of the chip to $H = 850$ μm. With that in hand, our parameter space is reduced to the distance between outer endcaps, L, and the currents, I_{end} and I_{mid}.

The benefit of adding the central endcap wire with counter-propagating current is that it both increases the trap depth and axial trapping frequency, as demonstrated by Fig. 7.14. This allows us to perform tunable axial trap compression during the BEC cooling process. Another interesting effect is the ability to generate a double-well axial potential, which has applications in atom interferometry. By increasing the center endcap

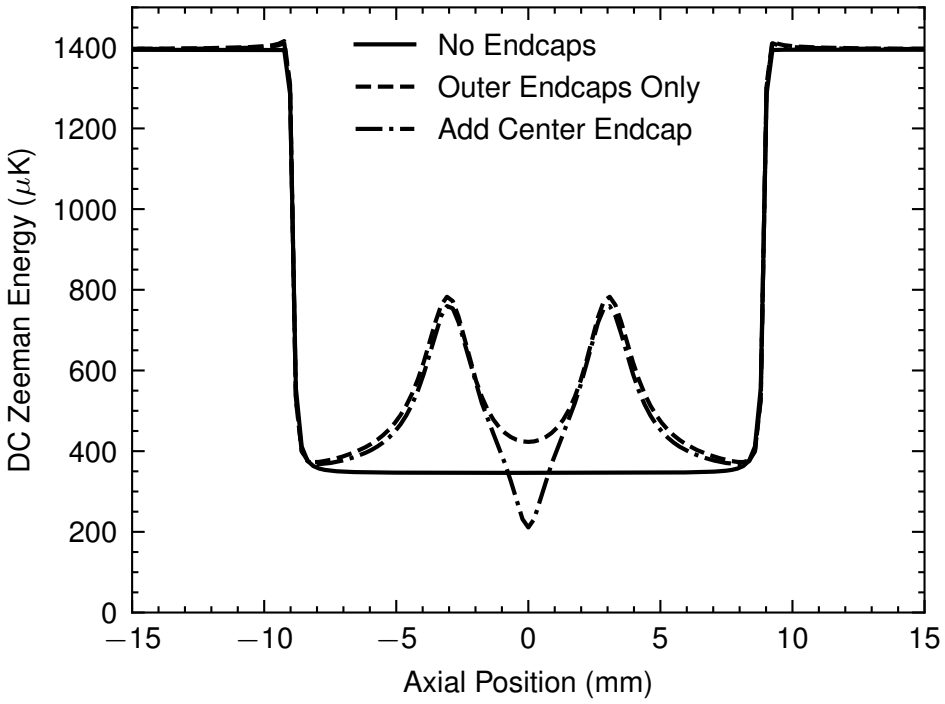

Figure 7.14: Microwave atom chip DC configuration without additional endcap wires. The outer endcaps use a current of 3 A, and the central endcap uses 1.5 A of current. The atom chip is 1 mm thick, and the outer endcap spacing is 5 mm. Here, the current through the z-wire is 1 A, the central section is 18 mm, and the endcaps are 7.5 mm long. There is a 5 G Ioffe field added along the $\hat{z}$-direction. The potential is evaluated at $x = 0$ and $y = y_{trap} \simeq 100$ μm.

current, eventually its field will become strong enough to create a bump in the harmonic potential, splitting it into two wells. This can also be accomplished at lower currents by flipping the direction of the central endcap current, such that it is co-propagating with the outer endcap wires. Both of these cases are shown in Fig. 7.15. For interferometry, this double-well splitting could act as a "beam-splitter" for the atoms, and recombination could occur through lowering of the central endcap current. In either case, this scheme has the disadvantage of the potential going through a flat region as it transitions from one to two wells, described by an x^4-type potential. When this occurs, if the atoms are not in a BEC state, the timescale for adiabaticity, set by the trapping frequency, breaks down, thereby heating up the atoms and causing dephasing in the interferometer. This points to an advantage of the microwave interferometry scheme we propose, as the "beam-splitter"

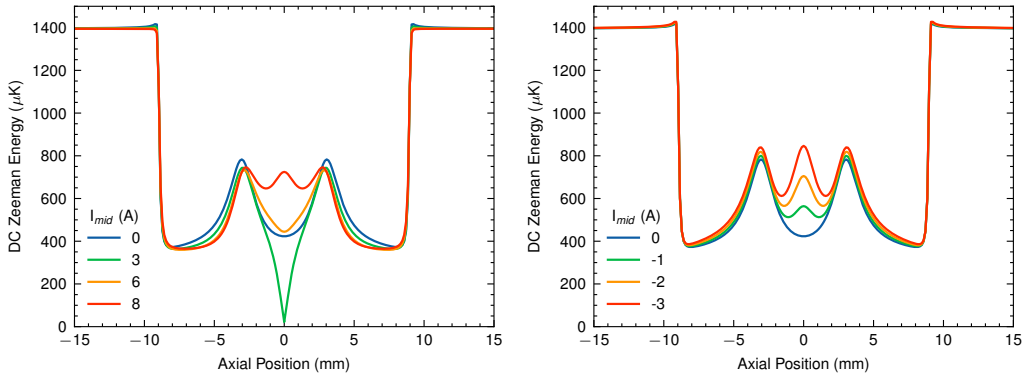

Figure 7.15: Axial double-well potential generation for the central endcap wire current counter- (a) and co- (b) propagating with respect to the outer endcaps, using the DC atom chip configuration in Fig. 7.13. Both simulations use $H = 0.85$ mm, $L = 6$ mm, and $I_{end} = 3$ A. The Z-shaped wire carries 1 A of current. The external fields are set to B_{hold}=20 G and B_{Ioffe}=5 G, oriented in the $+\hat{x}$ and $+\hat{z}$ directions, respectively.

is two independent harmonic traps, meaning there should be minimal dephasing so long as the movement of the traps is done adiabatically.

We investigate the axial trap depth and frequency for this trap design, putting the endcap wires a distance $H = 0.85$ mm below the Z-shaped microstrip. Figures 7.16 and 7.17 shows the results of the simulations across the parameter space. For modest amounts of current, i.e., a few Amps, we see that we are able to achieve milliKelvin trap depths with tunable trap frequencies. The resonant-type behavior of these plots is a result of the endcap wire field exactly canceling out the 5 G Ioffe field and then flipping the direction of the overall $B_z\hat{z}$ field. This canceling lowers the trap bottom and tightens the trap, thus increasing trap depth and frequency.

In the final design, we could place multiple encap wires beneath the microwave chip at different spacings to offer even more flexible control over the DC trap. We have also looked into thicker backing structures on the 1-2 mm scale and seen comparable results. These thicker materials would be more suitable for the 50 μm substrate deposition process, and is an active area of research in our group. Reference [30] contains the PYTHON code used for these simulations, which is easily adaptable for future studies using this design.

With the design and simulation of the new microwave atom chip complete, we now

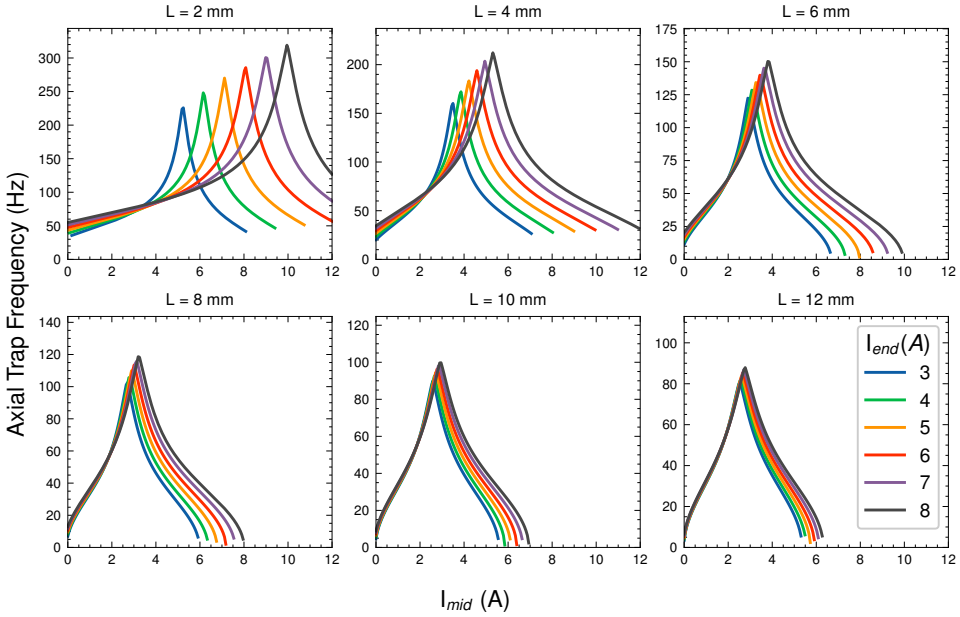

Figure 7.16: Simulated trap frequencies for the DC trapping scheme on the microwave atom chip, as shown in Fig. 7.13. The simulation uses a height of $H = 0.85$ mm, which matches the Cu-AlN-Cu sandwiches used as the backing material and ground plane, plus an additional 50 μm of AlON as the microwave substrate. The simulation results are cut off as soon as the trap transitions from a single to a double-well potential, thereby only showing the trap depth and frequency in the single-well trap. The Z-shaped wire carries 1 A of current. The external fields are set to B_{hold}=20 G and B_{Ioffe}=5 G, oriented in the $+\hat{x}$ and $+\hat{z}$ directions, respectively. The axial trap frequencies and depths are calculated at different outer endcap wire spacings, L (see Fig. 7.13).

move to the initial phases of manufacturing, which will be the remaining subject of this chapter.

7.5 Eddy Current Measurements

One design consideration in building a micro-fabricated atom chip trap is the presence of eddy currents in the system. This mainly comes into play when quickly turning off the DC currents used for trapping. From Maxwell's equations, we know that a time-varying magnetic field can induce an electric field (EMF) in a conductor to oppose the changing magnetic field. Or as David Griffiths would say: "Nature **abhors** a change in flux" [120]. These eddy currents themselves generate unwanted magnetic fields that can affect atoms in the trap and experiments if not properly accounted for. This section

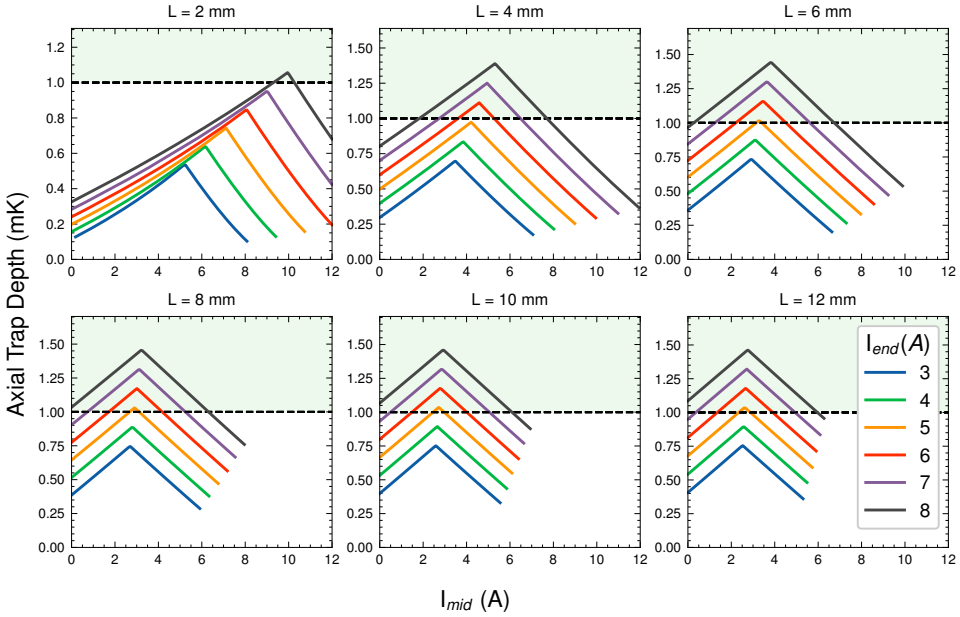

Figure 7.17: Simulated trap depths for the DC trapping scheme on the microwave atom chip, as shown in Fig. 7.13. The simulation uses a height of $H = 0.85$ mm, which matches the Cu-AlN-Cu sandwiches used as the backing material and ground plane, plus an additional 50 μm of AlON as the microwave substrate. The simulation results are cut off as soon as the trap transitions from a single to a double-well potential, thereby only showing the trap depth and frequency in the single-well trap. The Z-shaped wire carries 1 A of current. The external fields are set to B_{hold}=20 G and B_{Ioffe}=5 G, oriented in the $+\hat{x}$ and $+\hat{z}$ directions, respectively. The axial trap frequencies and depths are calculated at different outer endcap wire spacings, L (see Fig. 7.13).

describes measurements of eddy current decay times in different materials of different thicknesses, which allowed us to select a viable backing structure for the new atom chip.

7.5.1 Experimental Setup

The block diagram of the experimental setup is shown in Fig 7.18(left). A 10 Amp DC supply is run through a high-speed MOSFET switch that is turned on and off using a function generator. The current is then run through a brass rod above which the conducting sample is placed. This setup mimics the layout of the for the atom chip and its backing groundplane. Several mm above the sample is a magnetic field sensor (AKM EQ-730L Linear Hall Effect IC) whose signal is sent to an oscilloscope. An example signal from the sensor is shown in Fig. 7.18(right).

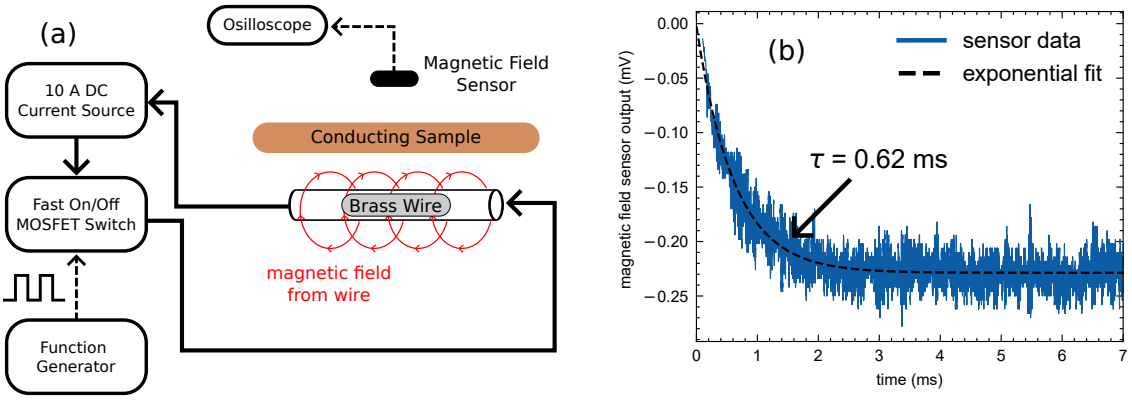

Figure 7.18: (a) Block diagram of the experimental setup used to measure eddy current decay in conducting samples. (b) Sample output of the magnetic field sensor and corresponding exponential decay fit. The data corresponds to the 1250 μm thick high conductivity copper in Fig. 7.19 with the sensor held 6 mm above the conductor. The signal is averaged over 32 trace sweeps on the scope and is amplified by a factor of 11 using a non-inverting op-amp amplifier circuit.

7.5.2 Results

We looked at five conducting samples of various thicknesses: (1) OFHC high-conductivity copper, (2) 250 μm thick alumina (Al203) sandwiched between two pieces of 127 μm thick copper, (3) 380 μm thick aluminum nitride (AlN) sandwiched between two pieces of 203 μm thick copper, (4) unhardened beryllium copper (BeCu), and (5) sheet of of aluminum. The results of the decay time measurement are shown in Fig. 7.19, displaying a linear relation between the material thickness and decay time. The fit was forced to go through zero, as it is assumed that when no conductor is present, there are no eddy currents. In practice, with no conductor present, we observe the signal decay with a 1/e decay time of $\simeq$25 μs. For the double-sided Al203 and AlN samples, the thicknesses are given as the total thickness of the copper (i.e., the substrate thickness is excluded). It was found that operating the sensor at different heights above the sample resulted in different decay times, though no clear trend was seen in this behavior. The error bars are given as the standard deviation of several decay time measurements with the sensor at different heights above the copper from 2-3 mm up to 11 mm.

We are primarily interested in thicknesses below 1 mm, as that is what we intend to

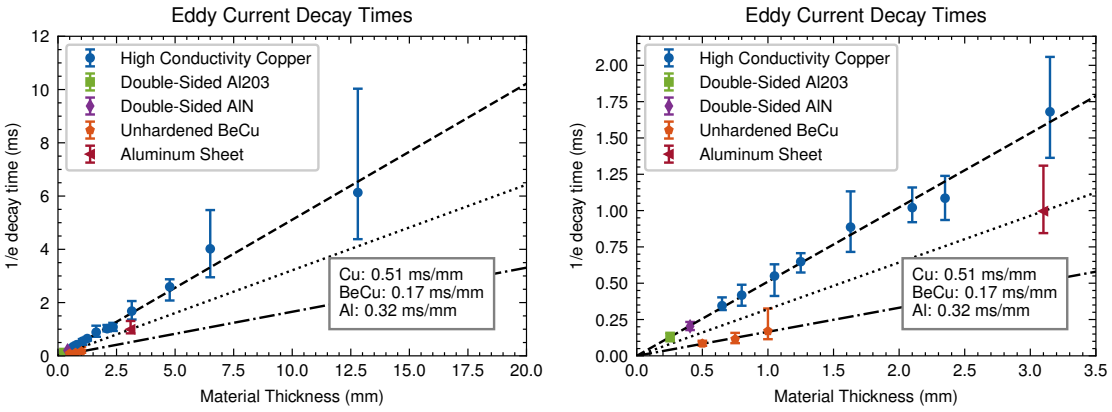

Figure 7.19: 1/e decay time measurements for a range of thicknesses of high-conductivity copper (blue dots). Also shown are decay time measurements for double-sided Al203 (green square) and AlN (purple diamond), as well as for unhardened Beryllium Copper (BeCu, orange stars). The red dashed line is a y=mx fit to the high-conductivity copper data. The right figure is zoomed in on copper thicknesses below 2 mm. Error bars display the spread of decay time measurements obtained by placing the magnetic sensor at different heights above the copper samples.

use for the microwave atom chip. We see from the decay time data that for thicknesses below 1 mm we should expect the eddy currents to decay by a factor of 1/e in less than half a millisecond, which is an acceptable value for performing our cold atom experiments. Notably, the double-sided AlN and Al203 samples exhibit decay constants that follow the trend of the high-conductivity copper, showing that the addition of the dielectric substrate does not affect the eddy current decay. This is advantageous as we can then use the substrate for mechanical stiffness during the deposition process while keeping low eddy current decay times. Based on these results, we proceeded with the double-sided AlN samples as the ground plane/backing material for the first generation microwave atom chip. It should be noted that single-sided AlN with copper would also be sufficient, though most likely requiring thicker AlN for mechanical stiffness.

7.6 Preparing the Substrate Surfaces: Diamond Turning

With our choice of ground plane/backing surface chosen for the microwave atom chip, we can move on to the actual construction of the new chip. The first step in that process is

getting 50 μm of AlN deposited onto the top copper surface of the Cu-AlN-Cu sandwiches. Prior to deposition, however, we need to make sure the copper surfaces onto which the dielectric will be deposited are extremely smooth and planar. Since the deposited AlN surface will match the surface of the copper, care must be taken to ensure smoothness of the copper, which will map onto the surface of the dielectric. Smoothness of the dielectric substrate is key in the design of the microstrips since roughness in the dielectric surface on the order of the skin depth of the conducting trace can increase loss in the transmission line [121]. For copper, the skin depth at 6.8 GHz is $\sim$0.79 μm. So to ensure a smooth layer of AlN, we must first achieve a smooth copper surface. Previous investigation [122] showed that the surface roughness of the Cu-AlN-Cu sandwich was in the 1-2 μm range, exactly on the order of the skin depth in copper. The planarity, or flatness, of the chip is also a key aspect in the manufacturing process, as it will make the lithography of the traces much easier. Additionally, sufficient bowing will make optical access more difficult when doing in-situ imaging of atoms trapped tens of microns from the chip surface. To achieve good smoothness and planarity of the atom chip copper groundplane, we use diamond turning.

We had the diamond turning done by a third-party company, NanoPhorm LLC, in which the pieces are lathed using an ultra-precise diamond bit to achieve mirrored planar surfaces with minimal roughness. After receiving the samples back, we inspected the surface roughness using a Bruker Dektak XT Surface Profilometer. This machine drags a small stylus across the surface of the sample and measures its variation in depth. Fig. 7.20 shows an example of the data from the profilometer across the diamond turned copper surface. A moving average is applied to reduce high-frequency noise, and a $\pm$50 nm shaded band is added to indicate the specified machining tolerance. After diamond turning, the surface roughness of the copper is below 50 nm, about a factor of 20 times smaller than measured prior to diamond turning. Fig. 7.20 only shows data from a single 2 mm scan, but this trend holds true across different areas of the same sample and across different samples.

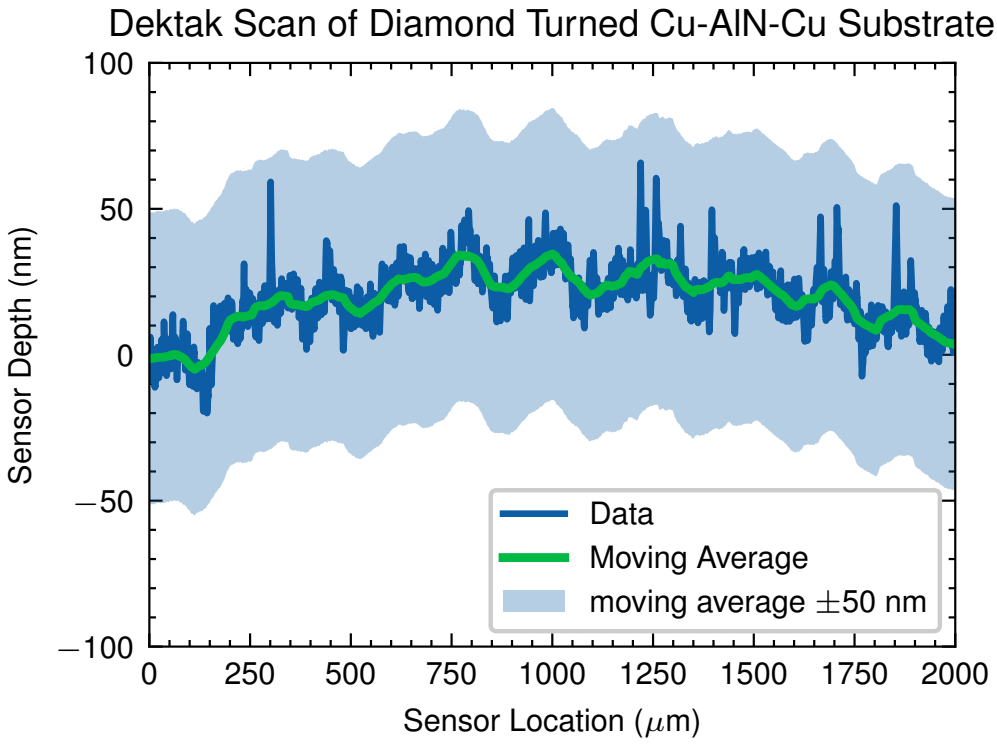

Figure 7.20: Dektak surface profilometer measurement of the diamond turned Cu-AlN-Cu copper surface. The stylus was scanned across a 2 mm long section of the copper. The blue line shows the data from the stylus, the green line provides a moving average for the eye, and the blue shaded region shows a ±50 nm tolerance from the moving average.

7.7 Dielectric Constant and Loss Tangent Measurements

In order to design 50 Ω microstrip transmission lines for the atom chip, we need to have certainty in the relative dielectric constant of the substrate being used. Without this knowledge, we can only make assumptions as to what it is, or base it on the manufacturer's listed values, which can sometimes vary by ten to twenty percent! For this first-generation microwave atom chip, we use aluminum oxynitride (AlON) [123], due to its ability to be deposited at tens of micron thicknesses. Since the AlON substrate being used for the atom chip is quite novel, the dielectric constant has not been measured and can only be guessed at based on the material composition. In addition to measuring the dielectric constant of the AlON, we are also interested in its loss tangent. While not crucial for determining

the correct microstrip width for obtaining 50 Ω impedance, the loss tangent informs us on power losses via the substrate. Having a high loss tangent could lead to increased heating of the material, increasing the risk of damaging the chip. Heating of the chip would also affect the performance of the trap, as the impedance of the microstrip transmission line would change [110], causing unwanted reflections.

7.7.1 Capacitor Measurements

The simplest way to measure the dielectric properties of a material is to make it into a capacitor. From this, we can obtain the dielectric constant from the resulting capacitance, as well as the loss tangent, which quantifies the ratio of energy dissipation to energy storage in the material. This is done by putting metal on both sides of the dielectric material and using a multimeter to measure the capacitance. For a parallel-plate capacitor, the DC capacitance can be related to the dielectric constant of the material inside as

$$C \simeq \epsilon_r \frac{\epsilon_0 A}{d}, \tag{7.7}$$

where ϵ_0 is the permittivity of free space, A is the area of the plates, d is the distance between plates, and ϵ_r is the dielectric constant. The above equation is not exact for our scenario since the capacitor is not infinitely large, thus requiring a correction to incorporate the effects of fringe fields on the capacitance. Several formulas exist to account for this [124] in the form $C = C_0(1 + \alpha)$, where C_0 is given by Eq. 7.7, and α is the fringe field correction. For our geometry, we find that $\alpha \approx 0.03$, putting fringe field effects on the few percent level. By measuring the capacitance, the above equation can be rearranged to determine the dielectric constant.

We were given a sample of AlON grown on copper from Nitride Global, Inc., which had a measured thickness of 31.4 ± 0.7 μm [125]. Our collaborators at Virginia Commonwealth University (VCU; David Pate and Prof. Vitaly Avrutin) then deposited a 1 cm diameter disk consisting of a 100 nm Ti adhesion layer with $\sim$2 μm of silver and a 70 nm gold

capping layer. Capacitance measurements from 10 kHz - 2 MHz were made using an HP 4275A LCR meter. Low-frequency measurements were verified with an HP 4284A. The device was also able to measure the loss tangent at these frequencies. The measured data is plotted in Fig. 7.21. Extrapolation to zero frequency gives $\epsilon_{r,DC} = 11.7 \pm 0.3$ and $\tan(\delta) = 0.00557 \pm 0.0003$. The error bar in ϵ_r is due to the uncertainty in the substrate thickness, while for the loss tangent we use the standard deviation of the data up to 400 kHz. This provided the first measurements of the dielectric constant and loss tangent of the AlON material.

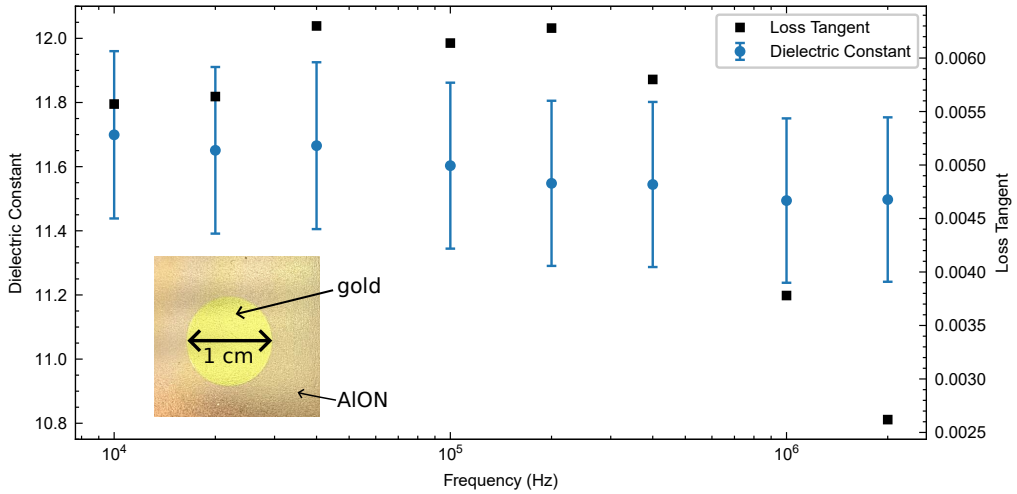

Figure 7.21: Dielectric constant (via capacitance) and loss tangent measurements for a 1 cm wide gold disk on 30 μm thick AlON substrate. Not shown is copper on which the AlON is deposited. Measurements were made using a HP 4275A LCR meter by David Pate (VCU). Low frequency measurements were verified with a HP 4284A. Errors in the dielectric constant come from the uncertainty in the AlON thickness. Extrapolation to zero frequency gives $\epsilon_{r,DC} = 11.7 \pm 0.3$ and $\tan(\delta) = 0.00557$.

7.7.2 Resonator Measurements

While the capacitor method is relatively straightforward to implement, our measurement equipment can only characterize the material at low frequencies, i.e., below 1 MHz. It is not uncommon, however, for a material's dielectric constant to vary as a function of frequency and be different in the microwave regime than at DC. For this reason, we need

an alternative measurement scheme to obtain the dielectric constant and loss tangent of the material in the range of DC−20 GHz, the largest operating bandwidth of the atom chip.

One method of doing this is to create a resonator structure on the material by intentionally creating impedance mismatches to form a "Fabry-Perot" cavity. At specific frequencies, the cavity will become resonant, allowing transmission of the injected signal, which manifests as dips in the reflection coefficient S_{11}. While there are many types of resonator designs, we opt for a simple "wide central resonator", as shown in Fig. 7.22. In

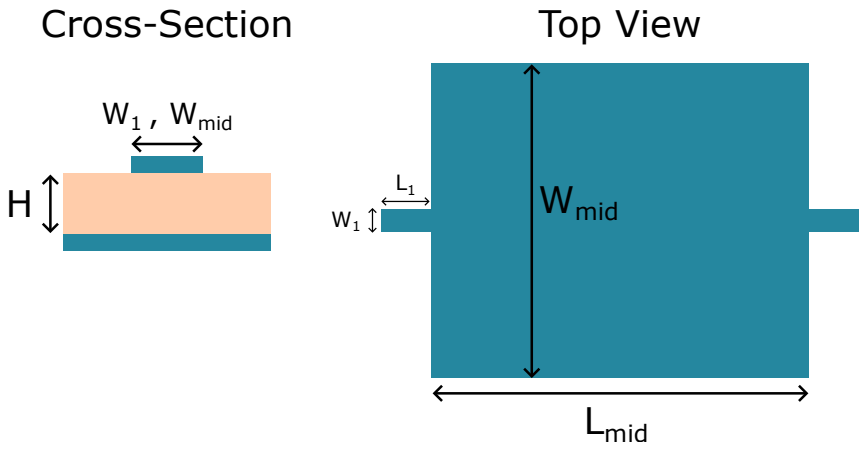

Figure 7.22: Diagram of the wide central resonator used for determining the dielectric constant and loss tangent of the atom chip substrate.

this design, a microstrip abruptly changes in width, resulting in an impedance mismatch at the boundary. A cavity is then formed within the wide central section, which transmits at specific resonant frequencies. The spacing between these resonances is related to the effective dielectric constant of the material, which in turn depends on the relative dielectric constant, ϵ_r, as well as the trace width and substrate thickness. The loss tangent can be inferred from the width of the resonances. In practice, one measures the response of the resonator and then varies ϵ_r and the loss tangent of the material in simulation to match the measured results. An example of the simulated S_{11} response of this resonator design is given in Fig. 7.23(a). In this model, $L_1 = 5$ mm, $L_{mid} = 27$ mm, $W_1 = 26$ μm, and W_{mid} is varied. Since we only know an estimated range of the dielectric constant, the process of

simulation, manufacturing, and testing may take a few iterations. These simulations use dimensions of AlON samples provided by Nitride Global, Inc., as discussed in a previous undergraduate thesis [125], notably a substrate thickness of 31.4 μm. For this thickness and an assumed dielectric constant of $\epsilon_r = 11$, a trace width of 26 μm yields a 50 Ω transmission line. We also elect to keep the "feedline" section ($L_1 << L_{mid}$ in Fig. 7.22) relatively short, i.e., a few mm, to make any resonances formed within that section at much higher frequencies than in the main central resonator region. These simulations elucidate the main sentiments behind the resonator design; however, the exact dimensions must be adapted to match the samples in the lab, which recently had AlON deposited onto them, with the biggest difference being the substrate height closer to 50 μm. Those simulations, manufacturing, and measurements will be discussed in future PhD theses.

One thing to be aware of when designing the wide central section resonator is the presence of transverse modes above certain threshold frequencies, instead of the longitudinal modes, which can be used to infer ϵ_r. These arise at frequencies above which the width of the wide central region matches the wavelength in the material. The wavelength in a given material is determined by the index of refraction:

$$\lambda = \frac{c_{vac}}{nf} \tag{7.8}$$

where c_{vac} is the speed of light in vacuum, n is the index of refraction, and f is the frequency of the wave. For a microstrip transmission line, the index of refraction is $n = \sqrt{\epsilon_{eff}}$, where ϵ_{eff} is the effective dielectric constant of the microstrip, given in Eq. 7.2.

Figure 7.23(b) shows the wavelength in the substrate material as a function of frequency for several different trace widths. The width of the microstrip does not significantly affect the effective dielectric constant, so the plotted lines lie close together. This calculation uses a substrate thickness of 31.4 μm and a relative dielectric constant of 11. We can see that as the central resonator section is increased in width, the S_{11} response begins to deviate from clean, equally spaced resonances at the frequency corresponding to the width of the

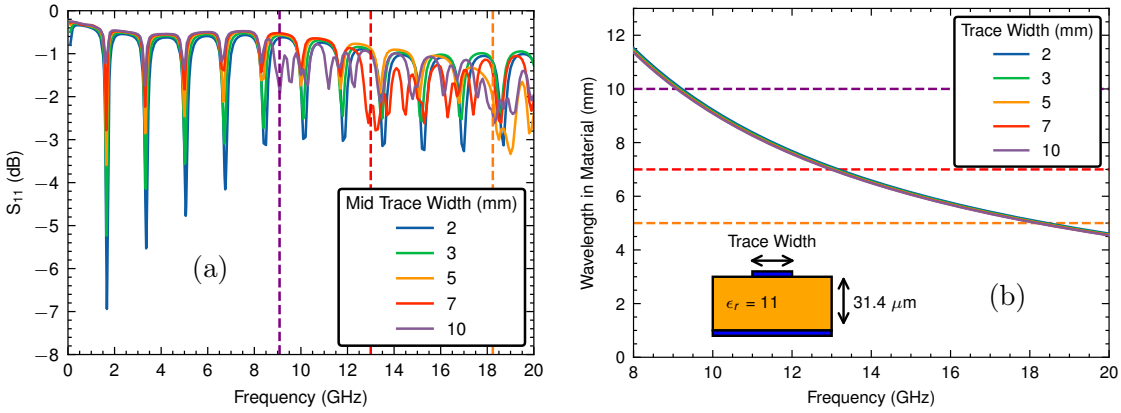

Figure 7.23: SONNET simulation of the wide central section microstrip resonator. (a) S_{11} for the resonator using different widths of the central trace. Vertical lines indicate the frequencies at which transverse modes appear, with the colors matching the corresponding central trace width. (b) Plot of the wavelength in the material as a function of frequency for different microstrip trace widths. Horizontal lines correspond to those in (a), where the crossing point with the wavelength (solid lines) gives the cutoff frequency for the resonator.

central region. For example, when the central region is 10 mm wide, we expect transverse modes to begin propagating when the wavelength in the material is 10 mm. This occurs at roughly 9 GHz, which is exactly where we see the S_{11} data break down. These simulations inform us that it is important to keep the width of the wide central section below a certain threshold width, which depends on the substrate thickness and dielectric constant, in order to obtain clear resonance data for experimental determination of the material properties.

7.7.3 Microwave Lattice

A third method for getting the dielectric constant of a material is to form a lattice on a microstrip made on that material. By sending counter-propagating microwaves along a single microstrip, one can form a standing wave. Using a pickup coil (fabricated by Sindu Shanmugadas [126]), the magnetic near-field from the microstrip can be measured on a spectrum analyzer. Moving the sensor across the length of the trace gives the standing wave structures seen in Fig. 7.24. The dielectric constant can be extracted from these measurements from the spacing between the minima or maxima of the lattice, i.e., the lattice wavelength. The effective dielectric constant for a microstrip can then be obtained

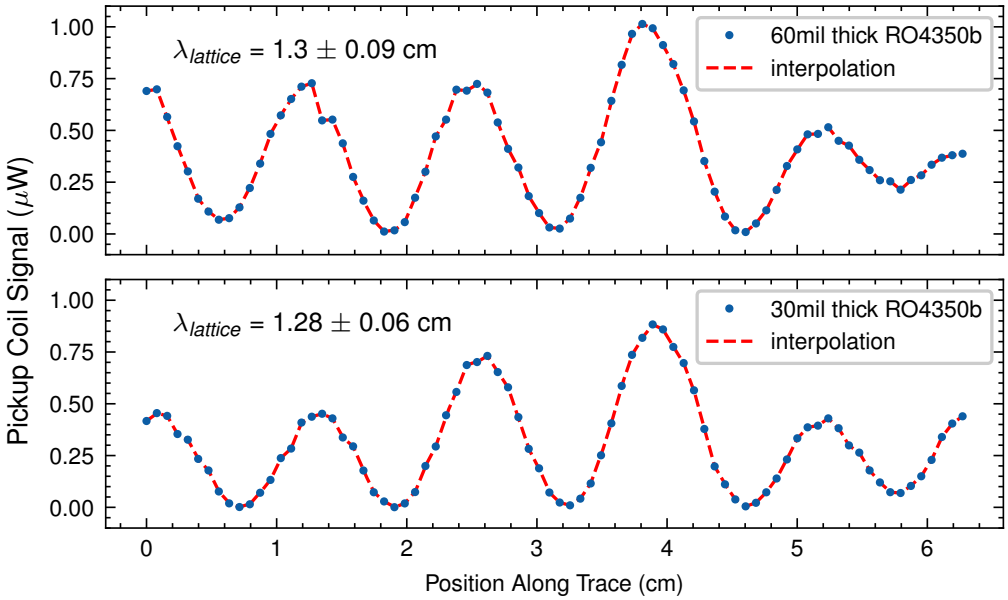

Figure 7.24: Measurements of the microwave lattice formed by sending counter-propagating microwaves at 6.8 GHz along a single microstrip transmission line. Data shows measurements for a 60 mil thick (top) and 30 mil thick (bottom) RO4350b substrate ($\epsilon_r = 3.66$).

as

$$\epsilon_{eff} \approxeq n_{eff}^2 = (\lambda_{vac}/2\lambda_{lattice})^2 \tag{7.9}$$

where λ_{vac} is the wavelength of the microwave signal in vacuum. At 6.8 GHz, $\lambda_{vac} =$ 4.4 cm. The factor of 2 in the denominator comes from the fact that the measured lattice wavelength, $\lambda_{lattice}$, is half of the true wavelength in the material. The dielectric constant is related to the effective dielectric constant through Eq. 7.2

As a proof-of-principle demonstration, we formed a lattice using two different-sized microstrip circuits, both fabricated using RO4350b as the dielectric. Table 7.2 gives the relevant dimensions of the boards. Counter-propagating microwaves a 6.8 GHz were sent along the microstrip to form the lattice, and the near-field strength was measured using a pick-up coil. Since the position resolution is rather coarse (roughly 0.08 cm), the data is interpolated to obtain the maxima and minima. We can use both to make two measurements of the dielectric constant. Table 7.2 gives the measured dielectric constant for the different RO4350b microstrip circuits using the average distance between either the lattice

H (mm)	W(mm)	ϵ_r from maxima	ϵ_r from minima	average ϵ_r	diff from [114]
1.524	3.7	3.71	3.59	3.65	0.01
0.762	1.75	3.73	3.86	3.78	0.12

Table 7.2: Dielectric constant measurements of RO4350b ($\epsilon_r = 3.66$ [114]) made using the microstrip lattice method. Measurements were made using microstrips on two different substrate thicknesses. The dielectric constants, ϵ_r, were calculated from the lattice wavelength via Eqs. 7.9 and 7.2. The wavelength was determined using either the distance between the lattice maxima or minima.

maxima or minima. From these measurements, we obtain dielectric constants at most a few percent different than the listed value of 3.66 [114], showing the practicality of this method. This could be repeated for other materials such as AlN, however, at the time we did not have sufficiently long samples to produce multiple maxima/minima.

While less reliable than the other methods mentioned here insofar as the spatial resolution must be sufficiently decent and the field amplitude appears to vary over the length of the trace, the lattice measurement could act as a simple method of cross-checking the capacitor and resonator. Moreover, the lattice can also be generated using a single input and reflecting it off a non-50 Ω load, relaxing some of the requirements for impedance matching.

7.8 Microwave ACZ Trapping on the Existing Chip – An Aside

The entirety of this chapter has dealt with the development of a novel microwave atom chip so that the lab can pursue inter-manifold microwave ACZ trapping. In introducing this topic, I claimed that we would need significant microwave power in order to produce a modest ACZ trap using the existing atom chip. While true, this is a possibility that could be explored to close out the life of the lab's original atom chip. Thanks to past [14] and current [127] PhD students, we have built a few 20 W microwave amplifiers operational at 6.8 GHz. Moreover, the IQ modulation system described in Chapter 4 allows precise frequency and phase control of microwave currents on the chip. In principle, then, we have

all the hardware necessary for creating a microwave ACZ trap; but what quality of traps would we be able to achieve with the chip already in place?

To explore this, I used an in-house microwave field simulator [16] built to model the ACZ trapping potentials generated by two parallel atom chip traces. Taking a quantization

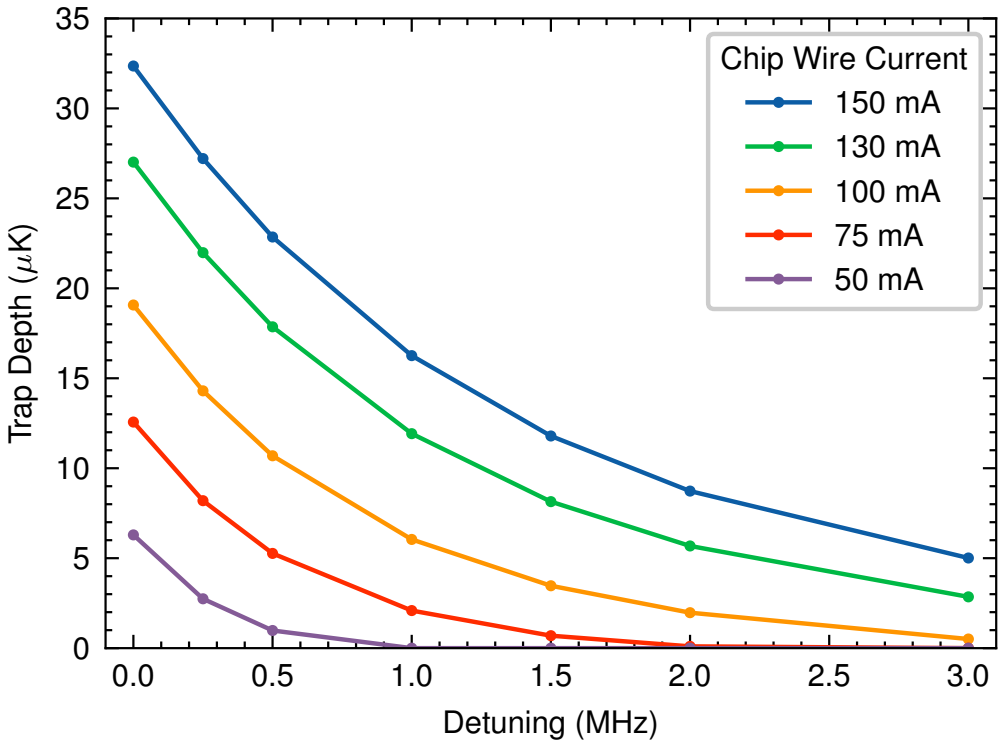

Figure 7.25: Atom trap simulations for microwave ACZ trapping using the existing atom chip in the lab. These results come from an in-house GUI used for modeling atom chip ACZ potentials [16]. The simulation uses a 28.5714 G quantization field strength, yielding a 20 MHz m_F splitting. For the $|2,2\rangle \leftrightarrow |1,1\rangle$ transition, this gives a resonance of 6.895 GHz. We input a given current with 90° phase difference through two chip wires spaced 100 μm center-to-center. Gravity is included in these calculations.

field strength of ∼28 G, we split the m_F Zeeman states by ∼20 MHz. Targeting the $|2,2\rangle \leftrightarrow |1,1\rangle$ inter-manifold transition, this sets the resonance at ∼6.895 GHz. To get an idea of the range of currents we would be able to produce on the chip, we can use the effective impedance of 2400 Ω at 6.8 GHz [16, 51], combined with the 20 W amplifier to get a max current of ∼90 mA. Figure 7.25 shows the simulated trap depth of the microwave ACZ traps generated using up to 150 mA of current through the chip wires across a range

of detunings. The current in the wires is set 90° out-of-phase, putting the trap roughly 50 μm above the chip surface. We found that for realistic currents, we should be able to achieve several μK trap depths at 0.5 MHz detuning. While there is significant risk in attempting to create this trap, insofar as the atom chip wires could be damaged due to resistive heating, it may be worth a brief exploration as the final project before switching to the new chip.

7.9 Summary and Outlook

This chapter covers the design, simulation, and initial manufacturing considerations for a novel microwave atom chip to carry out future microwave ACZ and atom interferometry experiments in the ultracold atom lab at W&M. In Sec. 7.1, we outline the design criteria for this new atom chip, settling on the microstrip transmission line as the building block, described in Sec. 7.2. Section 7.3 covers the design and simulation of the microwave atom chip, highlighting the UZU model as the design choice for the first-generation chip. In combination with the microwave chip, we present a design of a DC carrier chip in Sec. 7.4, supported by numerical simulations. We then progress to the initial manufacturing stages for the chip. In Sec. 7.5, we study the decay times of eddy currents in different conductor of varying thicknesses in order to select a suitable ground plane and backing structure for the chip. Section 7.6 then focuses on the preparation of the ground plane through diamond turning, ensuring a smooth and flat surface for deposition of the microstrip substrate. In Sec. 7.7, we cover three methods for measuring the dielectric properties of the microstrip substrate using a capacitor, resonator, and microwave lattice. We conclude with Sec. 7.8, in which we consider the feasibility of generating a microwave ACZ trap with the lab's existing atom chip. This chapter lays the groundwork for upcoming PhD theses which will cover the lithography and implementation of the microwave atom chip designs presented here.

Chapter 8

Development of a Tapered Microstrip Wedge Interface

To realize the full capabilities of the microwave atom chip discussed in the previous chapter, we need the ability to send broadband (DC-20 GHz) microwave signals onto the chip traces. This becomes challenging when working with narrow microstrip transmission lines, requiring mode-matching between the trace and a much larger SMA connector. This chapter covers our solution to the mode-matching issue, developed through simulation and prototyping. Section 8.1 discusses the motivation behind needing a new method of interfacing between the microwave atom chip and SMA connector. In Section 8.2, I investigate the first coupling method: the exponentially tapered microstrip, which turns out to be an inapplicable choice for us. Section 8.3 delves into a more suitable solution: the tapered microstrip wedge, through simulation using atom chip parameters. Initial manufacturing efforts of the wedge on aluminum nitride (AlN) are discussed in Section 8.4. We then perform large-scale prototypes of the tapered wedge design using Rogers 4350b substrate, the simulation and results of which are given in Section 8.5. Concluding remarks and outlook are given in Section 8.6.

8.1 Motivation

The previous chapter focuses on the engineering of a novel atom chip used for RF and microwave AC Zeeman (ACZ) trapping of ultracold atoms. The broadband nature of the device is unique as it allows us to target multiple atomic transitions as well as operate a microwave lattice for arbitrary axial positioning. Of interest in our lab are the inter-manifold transitions between hyperfine levels, which depend upon the atomic species, for example ^{87}Rb at 6.8 GHz, ^{40}K at 1.2 GHz, and ^{41}K at 240 MHz. The ability to trap and manipulate atoms of different species across this several GHz spectrum would allow for new and interesting experiments. From an interferometry perspective, operating at frequencies above 10 GHz opens the door for axial confinement and translation via a microwave lattice operating with the AC Stark effect [17]. Typically, however, microwave components found on atom chips are designed to target a specific frequency range for a given atomic species [128, 129, 130]. The atom chip being designed in the Aubin lab would have the unique feature of being broadband, capable of accessing a number of transitions in different atomic species. For this chip to be of practical use, it would require that microwave signals be sent through the chip efficiently with minimal reflections.

The piece in our atom chip design that makes broadband operation tricky is the narrow microstrip transmission lines. While the narrow microstrips themselves can operate at 50 Ω for tens of GHz, making a broadband connection to them from a mm-sized coaxial cable is much harder, though doable in principle. Typically, we think of reflections coming from a mismatch in the impedance between the elements being connected, i.e.

$$|S_{11}| = \frac{|Z_1 - Z_2|}{Z_1 + Z_2} \tag{8.1}$$

where $|S_{11}|$ is the reflection coefficient. However, even if the two devices are impedance matched, as they are in our case, abrupt changes in the size of the electromagnetic near-field can also result in reflections at the interface. One can liken this to the problem of mode-

matching in optics, in which the spatial profile of a laser must be well matched to a fiber or cavity for proper transmission. To elucidate this point, we simulated the connection of different-sized 50 Ω coaxial cables to a 54 μm wide microstrip trace on 50 μm of aluminum nitride (AlN, ϵ_r=8.9), giving a 50 Ω transmission line. The reflection coefficients across DC-20 GHz are shown in Fig. 8.1. From Eq. 8.1 we expect the reflection to be zero since both lines are 50 Ω. However, it is very much dependent on the size of the coaxial connector, which dictates the near-field mode size. As the connector is made smaller, the reflections are able to stay minimal up to higher frequencies. However, even for the smallest commercial connectors (SMPS), we only see about an 8 GHz usable bandwidth, limiting the use of an AC Stark lattice for axial confinement and interferometry.

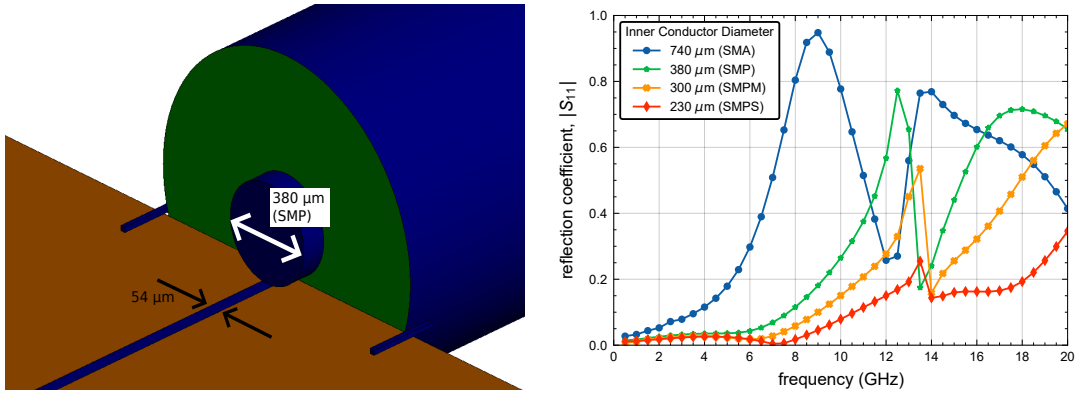

Figure 8.1: FEKO simulation of a coaxial connector directly coupling onto the atom chip. (Left) FEKO model of a 50 Ω coaxial cable (here shown with a center conductor width of 380 μm) directly attaching to a 54 μm wide microstrip trace (substrate 50 μm thick AlN with ϵ_r=8.9). The substrate used for the coaxial cable (green material) is PTFE (Teflon). The outer conductor diameter was chosen to give a 50 Ω transmission line. (Right) Simulation results showing the reflection coefficient versus frequency for different inner conductor diameters, corresponding to varying sizes of commercial connectors.

Any reflections in our system give way to the formation of a "natural" ACZ lattice that adds unwanted and uncontrollable axial confinement, analogous to the potential roughness effect discussed in Chapter 6. This is illustrated in Fig. 8.2, in which we simulate the strength of the naturally formed when the source and load are impedance mismatched from the 50 Ω microstrip. In this model, we send a 20 V microwave signal at 6.8 GHz onto a 50 Ω microstrip formed by a 54 μm wide trace on 50 μm thick aluminum nitride

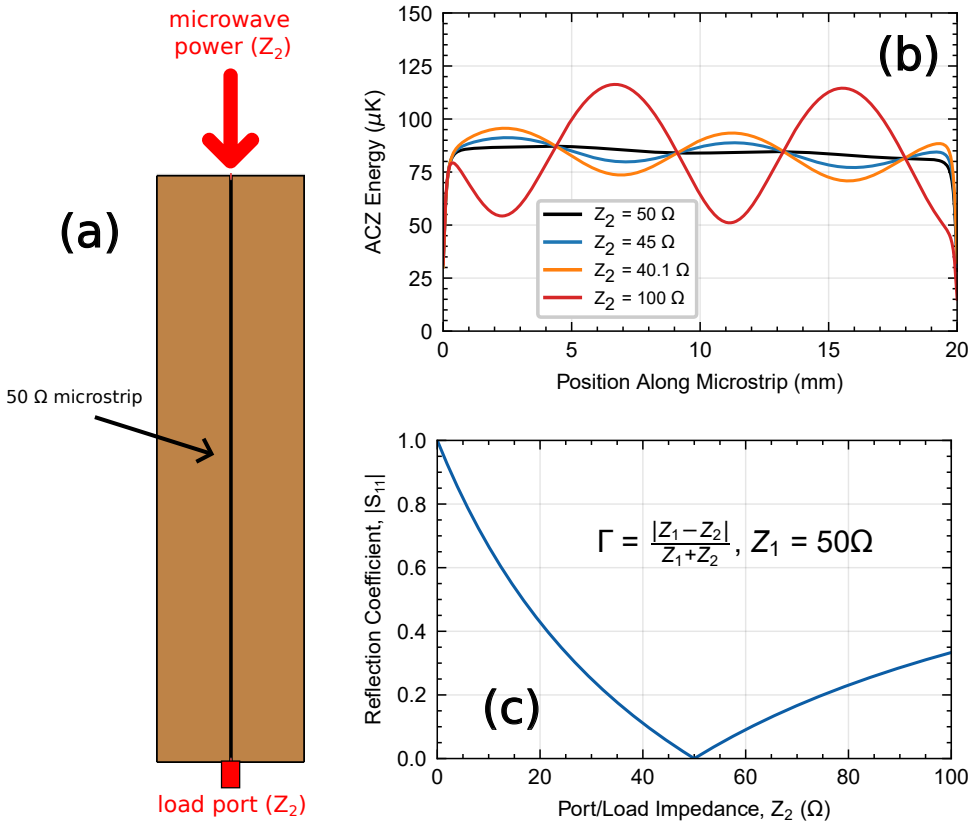

Figure 8.2: FEKO simulation of the natural ACZ lattice formed when the source and load are impedance mismatched from the 50 Ω microstrip. (a) The model uses a 54 μm wide trace on 50 μm thick aluminum nitride ($\epsilon_r = 8.9$). The source uses a 20 V microwave signal at 6.8 GHz, corresponding to 8 W of microwave power for a 50 Ω line ($P = V^2/R$). Both the source and load are set to a variable impedance, Z_2. (b) ACZ lattice for different values of Z_2, evaluated at 100 μm from the chip surface. The calculation of the ACZ potential uses the $|2,2\rangle \longleftrightarrow |1,1\rangle$ microwave transition and a detuning of $2\pi \times 1$ MHz. (c) Calculated reflection coefficient using Eq. 8.1.

($\epsilon_r = 8.9$), corresponding to 8 W of microwave power. The source and load are given variable impedance, Z_2, which results in a reflection calculable from Eq. 8.1. Figure 8.2(b) shows the ACZ energy evaluated 100 μm from the chip surface for different values of Z_2, using the $|2,2\rangle \longleftrightarrow |1,1\rangle$ microwave transition and a detuning of $2\pi \times 1$ MHz. We can see that when there is minimal reflections (Z_2 =50 Ω) the ACZ energy is essentially flat, with a small lattice due to the fact that the microstrip is not exactly 50 Ω. As soon as the reflections become non-negligible, we see a clear ACZ lattice that becomes larger with increased reflections. Scaling the natural ACZ lattice to the powers used in Fig. 3.7, we

see that the natural lattice formed with a reflection of $S_{11} = 10\%$ (1% power reflection) is a factor of 20 smaller than the intentionally made lattice formed with counter-propagating microwaves. One can therefore observe the importance of minimizing reflections from the coaxial connector onto the atom chip. Solving this problem will allow for a larger range of experimental capabilities.

An ideal approach would be a coaxial connector with a smaller mode suited for the narrow microstrip trace. This, however, was impractical given our lack of manufacturing capabilities. I investigated two potential solutions to this problem of broadband transmission: (1) an exponentially tapered microstrip, and (2) a tapered microstrip wedge, of which the development is the main subject of this chapter. The lab also pursued a third option for some time, a tapered grounded coplanar waveguide (GCPW) [131, 126], for which I developed some of the simulation tools [132].

8.2 Exponentially Tapered Microstrip

A standard, relatively broadband method of coupling rf/microwave signals onto a narrow trace is to use a continuous taper design. From the theory of small reflections, these tapers allow for a smooth transition from one electrical impedance to another over a given length. A common type of continuous taper is the exponential taper, in which the impedance changes from some initial value to a final value in an exponential fashion (see Fig. 8.3). The analytic expression for the reflection coefficient of the exponential taper based on the law of small reflections is [110]

$$|\Gamma| = \left| \frac{1}{2} \ln \left(\frac{Z_{initial}}{Z_{final}} \right) \frac{\sin(\beta L)}{\beta L} \right| \tag{8.2}$$

where $Z_{initial}$ and Z_{final} are the initial and final impedance of the tapered line, L is the length of the taper, and $\beta = \frac{2\pi f}{c\sqrt{\epsilon_{eff}}}$ is the phase constant for a microstrip, with f being the frequency, c the speed of light in vacuum, and ϵ_{eff} the effective dielectric constant of

the microstrip. At low frequency ($f \to 0 \Rightarrow \frac{\sin(\beta L)}{\beta L} \to 1$), the reflection coefficient reduces to $|\Gamma| = \left|\frac{1}{2}\ln\left(\frac{Z_{initial}}{Z_{final}}\right)\right|$.

We simulated the taper design in FEKO with a 50 Ω source and load, shown in Fig. 8.3. Here we find the reflection coefficient increasing with frequency before settling to a certain value. This value (given as the dashed lines in Fig. 8.3) is caused by the reflection between the 50 Ω source and the impedance of the microstrip line at the input of the taper, given by Eq. 8.1. This impedance mismatch at the input of the taper causes the reflection coefficient to increase.

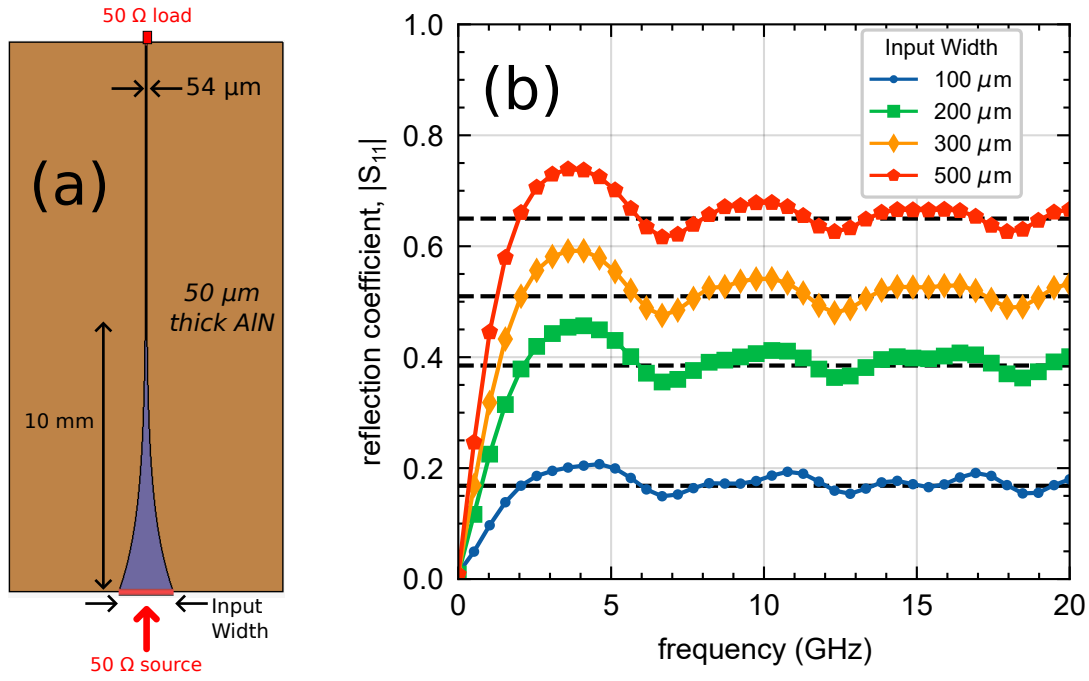

Figure 8.3: FEKO simulation of the exponentially tapered microstrip using a 50 Ω source for different input widths. (a) FEKO model for a 10 mm long taper on 50 μm of aluminum nitride (AlN, $\epsilon_r = 8.9$). The taper goes to a 10 mm long, 54 μm wide microstrip ($Z_0 \approx 50$ Ω) and is terminated by a 50 Ω load. (b) Simulation results for different input widths of the exponential taper. The dashed lines correspond to the reflection coefficient calculated from Eq. 8.1 for a 50 Ω source and the impedance of the microstrip at the input.

The reflection coefficient for the exponential taper design is plotted in Fig. 8.4 for different taper lengths, using atom chip parameters. We find that for sufficiently large taper lengths (recommended to be at least $\lambda/2$), the reflection remains low across a broad

range of frequencies. However, as we are constrained by the size of our current vacuum system, the more realistic lengths are at most ∼1 cm. The analytic expression yields large reflections for these short taper lengths, especially at low frequencies (i.e., below a couple GHz), which is a frequency range of interest for working with potassium isotopes. We also

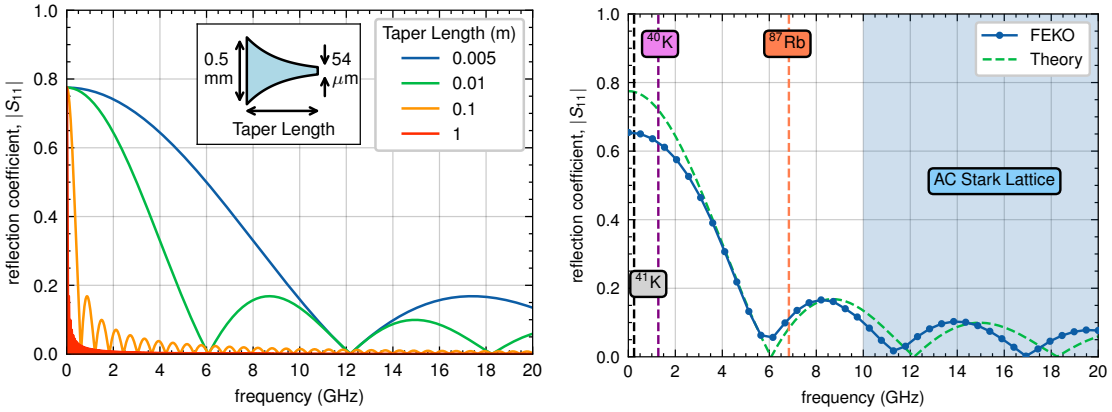

Figure 8.4: (Left) Reflection coefficient versus frequency for the exponentially tapered microstrip transmission line based on Eq. 8.2 for different taper lengths. The microstrip here is tapered from an initial width of 0.5 mm to a final width of 54 μm. The thickness of the dielectric is 50 μm and the dielectric constant is $\epsilon_r = 8.9$ (AlN). (Right) Simulation of the exponential tapered microstrip against the analytic expression in Eq. 8.2. Relevant experimental frequencies are labeled. The taper goes from a 0.5 mm to 54 μm width over 1 cm.

simulated this taper design using FEKO to validate the analytical solution. Of note is that for the same substrate thickness, the impedance of the microstrip line decreases as the width increases, so the source is no longer 50 Ω (e.g. for a 0.5 mm width on 50 μm AlN with ϵ_r=8.9, the impedance is 10.5 Ω). In the simulation, we set the source impedance to match the impedance of the transmission line at the wide end of the taper. Setting the source to be 50 Ω causes the reflection coefficient to settle about the reflection given by Eq. 8.1. We also label frequencies of interest for multiple atomic species and for the AC Stark lattice. For both rubidium and potassium, the reflection at the relevant atomic transitions is at least 10%, going above 60% below 2 GHz.

Other impedance matching schemes exist in addition to the exponential taper, such as stub tuners, quarter-wave transformers, or RF transformers [108, 110]. These alternatives, however, do not fit all of the needs we are seeking for the microwave atom chip, in that

they are narrow-band and/or not suitable for high power (20 W) operation. Additionally, RF transformers are not operational at DC, requiring a different DC operation design as that in Sec. 7.4. These devices could be used for future chip designs in which we focus on single-frequency operation, but are not suitable in the current design. To achieve the broadband performance desired from the microwave atom chip, we need to come up with a different solution to couple the microwaves onto the chip.

8.3 Tapered Microstrip Wedge Interface

Our solution to this problem of broadband RF and microwave transmission is to simultaneously taper the microstrip width and substrate thickness. Since for a given impedance the two are linearly related, varying them together maintains the same width-to-height ratio, resulting in a constant impedance along the length of the taper. Figure 8.5 shows a diagram of such a wedge coupler. In this design, the SMA connector attaches to a wide microstrip trace, compatible with its EM near-field mode size. The microstrip then tapers in width and substrate thickness over a given length until it reaches the dimensions of the microwave atom chip, namely a substrate thickness of 50 μm and a trace width of 54 μm (for AlN with $\epsilon_r = 8.9$). In the UZU chip design presented in Fig. 7.9, we require six tapered wedge interfaces, two for each of the traces. We discovered after much work that this impedance matching idea has previously seen use for increasing the size of the microstrip [133]; however, we are interested in seeing how this idea works for tapering the microstrip width down to very narrow traces. This section describes the simulation work performed in HFSS, a commercial high-frequency electromagnetic simulation software, using realistic atom chip parameters that showcase the broadband compatibility of the wedge design. We opt to use HFSS over FEKO for these simulations as it is able to better model the fields within the wedge substrate.

8.3.1 Different Wedge Lengths

The size of the current vacuum cell housing our atom chip is 4.6×4.6 cm (outer dimensions), which needs to accommodate the new atom chip and associated connectors. We would like to keep the atom chip as small as possible to negate the transition to a larger vacuum cell. Based on typical connector dimensions, we determined the maximum wedge length possible to be 10 mm. A shorter taper is preferable; however, this means a more abrupt funneling of the EM field, resulting in increased reflections. Figure 8.5 shows HFSS simulations for different wedge lengths, highlighting its effect on reflection. From this, we find we are able to maintain reflections below 4% for wedge lengths of at least 5 mm. Additionally, we see minimal change in the 10 and 7 mm long wedges, indicating we can save real estate within the vacuum cell without sacrificing performance.

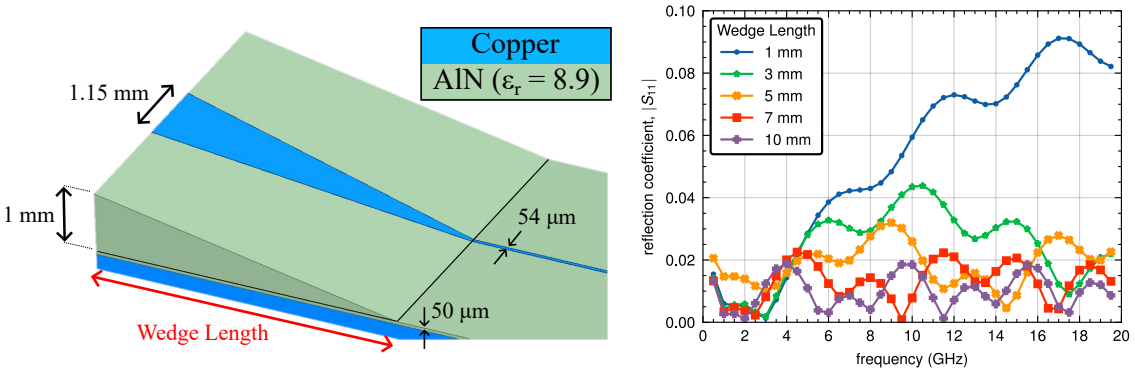

Figure 8.5: Effect wedge length on broadband reflection. HFSS model (left) and simulated reflection (right) for different lengths of the tapered microstrip wedge coupler.

8.3.2 Different Dielectric Constants

Since the wedges may be made of a different AlN than that of the atom chip, we wanted to see if having different dielectric constants between the wedge and the atom chip would affect performance. Figure 8.6 shows the simulation of a wedge with dielectric constant $\epsilon_r = 8.9$ transitioning to a microstrip with dielectric constant $\epsilon_r = 11$. The increased dielectric constant of the atom chip board meant a narrowing of the trace from 54 μm to

40.5 μm to give 50 Ω impedance, determined through simulation. Even with the difference in dielectric constant, the wedge is able to achieve reflections below 4% out to 20 GHz.

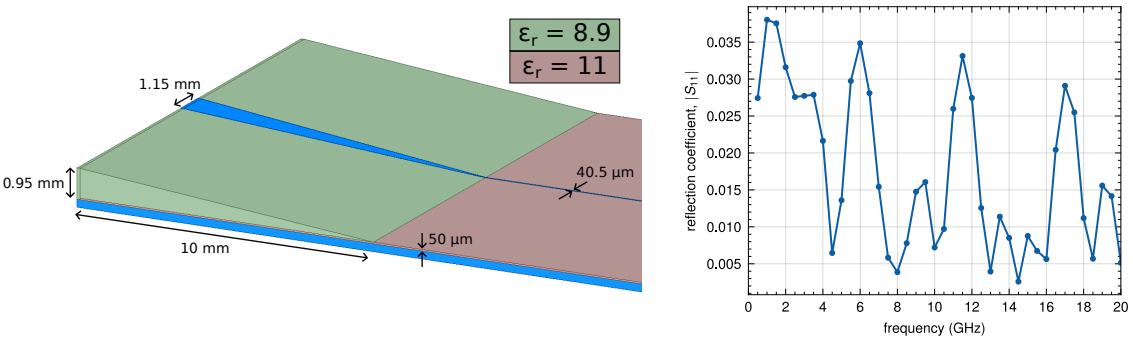

Figure 8.6: Effect of the wedge and atom chip substrates having different dielectric constants. HFSS model (left) and simulated reflection (right).

8.3.3 Effect of Cliff

In our simulations, we can force the wedge substrate to taper down to exactly zero height. In reality, however, it is impossible to machine the wedge to an infinitesimally small height at the tip. Rather, there is a cliff edge that produces a small EM field size mismatch at the interface, resulting in reflections. Figure 8.7 shows HFSS simulations of adding in a

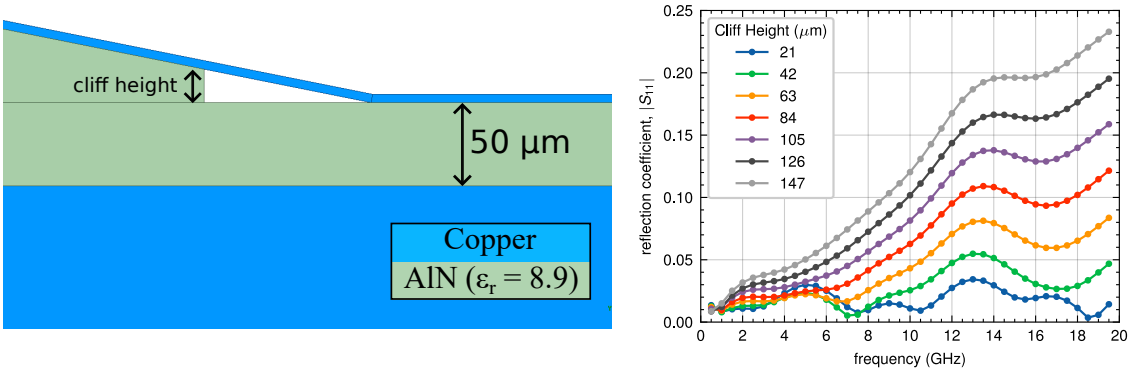

Figure 8.7: Effect of the cliff size of the tapered wedge. The cliff is modeled by removing the end of the tapered wedge substrate, leaving the trace continuous. The model uses the same parameters as that in Fig. 8.5, with a wedge length of 5 mm. For cliff sizes below ~40 μm, the reflection coefficient stays below ~5% out to 20 GHz.

cliff at the end of the tapered wedge. The microstrip trace is unchanged and bridges the

gap made from the cliff onto the atom chip microstrip. While not a realistic model, we use this as a baseline guide for the impact of the cliff. From the simulations, we see that if the cliff size is below ∼40 μm, the resulting reflection coefficient stays below ∼5% out to 20 GHz. For slightly larger cliff heights, we can maintain below 10% reflection, though for large cliffs, the reflection becomes undesirable at higher frequencies. In the manufacturing of the wedge on ceramic AlN, we found cliff heights of 10-20 μm, well below our desired threshold (see Sec. 8.4.2)

8.3.4 Effect of Wedge Size

One consideration of making the atom chip is that we have to fit six wedges onto the board. Thus, we would like to know how small we can make the wedges without affecting performance. Fig. 8.8 shows a simulation for different tapered substrate widths. These

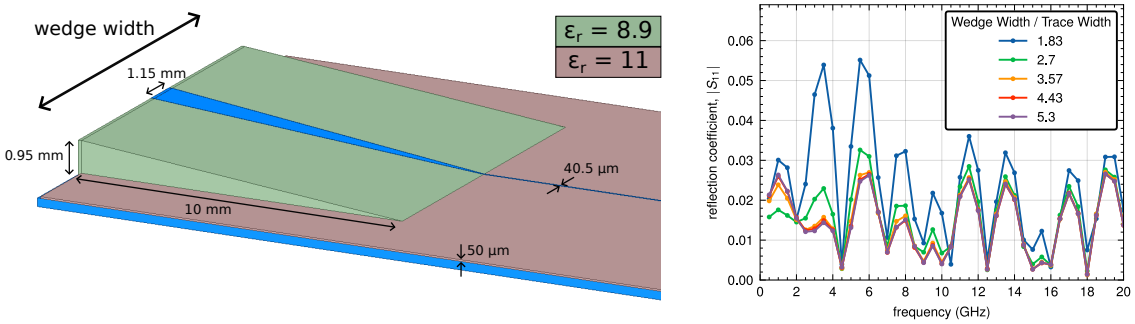

Figure 8.8: Effect of the wedge width on reflection. The model used is that diagrammed in Fig. 8.6 where the spatial extent of the wedge is varied. We find minimal difference when the width of the wedge gives at least one trace width to either side of the microstrip line.

simulations use the 40.5 μm wide atom chip microstrip on $\epsilon_r = 11$ dielectric from the model with the wedge and atom chip being different dielectric constants. The width of the initial trace is 1.15 mm. We see that the reflection coefficient does not change much as long as there is at least one trace width of substrate on either side of the signal trace. This makes sense since the size of the EM field produced extends roughly one trace width to either side, so we should at least have our wedges accommodate that size.

8.4 Manufactured Wedges on AlN

With promising results in simulation, we next turned to manufacturing of the tapered wedges. Given the number of companies selling various types of AlN, we found a wide range in the quoted dielectric constant, ranging from ∼8-10. We opted to purchase 1 mm thick ceramic AlN samples from three companies: McMaster-Carr, Sienna Tech, and Cercuits. From these samples, we could make dielectric constant measurements and find out how well each would machine to inform us for future purchases and modelling.

8.4.1 Dielectric Constant Measurements

Dielectric constant measurements were made using the capacitor method shown in Fig. 8.9, and described in Sec. 7.7. Each AlN sample was sandwiched between two pieces of high-conductivity copper, forming a capacitor. We measured the dielectric constant with the top piece of copper being 3×3 cm and 5×5 cm in size. The capacitance was measured using an LCR meter (Keysight U1731C), from which the dielectric constant can be determined via Eq. 7.7. Table 8.1 gives the measured dielectric constants using the capacitor method.

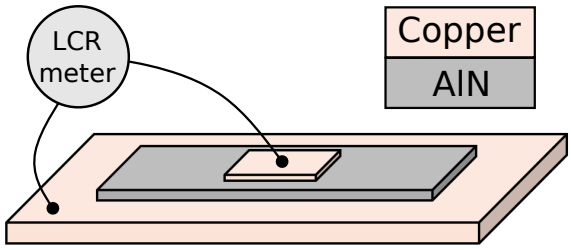

Figure 8.9: Capacitor method for measuring dielectric constant of ceramic aluminum nitride (AlN) samples. The AlN is sandwiched between two pieces of high-conductivity copper to form the capacitor. An LCR meter (Keysight U1731C) is used to measure capacitance which is related to the dielectric constant of the AlN.

Taking the averages of the 3×3 cm and 5×5 cm measurements, we find differences in the samples of $\lesssim$10%. While the measurements were relatively consistent using a given-sized capacitor plate, we did notice a difference between the 3×3 cm and 5×5 cm measurements of about $\Delta\epsilon_r = 2$. We do not try to provide a full explanation for this discrepancy, but

Manufacturer	Sample 1 ϵ_r (5x5)	Sample 2 ϵ_r (5x5)	Sample 1 ϵ_r (3x3)	Sample 2 ϵ_r (3x3)
McMaster-Carr	7.85	8.12	10.20	10.07
Cercuits	8.18	7.49	10.54	9.41
Sienna Tech	7.90	8.04	10.81	9.86

Table 8.1: Measured dielectric constants of three manufacturers of ceramic AlN using the capacitor method. Each sample was measured using both 3×3 cm and 5×5 cm copper as the top plate of the capacitor. The measurements were made at 1 kHz.

a possible explanation involves taking into account the finite size of the capacitor plates and incorporating the fringing field into the calculation of the capacitance. Including these fields acts to raise the measured capacitance, which aligns with a larger dielectric constant measured for the smaller plates. Several formulas exist for adding a contribution from the fringing fields [124]; however, we found they were not able to explain the observed difference. This apparent size-dependent effect indicates the method for determining the dielectric constant at DC must be improved. One sample of each manufacturer was sent for machining into wedges.

8.4.2 Machining

Machining of the ceramic AlN into wedges was done by an external company, Kadco Ceramics. Three wedge dimensions were made: (starting height, length) = {(1 mm, 9 mm), (1 mm, 5 mm), (0.5 mm, 5 mm)}. All wedges were 5 mm in width. As discussed previously, it is impossible to machine the AlN down to a perfect tip, resulting in a cliff edge, seen in Fig. 8.10(b). We measured an average cliff size of 21.4 μm for 35 samples, with most falling in the 15-25 μm range. From the simulation, this cliff size should be manageable and still provide low broadband reflection. We also discovered that the end of the wedge featured noticeable edge defects on the order of 100 μm, seen in Fig. 8.10(a). These edge defects would ideally be much smaller than the final trace width, i.e., ∼50 μm for the microwave atom chip, since they also affect the height of the cliff. This effect can be reduced by targeting specific regions of the wedge for lithography, where the cliff is expected to be small. These initial wedges provided confidence in our ability to obtain precision-machined

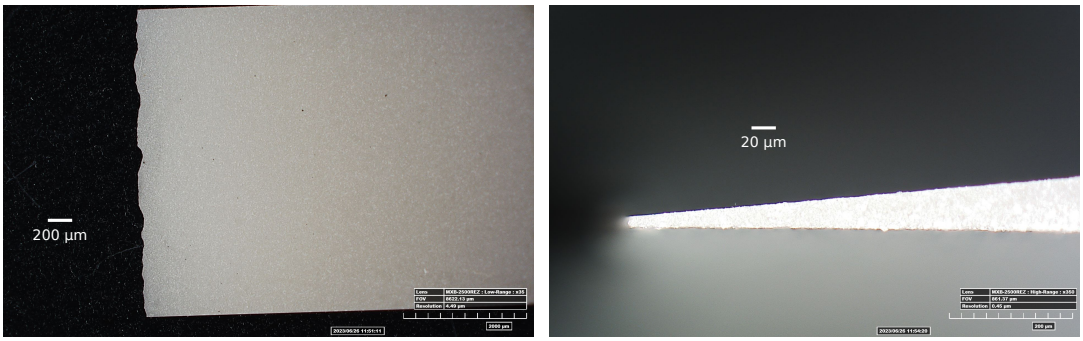

Figure 8.10: Example images of the machined AlN wedges, showing the edge defects (left) and cliff (right).

ceramic AlN. We have begun the process of depositing metallic traces onto these wedges for the future microwave atom chip [127] but this work is beyond the timescale for this thesis.

8.5 Prototypes on RO4350b

While simulations of the microstrip wedge looked promising, we wanted to perform tests on a large-scale prototype before dedicating time to manufacturing at the actual chip dimensions. We were able to find a suitable test substrate, Rogers 4350b [114], a standard microwave PCB material. With a dielectric constant of 3.66, a 50 Ω microstrip can be designed using a ∼2.2:1 width to height ratio. We opted to do our proof-of-principle testing on 254 μm thick substrates acting as our "atom chip". Simulations found that a trace width of 524 μm yielded a 50 Ω line. Taking that as the final width, we simulated a 1 cm long wedge with an initial thickness of 1.778 mm, which includes the 0.254 mm "chip" and 1.524 mm thick substrate that is machined into the wedge shape and glued onto the chip. Figure 8.11 shows the simulated reflection for this design, varying the initial input trace width of the wedge. Optimizing for minimal reflection, we chose an initial width of 4.1 mm for the prototype circuits. Figure 8.12 shows the simulated reflection (S_{11}) and transmission (S_{12}) parameters for the final prototype design.

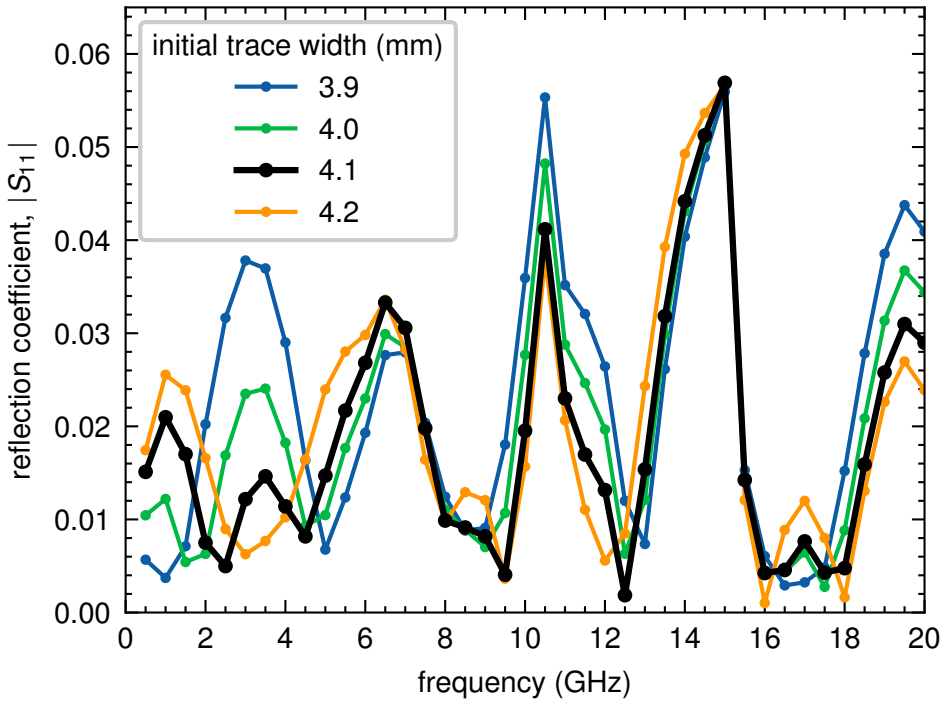

Figure 8.11: HFSS simulation of the RO4350b wedge circuit optimizing the input trace width for minimal reflections out to 20 GHz. An initial width of 4.1 mm was chosen for prototyping.

8.5.1 S-Parameters and Measurements

We can treat a microstrip transmission line as a device in which signals can be sent into and out of each end of the line. This can be visualized in Fig. 8.13 with $a_{1,2}$ being the input signals and $b_{1,2}$ the outgoing signals. We can characterize the device by measuring how much it reflects and transmits the signal we put in, which can be written as a 2×2 matrix of *S-parameters*, given as

$$\begin{pmatrix} b_1 \\ b_2 \end{pmatrix} = \begin{pmatrix} S_{11} & S_{12} \\ S_{21} & S_{22} \end{pmatrix} \begin{pmatrix} a_1 \\ a_2 \end{pmatrix} \tag{8.3}$$

The diagonal elements in the S-parameter matrix (S_{11}, S_{22}) correspond to the reflection of the input signal while the off-diagonals (S_{12}, S_{21}) give the transmission. For our microstrip transmission line circuits, the device is essentially symmetric, so S_{11}=S_{22} and S_{21}=S_{12}. Typically, we report the magnitude of the S-parameter, which can be expressed in decibels:

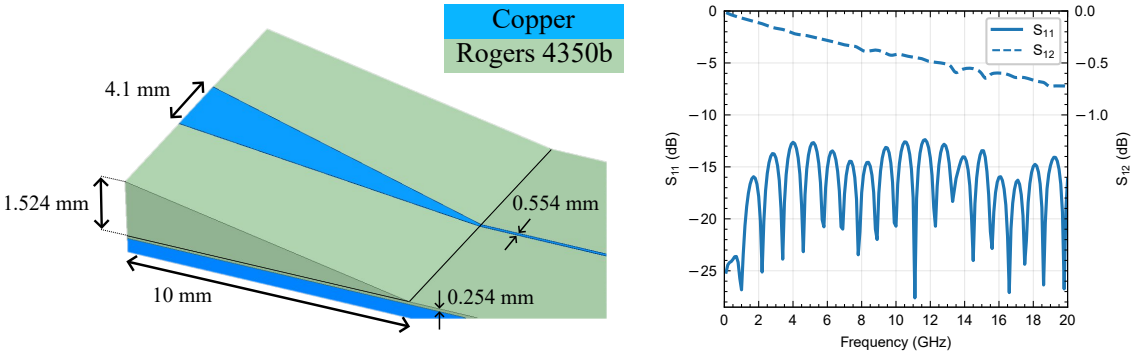

Figure 8.12: HFSS model (left) and results (right) for the RO4350b prototype wedge circuits.

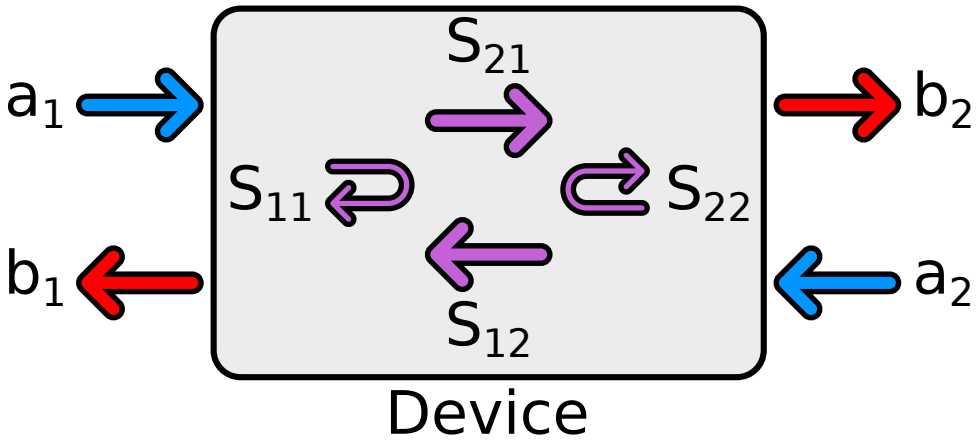

Figure 8.13: S-parameters in a two-port network. Input signals ($a_{1,2}$) enter the device and are reflected or transmitted into the outgoing signals ($b_{1,2}$). The relation between input and output signals is described by the S-parameters.

$S_{ij}[\text{dB}] = 10\log_{10}(|S_{ij}|)$. More comprehensive discussions on the topic of S-parameters can be found in Refs. [110, 108].

To measure the S-parameters for a given device, we use a vector network analyzer (VNA), specifically the Anritsu MS2038C, which is capable of measurements out to 20 GHz. An example setup for S-parameter measurements using the VNA is shown in Fig. 8.14. Signals are sent along high-quality coaxial cables onto the device under test, in this case, a microstrip transmission line. The VNA then calculates the S-parameters for the programmed frequency range, which can be exported for further analysis. Given the rigidity of the thick VNA cables and the delicate nature of some of the boards being tested, flexible

phase-stable SMA cables (Maury Microwave Stability Plus) were added to reduce the risk of breaking the circuit, with no observable change in the measurements.

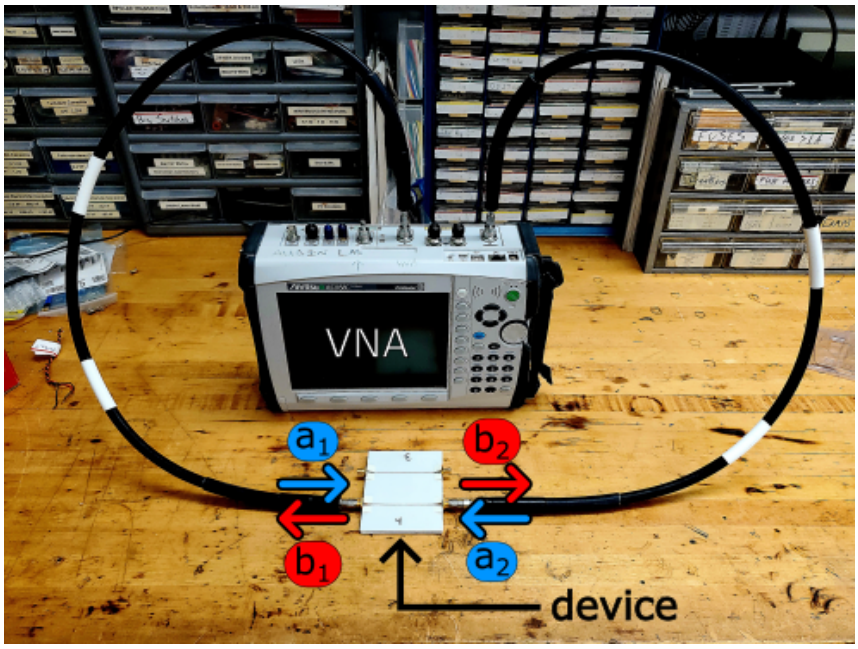

Figure 8.14: S-parameter measurement setup using a vector network analyzer (VNA).

8.5.2 Manufacturing

Figure 8.15 shows the operation workflow for manufacturing and testing the prototype RO4350b wedge circuits. In the first stage, two sets of boards were ordered from Rogers Co.: (1) 0.554 mm wide, 18 μm thick, 8 cm long copper microstrip traces on 0.254 mm thick RO4350b substrate ("straight microstrips"), and (2) the tapered traces on 1.524 mm thick RO4350b ("wedge boards"). Thinner boards (101 μm thick, 254 μm wide trace) were obtained but not used. The wedge boards were then sent to an external company (Kadco Ceramics) to be diced and have the substrate milled into a wedge shape. I will also acknowledge Will Henninger in the W&M machine shop, who aided tremendously with the initial machining of the wedges. Testing of the straight microstrip circuits without wedges was done in this initial stage, after which 1 cm of the trace was removed from each side of the microstrip to make room for the wedges.

Attaching the wedges onto the microstrip boards was done using a thin layer of commercial two-part epoxy on the underside of the wedge. The wedge trace was then aligned with the microstrip under a microscope, and firm pressure was applied for several minutes to achieve minimal air gaps between the wedge and microstrip board. Each microstrip featured two wedges, one at either end of the trace. While zero air gaps were the goal, I will note that they were still present in the final product. The wedge and straight microstrip are electrically connected by applying a small amount of silver-conductive epoxy (MG Chemicals 8331D) at the interface. While good enough for a proof-of-principle demonstration, I will note that the manufacturing of the wedge circuits could be greatly improved. This includes constant pressure for several hours when gluing the wedge onto the board, and precise application of the conductive glue such that it does not spill over the edges of the trace. Therefore, an apparatus for accurately and reproducibly attaching the wedges to the atom chip board is necessary. Such a device is currently under development.

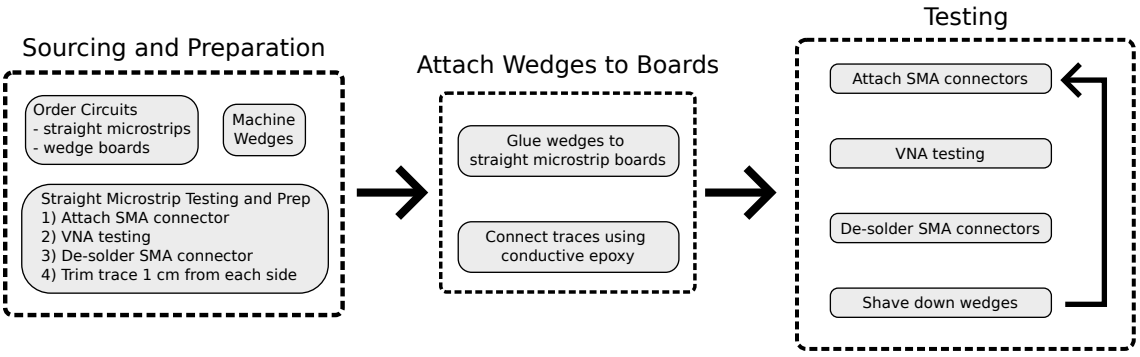

Figure 8.15: Operational workflow for manufacturing and testing the prototype microstrip wedge circuits. Each microstrip circuit uses two wedges at each end of the trace.

In testing, we found that removing the top ground pins of the SMA connector (Radiall PN: R124423223) significantly improves the bandwidth of the microstrip circuit. Figure 8.16 shows the impedance for a microstrip using SMA edge-launch connectors with and without the top ground pins removed. The process of removing the top grounds increases the bandwidth of the microstrip by ∼2.5 GHz. Throughout these tests, we continue to use SMA connectors with the top ground pins removed.

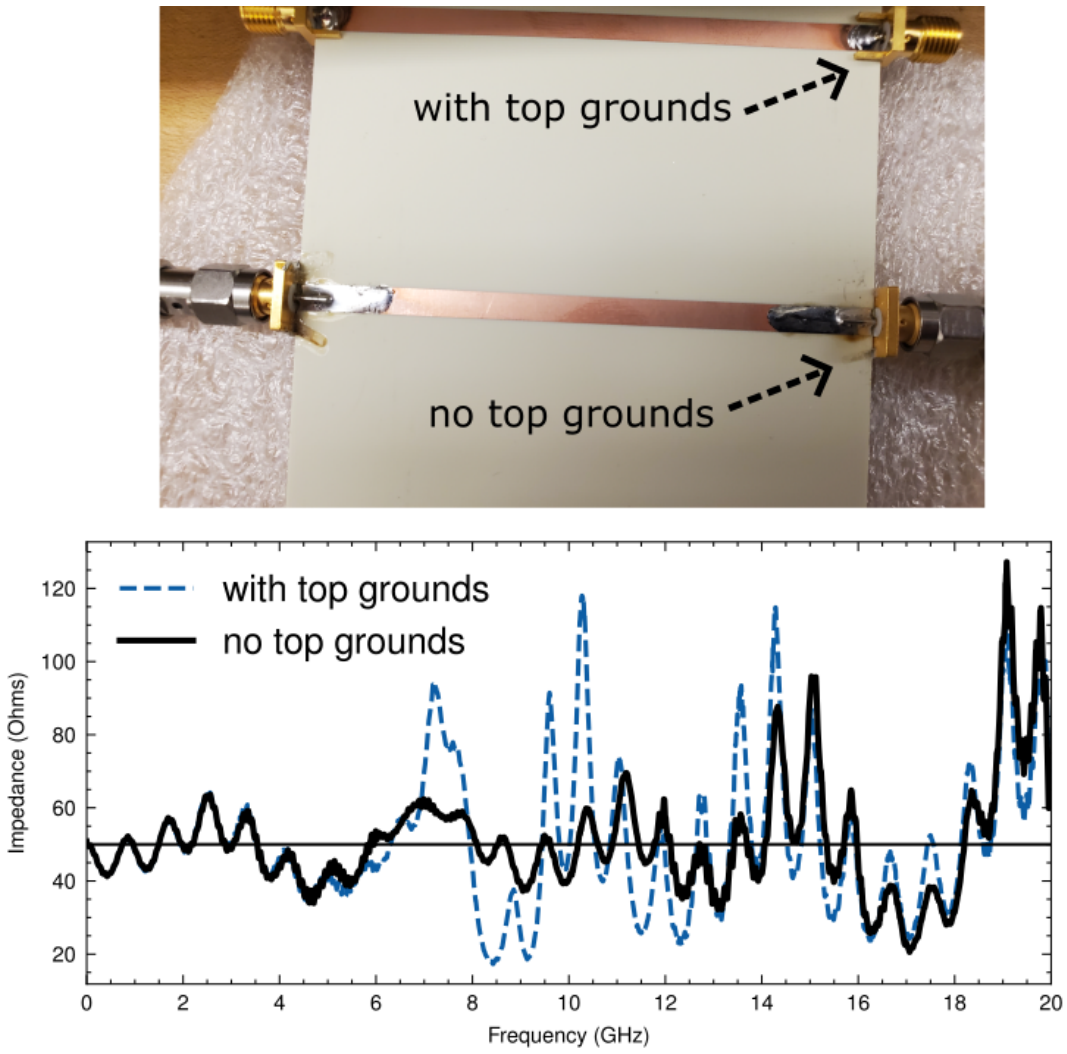

Figure 8.16: Impedance measurement of a microstrip using SMA connectors with and without top ground pins. The microstrip is made of a 3.7 mm wide copper trace on 1.524 mm thick RO4350b. Removing the top pins increases the bandwidth from ∼7 GHz to ∼12-14 GHz.

8.5.2.1 Cliff Size

During the manufacturing process, it is inevitable that one is left with a cliff edge at the end of the wedge. Ideally, this cliff would be as small as possible, but simulations reveal that there is some tolerance that can be achieved with precise machining. Figure 8.17 shows a picture of the RO4350b wedge's cliff edge using a high-resolution microscope (Hirox RH-2000). In our samples, we measured an average cliff size of 52.7 $\pm$18.6 μm for a sample size of 49 wedges. The majority of the measured cliff heights lie within $\approx$12 μm of the average, except for two at a cliff height of roughly 120 μm, which increase the standard deviation significantly.

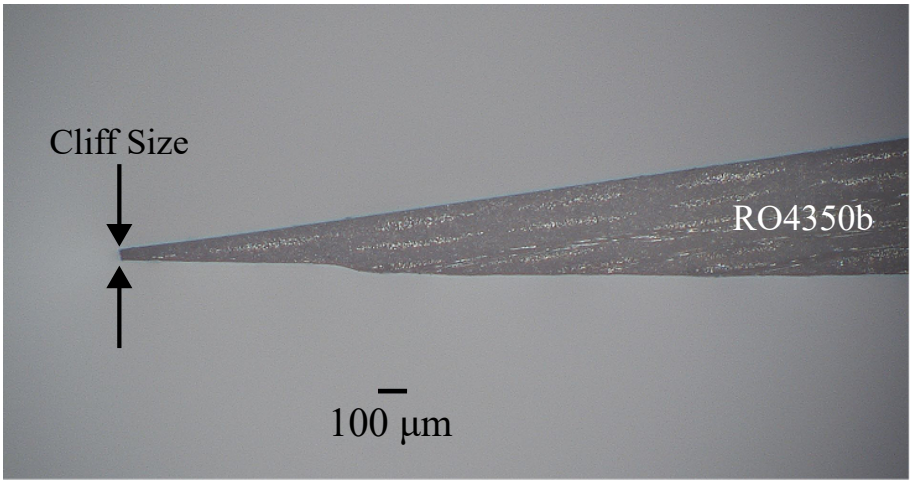

Figure 8.17: Side profile image of tip of the RO4350b wedge, illustrating the cliff edge. The average cliff size in our samples is 52.7 $\pm$18.6 μm.

8.5.3 Simulating Imperfections

We now move on to investigating how sources of manufacturing imperfections affect the broadband performance of the wedge circuits. Here, I consider two scenarios: the effect of the cliff and silver epoxy.

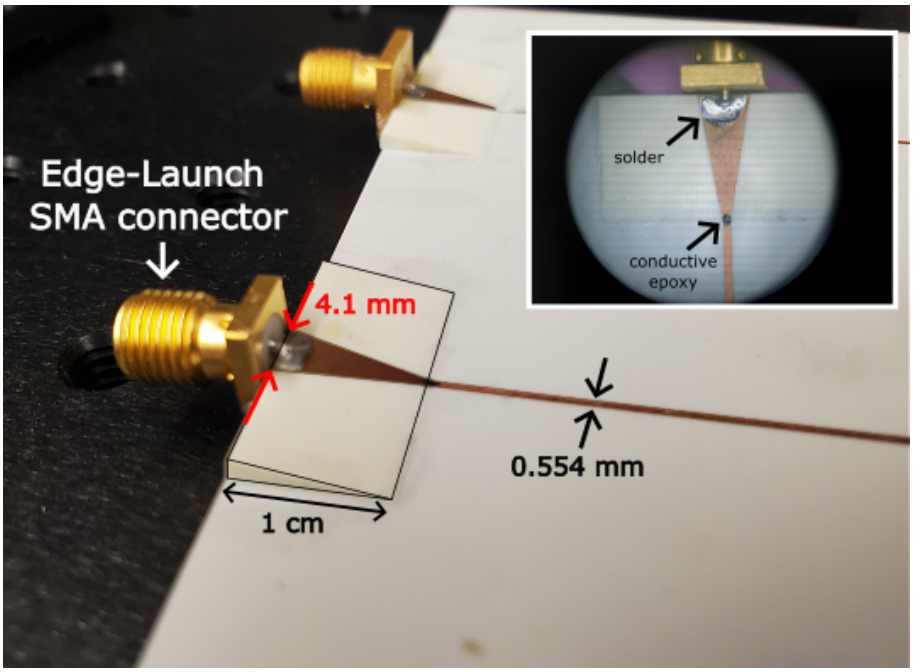

Figure 8.18: 1 cm long tapered microstrip wedge circuit on Rogers 4350b substrate with relevant dimensions labeled. The wedge and metallic traces were outlined for easier visualization. Inset: Birdseye view of the wedge to highlight the electrical connections via solder and conductive epoxy.

8.5.3.1 Modeling the Cliff

To model the effect of the cliff on the wedge coupling, we cut off the end of the wedge while keeping the tapered trace continuous, varying the cliff height up to 200 μm. We show the reflection coefficient across the DC-20 GHz range in Fig. 8.19, electing to display the maxima of the reflection for easier visualization. For cliff heights on the order of 50 μm or less, we observe minimal changes in the reflection coefficient magnitudes. Therefore, in our prototype wedges, we do not expect to see significant impacts on performance from the presence of the cliff.

8.5.3.2 Modeling the Epoxy

Taking an approach more in line with reality, we model the performance of the wedge coupler when the connection between the cliff and microstrip is made using a silver conductive epoxy, as is done during prototyping. Figure 8.20(a) shows the model with relevant pa-

rameters. Here, the cliff edge is brought flush with the 0.554 mm wide straight microstrip, and the electrical connection is made using epoxy. The simulation models the epoxy with a relative permittivity of $\epsilon_r = 4.1$, relative permeability of 1, a bulk conductivity of 10,000 $(\Omega{\cdot}\mathrm{m})^{-1}$, and a mass density of 2.4 $\mathrm{g/cm^3}$. We use a cliff height of 50 μm, which is similar to the manufactured cliff height for prototyping. We did not observe a significant dependence on the length of the silver epoxy in the simulation, so we opted for a 2 mm long section, which is similar to that during prototype work. The maxima of the simulated reflection coefficient across the DC-20 GHz range are given in Fig. 8.20(b). From these simulations, we determine that keeping epoxy solely on the trace is key to maintaining low reflections. While doable for large-scale microstrip sizes, this requirement becomes significantly harder when dealing with microstrip widths on the order of tens of microns, and requires more specialized application techniques. One could imagine designing the coupler in a "reverse wedge" configuration (see Fig. 8.25), which would eliminate the need for the epoxy.

8.5.4 Results

Once the wedge circuits are built, we attach each one to a vector network analyzer (VNA), which measures the reflection (S_{11}) and transmission (S_{12}). Figure 8.21 shows the main results of this prototype work: the comparison in performance between the SMA-to-microstrip connection with and without the addition of the tapered wedge interface. I will emphasize that each board uses two wedges at either end of the trace, in a "double-wedge" configuration, so the results presented here are for two wedge couplers. To demonstrate the repeatability of the wedge coupler construction, I built ten individual circuits. The performance shown here is the average of up to ten circuits. I note that during the process of sanding down the ends of the wedges (see Fig. 8.15), some of the wedges got removed from the boards. The minimum number of circuits used for the averaging and standard deviation was seven. The measurements of the wedge performance feature some noise, so a low-pass filter is added in post-processing for easier visualization of the data. We

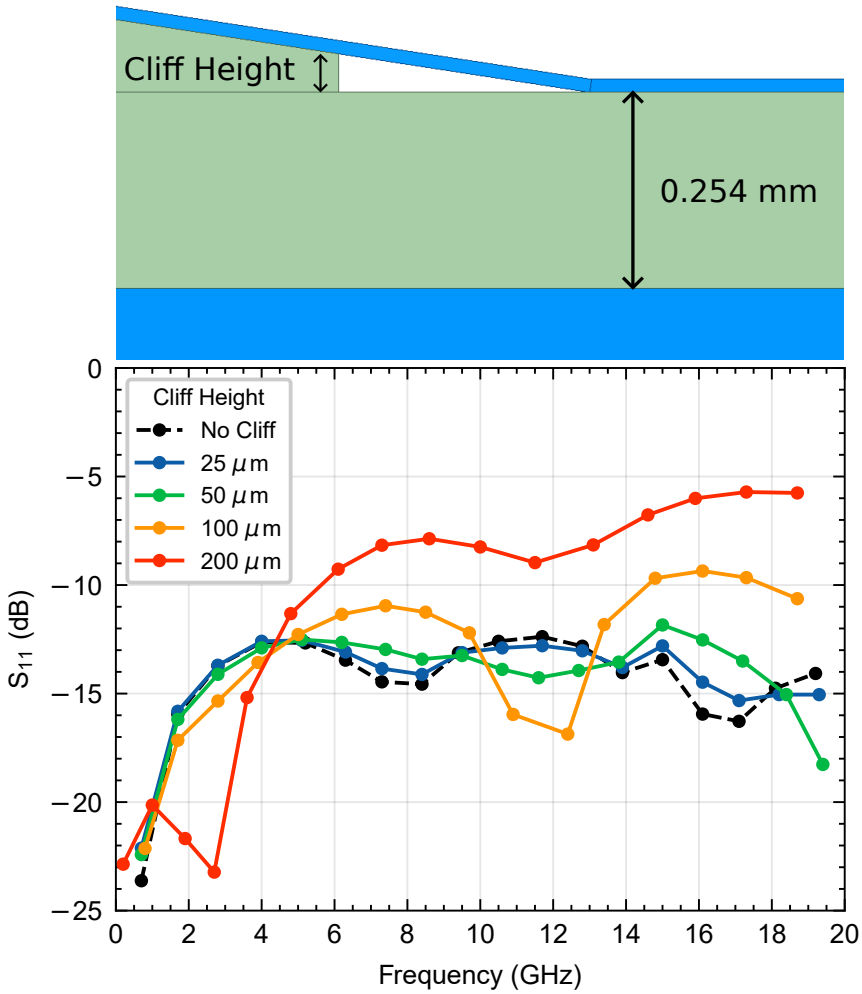

Figure 8.19: HFSS simulation showing the effect of the cliff on the performance of the tapered wedge coupler. (a) Simulation model including a cliff. This model uses the parameters in Fig. 8.18 with a wedge length of 10 mm. The value of the cliff height is scanned, and the length of the cliff is changed accordingly as $l_{cliff} = h_{cliff} * L/H_1$. Here, $L = 10$ mm. (b) Simulation results showing S_{11} for different values of the cliff height. The reflection for the wedge with no cliff is shown for comparison as the dashed black line.

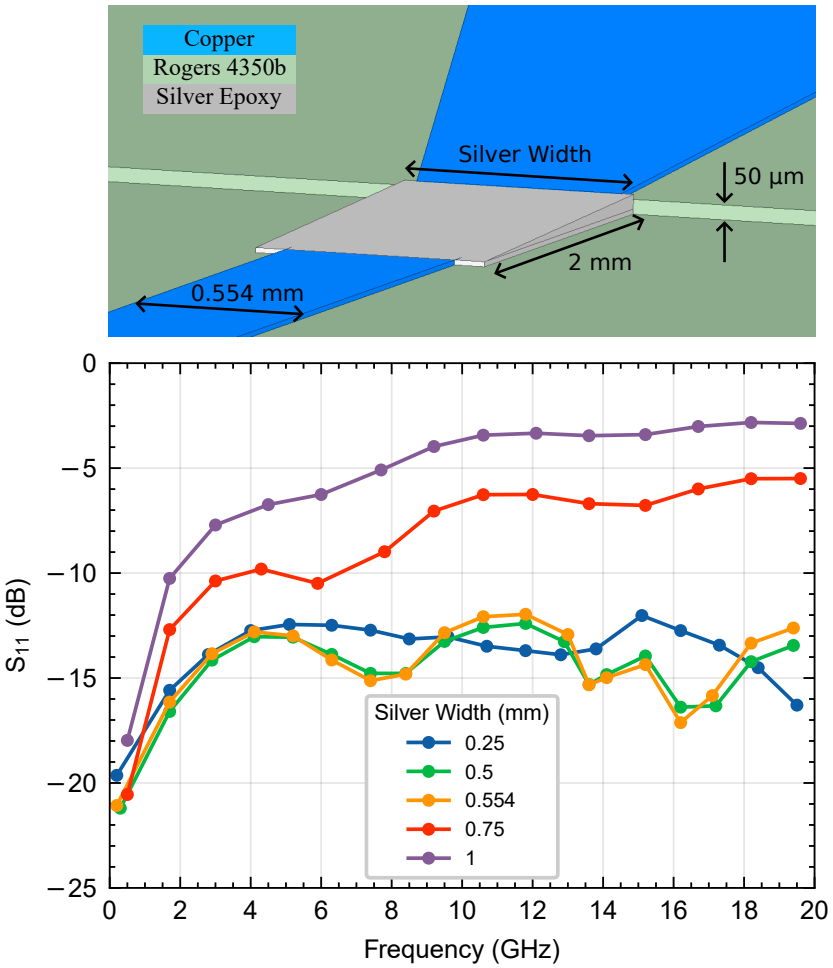

Figure 8.20: HFSS simulation modeling the use of silver conductive epoxy to electrically connect the tapered wedge coupler to the straight microstrip. (a) Simulation model with relevant parameters. Here, the cliff edge of the coupler is brought flush with the straight microstrip, upon which lies the triangular silver wedge. When the silver width exceeds the width of the straight microstrip, W_2, the gaps are filled with silver epoxy. (b) Simulation results showing S_{11} for different values of the width of the silver epoxy.

observe improved circuit performance with the tapered wedge interface across the entire DC-20 GHz frequency range. At worst, the wedge is on par with the circuit with no wedge, specifically in the 6-9 GHz range. Elsewhere, the addition of the wedge lowers the reflection coefficient (S_{11}) by 5-10 dB. The insertion loss, S_{12}, is similar between the two cases out to roughly 14 GHz, where the addition of the wedge aids in reducing loss. In this 14-20 GHz region, the S_{12} data have linear slopes of -0.29 and -0.75 dB/GHz with and without the wedge coupler, respectively. Additionally, the wedge coupler quells oscillations in the S_{12} parameter indicative of reflections at the ports. We note that $|S_{11}|^2 + |S_{12}|^2$ does not equal 1 across the entire frequency range, likely due to resistive heating losses or potential broadcasting. Variations in the impedance from 50 Ω are also reduced with the addition of the wedge, highlighting its enhanced compatibility with standard microwave devices.

A unique benefit of the wedge coupler design is the ability to adjust the initial width to best match the connector or application. To illustrate this, we shave down the ends of the wedges while attached to the circuit using a belt sander with 400-grit sandpaper and remeasure the circuit performance. Figure 8.22 shows the wedge circuit after shaving by roughly 5 mm. We demonstrate the effect of shaving via two metrics. Figure 8.23 shows the maxima of the measured S_{11} of the wedge coupler for different amounts of being shaved down. We also observe an improvement in the transmission of the circuit with the addition of the wedge, notably at higher frequencies, i.e., above 10 GHz. In Fig. 8.24 we plot the slope in dB/GHz of the S_{12} parameter for different amounts of shaving.

With this technique, one can also trade off performance over a given frequency range. For example, a microstrip-based microwave atom chip [17] has shown limited operation past roughly 10 GHz. As such, shaving down in the 1-2 mm range yields lower reflections while sacrificing higher frequency performance. This corresponds to an input width for the wedge of 3.39-3.75 mm, given by $W(l) = W_1 - \left(\frac{W_1 - W_2}{L}\right) l$, where l is the shave down length. If the user seeks a more broadband nature, shaving the wedge down 3 mm, giving an input width of 3.04 mm, produces smaller reflections out to 20 GHz at the cost of slightly larger reflections at lower frequencies. This highlights the flexibility of the three-

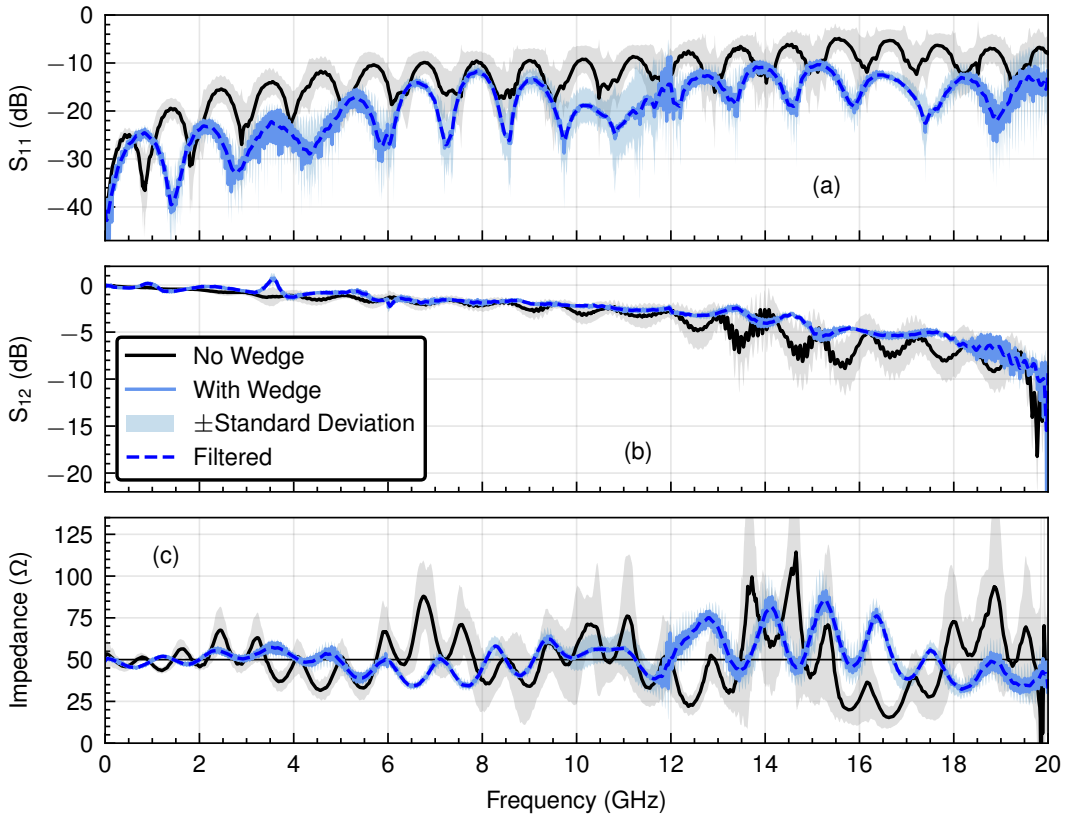

Figure 8.21: Comparison of the performance of the circuit with and without the tapered wedge interface. Measured S_{11} (a), S_{12} (b), and impedance (c) from a vector network analyzer. The data shown are an average of several of the same circuits, and the standard deviation is shown as the shaded region. A low-pass filter is applied to the wedge data (blue) for visualization. The wedges were shaved down roughly 3 mm for improved performance.

dimensional wedge design, showing how it can be tailored to a given application and edge launch connector.

8.6 Conclusion

This chapter demonstrates a unique method for broadband coupling of microwaves between a coaxial SMA cable and a narrow microstrip transmission line using a three-dimensional tapered substrate. We do this through simulations using realistic atom chip parameters as well as with large-scale prototypes with similar tapering factors. This proof-of-principle testing opens the possibility of making even more dramatic tapers. The taper factor of

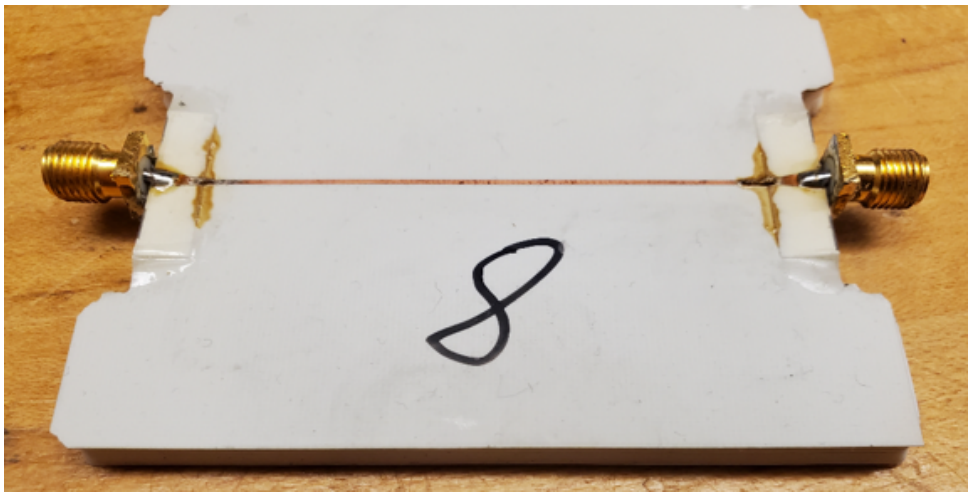

Figure 8.22: Wedge circuit after shaving each end down by roughly 5 mm.

7.4 is on the order of tapering down from an SMPM connector to a 50 μm microstrip transmission line, which we have proposed for ac Zeeman trapping on a microwave atom chip [17]. We also had wedges made for tapering down to 254 μm wide microstrips on 101 μm thick RO4350b, yielding a taper factor of 16, but these have yet to be tested. The process of precisely and reliably attaching the wedges is made more difficult by the smaller sizes, and will be left for a future project to build an apparatus for such an application. Improved machining of the wedge (smaller cliff size) and manufacturing of the circuit (precise application of conductive epoxy, no air gaps) could see enhanced performance to that presented here. We have shown that despite the sub-optimized connection of the wedge to the rest of the circuit, we are still able to substantially increase the operational bandwidth, opening up new avenues for atom chip-based experiments.

This design could also be used in a "reverse wedge" configuration similar to Ref. [133]. While this requires precise machining of the ground plane and more complex deposition techniques, it allows for a planar surface for making the microstrip traces. This would allow for a continuous wedge-to-chip trace, removing complications arising from the cliff or epoxy connection at the end of the wedge. However, this approach may be complicated by the manufacturing and deposition requirements. We have simulated this design and found

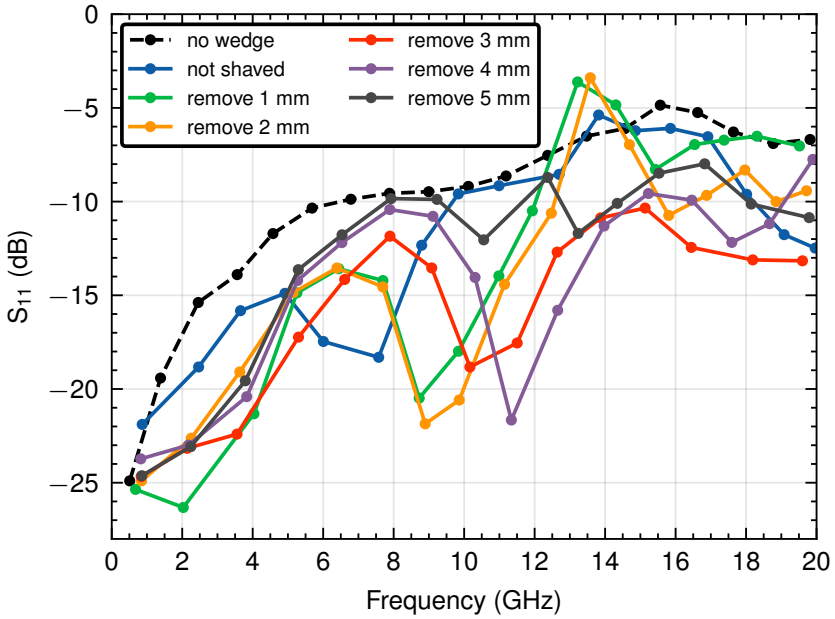

Figure 8.23: Maxima of the S_{11} data for the microstrip wedge when shaving down for different amounts. The performance of the wedge circuit without shaving is indicated by the black dashed line.

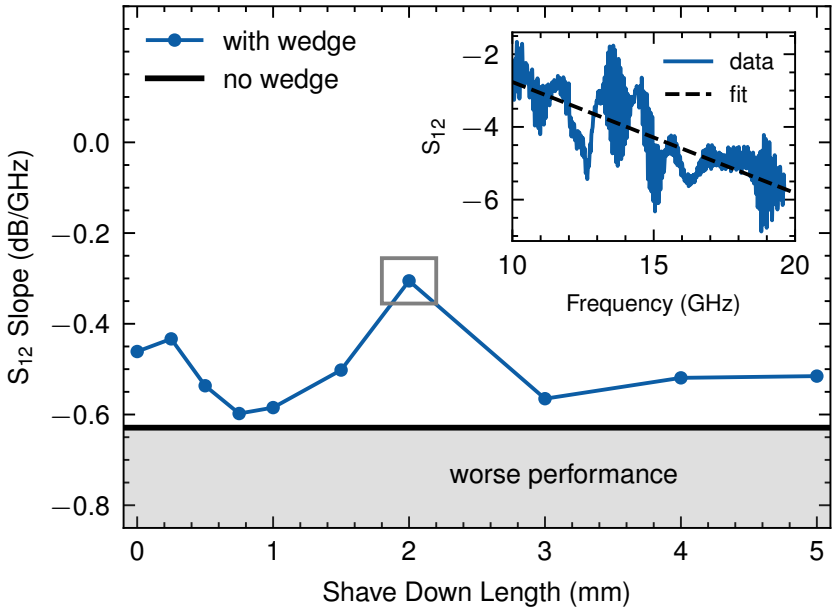

Figure 8.24: Linear fits to the S_{12} data in the 10-20 GHz range for different amounts of shaving of the wedge. The performance of the wedge circuit without shaving is indicated by the solid black line. Below this line (gray shaded region) is indicative of a decrease in performance when compared to the case without the wedge interface. Inset: example data and fit for the 2 mm shave down length.

comparable performance between the two configurations. While we only investigated a

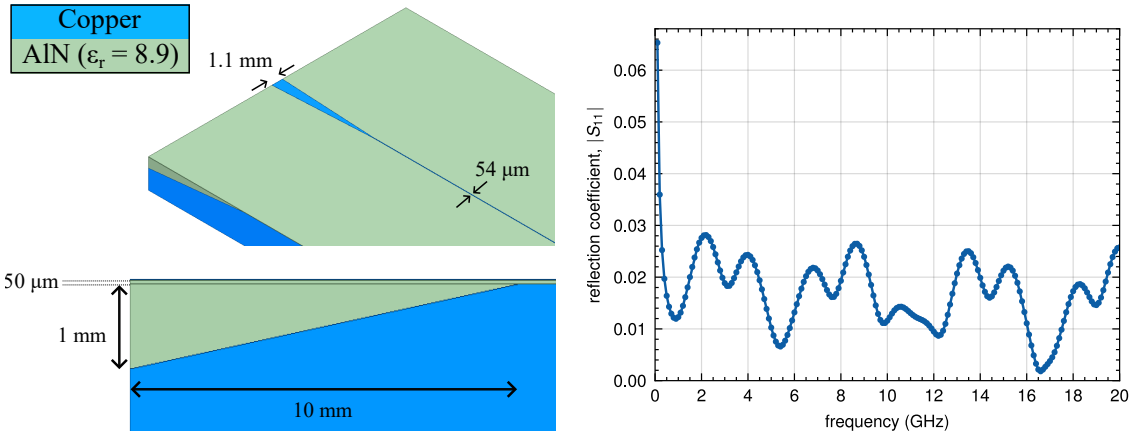

Figure 8.25: Reverse wedge taper design for broadband transmission to the atom chip. The substrate taper is made by cutting out the copper ground plane into the wedge shape and filling it with AlN. (Left) HFSS model and relevant parameters. (Right) Simulation results showing low reflection out to 20 GHz.

linear taper design in this work, other more complex geometries, such as an exponential or Klopfenstein taper [110, 108], could be explored for improved performance.

Chapter 9

Outlook and Conclusion

In the introduction to this thesis, I described how spin-specific AC Zeeman (ACZ) potentials generated on an atom chip could be used to measure inertial forces and probe fundamental interactions. While the proposed atom interferometer will be realized in future PhD work within our group, this thesis has advanced both the understanding and practical implementation of ACZ potentials in preparation for those experiments.

In particular, I characterized the longitudinal behavior of the ACZ trap, demonstrating suppression of potential roughness over its traditional DC Zeeman counterpart (see Chapter 6). A key aspect we observed is the elimination of fragmentation in the atom cloud. In the context of interferometry, in which the atoms are translated axially along the atom chip traces, the ACZ trap will not be subjected to climbing over "hills" in the potential, thus maintaining coherence during the interferometry sequence.

Beyond exploring the underlying physics of ACZ trapping (see also Chapter 5), I designed a novel broadband microwave atom chip for generating microwave ACZ traps (Chapter 7). This chip will allow for spin-specific trapping and manipulation of atoms, fully realizing the interferometry scheme. As part of this work, I also developed the tapered microstrip wedge interface, which allows broadband signal transmission from a coaxial cable onto the atom chip (Chapter 8).

In the remainder of this chapter, I discuss practical considerations for implementing

the atom interferometer, focusing on the tolerances of key ACZ trap parameters required to achieve realistic interferometer integration times. I conclude by outlining directions for future research involving ACZ traps.

9.1 Interferometry

With the end goal of performing atom interferometry with spin-specific ACZ traps, I will discuss the proposed interferometry schemes, as well as some of the practical stability constraints of such an interferometer. This section comes from a paper published by our group [17]. Calculations for this section can be found in Appendix E.

Microwave lattices enable potentially large interferometer arm separations on the cm scale. Spin-specific transverse trap positioning can be used to beamsplit and separate spin states towards the outer traces of the three-microstrip geometry, while microwave lattices on these outer traces can then be used to translate the spin states axially for cm-scale interferometer arm separations. Microwave lattices on the outer traces can use an ACZ potential (spin-dependent) or an AC Stark potential (spin-independent). In the latter case, the lattice can be operated at a much higher microwave frequency for tighter axial confinement. As shown in Figure 9.1, this interferometer architecture can operate in a gravimeter configuration (outer lattices translate in opposite directions for a large arm separation) or in a Sagnac configuration (outer lattices translate in the same direction for a large enclosed area).

While each lattice is localized on an outer trace, there can be residual "crosstalk", where the lattice potential from one trace perturbs the trapping potential for spin states on the other trace. This crosstalk between the lattices on the outer traces can be minimized by applying lattice currents (at a given microwave frequency) to multiple microstrips with the appropriate phases and amplitudes to further suppress the unwanted lattice at a spin state's location, i.e., make a "trap" or microwave lattice field minimum (zero) at its location.

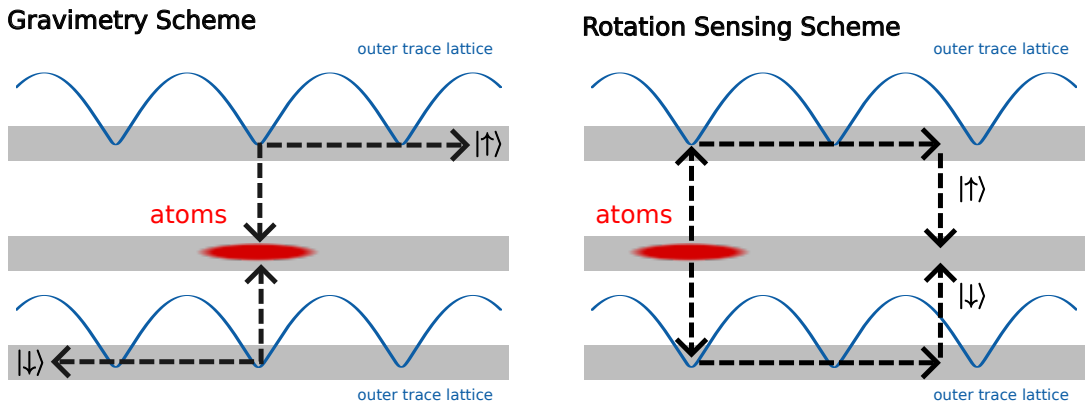

Figure 9.1: Schematic representation of gravimetry (maximum arm separation) and rotation-sensing (maximum enclosed area) configurations for the interferometer. The outer trace lattices can employ either an ACZ or an AC Stark potential for axial confinement. Figure adapted from Ref. [17].

9.1.1 Interferometer Stability

The viability of the spin-dependent interferometry approach depends on the stability of the interferometric phase with respect to imperfections and noise in the system parameters, as well as to external magnetic field noise. We identify three main decoherence and dephasing mechanisms: (1) Asymmetry of the two spin-dependent traps that constitute the interferometer arms, (2) gravimetric sensitivity of arm displacements to microwave trapping parameter fluctuations, and (3) differential DC Zeeman shifts between the two spin states.

9.1.1.1 Asymmetry Decoherence

Any asymmetry in the trap frequency of the harmonic traps for the two spin states leads to decoherence, since the spin states then have slightly different trap state energies and thus dephase over time. This decoherence mechanism has been studied both theoretically [134, 135] and experimentally [136]: the coherence time is given by $t_c = \hbar\omega_{trap}/(|\delta\omega_{trap}|k_BT)$, where ω_{trap} is the trap frequency, $\delta\omega_{trap}$ is the trap frequency asymmetry, and T is the temperature of the atoms (k_B is Boltzmann's constant). While the symmetry of the traps can be enforced by the careful adjustments of trap parameters over the course of

the interferometry process, uncontrolled deviations in the parameters ultimately lead to asymmetry fluctuations in the two traps. In a microwave ACZ trap, deviations in the trap frequency $\delta\omega_{trap}/\omega_{trap}$ are directly related to the microwave power fluctuations $\delta P/P$ (via the Rabi frequency Ω) and the microwave frequency stability $\delta\omega_{\mu w}/\omega_{\mu w}$ (via the detuning δ).

Table 9.1 shows the tolerance on trap system parameters to ensure a coherence time of $t_c = 1$ s. We use a target coherence time $t_c = 1$ s, since such a time is useful for competitive atom interferometry measurements [3], and such a time has been demonstrated in atom chip-based Ramsey interferometers [137, 14]. The power and frequency tolerance requirements are derived from the trap frequency asymmetry requirement. A power stability of $\delta P/P < 5 \times 10^{-5}$ requires active microwave amplitude stabilization. The microwave frequency stability of $\delta\omega_{\mu w}/\omega_{\mu w} < 10^{-8}$ is based on a detuning of 1 MHz and is well within the stability of commercial oscillators referenced to a high-quality clock.

Parameter	**Asymmetry Tolerance**
Trap Frequency, ω_{trap}	$\frac{\delta\omega_{trap}}{\omega_{trap}} < 2.5 \times 10^{-5}$
Power, P	$\frac{\delta P}{P} < 5 \times 10^{-5}$
Frequency, $\omega_{\mu w}$	$\frac{\delta\omega_{\mu w}}{\omega_{\mu w}} < 10^{-8}$

Table 9.1: Twin trap asymmetry decoherence: Asymmetry tolerance on the trap frequency ω_{trap} of the two traps of the interferometer in order to ensure a coherence time $t_c = 1$ s. The table includes the corresponding requirements on the microwave power P and frequency $\omega_{\mu w}$ of the microwaves that generate the two traps to limit the asymmetry on ω_{trap}.

9.1.1.2 Gravimetric Dephasing

If the two traps of the interferometer experience a differential vertical position fluctuation, i.e., along the local direction of gravity, then a corresponding gravimetric fluctuation in the interferometer phase accrues. This gravimetric contribution to the interferometer phase φ is given by $\delta\varphi = mg\delta ht/\hbar$, where m is the mass of the atom, g is the local acceleration due to gravity, t is the interrogation time, and δh is the vertical position fluctuation. In a three-trace trap, the trap position is controlled by the microwave power (y-axis), the phase

of the transverse trapping microwave currents (x-axis), and the microwave lattice phase (z-axis).

Table 9.2 shows the required stability on the vertical position δh and the corresponding stability on the microwave parameters to ensure an interferometer phase variation $\delta\varphi < 2\pi$ for an interrogation time of $t = 1$ s (for an ultracold rubidium-based interferometer). The stability requirements on the microwave parameters (power and phase) necessitate their active stabilization. Shortening the interrogation to $t = 100$ ms relaxes the stability requirements by a factor of 10.

Parameter	**Stability Tolerance**
Trap Height, h	$\delta h < 5 \times 10^{-10}$ m
Power, P (center trace)	$\frac{\delta P}{P} < 9 \times 10^{-6}$
Microwave Phase, ϕ	Transverse: $\delta\phi_M < 5 \times 10^{-6}$ rads Lattice/axial: $\delta\phi_{lattice} < 3 \times 10^{-7}$ rads

Table 9.2: Required gravimetric stability. The stability requirements ensure an interferometer phase fluctuation $\delta\varphi < 2\pi$ for an interrogation time of $t = 1$ s. The required stability is computed with gravity (9.8 m/s^2) oriented along the direction that the parameter controls (i.e. orientation of maximum sensitivity to gravity) for a ^{87}Rb-based interferometer.

9.1.1.3 Differential Zeeman Shifts – "Magic" Magnetic Fields

Technical and environmental magnetic field noise generates spin-dependent DC Zeeman energy shifts in the two spin states used in the interferometer. The resulting energy fluctuations quickly dephase the interferometer signal, so a mitigation strategy is needed. If the spin state pair has a "magic" magnetic field, then at this field the differential Zeeman shift between the two spin states is zero and thus immune to magnetic field noise (to first order). Table 9.3 shows the low-field magic magnetic fields for rubidium and potassium isotopes of interest. Notably, the use of the 3.23 G magic magnetic field for the $|F = 2, m_F = 1\rangle$, and $|F = 1, m_F = -1\rangle$ spin states of ^{87}Rb has resulted in a coherence time of about 1 s for a Ramsey interferometer based on atoms in a micromagnetic chip trap [137] and in a laser dipole trap [14].

When using atoms as sensitive clocks or matter-wave interferometers, reducing the

sensitivity to environmental magnetic field fluctuations and noise is generally necessary. Given the ACZ effect's ability to utilize any spin state, we can target so-called "clock states" that have identical linear DC Zeeman shifting, accounting for higher-order effects, turning noise in the magnetic field into a common-mode noise, and leaving a second-order magnetic dependence instead. The classic example is between ^{87}Rb's $|2,1\rangle$ and $|1,-1\rangle$ at 3.23 Gauss, but this is a two-photon transition, where one photon is nearly 6.8 GHz.

Isotopes of potassium, both fermions and bosons, have hyperfine splittings much lower, around 250 MHz and 1.3 GHz. We list some available "magic" magnetic fields that produce good clock states in Rb and K in Table 9.3. Operating at lower frequencies relaxes some chip design constraints needed for microwave frequencies, as well as allows for easier phase control and more precise signal generation. Additionally, potassium benefits from improved spin-specificity because the magic magnetic fields are typically an order of magnitude larger than in ^{87}Rb, so neighboring (unwanted) transitions are also an order of magnitude further off resonance.

Isotope	**"Magic" Field (Gauss)**	**Transition**	**Energy (MHz)**	**Splitting (MHz)**
^{87}Rb	3.23	$\|2,1\rangle$ & $\|1,-1\rangle$	6834.7	∼2
^{41}K	24.47	$\|2,-1\rangle$ & $\|1,0\rangle$	245.4	15–21
	24.36	$\|2,0\rangle$ & $\|1,-1\rangle$	245.3	15–18
	45.36	$\|2,-1\rangle$ & $\|1,-1\rangle$	219.9	32–47
^{40}K	0.72	$\|9/2,7/2\rangle$ & $\|7/2,-7/2\rangle$	1285.0	∼0.2
	50.96	$\|9/2,1/2\rangle$ & $\|7/2,1/2\rangle$	1277.8	∼16
	53.56	$\|9/2,-1/2\rangle$ & $\|7/2,3/2\rangle$	1277.4	16–18
	53.74	$\|9/2,3/2\rangle$ & $\|7/2,-1/2\rangle$	1277.4	16–18
	63.55	$\|9/2,-3/2\rangle$ & $\|7/2,5/2\rangle$	1275.9	19–22
	63.95	$\|9/2,5/2\rangle$ & $\|7/2,-3/2\rangle$	1275.8	19–22

Table 9.3: Low-field "magic" magnetic fields for ^{87}Rb, ^{41}K, and ^{40}K. All values are computed. "Zeeman splittings" refers to the energy splittings with states neighboring the "state pair".

9.1.1.4 Mitigating Magnetic Gradient Noise – "Doubly Magic" Magnetic Fields

While the "magic" magnetic fields in Table 9.3 help protect the interferometer against magnetic noise, they do not mitigate magnetic *gradient* noise. Since the interferometer

scheme (see Fig. 9.1, left) is predicated on the two traps being spatially separated by up to a centimeter, any magnetic gradient will differentially shift the atoms along the Breit-Rabi curves. This will induce a DC Zeeman energy difference between the two traps, which can skew the interferometer measurement. For example, to measure gravity to the part per billion level, we would need the magnetic gradient to be less than $|\vec{B}'| = m(10^{-9}g)/m_F g_F \mu_B = 15$ nG/cm, essentially impossible to achieve in experiment. If the magnetic gradient is constant, one could imagine measuring and decoupling it from the gravity measurement. However, if the gradient changes in time, as is most likely the case for magnetic noise, then we will not be able to account for it in the interferometer.

One approach is to time-average out any magnetic gradient by constantly flipping the quantization field direction, though this may be difficult in practice with the ACZ trap. Alternatively, one could implement RF or microwave frequency sweeps to flip back and forth between states with opposite magnetic moment to achieve the time-averaging. Other researchers have found success in adding an additional RF [138] or microwave [139] dressing field to suppress second-order differential Zeeman shifts in an atomic clock, though it will have to be investigated further whether this could be used in our interferometry scheme.

Here, I briefly describe a scheme using what we dub, "doubly magic" magnetic field to suppress the effect of magnetic gradients in our interferometer. This takes advantage of the nonlinearity in the Breit-Rabi energy curves, which allows us to find turning points where the first derivative goes to zero. At these points, any small change in the magnetic field due to gradients in the system will shift the energy quadratically. As an example, we consider ground-state ^{41}K, for which we show the Breit-Rabi energy curves for in Fig. 9.2(a). We can see that at around 45 G, the $|2,-1\rangle$ and $|1,-1\rangle$ states each have a turning point. Zooming in on this point in Fig. 9.2(b), it is clear that these states are quadratic with a zero derivative at nearly the same magnetic field. The turning points are at 45.312 and 45.324 G for the $|2,-1\rangle$ and $|1,-1\rangle$ states, respectively, obtained by numerically finding the zeros in the derivative of the energies. The curvature of each state's energy is 9 kHz/G^2. If we work at a magnetic field of 45.318 G, i.e., the field between the two state's turning points, then in

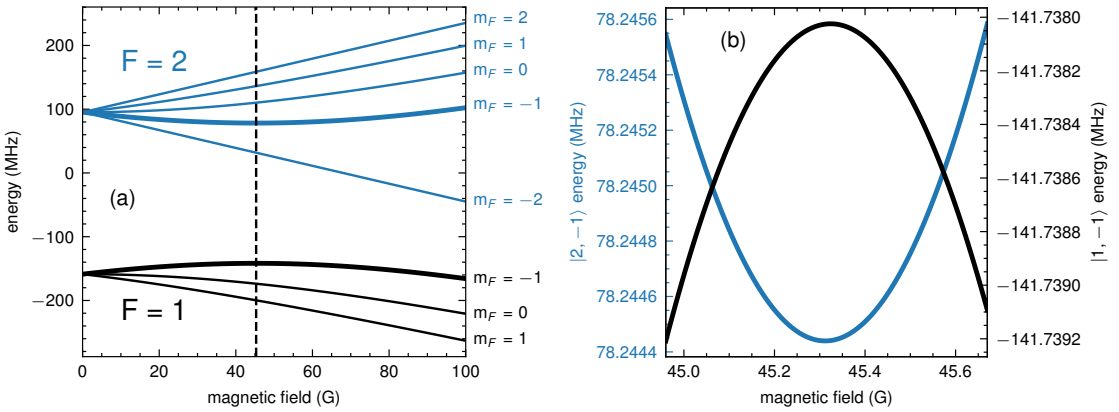

Figure 9.2: 'Doubly magic" magnetic field in ^{41}K. (a) Breit-Rabi energy curves as a function of magnetic field for ground-state ^{41}K. The $|2,-1\rangle$ and $|1,-1\rangle$ states, which feature the "doubly magic" field, are highlighted by thicker lines. The vertical dashed line indicates the doubly magic field point for the $|2,-1\rangle$ and $|1,-1\rangle$ states. (b) At $\sim$45.3 G, the $|2,-1\rangle$ and $|1,-1\rangle$ states have equal and opposite curvature. The curvature of each state's energy is 9 kHz/G^2.

the presence of a gradient pushing the states apart by ± 1 mG, the energy difference will change by less than 1 Hz. Note that this in-between field is also a "magic" magnetic field as described in the previous section. The local slope at this "magic" field is $\simeq$109 Hz/G for both states. The turning points and curvatures for the "doubly magic" state pairs is given in Table 9.4 for different isotopes of K and Rb. While this does not completely eliminate the effect of magnetic gradients on the interferometer, the "doubly magic" condition does mitigate the problem by pushing it to quasi second-order in the magnetic field. Future investigation into the usefulness of this scheme involves devising ACZ traps for each state pair, given some of the inter-manifold transitions become degenerate at these fields, and is beyond the scope of this thesis.

9.2 Future ACZ Experiments

With the ACZ chip trap still a relatively new technology, a better understanding of its core physics is essential for future experiments. Here, I describe some areas of direction that could be explored in the future.

Evaporation in the ACZ Trap

Isotope	State 1	Turning Point (G)	State 2	Turning Point (G)	Curvature (kHz/G^2)
^{41}K	$\|2,-1\rangle$	45.312	$\|1,-1\rangle$	45.324	8.926
^{40}K	$\|9/2,1/2\rangle$	51.023	$\|7/2,1/2\rangle$	50.943	1.536
	$\|9/2,3/2\rangle$	153.064	$\|7/2,3/2\rangle$	152.835	1.619
	$\|9/2,5/2\rangle$	255.083	$\|7/2,5/2\rangle$	254.747	1.836
	$\|9/2,7/2\rangle$	357.059	$\|7/2,7/2\rangle$	356.703	2.429
^{87}Rb	$\|2,-1\rangle$	1216.682	$\|1,-1\rangle$	1220.877	0.332
^{85}Rb	$\|3,-1\rangle$	360.720	$\|2,-1\rangle$	361.319	0.686
	$\|3,-2\rangle$	721.566	$\|2,-2\rangle$	722.513	0.868

Table 9.4: "Doubly magic" magnetic fields for different isotopes of Rb and K. The turning points are calculated numerically by finding the zeros of the derivative of the Breit-Rabi curves. The curvature is obtained by fitting the energy curves to a second-order polynomial.

To enhance the usefulness of the ACZ trap, it would be beneficial to be able to perform evaporative cooling to BEC. Previous investigation has demonstrated the ability to cool with the addition of an RF or microwave knife [16], without a significant improvement in phase space density, however. In the RF, there are two natural choices of evaporation frequency. As done in Ref. [16], one can target the energy splitting between dressed states, roughly given by the detuning of the trapping field. We can also try to evaporate in a more traditional sense by using an evaporation frequency tuned to the energy spacing between m_F states. I have demonstrated the ability to perform spectroscopy in this regime in Sec. 5.8, opening the avenue for exploring evaporative cooling. One could also imagine performing spectroscopy between the $|{+}{+}\rangle$ state and the other dressed states, perhaps finding more efficient evaporation paths than explored in Ref. [16].

ACZ Shift for Improved Lifetimes

Previous data [16] found that the lifetimes in the ACZ trap improved when working at lower RF power in the chip. A possible explanation for this observation is that the weaker trap is more susceptible to gravitational sag, shifting the trap bottom off of $\Omega = 0$. In this case, atoms are less likely to pass through the point where the Rabi frequency goes to zero, avoiding transitions into other untrapped dressed states, akin to Majorana spin-flip losses in magnetic traps. This can be explored by applying a secondary RF or microwave

field onto the ACZ trap, which I have demonstrated gives a positional shift to the trap (see Sec. 5.8). Additionally, as seen in the Sec. 3.5, the addition of a microwave field results in a shifting of the ACZ trap away from the zero energy point. In any case, lifetime measurements in the high-power ACZ trap could be done with and without the addition of the secondary field. Improved lifetimes with the additional field on would point towards dressed state transitions at the $\Omega = 0$ trap bottom as a loss mechanism.

Spin-Flipping in the ACZ Trap

We can attempt to better characterize the spin-flip losses in the ACZ trap by monitoring the relative population in each of the dressed states as a function of time. A previous study on the RF ACZ force applied to atoms by our group [61] found that the time it takes the $|{+}{+}\rangle$ dressed state to mix into the other dressed states is resonant in nature, consistent with lower trap lifetimes close to resonance. This study is more difficult since we need to find a way to trap the atoms ejected from the trap in a spin-dependent manner to avoid further collisional losses between atoms in different dressed states.

Microwave Atom Chip Generation 2

The microwave atom chip developed in Chapters 7 and 8 will allow us to perform initial microwave ACZ trapping and interferometry; however, in future generations of this atom chip, we should consider the following:

- If we desire tighter ACZ traps by decreasing the separation between microstrip traces, the coupling between traces will necessarily increase, affecting the operational bandwidth of the chip. Investigations should be made into possible methods to reduce the cross-talk between chip traces.

- I briefly touch on the idea of the "inverted wedge" method for coupling broadband microwave signals onto the atom chip in Chapter 8. While still challenging in terms of manufacturing, I see this as the future method for signal transmission, especially if we go to narrower chip traces.

- Other materials for the microstrip substrate and backing structure should be con-

sidered, which offer competitive, if not possibly better, characteristics over that described in this thesis (see Table 7.1).

- In principle, we should be able to make an optical waveguide [140] in the atom chip substrate, opening the door for dipole trapping and optical manipulation on the chip. Such a system must first be simulated to show its feasibility.

- Are there more complex geometries beyond the pair or trio of parallel atom chip traces we can leverage for sculpting the ACZ potential?

- Can we better understand the coupling between neighboring traces through the use of large-scale systems that mimic the atom chip, as in Refs. [95, 96, 101]? Previous investigation showed promising initial results [101], but a deeper study may prove beneficial.

Roughness in the $|F = 2, m_F = -2\rangle$ State

In the experiments on ACZ potential roughness suppression in this thesis (see Chapter 6), we were limited in that we could only prepare the trapped $|{+}{+}\rangle$ state to essentially be the $|F = 2, m_F = +2\rangle$ bare state. It is a natural question, however, to want to look at the roughness in the $|F = 2, m_F = -2\rangle$ state, or another DC untrappable state, such as the $|F = 1, m_F = +1\rangle$ absolute ground state. In our current setup, we are unable to prepare the $|{+}{+}\rangle$ state in these DC untrapped states, as the axial confinement provided by the Ioffe coil field anti-traps those bare states. A weak optical dipole trap (axial trap frequency $\simeq$20 Hz) was used previously to provide axial endcapping, not allowing atoms to spill out of the trap. The lab's previous ODT laser broke, however, and a new one is currently being installed into the apparatus by Russell Kamback. Once aligned, it should be a (relatively) straightforward task to investigate the $|2, -2\rangle$ or $|1, 1\rangle$ state roughness, marking the first measurement of its kind.

Appendix A

Magnetic Field Calibration Data

Having precise calibrations of the magnetic fields felt by the atoms while in the chip trap (AC or DC Zeeman) is key in order to model and understand the experiments. This appendix provides the data used for calibrations of the Ioffe, push coil, vertical bias, and hold fields.

A.1 Calibration Scheme

Following the method outlined in Fig. 5.6, we use microwave spectroscopy to probe the $|F = 2, m_F = 2\rangle \leftrightarrow |F = 1, m_F = 1\rangle$ transition as a function of applied magnetic field. The response of the ^{87}Rb $5S_{1/2}$ ground hyperfine levels to a static magnetic field is described exactly by the Breit-Rabi formula [53]. For low magnetic fields, the states split nearly linearly as $\Delta f_{m_F} \approx 0.7$ MHz/G. A linear fit to the $|F = 2, m_F = 2\rangle \leftrightarrow |F = 1, m_F = 1\rangle$ splitting gives a slope of 2.107 MHz/G. For a given control parameter, α (a current or voltage setting), we measure the frequency shift of the $|F = 2, m_F = 2\rangle \leftrightarrow |F = 1, m_F = 1\rangle$ resonance, referenced to the $\simeq$6834.7 MHz splitting at zero field. This data is then fit to a line which give a slope, m (units of frequency/α), and offset, b (units of frequency), which tells us the "natural" field present in the lab. The change in the field in response to the

control parameter, α, is then

$$B(\alpha) = \frac{m\alpha + b}{2.107 \text{ MHz/G}} \tag{A.1}$$

A.2 Field Calibrations

As an example to highlight the methodology, I plot the resonance shift as a function of current through the Ioffe coils in Fig. A.1. The data points correspond to the resonance

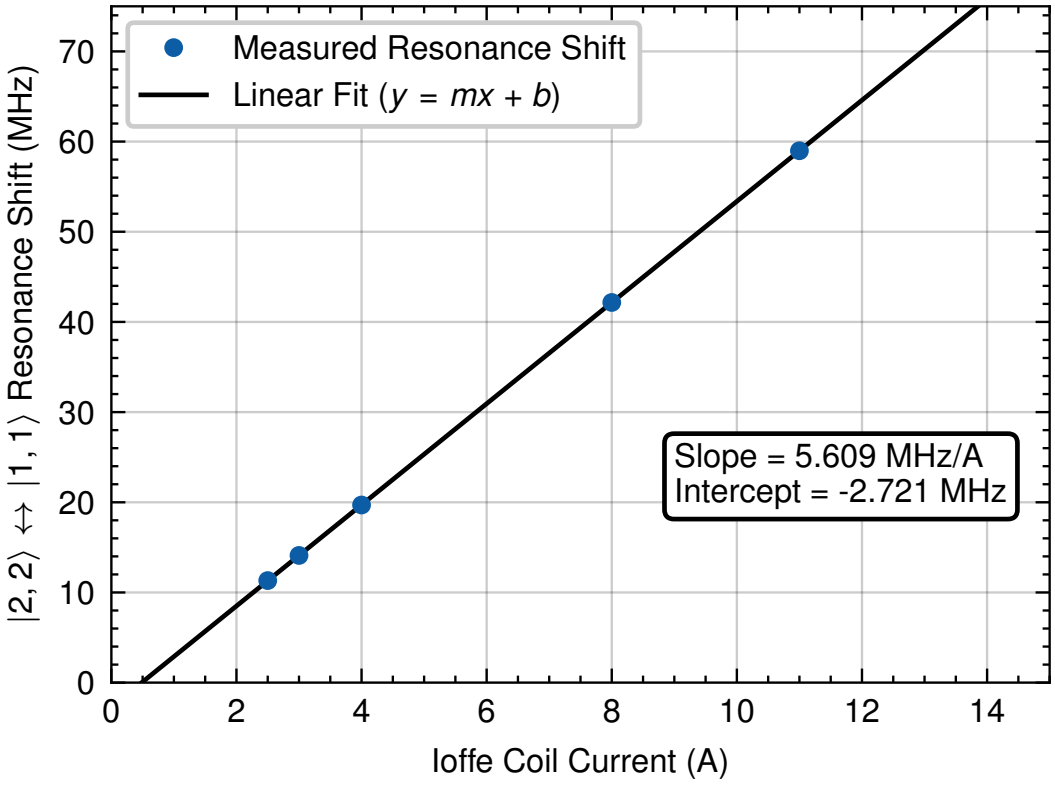

Figure A.1: Measured $|2,2\rangle \leftrightarrow |1,1\rangle$ state shift from the zero field splitting (≈6.834 GHz) at different Ioffe coil currents. The splittings are obtained from microwave spectroscopy measurements, outlined in Fig. 5.6. A linear fit to the data yields a conversion from Amps to MHz, which can be used to get a calibration from Amps to Gauss (see text for details).

frequency from a Lorentzian fit of the $|1,1\rangle$ state population at different applied microwave frequencies (see Fig. 5.6(c)). A linear fit to the resonance shift data gives a slope and intercept of 5.609 MHz/A and -2.721 MHz, respectively. We convert this into a calibration

of current (set in the AdWin sequencer) to magnetic field as:

$$(5.609\ \text{MHz/A}) \times I_{Ioffe} - 2.721\ \text{MHz} = (2.107\ \text{MHz/G}) \times B_{Ioffe}$$
$$\Rightarrow B_{Ioffe} = (2.66\ \text{G/A}) \times I_{Ioffe} - 1.29\ \text{G}$$

The same procedure is done to calibrate the other magnetic field coils at the chip, which we summarize in Table A.1.

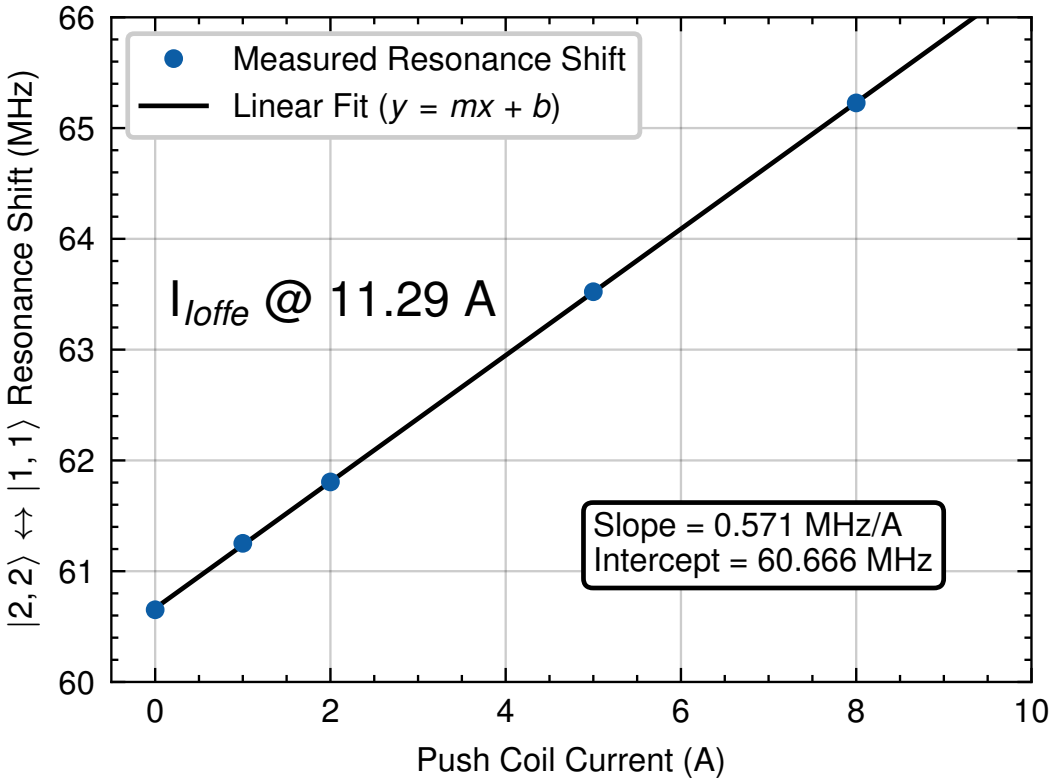

Figure A.2: Measured $|2,2\rangle \leftrightarrow |1,1\rangle$ state shift from the zero field splitting (≈6.834 GHz) at different push coil currents. The Ioffe field is kept constant at 11.29 A during these measurements. The splittings are obtained from microwave spectroscopy measurements, outlined in Fig. 5.6. A linear fit to the data yields a conversion from Amps to MHz, which can be used to get a calibration from Amps to Gauss (see text for details).

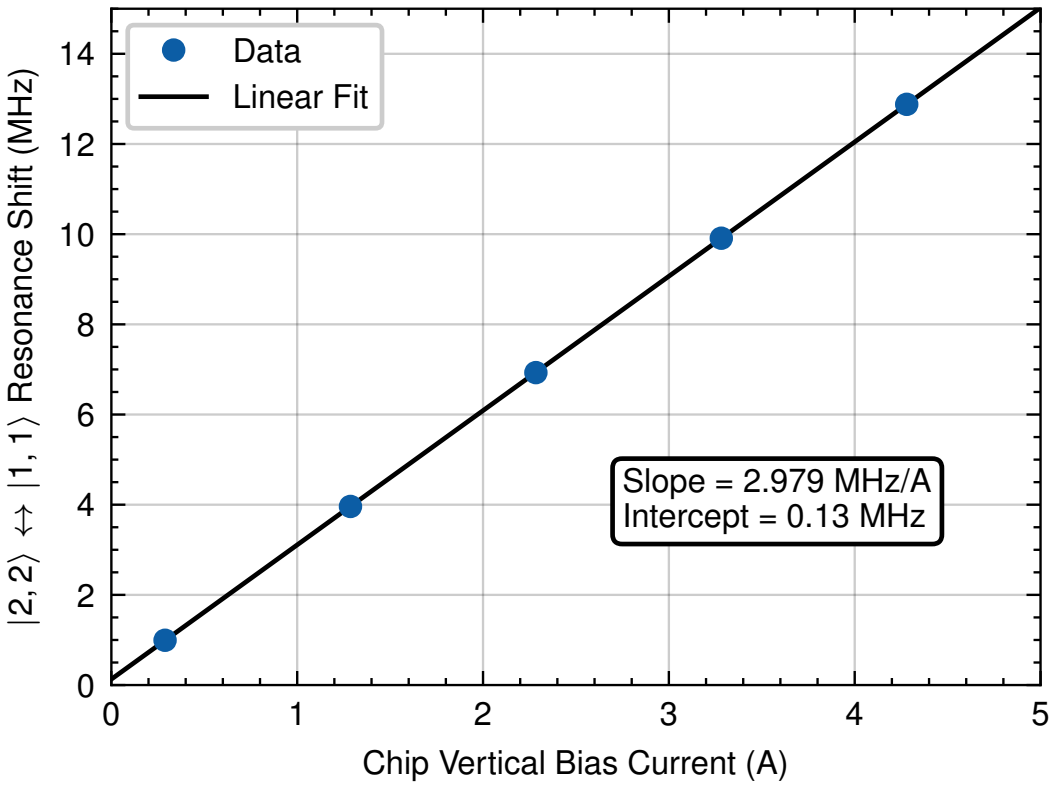

Figure A.3: Measured $|2,2\rangle \leftrightarrow |1,1\rangle$ state shift from the zero field splitting (≈6.834 GHz) at different vertical bias coil currents. The splittings are obtained from microwave spectroscopy measurements, outlined in Fig. 5.6. A linear fit to the data yields a conversion from Amps to MHz, which can be used to get a calibration from Amps to Gauss (see text for details).

Coil	Power Supply	Proportionality	Offset
Ioffe	Kepco	(2.66 G/A)I_{Ioffe}	-1.29 G
Chip Vertical Trim	Kepco BOP	(1.41 G/A)I_{vert}	+0.06 G
Chip Hold Field	Kepco BOP	(5.33 G/V)V_{adwin}	-0.118 G
Push Coil Field ($I_{Ioffe} = 11.29$ A)	Agilent 6571A-J03 (PSC)	(0.271 G/A)I_{push}	

Table A.1: Magnetic field calibrations for various coils in the lab.

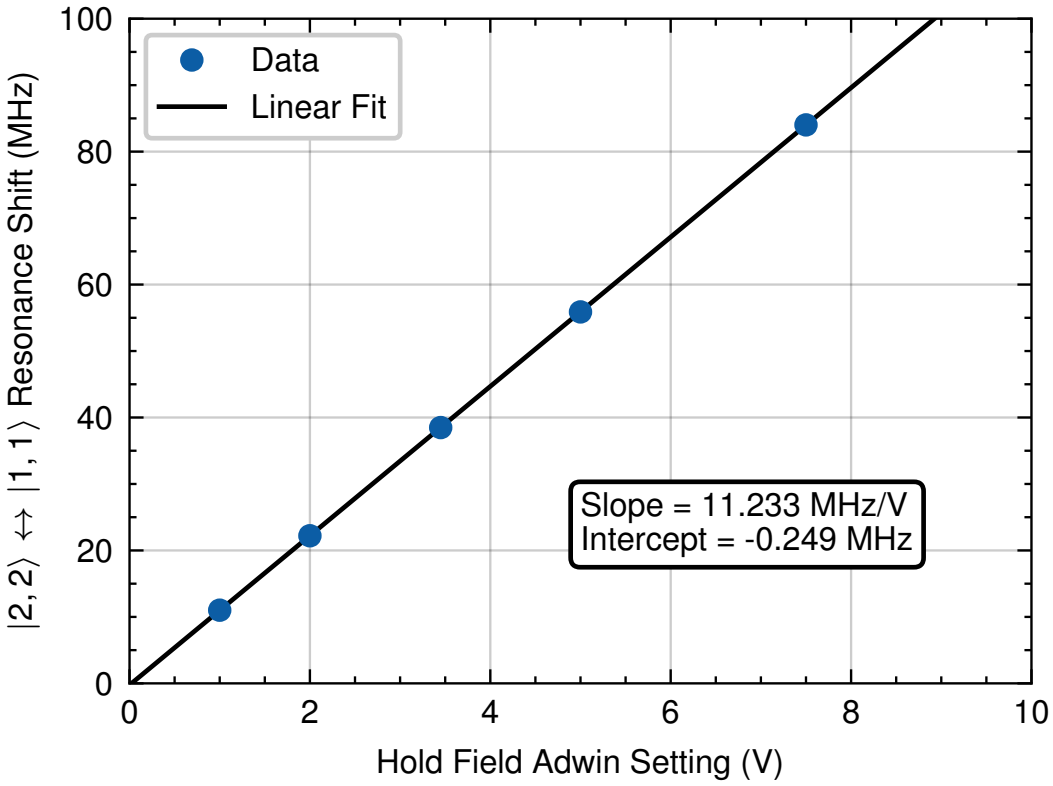

Figure A.4: Measured $|2,2\rangle \leftrightarrow |1,1\rangle$ state shift from the zero field splitting (≈6.834 GHz) at different hold field voltage settings. The splittings are obtained from microwave spectroscopy measurements, outlined in Fig. 5.6. A linear fit to the data yields a conversion from Amps to MHz, which can be used to get a calibration from Amps to Gauss (see text for details).

Appendix B

Circularly Polarized Magnetic Fields Generated by Two Parallel Wires

This appendix supplements Fig. 5.1, in which we look at the circularly polarized magnetic field landscape generated by two parallel atom chip wires. Here, we explicitly derive the magnetic field, showing the formation of pure polarization at a single point, indicating a minimum in the opposite polarization.

We consider the layout in Fig. B.1. Here, two infinitely thin wires are located at $(x_0, y_0) = (\pm d, 0)$. Each wire carries equal current, however, wire 2 is offset in phase by ϕ, so, $I_2 = Ie^{i(\omega t+\phi)}$ and $I_1 = Ie^{i\omega t}$. The magnetic field from each wire is then

$$\vec{B}_1 = \frac{\mu_0 I}{2\pi} e^{i\omega t} \left\{ -\frac{y}{r_1^2}\hat{x} + \frac{x-d}{r_1^2}\hat{y} \right\}, \tag{B.1}$$

$$\vec{B}_2 = \frac{\mu_0 I}{2\pi} e^{i(\omega t+\phi)} \left\{ -\frac{y}{r_2^2}\hat{x} + \frac{x+d}{r_2^2}\hat{y} \right\} \tag{B.2}$$

where $r_1^2 = (x-d)^2 + y^2$ and $r_2^2 = (x+d)^2 + y^2$. The total field is then

$$\vec{B}_{total} = \frac{\mu_0 I}{2\pi} e^{i\omega t} \left\{ \left[-y\left(\frac{1}{r_1^2} + \frac{e^{i\phi}}{r_2^2} \right) \right] \hat{x} + \left[\frac{x-d}{r_1^2} + \frac{x+d}{r_2^2} e^{i\phi} \right] \hat{y} \right\} \tag{B.3}$$

If we restrict ourselves to look along the $x = 0$ axis, then $r_1^2 = r_2^2 = y^2 + d^2 \equiv r_0^2$. After a

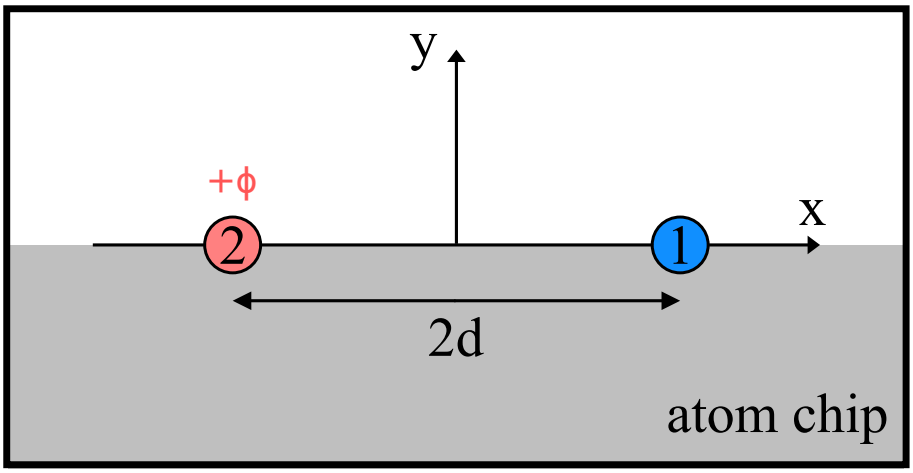

Figure B.1: Two-wire layout for producing the $B_{\pm}$ field landscape for AC Zeeman trapping. Figure adapted from Ref. [17].

few lines of algebra, the total magnetic field becomes

$$\vec{B}_{total} = \frac{\mu_0 I}{\pi r_0^2} e^{i\omega t} e^{i\phi/2} \{-y\cos(\phi/2)\hat{x} + id\sin(\phi/2)\hat{y}\} \tag{B.4}$$

We now consider the case shown in Fig. 5.1, where $\phi = -\pi/2$, so

$$\vec{B}_{total} = -\frac{2\mu_0 I}{\pi r_0^2} e^{i\omega t} \{y(1-i)\hat{x} + d(1+i)\hat{y}\} \tag{B.5}$$

At the location $y = \pm d$, $r_0^2 = 2d^2$, and

$$\vec{B}_{total} = -\frac{\mu_0 I}{\pi d} e^{i\omega t} \{\pm(1-i)\hat{x} + (1+i)\hat{y}\} \tag{B.6}$$

Let us now consider how this field behaves in time at this location, $(x, y) = (0, \pm d)$. For $\omega t = \pi/4$, $e^{i\omega t} = \sqrt{2}(1+i)/2$, and the field is

$$\vec{B}_{total}(x = 0, y = \pm d, \omega t = \pi/4) = \frac{\sqrt{2}\mu_0 I}{\pi d} \{\mp\hat{x} + i\hat{y}\} \tag{B.7}$$

We see that the real part of the field points solely in the $\mp\hat{x}$ direction at $y = \pm d$. Stepping

forward in time to $\omega t = 3\pi/4$, we find the total field is

$$\vec{B}_{total}(x = 0, y = \pm d, \omega t = 3\pi/4) = \frac{\sqrt{2}\mu_0 I}{\pi d}\left\{\mp i\hat{x} + \hat{y}\right\}, \tag{B.8}$$

so the field at both locations points in the $+\hat{y}$ direction. Continuing this, we see that the field rotates clockwise ($+d$) or counter-clockwise ($y = -d$) in time at a frequency of ω (see Fig. B.2). These two locations are found to be points of perfect circular polarization,

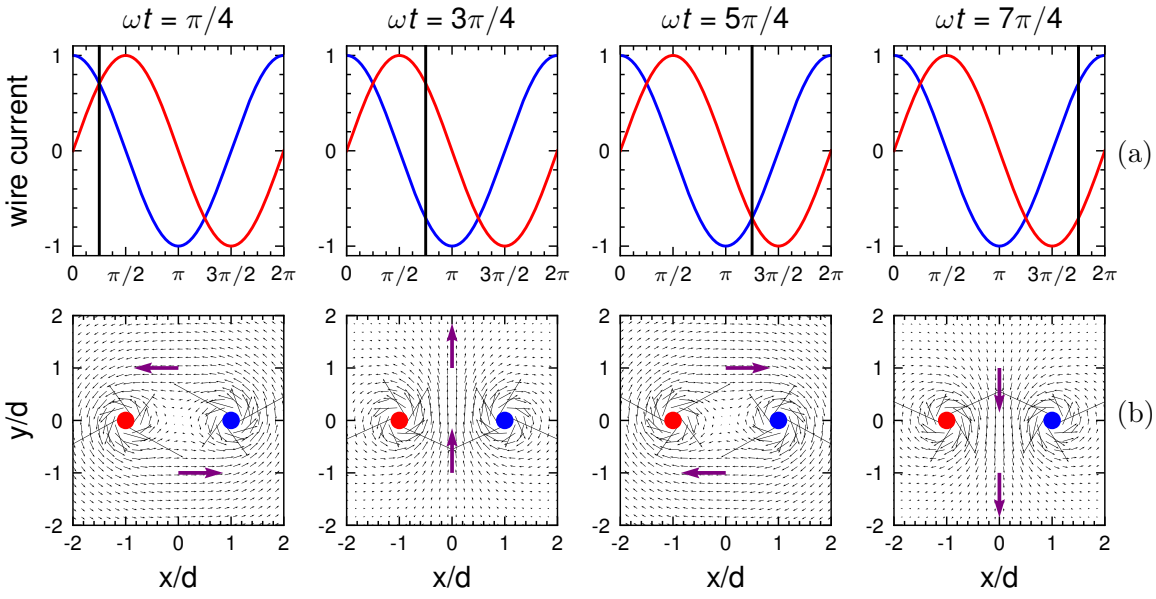

Figure B.2: Circularly polarized magnetic field generated by a pair of wires. Currents (a) and magnetic field vector plots (b) for a pair of point-like wires. The red wire is offset in phase from the blue wire by -90°. Both wires have equal current and are separated by a distance $2d$. The vertical lines in (a) indicate the value of ωt at which we evaluate the magnetic field shown by the vector plots in (b). The purple arrows in (b) show the total magnetic field at $(x, y) = (0, \pm d)$.

$B_\pm = B_x \pm iB_y$, corresponding to the clockwise (B_+) and counter-clockwise (B_-) rotating fields. At this point of pure polarization, the oppositely polarized field is exactly zero, serving as the $B_\pm$ minimum used for AC Zeeman trapping. Going off these points, the field becomes elliptical, written as a combination of B_+ and B_-, generating the $B_\pm$ gradient.

Appendix C

Derivation of Density after Time-of-Flight

This appendix describes the derivation of the expansion of a cloud of atoms after a given time-of-flight. Originally taken into consideration in Refs. [91, 98], this derivation pairs with the experimental demonstration of potential roughness suppression in a RF AC Zeeman trap. The main result of this derivation is determining how the amplitude of a sinusoidal atom density distribution decays over time, which tells us how much we expect the roughness features to wash out in our experiment.

C.1 Single Particle Expansion

As a simple first example, consider a particle moving in one dimension initially at position $z_0 = 0$ at time $t_0 = 0$. At $t_0 = 0$, the particle gains some velocity governed by the Maxwell-Boltzmann distribution:

$$f(v) = \exp\left[-\frac{mv_z^2}{2k_BT}\right], \tag{C.1}$$

where m is the mass of the particle, T is the temperature, and k_B is Boltzmann's constant. This equation tells us the probability that the particle has velocity v_z, given its mass and

temperature. Note that the above expression is **not** normalized, that is, $\int_{-\infty}^{\infty} f(v) \neq 1$.

What if we want to know what the probability is that the particle is at some position, z, after a given time, t? We can note that $v = \frac{dz}{dt} = \frac{z-z_0}{t-t_0} = \frac{z}{t}$, since $z_0 = t_0 = 0$. Equation C.1 then becomes

$$f(z) = \exp\left[-\frac{mz^2}{2k_BTt^2}\right] \tag{C.2}$$

Normalizing Equation C.2 we get that

$$\begin{aligned} 1 &= A\int_{-\infty}^{\infty} \exp\left[-\frac{mz^2}{2k_BTt^2}\right] \\ &= A\sqrt{\frac{2\pi k_BTt^2}{m}} \\ \Rightarrow A &= \frac{1}{\sqrt{2\pi\frac{k_BT}{m}}}\frac{1}{t} \end{aligned} \tag{C.3}$$

The normalized distribution is then

$$\boxed{f(z) = \frac{1}{\sqrt{2\pi\frac{k_BT}{m}}}\frac{1}{t}\exp\left[-\frac{mz^2}{2k_BTt^2}\right]} \tag{C.4}$$

If we know the velocity of the particle we can obtain the position via

$$z(t) = z_0 + v_z t = z_0 + \sqrt{\frac{k_BT}{m}}t = z_0 + \delta(t) \tag{C.5}$$

where $\delta(t) = \sqrt{\frac{k_BT}{m}}t$ is the distance travelled by the particle with velocity v. This form is derived from the relation between kinetic and thermal energy:

$$\frac{1}{2}mv^2 = \frac{1}{2}k_BT \tag{C.6}$$

$$\Rightarrow v = \sqrt{\frac{k_BT}{m}} \tag{C.7}$$

Figure C.1 shows this "expansion" by simulating 100,000 particles given a random velocity from Equation C.1 (with proper normalization factor included) and calculating their posi-

tion for a given expansion time via Equation C.5. Plotting the histogram of the positions we can see a flattening out of the distribution over time as expected.

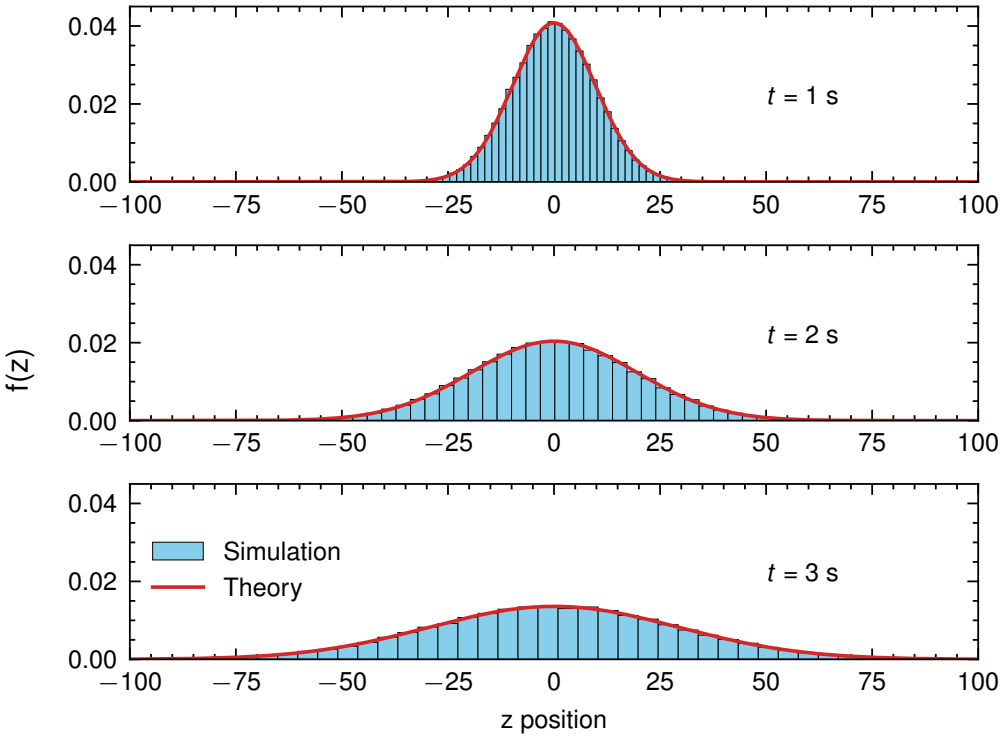

Figure C.1: Single particle "expansion". We simulate 100,000 particles each given a random velocity sampled from the Maxwell-Boltzmann distribution. The position of each particle is calculated for a given expansion time, and the position distribution is plotted as the blue histogram. The red theory curve is calculated from Equation C.4. We use the mass of a ^{87}Rb atom as the particle mass and a temperature of 1 K.

C.2 Expansion for a General Density Distribution

The Maxwell-Boltzmann velocity distribution is given as

$$f(v_z) = \frac{1}{\sqrt{2\pi\frac{k_B T}{m}}} \exp\left[-\frac{mv^2}{2k_B T}\right] \tag{C.8}$$

We can turn this into a function of position by using the relation $z(t) = z_i + v_i t$, where z_i and v_i are the initial position and velocity of a given atom. We can then rewrite the above

equation as

$$f(z,t) = \frac{1}{\sqrt{2\pi\frac{k_B T}{m}}}\frac{1}{t}\exp\left[-\frac{m(z-z_i)^2}{2k_B T t^2}\right], \tag{C.9}$$

with the factor of $1/t$ is required for normalization, i.e. $\int_{-\infty}^{\infty} f(z) = 1$. This expression is essentially the atom density distribution, telling us the probability of finding a particle with initial position z_i at position z after a given time t. If the atoms follow some initial density distribution, $n(z, t = 0)$, then we have to integrate over all possible initial positions weighted by the initial density distribution. So,

$$n(z,t) = \frac{1}{\sqrt{2\pi\delta(t)^2}}\int_{-\infty}^{\infty} e^{-\frac{(z-z')^2}{2\delta(t)^2}} n(z', t=0)dz' \tag{C.10}$$

where $\delta(t) = \sqrt{k_B T/m}t$ is the distance travelled by a particle with temperature T after a time t.

C.2.1 Initial Gaussian Density Distribution

For an initial atom density distribution

$$n(z, t=0) = \frac{1}{\sqrt{2\pi}\sigma_0}\exp\left[-\frac{z^2}{2\sigma_0}\right] \tag{C.11}$$

the density distribution after time t is

$$\begin{aligned} n(z,t) &= \frac{1}{2\pi\delta(t)\sigma_0}\int_{-\infty}^{\infty} e^{-\frac{(z-z')^2}{2\delta(t)^2}} e^{-\frac{(z')^2}{2\sigma_0}} dz' \\ &= \frac{1}{2\pi\delta(t)\sigma_0}\sqrt{\frac{2\pi}{\frac{1}{\sigma_0^2}+\frac{1}{\delta(t)^2}}}\exp\left[-\frac{z^2}{2(\sigma_0^2+\delta(t)^2}\right] \\ &= \boxed{\frac{1}{\sqrt{2\pi}\sigma(t)}\exp\left[-\frac{z^2}{2(\sigma(t)^2}\right]} \end{aligned} \tag{C.12}$$

where $\sigma(t) = \sqrt{\sigma_0^2 + \delta(t)^2}$, and we get the well known equation for the width of the atom cloud versus time used in time-of-flight temperature measurements. This relation is plotted in Figure C.3. Figure C.2 shows the simulated expansion of the cloud from an

initial Gaussian atom density distribution and we observe the simulation and theory from Equation C.12 perfectly match.

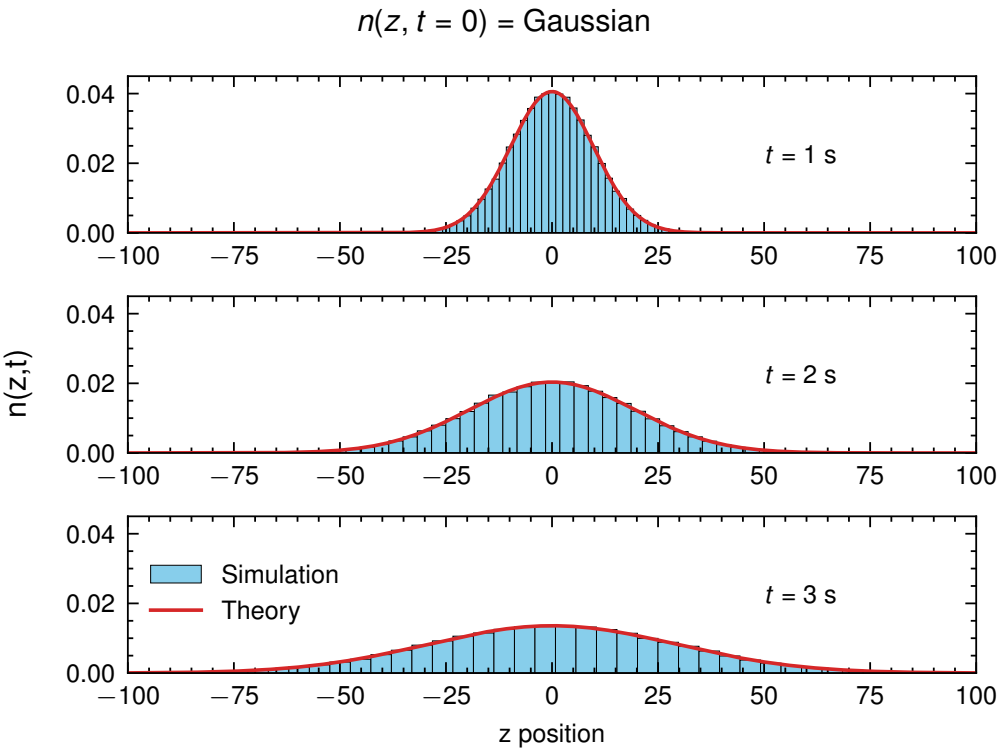

Figure C.2: Gaussian cloud expansion. We simulate 100,000 particles each given a random velocity sampled from the Maxwell-Boltzmann distribution. The initial position of each particle is sampled from a Gaussian distribution of width $\sigma_0 = 1$. The position of each particle is calculated via $z(t) = z_i + v_i t$ and are shown as the blue histogram. The red theory curve is calculated from Equation C.12. We use the mass of a ^{87}Rb atom as the particle mass and a temperture of 1 K.

C.2.2 Initial Sinusoidal Density Distribution

We can model the potential roughness simply as a sinusoidal density distribution characterized by some length scale, λ:

$$n(z, t = 0) = \sin\left(\frac{2\pi z}{\lambda}\right) \tag{C.13}$$

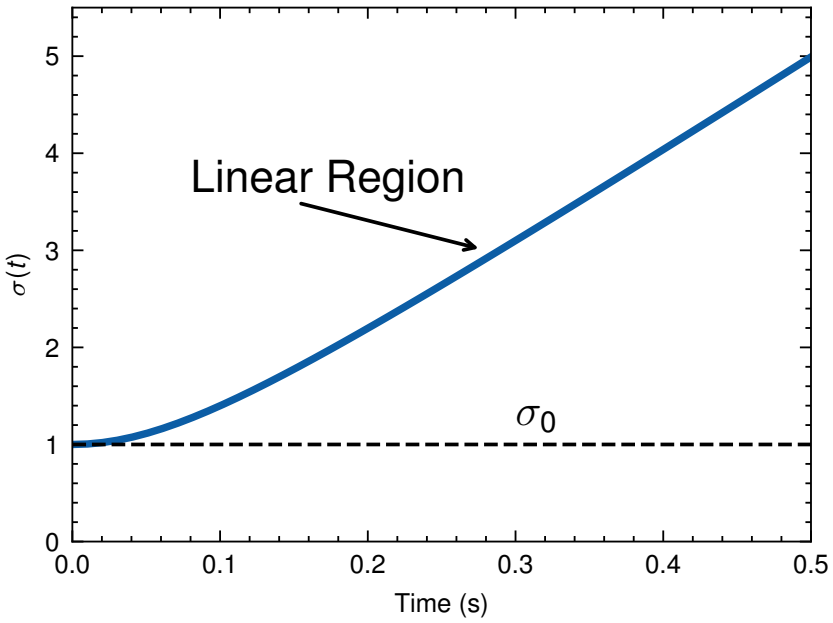

Figure C.3: Gaussian cloud expansion from Equation C.12.

Plugging this into Equation C.10 gives

$$n(z,t) = \frac{1}{\sqrt{2\pi\delta(t)^2}} \int_{-\infty}^{\infty} e^{-\frac{(z-z')^2}{2\delta(t)^2}} \sin\left(\frac{2\pi z'}{\lambda}\right) dz' \tag{C.14}$$

Making the substitution $y = z - z'$ we can write this as

$$\begin{aligned} n(z,t) &= \frac{1}{\sqrt{2\pi\delta(t)^2}} \int_{-\infty}^{\infty} e^{-\frac{y^2}{2\delta(t)^2}} \sin\left(\frac{2\pi(y+z)}{\lambda}\right) dy \\ &= \frac{1}{\sqrt{2\pi\delta(t)^2}} \int_{-\infty}^{\infty} e^{-\frac{y^2}{2\delta(t)^2}} \left\{\sin\left(\frac{2\pi y}{\lambda}\right)\cos\left(\frac{2\pi z}{\lambda}\right) + \cos\left(\frac{2\pi y}{\lambda}\right)\sin\left(\frac{2\pi z}{\lambda}\right)\right\} \\ &= \frac{1}{\sqrt{2\pi\delta(t)^2}} \left\{\cos\left(\frac{2\pi z}{\lambda}\right)\int_{-\infty}^{\infty} e^{-\frac{y^2}{2\delta(t)^2}} \sin\left(\frac{2\pi y}{\lambda}\right) + \sin\left(\frac{2\pi z}{\lambda}\right)\int_{-\infty}^{\infty} e^{-\frac{y^2}{2\delta(t)^2}} \cos\left(\frac{2\pi y}{\lambda}\right)\right\} \end{aligned} \tag{C.15}$$

where we've used the addition rule $\sin(a+b) = \sin(a)\cos(b) + \cos(a)\sin(b)$. We can note that the first term is zero since we are integrating an even times and odd function with

symmetric limits. Thus

$$\begin{aligned} n(z,t) &= \frac{1}{\sqrt{2\pi\delta(t)^2}} \sin\left(\frac{2\pi z}{\lambda}\right) \int_{-\infty}^{\infty} e^{-\frac{y^2}{2\delta(t)^2}} \cos\left(\frac{2\pi y}{\lambda}\right) \\ &= \frac{1}{\sqrt{2\pi\delta(t)^2}} \sin\left(\frac{2\pi z}{\lambda}\right) \sqrt{2\pi\delta(t)^2} e^{-2\pi^2\delta(t)^2/\lambda^2} \\ &= \boxed{\sin\left(\frac{2\pi z}{\lambda}\right) e^{-2\pi^2\delta(t)^2/\lambda^2}} \end{aligned} \tag{C.16}$$

This result agrees with the one obtained in Ref. [98] (Eq. 4.19 on pg 87). From this we can see that the amplitude of our sinusoidal density distribution decreases over time as $\exp\left[-2\pi^2\delta(t)^2/\lambda^2\right]$. We plot this amplitude for $T = 800$ nK, $\lambda = 100$ μm, and $m = m_{Rb87}$ in Figure C.4.

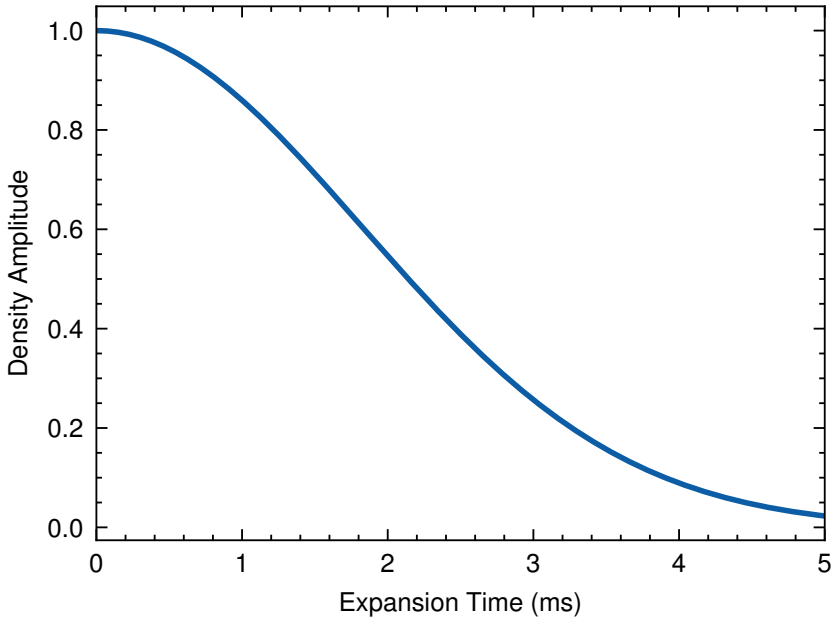

Figure C.4: Amplitude of the sinusoidal density distribution after expansion. The parameters here are: $T = 800$ nK, $\lambda = 100$ μm, and $m = m_{Rb87}$.

Appendix D

AC Zeeman Hamiltonian: 3 Levels with 2 Fields

Consider the system in Fig. D.1, in which three atomic energy levels are coupled via two AC magnetic fields. Following the derivation of the two-level system in Chapter 3, the

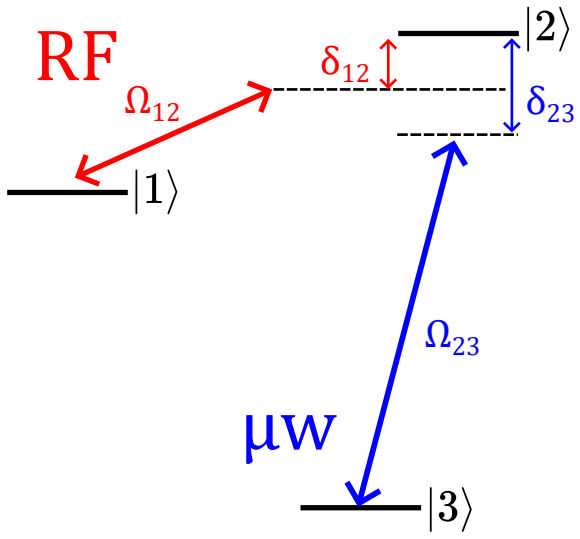

Figure D.1: Energy level diagram for three states coupled to two external AC magnetic fields.

total Hamiltonian is given by

$$H = H_{atom} + H_{int} \tag{D.1}$$

The atom Hamiltonian is simply

$$H_{atom} = \hbar \begin{pmatrix} \omega_1 & 0 & 0 \\ 0 & \omega_2 & 0 \\ 0 & 0 & \omega_3 \end{pmatrix} \begin{matrix} |1\rangle \\ |2\rangle \\ |3\rangle \end{matrix} \tag{D.2}$$

where the kets indicate the arrangement of the states within the matrix. The interaction Hamiltonian is a result of the ACZ effect, this time incorporating both the RF and microwave (μw) fields:

$$H_{int} = \vec{\mu} \cdot (\vec{B}_{rf} + \vec{B}_{\mu w}) \tag{D.3}$$

$$= \vec{\mu} \cdot \vec{B}_{rf} \cos(\omega_{rf} t) + \vec{\mu} \cdot \vec{B}_{\mu w} \cos(\omega_{\mu w} t + \phi) \tag{D.4}$$

where we include a phase difference, ϕ, between the fields. From our earlier assumption that the RF field couples states $|1\rangle \longleftrightarrow |2\rangle$ and the μw field couples states $|2\rangle \longleftrightarrow |3\rangle$, we can simplify the matrix elements of H_{int}. For example,

$$\langle 1|H_{int}|2\rangle = \langle 1| \vec{\mu} \cdot \vec{B}_{rf} |2\rangle \cos(\omega_{rf} t) + \overbrace{\langle 1| \vec{\mu} \cdot \vec{B}_{\mu w} |2\rangle}^{=0 \text{ by assumption}} \cos(\omega_{\mu w} t + \phi) \tag{D.5}$$

$$= \langle 1| \vec{\mu} \cdot \vec{B}_{rf} |2\rangle \cos(\omega_{rf} t) \tag{D.6}$$

$$= \hbar \Omega_{12} \cos(\omega_{rf} t) \tag{D.7}$$

Likewise,

$$\langle 2|H_{int}|3\rangle = \overbrace{\langle 2| \vec{\mu} \cdot \vec{B}_{rf} |3\rangle}^{=0 \text{ by assumption}} \cos(\omega_{rf} t) + \langle 2| \vec{\mu} \cdot \vec{B}_{\mu w} |3\rangle \cos(\omega_{\mu w} t + \phi) \tag{D.8}$$

$$= \langle 2| \vec{\mu} \cdot \vec{B}_{\mu w} |3\rangle \cos(\omega_{\mu w} t + \phi) \tag{D.9}$$

$$= \hbar \Omega_{23} \cos(\omega_{\mu w} t + \phi) \tag{D.10}$$

If we also take $\langle 1|\,\vec{\mu}\cdot\vec{B}_{\mu w}\,|3\rangle = \langle 1|\,\vec{\mu}\cdot\vec{B}_{rf}\,|3\rangle = 0$, since there is no field connecting states $|1\rangle \longleftrightarrow |3\rangle$, and the self-interaction terms are also zero, then we can write

$$H_{int} = \hbar \begin{pmatrix} 0 & \Omega_{12}\cos(\omega_{rf}t) & 0 \\ \Omega_{12}^{*}\cos(\omega_{rf}t) & 0 & \Omega_{23}\cos(\omega_{\mu w}t+\phi) \\ 0 & \Omega_{23}^{*}\cos(\omega_{\mu w}t+\phi) & 0 \end{pmatrix} \begin{matrix} |1\rangle \\ |2\rangle \\ |3\rangle \end{matrix} \tag{D.11}$$

where the asterisk corresponds to taking the complex conjugate. The full 2-field Hamiltonian is then

$$H = H_{atom} + H_{int} \tag{D.12}$$

$$= \hbar \begin{pmatrix} \omega_1 & \Omega_{12}\cos(\omega_{rf}t) & 0 \\ \Omega_{12}^{*}\cos(\omega_{rf}t) & \omega_2 & \Omega_{23}\cos(\omega_{\mu w}t+\phi) \\ 0 & \Omega_{23}^{*}\cos(\omega_{\mu w}t+\phi) & \omega_3 \end{pmatrix} \begin{matrix} |1\rangle \\ |2\rangle \\ |3\rangle \end{matrix} \tag{D.13}$$

We now turn to solving the Schrodinger equation, using the wavefuntion

$$|\Psi(t)\rangle = \begin{pmatrix} c_1(t)e^{-i\omega_1 t} \\ c_2(t)e^{-i\omega_2 t} \\ c_3(t)e^{-i\omega_3 t} \end{pmatrix} \begin{matrix} |1\rangle \\ |2\rangle \\ |3\rangle \end{matrix} \tag{D.14}$$

For readability, I will drop writing the explicit time dependence of the c coefficients. The Schrodinger equation is then

$$i\hbar\frac{d}{dt}\,|\Psi\rangle = H\,|\Psi\rangle \tag{D.15}$$

$$i\hbar\frac{d}{dt}\begin{pmatrix} c_1e^{-i\omega_1 t} \\ c_2e^{-i\omega_2 t} \\ c_3e^{-i\omega_3 t} \end{pmatrix} = \hbar \begin{pmatrix} \omega_1 & \Omega_{12}\cos(\omega_{rf}t) & 0 \\ \Omega_{12}^{*}\cos(\omega_{rf}t) & \omega_2 & \Omega_{23}\cos(\omega_{\mu w}t+\phi) \\ 0 & \Omega_{23}^{*}\cos(\omega_{\mu w}t+\phi) & \omega_3 \end{pmatrix} \begin{pmatrix} c_1e^{-i\omega_1 t} \\ c_2e^{-i\omega_2 t} \\ c_3e^{-i\omega_3 t} \end{pmatrix} \tag{D.16}$$

With a little bit of algebra, we obtain a set of three coupled differential equations:

$$i\dot{c}_1 = \Omega_{12}\cos(\omega_{rf}t)e^{-i\omega_{12}t}c_2 \tag{D.17}$$

$$i\dot{c}_2 = \Omega_{12}^{*}\cos(\omega_{rf}t)e^{i\omega_{12}t}c_1 + \Omega_{23}\cos(\omega_{\mu w}t+\phi)e^{i\omega_{23}t}c_3 \tag{D.18}$$

$$i\dot{c}_3 = \Omega_{23}^{*}\cos(\omega_{\mu w}t+\phi)e^{-i\omega_{23}t}c_2 \tag{D.19}$$

where $\omega_{12} = |\omega_2 - \omega_1|$ and $\omega_{23} = |\omega_2 - \omega_3|$ are the frequency differences between energy levels. We can next rewrite the cosine terms as the sum of exponentials: $2\cos(x) = e^x + e^{-x}$ and invoke the *Rotating Wave Approximation (RWA)*, in which we neglect terms in the exponentials that go as $\omega_{rf} + \omega_{12}$ and $\omega_{\mu w} + \omega_{23}$. This approximation is valid here since we assume the RF and μw fields are close to resonance such that $\omega_{rf} + \omega_{12} >> |\omega_{rf} - \omega_{12}| = |\delta_{12}|$ and $\omega_{\mu w} + \omega_{23} >> |\omega_{\mu w} - \omega_{23}| = |\delta_{23}|$, where we have defined the detunings δ_{12} and δ_{23}. Those fast oscillating terms in the exponentials will get time-averaged out of our calculations, so we can just get rid of them now and focus on the slowly evolving terms. After the RWA the coupled equations become

$$i\dot{c}_1 \simeq \frac{\Omega_{12}}{2} e^{i\delta_{12}t} c_2 \tag{D.20}$$

$$i\dot{c}_2 \simeq \frac{\Omega_{12}^*}{2} e^{-i\delta_{12}t} c_1 + \frac{\Omega_{23}}{2} e^{-i\delta_{23}t - i\phi} c_3 \tag{D.21}$$

$$i\dot{c}_3 \simeq \frac{\Omega_{23}^*}{2} e^{i\delta_{23}t + i\phi} c_2 \tag{D.22}$$

To remove the time-dependence from the above equations, we move into the *rotating frame* by applying the transformation

$$\tilde{c}_1 = c_1 e^{-i\delta_{12}t} \tag{D.23}$$

$$\tilde{c}_2 = c_2 \tag{D.24}$$

$$\tilde{c}_3 = c_3 e^{-i\delta_{23}t} \tag{D.25}$$

Making this transformation, we can obtain a Schrodinger-like equation:

$$i\hbar \frac{d}{dt} \begin{pmatrix} \tilde{c}_1 \\ \tilde{c}_2 \\ \tilde{c}_3 \end{pmatrix} = \hbar \begin{pmatrix} \delta_{12} & \Omega_{12}/2 & 0 \\ \Omega_{12}^*/2 & 0 & \Omega_{23} e^{-i\phi}/2 \\ 0 & \Omega_{23}^* e^{i\phi}/2 & \delta_{23} \end{pmatrix} \begin{pmatrix} \tilde{c}_1 \\ \tilde{c}_2 \\ \tilde{c}_3 \end{pmatrix} \tag{D.26}$$

which gives the dressed atom ACZ Hamiltonian:

$$\boxed{H_{ACZ,\text{3 levels+2 fields}} = \hbar \begin{pmatrix} \delta_{12} & \Omega_{12}/2 & 0 \\ \Omega_{12}^*/2 & 0 & \Omega_{23}e^{-i\phi}/2 \\ 0 & \Omega_{23}^* e^{i\phi}/2 & \delta_{23} \end{pmatrix}} \tag{D.27}$$

Appendix E

Interferometer Stability Calculations

This appendix goes over the calculations outlining the technical requirements of the AC Zeeman microwave lattice interferometer given in Section 9.1 of Chapter 9.

E.1 Asymmetry Decoherence

According to Ref. [135], the coherence time, t_c, in a thermal atom interferometer using two spin-dependent harmonic traps is

$$t_c \simeq \frac{\omega}{\delta\omega}\frac{\hbar}{k_B T} \tag{E.1}$$

where ω is the average trap frequency, $\delta\omega$ is the trap asymmetry, $\hbar$ is the reduced Plank's constant, k_B is Boltzmann's constant, and T is the temperature of the atoms. We can re-arrange the above equation to determine the fractional trap asymmetry required to achieve a certain coherence time:

$$\frac{\delta\omega}{\omega} = \frac{\hbar}{k_B T t_c} \tag{E.2}$$

For atoms at a temperature of 300 nK, a fractional asymmetry of $\delta\omega/\omega \leq 2.5 \times 10^{-5}$ is needed to reach a coherence time of 1 s.

To calculate the effect of power and frequency stability on the interferometer's coherence time, we can connect them to the current in the wire and the detuning of the AC field, respectively. First, we can create a simple analytic model of the trap frequency for an ACZ

trap by considering a single wire carrying AC current and an external AC bias field that cancels the wire field at a single point to create the trap [58]. The magnetic field generated by the wire along the vertical y-axis is

$$B_{wire} = \frac{\mu_0 I}{2\pi y}\hat{x} \tag{E.3}$$

To cancel B_{wire} a distance $y = h$ above the wire, the external bias field needs to be

$$B_{bias} = -\frac{\mu_0 I}{2\pi h}\hat{x} \tag{E.4}$$

The total field can be written as

$$B_{total} = B_{wire} + B_{bias} = \frac{\mu_0 I}{2\pi}\left(\frac{1}{y} - \frac{1}{h}\right)\hat{x} \tag{E.5}$$

If we consider small fluctuations in the trap location, i.e., $y = h + \Delta y$, then

$$B_{total} \simeq -\frac{\mu_0 I}{2\pi}\frac{\Delta y}{h^2}\hat{x} \tag{E.6}$$

where we have ignored terms of $\mathcal{O}(\Delta y^2)$ and above. At the bottom of the trap, the Rabi frequency goes to zero, so $|\delta| >> \Omega$. In this limit, the AC Zeeman energy can be written as $E_{ACZ} \simeq \hbar|\Omega|^2/4|\delta|$. Using the magnetic field at the trap minimum we just derived, we can calculate the Rabi frequency as

$$\Omega = \frac{\mu_B}{\hbar^2}\langle g| S_+B_- + S_-B_+ + 2S_zB_z |e\rangle \tag{E.7}$$

Using the $|2,2\rangle \longleftrightarrow |1,1\rangle$ microwave transition in ^{87}Rb, we can note that the only surviving term in the Rabi frequency contains S_+B_-, while the other two are zero. This reduces the

Rabi frequency to

$$\Omega = \frac{\mu_B}{\hbar^2} B_{total,x} \langle g|S_+|e\rangle \tag{E.8}$$

$$= -\frac{\mu_B}{\hbar^2}\frac{\mu_0 I}{2\pi}\frac{\Delta y}{h^2}\frac{\hbar\sqrt{12}}{4} \tag{E.9}$$

$$\Rightarrow |\Omega| = \frac{\mu_B}{\hbar}\frac{\sqrt{3}}{2}\frac{\mu_0}{2\pi} I \frac{\Delta y}{h^2} \tag{E.10}$$

The resulting ACZ energy is

$$E_{ACZ} = \frac{3}{16\hbar}\left(\frac{\mu_0\mu_B}{2\pi}\right)^2 \frac{\Delta y^2}{h^4|\delta|} \tag{E.11}$$

Setting $E_{ACZ} = \frac{1}{2}m\omega^2\Delta y^2$ for a harmonic trap, we get the analytic form for the trap frequency:

$$\omega = \sqrt{\frac{3}{8m\hbar}}\frac{\mu_0\mu_B}{2\pi}\frac{I}{h^2\sqrt{|\delta|}} \tag{E.12}$$

If we consider small perturbations in the current and detuning, i.e., $I = I_0 + \delta I$ and $\delta = \delta_0 + \Delta\delta$, then the trap frequency can be written as

$$\omega \simeq \sqrt{\frac{3}{8m\hbar}}\frac{\mu_0\mu_B}{2\pi}\frac{I_0}{h^2\sqrt{|\delta_0|}}\left(1+\frac{\delta I}{I_0}\right)\left(1-\frac{1}{2}\frac{\Delta\delta}{\delta_0}\right) \tag{E.13}$$

$$= \omega\left(1+\frac{\delta I}{I_0}\right)\left(1-\frac{1}{2}\frac{\Delta\delta}{\delta_0}\right) \tag{E.14}$$

We can relate current and detuning perturbations to trap frequency asymmetry as

$$\omega\left(1+\frac{\delta\omega}{\omega}\right) = \omega\left(1+\frac{\delta I}{I_0}\right)\left(1-\frac{1}{2}\frac{\Delta\delta}{\delta_0}\right) \tag{E.15}$$

$$\Rightarrow \boxed{\frac{\delta\omega}{\omega} = \frac{\delta I}{I_0}} \quad \text{and} \quad \boxed{\frac{\delta\omega}{\omega} = -\frac{1}{2}\frac{\Delta\delta}{\delta_0}} \tag{E.16}$$

From the current requirement, we can get a power stability requirement by noting that $P = (I_0/\sqrt{2})^2 R$. Then

$$\boxed{\frac{\delta P}{P} = 2\frac{\delta I}{I_0} = 2\frac{\delta\omega}{\omega}} \tag{E.17}$$

For the frequency stability, using a 1 MHz detuning, the detuning stability requires $\Delta\delta =$ 50 Hz. Using the ^{87}Rb microwave transition at 6.834 GHz, this corresponds to a frequency stability of $\Delta\delta/6.834\text{ GHz} = 7.45\times10^{-9}$. Figure E.1 shows the calculated stabilities across a range of coherence times and atom temperatures (via Eq. E.2).

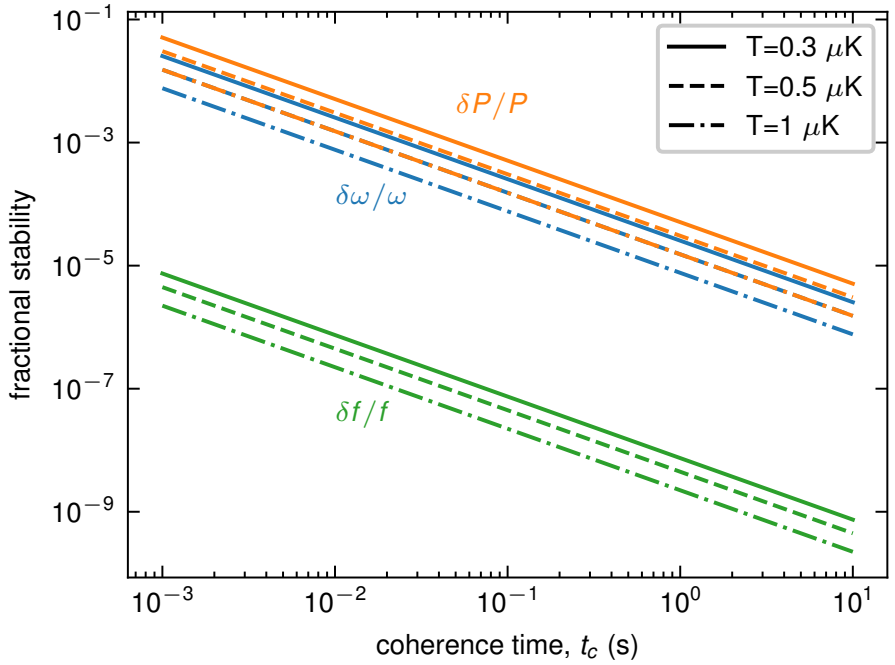

Figure E.1: Calculated fractional stability for the trap frequency (blue), power (orange), and frequency (green) for different temperatures.

E.2 Gravimetric Dephasing

We now consider the case when the interferometer is sensitive to gravity. If the two traps are translated in the direction along gravity, there will be a differential phase shift given as $\phi = mght/\hbar$, where m is the mass of the atom, $g = 9.81$ m/s is the acceleration due to gravity, h is the difference in height between the two traps, t is the interrogation time, and $\hbar$ is the reduced Plank's constant. While this geometry can be used to measure g and variations in it, any fluctuations in the positional difference between the traps will show

up as fluctuations in the interferometer's phase

$$\delta\phi = (mgt/\hbar)\delta h \tag{E.18}$$

To ensure phase fluctuations $\delta\phi < 2\pi$ for an interrogation time of $t = 1$ s, we require height deviations of $\delta h < 5 \times 10^{-10}$ m, using the mass of ^{87}Rb.

Since we do the translation of the interferometer arms via a microwave lattice operating on the ACZ or AC Stark effect, we need to know how deviations in the axial position of the atoms affect the interferometer phase. We can relate these positional fluctuations to fluctuations in the phase of the microwaves generating the lattice. From Section 3.4.2 in Chapter 3, we know that the position of the microwave lattice is linearly related to the phase difference between the generating microwaves with slope $\lambda_{eff}/4\pi$, where λ_{eff} is the effective wavelength of microwaves in the microstrip. Thus, fluctuations in the lattice phase, $\delta\varphi$, will manifest in the interferometer phase as

$$\delta\phi = (mgt/\hbar)\delta z \tag{E.19}$$

$$= (mgt/\hbar)(\lambda_{eff}/4\pi)\delta\varphi \tag{E.20}$$

To ensure phase fluctuations $\delta\phi < 2\pi$ for an interrogation time of $t = 1$ s, we require phase deviations of $\delta\varphi < 3.3 \times 10^{-7}$, using the mass of ^{87}Rb.

Considering now fluctuations in the transverse position of the trap, we can use the analytic expression for the trap location of three parallel wires with spacing d, equal currents, and the center wire being π out of phase with the outer wires [17]. The location of the trap is then (see Eq. 13 in Ref. [17])

$$y + ix = id\frac{\sqrt{e^{i(\pi+\delta\varphi)}}}{\sqrt{2 + e^{i(\pi+\delta\varphi}}} \tag{E.21}$$

where $\delta\varphi$ is the variation in the center wire's phase. Taylor expanding the square root terms, we see that the phase fluctuations manifest in the horizontal position only as $\delta x =$

$\mp d\delta\varphi$. Assuming the x-direction is pointed along gravity, the positional fluctuations will show up in the interferometer phase as

$$\delta\phi = (mgt/\hbar)\delta x \tag{E.22}$$

$$= (mgtd/\hbar)\delta\varphi \tag{E.23}$$

To ensure phase fluctuations $\delta\phi < 2\pi$ for an interrogation time of $t = 1$ s, we require phase deviations of $\delta\varphi < 4.7\times10^{-6}$, using the mass of ^{87}Rb and a wire separation of $d = 100$ μm.

Finally, we look at the current jitter in the central trapping wire and its effect on the interferometer phase. Using the same three-wire scheme with the center wire being π out of phase with the outer wires, we let the ratio between the center and outer wires be $r_M = 1 + \epsilon$. The trap position is then

$$y + ix = id\frac{\sqrt{(1+\epsilon)e^{i\pi}}}{\sqrt{2+(1+\epsilon)e^{i\pi}}} \tag{E.24}$$

Restricting ourselves to $x = 0$ and Taylor expanding the square root terms, the current jitter shows up as variation in the trap height: $\delta y = d(\delta I/I)$. Using this to calculate the power deviation requirements adds a factor of 2, as seen previously. Assuming the y-direction is pointed along gravity, the positional fluctuations will show up in the interferometer phase as

$$\delta\phi = (mgt/\hbar)\delta y \tag{E.25}$$

$$= (mgtd/2\hbar)\delta P/P \tag{E.26}$$

To ensure phase fluctuations $\delta\phi < 2\pi$ for an interrogation time of $t = 1$ s, we require power deviations of $\delta P/P < 9.4\times10^{-6}$, using the mass of ^{87}Rb and a wire separation of $d = 100$ μm.

Appendix F

Experiments with ^{87}Rb 5D states

During the winter break of 2024-25, I had the opportunity to use a spare 776 nm laser to do spectroscopy of the $5D_{5/2}$ state of ^{87}Rb. The ultimate goal of the project was to perform a two-photon excitation to the nF Rydberg states for electrometry applications [141, 142, 143]. My contribution to this project were in the improvement of the setup developed by Mia Bridges [142], and the demonstration of electromagnetically induced transparency (EIT) for initial spectroscopy of the $5D_{5/2}$ hyperfine splittings.

F.1 EIT

To probe the $5D_{5/2}$ state, we require a two-photon transition, going from $5S_{1/2} \rightarrow 5P_{3/2} \rightarrow 5D_{5/2}$. It is also possible to reach the $5D_{3/2}$ state; however that was beyond the scope of my time working on this. These transitions are made using near-IR wavelength lasers at 780 and 776 nm for the $5S_{1/2} \rightarrow 5P_{3/2}$ and $5P_{3/2} \rightarrow 5D_{5/2}$ transitions, respectively (see the inset of Fig. F.1). This forms a ladder EIT system, in which we can realize reductions in the absorption spectrum of the atomic medium when the two photon detuning is zero. For example, if the 780 nm laser is on resonance with the $5S_{1/2} \rightarrow 5P_{3/2}$ transition, EIT will occur when the 776 nm laser is resonant with transitions to each of the $5D_{5/2}$ hyperfine levels. A comprehensive review of EIT can be found in Ref. [33] and the references within. We can use this to perform spectroscopy on the system, probing the hyperfine level spacing.

EIT can also be used as a method for locking the 776 nm laser [144].

The experimental setup for EIT spectroscopy is shown in Fig. F.1. Counter-propagating 780 and 776 nm pass through a Rb vapor cell, which is angled to avoid reflections in the cell. The two beams are chosen to have parallel polarizations, which was found to enhance the EIT signal. Once in the $5D_{5/2}$ state, the atoms can decay back to the ground state via the intermediate $6P_{3/2}$ state, emitting 420 nm blue light in the process. This can be picked up by a photomultiplier tube (PMT) with a 420 nm filter for monitoring or fluorescence spectroscopy. The 780 nm probe light is monitored using a photodiode.

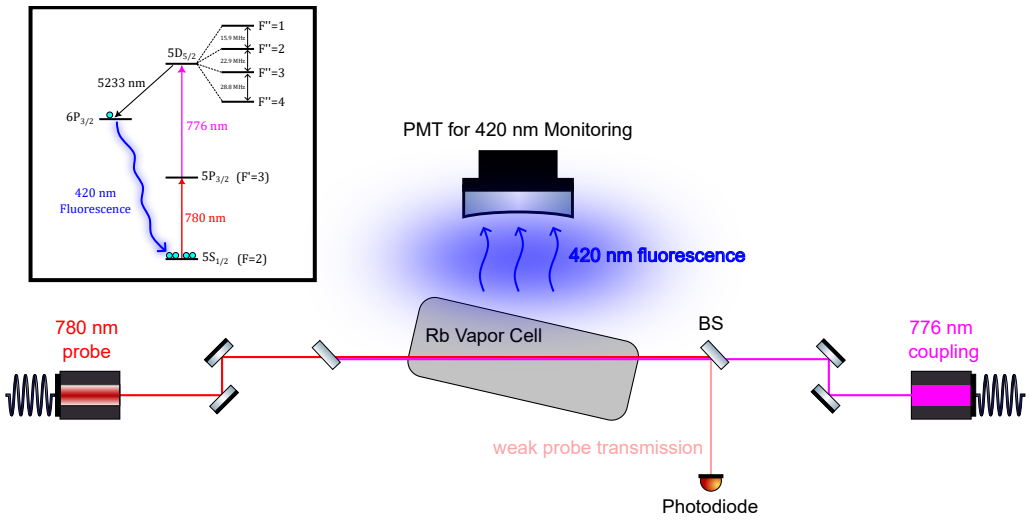

Figure F.1: Setup for two-photon EIT. Counter-propagating 780 nm (probe) and 776 nm (coupling) light is sent through a Rb vapor cell, angled to avoid reflections. 420 nm fluorescence from $6P_{3/2} \rightarrow 5S_{1/2}$ decay is detected on a PMT. Probe light transmission is monitored on a photodiode. Inset: energy level diagram for relevant transitions.

In practice, we sweep the probe light frequency on our saturation spectroscopy system used for locking the trap light for laser cooling (see Chapter 4) with the 776 nm coupling light at a set frequency. This set frequency is chosen to be around the 420 nm fluorescence signal on the PMT. From this, we can obtain a frequency reference from the saturation spectroscopy, allowing us to convert from the temporal signal from the oscilloscope photodiode signal into frequency space. We use the two largest crossover peaks in the saturation spectroscopy signal, separated by 78.47025 MHz [53], to provide the conversion. Figure F.2

shows the Lorenztian fit of the two largest crossover peaks in the saturation spectroscopy signal. The conversion from time to frequency space is the known frequency difference divided by the fitted peaks. This gives a conversion of 2659.114±0.186 MHz/s, where the error bar is given as the quadrature sum of the $1-\sigma$ error for the position of each peak.

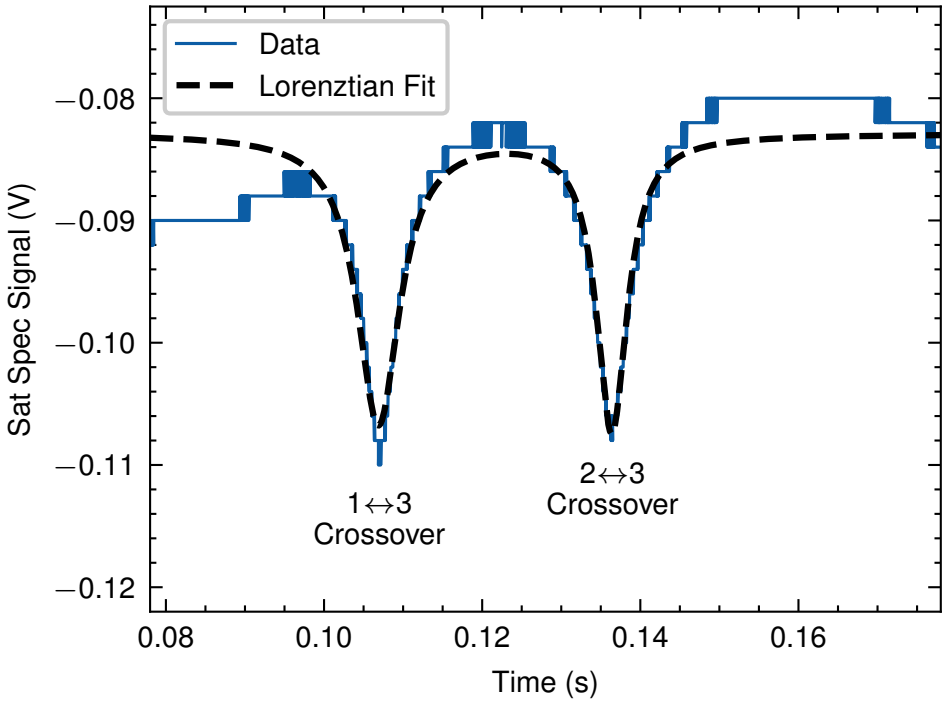

Figure F.2: Fit of the two large crossover peaks in the ^{87}Rb D2 saturation spectroscopy signal. The data is fit to the sum of two Lorenztians. This gives a time to frequency conversion of 2659.114±0.186 MHz/s.

Figure F.3 shows the saturation spectroscopy signal along with the EIT peaks. Due to atomic selection rules, $\Delta F = 0, \pm 1$, so we can only access the $F'' = 2, 3, 4$ hyperfine levels in the $5D_{5/2}$ state, which manifest as three EIT peaks. Doing a Lorentzian fit to these peaks gives the frequency splitting, which we list in Table F.1, along with accepted values from Ref. [145]. Our measurements show excellent agreement with the accepted values, differing by about one MHz.

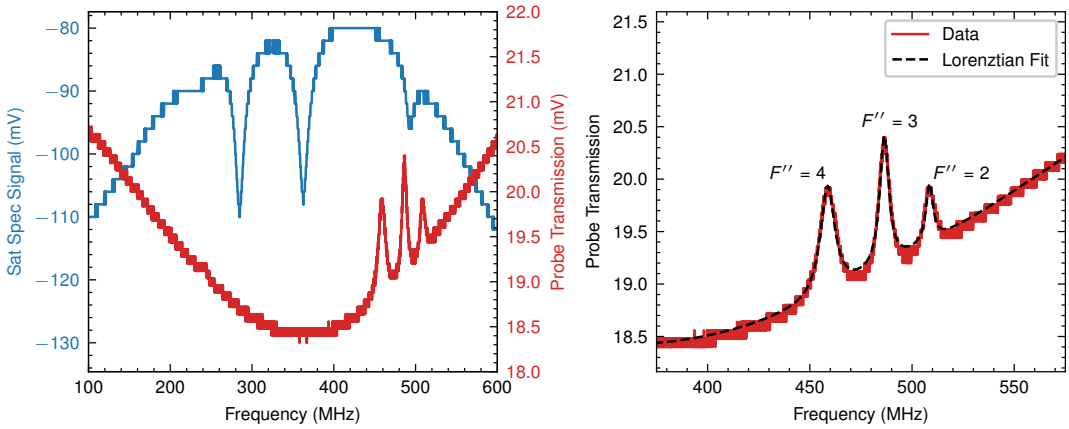

Figure F.3: (Left) Saturation spectroscopy (blue) and EIT (red) signals in frequency space. (Right) EIT signal fitted to the sum of three Lorentzians.

Hyperfine State Splitting	Measured (MHz)	Ref. [145] (MHz)	% difference
$F'' = 2 \leftrightarrow 3$	22.138±0.006	22.9	3.3%
$F'' = 3 \leftrightarrow 4$	27.715±0.0005	28.8	3.8%

Table F.1: Measured hyperfine splittings for the $5D_{5/2}$ state in ^{87}Rb, compared with that found in Ref. [145].

F.2 Blue MOT

Once achieving EIT in the vapor cell, our top priority became injecting the 776 nm light into the magneto-optical trap (MOT). Atoms in the MOT, which are already interacting with 780 nm light, are then excited to the $5D_{5/2}$ state, from which they decay back to the ground state via the $6P_{3/2}$ state, emitting 420 nm blue light in the process. Our MOT, typically invisible to the naked eye since the atoms fluoresce near-IR 780 nm light, would then suddenly turn blue! There were, of course, some science-related applications of this, such as precision spectroscopy or background-free detection [146]; however, the 776 nm laser's time in our lab was short lived before moving to another optics lab, so we could only focus on the cool visuals, as well as some initial spectroscopy, shown in Fig. F.4. Spectroscopy on the $5D$ states was done by imaging the 420 nm fluorescence while scanning the 776 nm laser across the different accessible hyperfine levels in the $5D_{5/2}$ state using the MOT CCD camera equipped with a 420 nm filter (ThorLabs FBH420-10). While we

were not going for precision spectroscopy, the three hyperfine peaks are clearly visible.

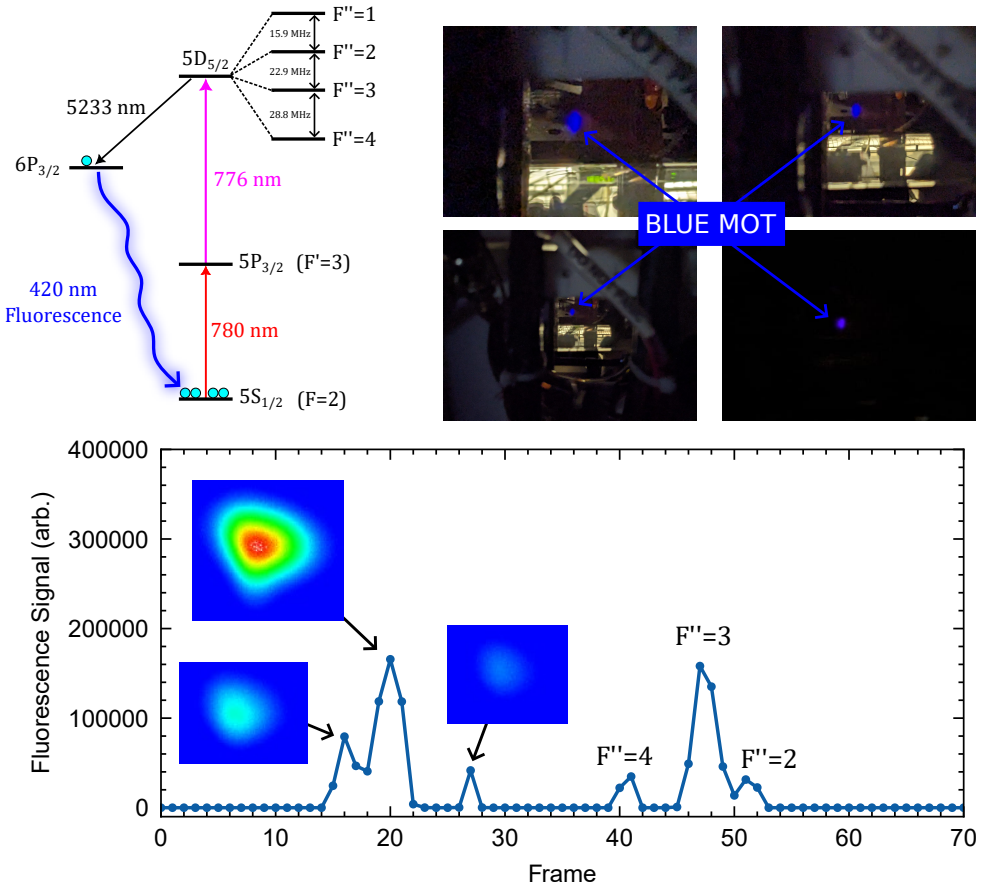

Figure F.4: The blue MOT. (Top Left) The energy level diagram for inducing 420 nm fluorescence for atoms in the MOT [145]. (Top Right) Pictures captured on a phone camera of the blue MOT. (Bottom) Fluorescence data were captured on the MOT CCD camera while scanning the 776 nm laser across the accessible transitions.

Appendix G

RF AC Zeeman Trap Lifetime Simulations

In initial atom chip based RF AC Zeeman (ACZ) trapping experiments [16], it was found that longer lifetimes were achieved when using lower inserted RF power. A possible explanation for this is that the weaker power trap is more susceptible to gravitational sag, shifting the trap bottom off of $\Omega = 0$. This would then make the atoms less likely to cross this point and undergo Majorana-like transitions to other untrapped dressed states. The higher power trap is tighter and therefore more likely to undergo these losses.

I began investigating this by looking at the atom lifetime in the ACZ trap solely due to thermal motion. In short, I place an atom in an ACZ potential with a certain temperature and watch it evolve, waiting to see if it leaves the trap area. Doing this for N_0 atoms will give us the number of atoms remaining as a function of time, $N(t)$. For short time scales compared to the lifetime, τ, this becomes

$$\frac{N(t)}{N_0} = e^{-t/\tau} \simeq 1 - \frac{t}{\tau} + \mathcal{O}(t^2) \tag{G.1}$$

where N_0 is the initial atom number. Relevant code for these simulations can be found in Ref. [30].

G.1 Initial Conditions

To solve a second-order differential equation, we need two initial conditions: the starting position and velocity. For an atom with temperature T in a harmonic trap with frequency ω_i, where i corresponds to the $\{x, y\}$ spatial dimension, the initial position can be sampled from a Gaussian distribution of width σ_i given as

$$\frac{1}{2}m\omega_i^2\sigma_i^2 = \frac{1}{2}k_BT \Rightarrow \sigma_i = \sqrt{\frac{k_BT}{m\omega_i^2}} \tag{G.2}$$

where k_B is Boltzmann's constant, and m is the atom mass. The initial velocity of the particle is sampled from the Maxwell-Boltzmann distribution, which is just a Gaussian (or normal) distribution centered at zero with width $\sigma = \sqrt{k_BT/m}$. The distribution of speed in two-dimensions is

$$f(v) = \frac{mv}{k_BT}e^{-\frac{m}{2k_BT}v^2} \tag{G.3}$$

In Fig. G.1, we sample 10,000 ^{87}Rb atoms with a temperature of $T = 1$ μK in a harmonic trap with frequency $\omega/2\pi = 300$ Hz. The sampling agrees with the expected distributions, and demonstrates the validity of how we generate the initial conditions for each particle.

G.2 Calculating Particle Trajectory

With the initial conditions in place, we now move onto the task of calculating how the particle will move in the ACZ potential. The transverse (xy) potential is generated using an in-house MATLAB GUI [16]. In the ACZ trap, the atoms experience a force $\vec{F}_{ACZ} = -\nabla U_{ACZ}$, where U_{ACZ} is the trapping potential for the atoms. I only consider the transverse trapping potential in the xy-plane since the axial (z) trapping in the RF ACZ trap is done via a weak optical dipole trap. The differential equation we want to solve is just given by Newton's 2nd Law:

$$F(x, v) = m\frac{d^2x}{dt^2} \tag{G.4}$$

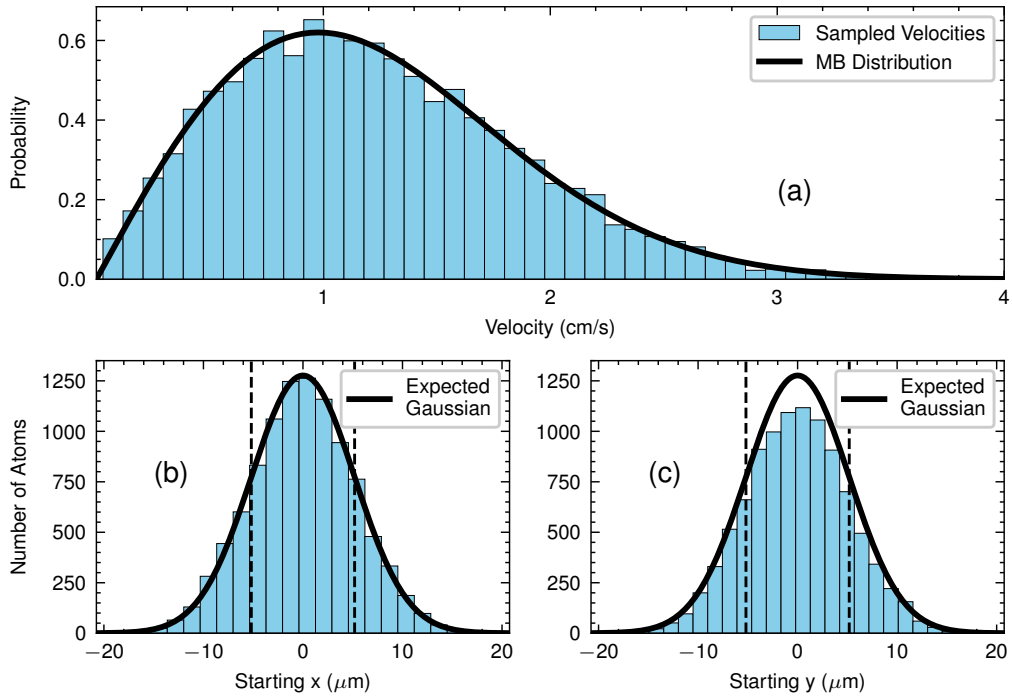

Figure G.1: Initial conditions for sampling 10,000 atoms. (a) Initial velocity sampled from a Maxwell-Boltzmann distribution with a temperature of $T = 1$ μK (black line). (b) Initial x position sampled from a Gaussian of width $\sigma = \sqrt{k_B T/m\omega^2}$ (vertical dashed lines), where k_B is Boltzmann's constant, m is the atom mass, and $\omega/2\pi = 300$ Hz is the trap frequency. (c) Initial y position sampled in the same manner as (b).

Since this is a 2nd-order differential equation we want to break it up into two 1st-order ODEs given by

$$\frac{d}{dt}\left(\frac{dx}{dt}\right) = \frac{dv}{dt} = \frac{F}{m}; \tag{G.5}$$

$$\frac{dx}{dt} = v \tag{G.6}$$

I implemented a custom 4th-Order Runge Kutta (RK4) algorithm to numerically integrate the above equations to solve for the trajectory of the particle in time [147]. This method discretizes time in steps of h. Importantly, the timestep h must be chosen such that the solution is accurate while not taking up too much computational time. For solving simultaneous ODEs, i.e. $\frac{dx}{dt} = f(t, x, v)$ and $\frac{dv}{dt} = g(t, x, v)$, the RK4 steps for calculating

the position and velocity at the next time step are

$$
\begin{aligned}
r_1 &= f(t, x, v) \\
k_1 &= g(t, x, v) \\
r_2 &= f(t + h/2, x + hk_1/2, v + hr_1/2) \\
k_2 &= g(t + h/2, x + hk_1/2, v + hr_1/2) \\
r_3 &= f(t + h/2, x + hk_2/2, v + hr_2/2 \\
k_3 &= g(t + h/2, x + hk_2/2, v + hr_2/2) \\
r_4 &= f(t + h, x + hk_3, v + hr_3) \\
k_4 &= g(t + h, x + hk_3, v + hr_3) \\
\Rightarrow x(t + h) &= x(t) + \frac{h}{6}(r_1 + 2r_2 + 2r_3 + r_4) \qquad \text{(G.7)} \\
\Rightarrow v(t + h) &= v(t) + \frac{h}{6}(k_1 + 2k_2 + 2k_3 + k_4) \qquad \text{(G.8)}
\end{aligned}
$$

With initial position $x(t = 0)$ and velocity $v(t = 0)$, we can solve for the particle's trajectory in time. Since we have a two-dimensional ACZ potential, this must be done for both x and y.

G.2.1 Testing on a Simple Harmonic Oscillator

As a check to make sure our (and by our I mean my) RK4 algorithm is correctly calculating the particle trajectory, we can use a fictitious simple harmonic oscillator (SHO) potential in which we let the particle move around. Using realistic trap frequencies similar to the ACZ potential, we can also use this to benchmark the time step, h, for the simulations. Since the RK4 algorithm does not conserve energy, it is necessary to choose a value for h such that the energy of the system does not change significantly over the simulation time. Since we are only concerned with short time scales (i.e. tens of ms), we only go up to a simulation time of 50 ms. The trajectory of a particle in the SHO potential is shown in Fig. G.2 for time steps of 10 and 0.1 μs. The numerical RK4 result can be compared to

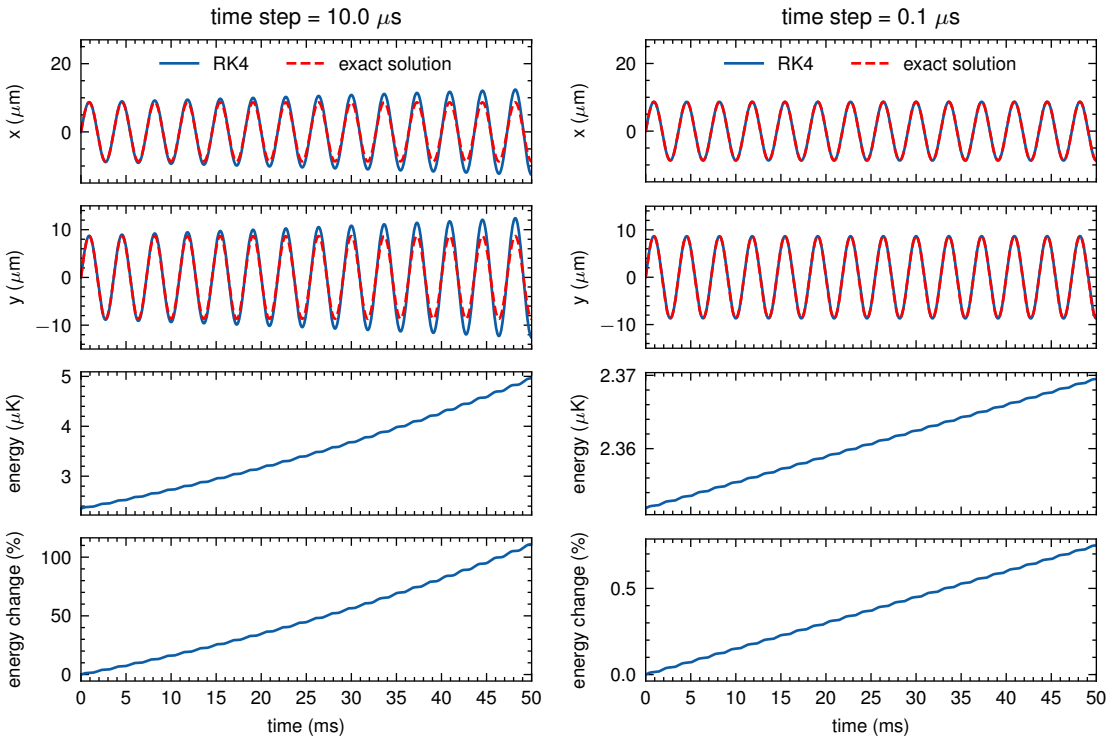

Figure G.2: Particle trajectory in a 2D simple harmonic oscillator (SHO) potential with frequency $\omega_{xy}/2\pi = 275$ Hz using a time steps of $h = 10$ μs (left) and $h = 0.1$ μs (right). The particle is given initial conditions of $x(t = 0) = y(t = 0) = 0$ and $v_x(t = 0) = v_y(t = 0) = 1.5$ cm/s, corresponding to a temperature of $\simeq$2.35 μK. The numerical solution from the RK4 algorithm is compared to the exact solution for a particle moving in a SHO potential (red dashed line). The particle's energy is given as the sum of kinetic and potential energy at each time step.

the exact solution for this differential equation, given as

$$x(t) = x_0 \cos(\omega t) + \frac{v_{x,0}}{\omega} \sin(\omega t) \tag{G.9}$$

and similarly for $y(t)$, where the subscripts correspond to the initial conditions at $t = 0$. This is plotted as the red dashed lines in Fig. G.2. We can clearly see that for an insufficiently large time step of 10 μs, the energy of the particle increases with time, and the numerical result diverges from the exact solution. Lowering the time step to $h = 0.1$ μs, the RK4 algorithm matches the exact solution nearly perfectly. Importantly, the energy of the particle, i.e., kinetic plus potential energy, changes by less than 1% ($\lesssim$20 nK) over the

50 ms simulation time for $h = 0.1$ μs. This energy change is deemed sufficiently small for our purposes, though comes at the cost of a much longer calculation time. For example, in Fig. G.2, for $h = 10$ μs, the simulation took about 1 second, while for $h = 0.1$ μs, the simulation time went up to about 80 seconds. However, we can vectorize the simulation to solve for n atoms simultaneously, cutting down the total simulation time to roughly 1 hour for 10,000 total atoms with $h = 0.1$ μs.

G.3 Preliminary Results

With the algorithm and initial conditions proven to work, we can now apply them to particles moving in a 2D AC Zeeman (ACZ) potential. The algorithm given below outlines the steps for calculating the trajectory of N particles in the ACZ potential. In short, we simulate how the particle moves around in the trap and see if it ever crosses a hand-picked exit boundary, r_{exit}, at which point we record the time it took the particle to exit the trap. This boundary could, in principle, be determined by seeing when the sign of the gradient of the potential changes sign. In this initial work, however, we simply select a radius at which the particle will most certainly be outside of the trap.

The initial simulations used parameters from Ref. [16], specifically the caption of Fig. 7.8, to generate the 2D ACZ potential from the MATLAB GUI. The resulting transverse

I_U	I_Z	ϕ	B_{DC}	Applied RF	State
225 mA	250 mA	130°	28.5718 G	19.5 MHz	$\|{+}{+}\rangle$

Table G.1: MATLAB GUI parameters for generating the ACZ potential used for trap lifetime simulations.

potentials from the GUI are given in Fig. G.3, with and without gravity. Adding in gravity lowers the trap depth in the vertical direction by about a factor of three. In the preliminary simulations of the trap lifetime, we use a positional cutoff of $x_{cutoff} = y_{cutoff} = 125$ μm, giving $r_{exit} = \sqrt{x_{cutoff} + y_{cutoff}} \simeq 177$ μm. Using time-of-flight temperature data from November 16, 2020, the atom temperature at 19.5 MHz for 400 mW of RF power was 2.47 μK.

Algorithm 1 Particle Trajectory Calculation

Generate the 2D ACZ potential using the MATLAB GUI
Reposition the potential to sit at the origin
Interpolate the potential to a finer spatial grid
Take gradient of interpolated potential to get the force
Choose simulation parameters
    → Start (t_0) and end (t_{end}) time, temperature (T), time step (h), number of particles (N), and escape radius (r_{exit})
for $n = 1$ to N **do**
    Get initial position and velocity for the particle
    for $t = t_0 \rightarrow t_{end}$ **do**
        Get the force acting on the particle at the current position
        Use the RK4 algorithm to step the particle's position and velocity forward in time by a step h
        if $r(t) = \sqrt{x(t)^2 + y(t)^2} > r_{exit}$ **then**
            Record the time t at which the particle leaves the trap and ignore all future times for this particle
        end if
    end for
end for

The lifetime in this trap was measured on two separate occasions, shown in Fig. 7.9 in Ref. [16]. In a measurement across a large (several MHz) range of RF frequencies, taken on 16nov20, the lifetime at 19.5 MHz was 140 ± 11 ms. Another set of data at 400 mW power, taken on 23dec20, focused on RF frequencies around 20 MHz. In this data set, the lifetime at 19.5 MHz was measured to be 69 ± 13 ms. The factor of two discrepancy between the lifetime measurements is unknown, but provides a range for us to compare the simulation to. Figure G.4 shows the initial results of the simulation. Using Eq. G.1, we fit the initial atom decay to a line, the slope of which is $1/\tau$, where τ is the lifetime. Without gravity, the lifetime is $\tau = 225.53$ ms, dropping to $\tau = 17.39$ ms when gravity is included in the potential.

In the model for the ACZ trapping potential, there are two primary sources of uncertainty. First is the current in each of the atom chip wires. In Ref. [16], there is decent confidence in the values given in Table G.1, which were obtained via independent Rabi frequency measurements from each of the wires. The main uncertainty is the relative

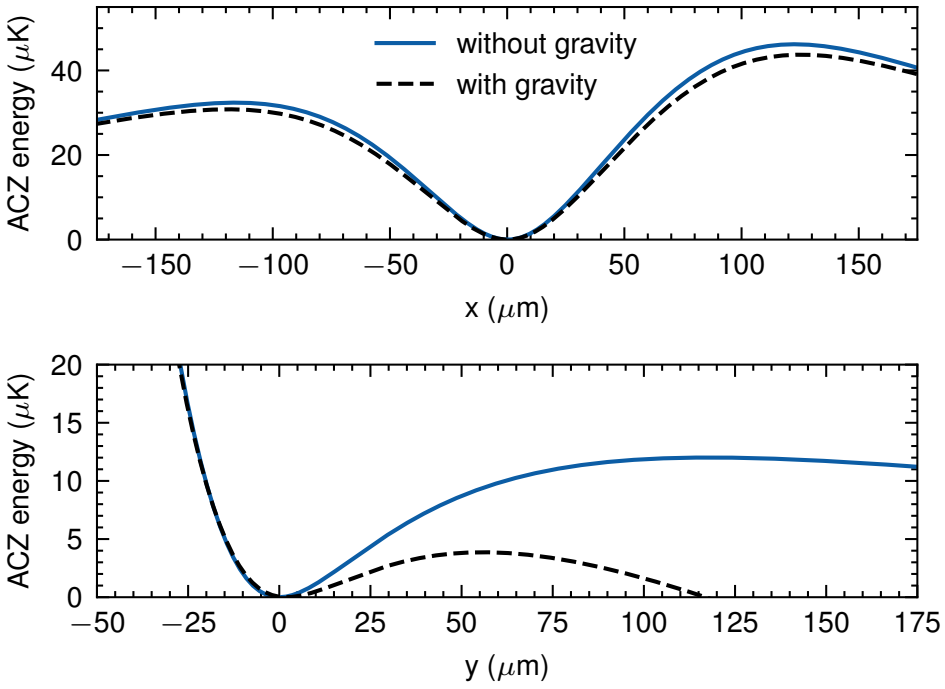

Figure G.3: Slices of the ACZ potential used to simulate the trap lifetime, evaluated at the trap bottom. The potential was created using the MATLAB GUI with the parameters given in Table G.1.

phase between wires. For instance, a hand-picked phase of 121° gives very good agreement between the theory and measured trap frequencies as a function of RF power. We can then do these atom trajectory simulations with this phase (keeping all other parameters the same) to see its effect on the lifetime. Notably, the trap frequencies are increased to $\omega_x/2\pi = 422$ Hz and $\omega_x/2\pi = 400$ Hz (with gravity included), so the time step is decreased to $h = 0.05$ μs. The results of this simulation are given in Fig. G.5, which yields a lifetime of $\tau = 197$ ms. This lifetime is consistent with, but larger than, the measured lifetimes of 140 ± 11 ms and 69 ± 13 ms.

G.4 Summary and Remaining Work

I have developed code for simulating the trajectory of atoms in a 2D RF ACZ trapping potential. By tracking when the atoms leave the trap, we can determine the lifetime due to

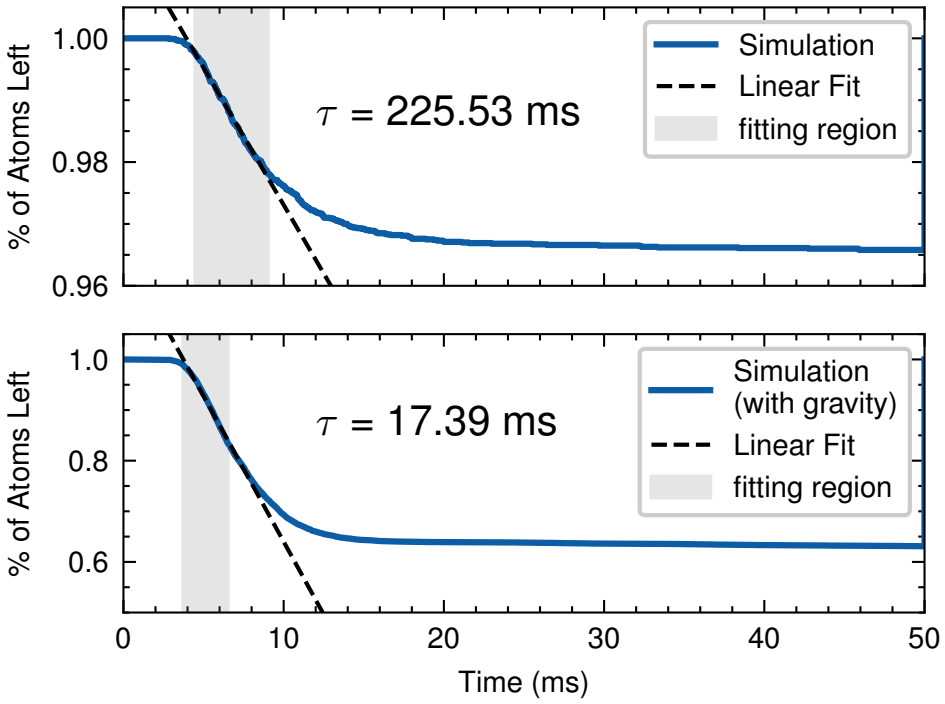

Figure G.4: Percentage of atoms remaining in the RF ACZ trap as a function of time. Atoms are left to evolve in an ACZ trap potential generated using the parameters in Table G.1. The simulation is done without (top) and with (bottom) gravity. For both, the time step is $h = 0.1$ μs.

thermal motion of atoms in the trap. Preliminary results of these simulations show decent agreement with the experimentally observed lifetimes, especially when the relative phase between trapping wires is adjusted. So far, we cannot conclusively say there is additional physics limiting the trap lifetime, insofar that the simulations do not give expected lifetimes much larger than the data.

This work was in some regards a side project that I would spend a couple days on every so often, so there is still some work that must be done which I outline here.

- The relative phase between wires clearly has a significant impact on the lifetime. A study on the trend of lifetime versus phase in the expected range of phases given in Ref. [16] would provide a better benchmark on the expected lifetime.

- In experiment [16], we saw a spike in the lifetime around 20 MHz, corresponding to the RF resonance. A numerical study of lifetime versus RF frequency should be

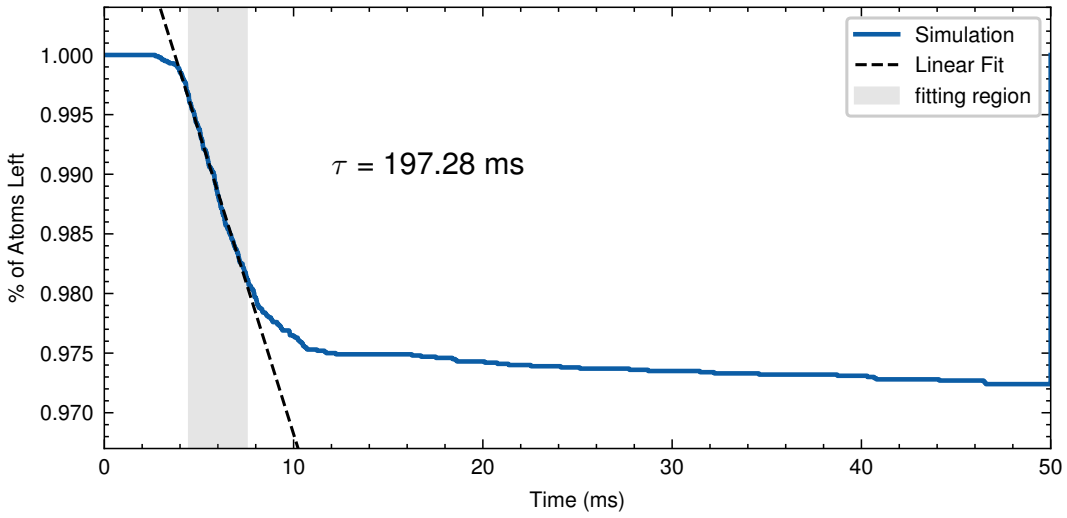

Figure G.5: Percentage of atoms remaining in the RF ACZ trap as a function of time. Atoms are left to evolve in an ACZ trap potential generated using the parameters in Table G.1, except with the phase set to 121°. The simulation is done with gravity. The time step is $h = 0.05$ μs.

done.

- This model does not incorporate atom-atom interactions nor does it try to take into account possible Majorana-type losses when crossing the $\Omega = 0$ point. Adding these to the model necessarily adds complexity, but may reveal the effect of each on the lifetime.

References

[1] C. J. Bordé, C. Salomon, S. Avrillier, A. Van Lerberghe, C. Bréant, D. Bassi, and G. Scoles, "Optical ramsey fringes with traveling waves," *Physical Review A*, vol. 30, no. 4, p. 1836, 1984.

[2] A. Peters, K. Y. Chung, and S. Chu, "High-precision gravity measurements using atom interferometry," *Metrologia*, vol. 38, no. 1, p. 25, 2001.

[3] S. M. Dickerson, J. M. Hogan, A. Sugarbaker, D. M. Johnson, and M. A. Kasevich, "Multiaxis inertial sensing with long-time point source atom interferometry," *Physical review letters*, vol. 111, no. 8, p. 083001, 2013.

[4] A. D. Ludlow, M. M. Boyd, J. Ye, E. Peik, and P. O. Schmidt, "Optical atomic clocks," *Reviews of Modern Physics*, vol. 87, no. 2, pp. 637–701, 2015.

[5] T. S. Roussy, L. Caldwell, T. Wright, W. B. Cairncross, Y. Shagam, K. B. Ng, N. Schlossberger, S. Y. Park, A. Wang, J. Ye, *et al.*, "An improved bound on the electron's electric dipole moment," *Science*, vol. 381, no. 6653, pp. 46–50, 2023.

[6] N. eEDM collaboration, P. Aggarwal, H. L. Bethlem, A. Borschevsky, M. Denis, K. Esajas, P. A. Haase, Y. Hao, S. Hoekstra, K. Jungmann, *et al.*, "Measuring the electric dipole moment of the electron in baf," *The European Physical Journal D*, vol. 72, no. 11, p. 197, 2018.

[7] M. Abe, P. Adamson, M. Borcean, D. Bortoletto, K. Bridges, S. P. Carman, S. Chattopadhyay, J. Coleman, N. M. Curfman, K. DeRose, *et al.*, "Matter-wave atomic gradiometer interferometric sensor (magis-100)," *Quantum Science and Technology*, vol. 6, no. 4, p. 044003, 2021.

[8] M. Raudonis, A. Roura, M. Meister, C. Lotz, L. Overmeyer, S. Herrmann, A. Gierse, C. Lämmerzahl, N. P. Bigelow, M. Lachmann, *et al.*, "Microgravity facilities for cold atom experiments," *Quantum Science and Technology*, vol. 8, no. 4, p. 044001, 2023.

[9] J. R. Williams, C. A. Sackett, H. Ahlers, D. C. Aveline, P. Boegel, S. Botsi, E. Charron, E. R. Elliott, N. Gaaloul, E. Giese, *et al.*, "Pathfinder experiments with atom interferometry in the cold atom lab onboard the international space station," *Nature Communications*, vol. 15, no. 1, p. 6414, 2024.

[10] G. Raithel, A. Duspayev, B. Dash, S. C. Carrasco, M. H. Goerz, V. Vuletić, and V. S. Malinovsky, "Principles of tractor atom interferometry," *Quantum Science and Technology*, vol. 8, no. 1, p. 014001, 2022.

[11] C. D. Panda, M. J. Tao, M. Ceja, J. Khoury, G. M. Tino, and H. Müller, "Measuring gravitational attraction with a lattice atom interferometer," *Nature*, vol. 631, no. 8021, pp. 515–520, 2024.

[12] M. Keil, O. Amit, S. Zhou, D. Groswasser, Y. Japha, and R. Folman, "Fifteen years of cold matter on the atom chip: promise, realizations, and prospects," *Journal of modern optics*, vol. 63, no. 18, pp. 1840–1885, 2016.

[13] J. Reichel and V. Vuletic, *Atom chips*. John Wiley & Sons, 2011.

[14] S. Du, *AC & DC Zeeman Interferometric Sensing with Ultracold Trapped Atoms on a Chip*. PhD thesis, The College of William and Mary, 2021.

[15] B. Wirtschafter, *Interféromètre à atomes froids piégés sur puce avec séparation spatiale*. PhD thesis, Université Paris-Saclay, 2022.

[16] A. P. Rotunno, *Radiofrequency AC Zeeman Trapping for Neutral Atoms*. PhD thesis, The College of William and Mary, 2021.

[17] W. Miyahira, A. P. Rotunno, S. Du, and S. Aubin, "Microwave atom chip design," *Atoms*, vol. 9, no. 3, p. 54, 2021.

[18] M. Ivory, A. Ziltz, C. Fancher, A. Pyle, A. Sensharma, B. Chase, J. Field, A. Garcia, D. Jervis, and S. Aubin, "Atom chip apparatus for experiments with ultracold rubidium and potassium gases," *Review of Scientific Instruments*, vol. 85, no. 4, p. 043102, 2014.

[19] V. Ménoret, P. Vermeulen, N. Le Moigne, S. Bonvalot, P. Bouyer, A. Landragin, and B. Desruelle, "Gravity measurements below 10- 9 g with a transportable absolute quantum gravimeter," *Scientific reports*, vol. 8, no. 1, p. 12300, 2018.

[20] C. Talmadge, J.-P. Berthias, R. Hellings, and E. Standish, "Model-independent constraints on possible modifications of newtonian gravity," *Physical Review Letters*, vol. 61, no. 10, p. 1159, 1988.

[21] M. Safronova, D. Budker, D. DeMille, D. F. J. Kimball, A. Derevianko, and C. W. Clark, "Search for new physics with atoms and molecules," *Reviews of Modern Physics*, vol. 90, no. 2, p. 025008, 2018.

[22] J. Lee, E. Adelberger, T. Cook, S. Fleischer, and B. Heckel, "New test of the gravitational 1/r 2 law at separations down to 52 μ m," *Physical Review Letters*, vol. 124, no. 10, p. 101101, 2020.

[23] H. B. Casimir and D. Polder, "The influence of retardation on the london-van der waals forces," *Physical Review*, vol. 73, no. 4, p. 360, 1948.

[24] C. Sukenik, M. Boshier, D. Cho, V. Sandoghdar, and E. Hinds, "Measurement of the casimir-polder force," *Physical review letters*, vol. 70, no. 5, p. 560, 1993.

[25] J. M. Obrecht, R. J. Wild, M. Antezza, L. P. Pitaevskii, S. Stringari, and E. A. Cornell, "Measurement of the temperature dependence of the casimir-polder force," *Physical review letters*, vol. 98, no. 6, p. 063201, 2007.

[26] C. A. Sackett and J. R. Boynewicz, "Probing short-range gravity using quantum reflection." Poster 153, Poster Session II, APS DAMOP 2025 Meeting, June 18 2025. Oregon Convention Center, Exhibit Hall E.

[27] Y. Balland, L. Absil, and F. Pereira Dos Santos, "Quectonewton local force sensor," *Physical Review Letters*, vol. 133, no. 11, p. 113403, 2024.

[28] M. Antezza, L. P. Pitaevskii, and S. Stringari, "New asymptotic behavior of the surface-atom force out of thermal equilibrium," *Physical review letters*, vol. 95, no. 11, p. 113202, 2005.

[29] M. O. Scully and J. P. Dowling, "Quantum-noise limits to matter-wave interferometry," *Physical Review A*, vol. 48, no. 4, p. 3186, 1993.

[30] https://github.com/willmiyahira/thesisCode.

[31] E. MacKinnon, "De broglie's thesis: A critical retrospective," *American Journal of Physics*, vol. 44, no. 11, pp. 1047–1055, 1976.

[32] F. Dalfovo, S. Giorgini, L. P. Pitaevskii, and S. Stringari, "Theory of bose-einstein condensation in trapped gases," *Reviews of modern physics*, vol. 71, no. 3, p. 463, 1999.

[33] R. Finkelstein, S. Bali, O. Firstenberg, and I. Novikova, "A practical guide to electromagnetically induced transparency in atomic vapor," *New Journal of Physics*, vol. 25, no. 3, p. 035001, 2023.

[34] W. Ketterle, D. S. Durfee, and D. Stamper-Kurn, "Making, probing and understanding bose-einstein condensates," in *Bose-Einstein condensation in atomic gases*, pp. 67–176, IOS Press, 1999.

[35] A. Einstein, "Quantentheorie des einatomigen idealen gases, sitzungsber. k," *Preuss. Akad. Wiss*, vol. 261, no. 1, 1924.

[36] T. H. Maiman, "Stimulated optical radiation in ruby," *nature*, vol. 187, no. 4736, pp. 493–494, 1960.

[37] A. Ashkin, "Trapping of atoms by resonance radiation pressure," *Physical Review Letters*, vol. 40, no. 12, p. 729, 1978.

[38] S. Chu, L. Hollberg, J. E. Bjorkholm, A. Cable, and A. Ashkin, "Three-dimensional viscous confinement and cooling of atoms by resonance radiation pressure," *Physical review letters*, vol. 55, no. 1, p. 48, 1985.

[39] J. Prodan, A. Migdall, W. D. Phillips, I. So, H. Metcalf, and J. Dalibard, "Stopping atoms with laser light," *Physical review letters*, vol. 54, no. 10, p. 992, 1985.

[40] A. L. Migdall, J. V. Prodan, W. D. Phillips, T. H. Bergeman, and H. J. Metcalf, "First observation of magnetically trapped neutral atoms," *Physical review letters*, vol. 54, no. 24, p. 2596, 1985.

[41] E. L. Raab, M. Prentiss, A. Cable, S. Chu, and D. E. Pritchard, "Trapping of neutral sodium atoms with radiation pressure," *Physical review letters*, vol. 59, no. 23, p. 2631, 1987.

[42] P. D. Lett, R. N. Watts, C. I. Westbrook, W. D. Phillips, P. L. Gould, and H. J. Metcalf, "Observation of atoms laser cooled below the doppler limit," *Physical review letters*, vol. 61, no. 2, p. 169, 1988.

[43] J. Dalibard and C. Cohen-Tannoudji, "Laser cooling below the doppler limit by polarization gradients: simple theoretical models," *Journal of the Optical Society of America B*, vol. 6, no. 11, pp. 2023–2045, 1989.

[44] M. H. Anderson, J. R. Ensher, M. R. Matthews, C. E. Wieman, and E. A. Cornell, "Observation of bose-einstein condensation in a dilute atomic vapor," *science*, vol. 269, no. 5221, pp. 198–201, 1995.

[45] K. B. Davis, M.-O. Mewes, M. R. Andrews, N. J. van Druten, D. S. Durfee, D. Kurn, and W. Ketterle, "Bose-einstein condensation in a gas of sodium atoms," *Physical review letters*, vol. 75, no. 22, p. 3969, 1995.

[46] R. Folman, P. Krüger, D. Cassettari, B. Hessmo, T. Maier, and J. Schmiedmayer, "Controlling cold atoms using nanofabricated surfaces: Atom chips," *Physical Review Letters*, vol. 84, no. 20, p. 4749, 2000.

[47] H. Ott, J. Fortagh, G. Schlotterbeck, A. Grossmann, and C. Zimmermann, "Bose-einstein condensation in a surface microtrap," *Physical review letters*, vol. 87, no. 23, p. 230401, 2001.

[48] W. Hänsel, P. Hommelhoff, T. Hänsch, and J. Reichel, "Bose–einstein condensation on a microelectronic chip," *Nature*, vol. 413, no. 6855, pp. 498–501, 2001.

[49] H. J. Metcalf and P. Van der Straten, *Laser cooling and trapping*. Springer Science & Business Media, 1999.

[50] C. J. Pethick and H. Smith, *Bose–Einstein condensation in dilute gases*. Cambridge university press, 2008.

[51] C. Fancher, *Ac Zeeman Force with Ultracold Atoms*. PhD thesis, The College of William and Mary, 2016.

[52] S. Aubin, "Lecture19– doppler cooling temperature." Physics482 & 690: Quantum Optics and Atomics (Spring 2024) lecture notes, College of William Mary, Apr. 2024. Available online.

[53] D. A. Steck, "Rubidium 87 d line data," 2021.

[54] S. Earnshaw, "On the nature of the molecular forces which regulate the constitution of the luminiferous ether," *Transactions of the Cambridge Philosophical Society*, vol. 7, p. 97, 1848.

[55] W. H. Wing, "On neutral particle trapping in quasistatic electromagnetic fields," *Progress in Quantum Electronics*, vol. 8, no. 3-4, pp. 181–199, 1984.

[56] C. Sackett, "Limits on weak magnetic confinement of neutral atoms," *Physical Review A—Atomic, Molecular, and Optical Physics*, vol. 73, no. 1, p. 013626, 2006.

[57] A. R. Ziltz, *Ultracold rubidium and potassium system for atom chip-based microwave and RF potentials*. PhD thesis, The College of William and Mary, 2015.

[58] S. Du, A. Ziltz, W. Miyahira, and S. Aubin, "Suppression of potential roughness in atom-chip ac zeeman traps," *Physical Review A*, vol. 105, no. 5, p. 053127, 2022.

[59] J. Reichel, "Trapping and manipulating atoms on chips," *Atom chips*, pp. 33–60, 2011.

[60] C. Monroe, E. A. Cornell, C. Sackett, C. Myatt, and C. Wieman, "Measurement of cs-cs elastic scattering at t= 30 μk," *Physical review letters*, vol. 70, no. 4, p. 414, 1993.

[61] A. Rotunno, W. Miyahira, S. Du, and S. Aubin, "Radio-frequency ac zeeman force for ultracold atoms," *Physical Review A*, vol. 110, no. 6, p. 063321, 2024.

[62] S. Hofferberth, B. Fischer, T. Schumm, J. Schmiedmayer, and I. Lesanovsky, "Ultracold atoms in radio-frequency dressed potentials beyond the rotating-wave approximation," *Physical Review A—Atomic, Molecular, and Optical Physics*, vol. 76, no. 1, p. 013401, 2007.

[63] A. Pyle, *Scattering a Bose-Einstein Condensate Off a Modulated Barrier*. PhD thesis, The College of William and Mary, 2019.

[64] M. K. Ivory, *Experimental Apparatus for Quantum Pumping with a Bose-Einstein Condensate*. PhD thesis, The College of William and Mary, 2016.

[65] D. W. Preston, "Doppler-free saturated absorption: Laser spectroscopy," *American Journal of Physics*, vol. 64, no. 11, pp. 1432–1436, 1996.

[66] A. J. Barker, H. Style, K. Luksch, S. Sunami, D. Garrick, F. Hill, C. J. Foot, and E. Bentine, "Applying machine learning optimization methods to the production of a quantum gas," *Machine Learning: Science and Technology*, vol. 1, no. 1, p. 015007, 2020.

[67] Z. Chen, J. G. Bohnet, J. M. Weiner, and J. K. Thompson, "A low phase noise microwave source for atomic spin squeezing experiments in 87rb," *Review of Scientific Instruments*, vol. 83, no. 4, p. 044701, 2012.

[68] P. Wade, "Pipe-cap filters revisited," *W1GHz*, 2008.

[69] R. J. Spreeuw, C. Gerz, L. S. Goldner, W. D. Phillips, S. Rolston, C. Westbrook, M. Reynolds, and I. F. Silvera, "Demonstration of neutral atom trapping with microwaves," *Physical review letters*, vol. 72, no. 20, p. 3162, 1994.

[70] S. C. Wright, T. Wall, and M. Tarbutt, "Microwave trap for atoms and molecules," *Physical Review Research*, vol. 1, no. 3, p. 033035, 2019.

[71] A. Rotunno, W. Miyahira, S. Du, and S. Aubin, "Radio-frequency acz trap for neutral atoms," *Physical Review Letters*, 2024.

[72] T. Bergeman, G. Erez, and H. J. Metcalf, "Magnetostatic trapping fields for neutral atoms," *Physical Review A*, vol. 35, no. 4, p. 1535, 1987.

[73] M. Pappa, P. Condylis, G. Konstantinidis, V. Bolpasi, A. Lazoudis, O. Morizot, D. Sahagun, M. Baker, and W. Von Klitzing, "Ultra-sensitive atom imaging for matter-wave optics," *New Journal of Physics*, vol. 13, no. 11, p. 115012, 2011.

[74] Analog Devices, Inc., *AD9910: 1 GSPS, 14-Bit, High Performance, DDS*. Analog Devices, Inc., 2010. Datasheet.

[75] C. Chin, R. Grimm, P. Julienne, and E. Tiesinga, "Feshbach resonances in ultracold gases," *Reviews of Modern Physics*, vol. 82, no. 2, pp. 1225–1286, 2010.

[76] F. Bloch and A. Siegert, "Magnetic resonance for nonrotating fields," *Physical Review*, vol. 57, no. 6, p. 522, 1940.

[77] D. C. Aveline, J. R. Williams, E. R. Elliott, C. Dutenhoffer, J. R. Kellogg, J. M. Kohel, N. E. Lay, K. Oudrhiri, R. F. Shotwell, N. Yu, *et al.*, "Observation of bose–einstein condensates in an earth-orbiting research lab," *Nature*, vol. 582, no. 7811, pp. 193–197, 2020.

[78] C. J. Straatsma, M. K. Ivory, J. Duggan, J. Ramirez-Serrano, D. Z. Anderson, and E. A. Salim, "On-chip optical lattice for cold atom experiments," *Optics letters*, vol. 40, no. 14, pp. 3368–3371, 2015.

[79] S. Aubin, S. Myrskog, M. Extavour, L. LeBlanc, D. McKay, A. Stummer, and J. Thywissen, "Rapid sympathetic cooling to fermi degeneracy on a chip," *Nature Physics*, vol. 2, no. 6, pp. 384–387, 2006.

[80] B. M. Garraway and H. Perrin, "Recent developments in trapping and manipulation of atoms with adiabatic potentials," *Journal of Physics B: Atomic, Molecular and Optical Physics*, vol. 49, no. 17, p. 172001, 2016.

[81] P. Krüger, L. M. Andersson, S. Wildermuth, S. Hofferberth, E. Haller, S. Aigner, S. Groth, I. Bar-Joseph, and J. Schmiedmayer, "Potential roughness near lithographically fabricated atom chips," *Physical Review A*, vol. 76, no. 6, p. 063621, 2007.

[82] P. Krüger, S. Wildermuth, S. Hofferberth, L. M. Andersson, S. Groth, I. Bar-Joseph, and J. Schmiedmayer, "Cold atoms close to surfaces: measuring magnetic field roughness and disorder potentials," in *Journal of Physics: Conference Series*, vol. 19, p. 56, IOP Publishing, 2005.

[83] T. Schumm, J. Estève, C. Figl, J.-B. Trebbia, C. Aussibal, H. Nguyen, D. Mailly, I. Bouchoule, C. I. Westbrook, and A. Aspect, "Atom chips in the real world: the effects of wire corrugation," *The European Physical Journal D-Atomic, Molecular, Optical and Plasma Physics*, vol. 32, no. 2, pp. 171–180, 2005.

[84] J. Estève, C. Aussibal, T. Schumm, C. Figl, D. Mailly, I. Bouchoule, C. I. Westbrook, and A. Aspect, "Role of wire imperfections in micromagnetic traps for atoms," *Physical Review A—Atomic, Molecular, and Optical Physics*, vol. 70, no. 4, p. 043629, 2004.

[85] A. Leanhardt, Y. Shin, A. Chikkatur, D. Kielpinski, W. Ketterle, and D. Pritchard, "Bose-einstein condensates near a microfabricated surface," *Physical review letters*, vol. 90, no. 10, p. 100404, 2003.

[86] J. Fortágh, H. Ott, S. Kraft, A. Günther, and C. Zimmermann, "Surface effects in magnetic microtraps," *Physical Review A*, vol. 66, no. 4, p. 041604, 2002.

[87] A. Leanhardt, A. Chikkatur, D. Kielpinski, Y. Shin, T. Gustavson, W. Ketterle, and D. Pritchard, "Propagation of bose-einstein condensates in a magnetic waveguide," *Physical review letters*, vol. 89, no. 4, p. 040401, 2002.

[88] S. Groth, P. Krüger, S. Wildermuth, R. Folman, T. Fernholz, J. Schmiedmayer, D. Mahalu, and I. Bar-Joseph, "Atom chips: Fabrication and thermal properties," *Applied Physics Letters*, vol. 85, no. 14, pp. 2980–2982, 2004.

[89] K. Wongcharoenbhorn, R. Crawford, N. Welch, F. Wang, G. Sinuco-León, P. Krueger, F. Intravaia, C. Koller, and T. Fromhold, "Using graphene conductors to enhance the functionality of atom chips," *Physical Review A*, vol. 104, no. 5, p. 053108, 2021.

[90] I. L. García, B. Darquié, E. Curtis, C. Sinclair, and E. Hinds, "Experiments on a videotape atom chip: fragmentation and transport studies," *New Journal of Physics*, vol. 12, no. 9, p. 093017, 2010.

[91] J.-B. Trebbia, C. L. Garrido Alzar, R. Cornelussen, C. I. Westbrook, and I. Bouchoule, "Roughness suppression via rapid current modulation on an atom chip," *Phys. Rev. Lett.*, vol. 98, p. 263201, 2007.

[92] J. Fekete, P. Joshi, T. J. Barrett, T. M. James, R. Shah, A. Gadge, S. Bhumbra, W. Evans, M. Tripathi, M. Large, *et al.*, "Quantum gas-enabled direct mapping of active current density in percolating networks of nanowires," *Nano Letters*, vol. 24, no. 4, pp. 1309–1315, 2024.

[93] S. Aigner, L. D. Pietra, Y. Japha, O. Entin-Wohlman, T. David, R. Salem, R. Folman, and J. Schmiedmayer, "Long-range order in electronic transport through disordered metal films," *Science*, vol. 319, no. 5867, pp. 1226–1229, 2008.

[94] H. Perrin and B. M. Garraway, "Trapping atoms with radio frequency adiabatic potentials," in *Advances in Atomic, Molecular, and Optical Physics*, vol. 66, pp. 181–262, Elsevier, 2017.

[95] A. E. Blackwell, A. P. Rotunno, and S. Aubin, "Demonstration of the lateral ac skin effect using a pickup coil," *American Journal of Physics*, vol. 88, no. 8, pp. 676–684, 2020.

[96] S. Sasinowska, "Suppressing current deviations via the ac skin effect," bachelor's thesis, William Mary, 2025.

[97] V. Bagnato, D. E. Pritchard, and D. Kleppner, "Bose-einstein condensation in an external potential," *Physical Review A*, vol. 35, no. 10, p. 4354, 1987.

[98] J.-B. Trebbia, *Etude de gaz quantiques dégénérés quasi-unidimensionnels confinés par une micro-structure*. PhD thesis, Université Paris Sud-Paris XI, 2007.

[99] S. Kraft, A. Günther, H. Ott, D. Wharam, C. Zimmermann, and J. Fortágh, "Anomalous longitudinal magnetic field near the surface of copper conductors," *Journal of Physics B: Atomic, Molecular and Optical Physics*, vol. 35, no. 21, p. L469, 2002.

[100] J. Van Es, S. Whitlock, T. Fernholz, A. Van Amerongen, and N. Van Druten, "Longitudinal character of atom-chip-based rf-dressed potentials," *Physical Review A—Atomic, Molecular, and Optical Physics*, vol. 77, no. 6, p. 063623, 2008.

[101] S. Rego, "A microwave analog of a quantum double well potential," bachelor's thesis, William Mary, 2023.

[102] C. Fancher, A. Pyle, A. Rotunno, and S. Aubin, "Microwave ac zeeman force for ultracold atoms," *Physical Review A*, vol. 97, no. 4, p. 043430, 2018.

[103] D. Grieg and H. Engelmann, "Microstrip-a new transmission technique for the klilomegacycle range," *Proceedings of the IRE*, vol. 40, no. 12, pp. 1644–1650, 1952.

[104] P. Böhi, M. F. Riedel, J. Hoffrogge, J. Reichel, T. W. Hänsch, and P. Treutlein, "Coherent manipulation of bose–einstein condensates with state-dependent microwave potentials on an atom chip," *Nature Physics*, vol. 5, no. 8, pp. 592–597, 2009.

[105] B. Lowry, R. Wyllie, M. Chapman, and C. Herold, "Characterization of an atom chip with integrated coplanar waveguides," in *APS Division of Atomic, Molecular and Optical Physics Meeting Abstracts*, vol. 63, (College Park, MD, USA), American Physical Society, 2018.

[106] Z. Lu, J. A. Murakowski, C. A. Schuetz, S. Shi, G. J. Schneider, J. P. Samluk, and D. W. Prather, "Perfect lens makes a perfect trap," *Optics express*, vol. 14, no. 6, pp. 2228–2235, 2006.

[107] S. J. Orfanidis, "Electromagnetic waves and antennas," 2002.

[108] R. E. Collin, *Foundations for microwave engineering*. John Wiley & Sons, 2007.

[109] A. J. Burkhardt, C. S. Gregg, and J. A. Staniforth, "Calculation of pcb track impedance," tech. rep., Polar Instruments, 2000.

[110] D. M. Pozar, *Microwave engineering: theory and techniques*. John wiley & sons, 2021.

[111] T. C. Edwards and M. B. Steer, *Foundations for microstrip circuit design*. John Wiley & Sons, 2016.

[112] M. K. Kazimierczuk, *Pulse-width modulated DC-DC power converters*. John Wiley & Sons, 2015.

[113] J. Krupka, M. Zając, R. Kucharski, and D. Gryglewski, "Dielectric properties of highly resistive gan crystals grown by ammonothermal method at microwave frequencies," *AIP Advances*, vol. 6, no. 3, 2016.

[114] Rogers Corporation, *RO4000®Series High Frequency Circuit Materials*, 2018.

[115] T. H. Lee and T. H. Lee, *Planar microwave engineering: a practical guide to theory, measurement, and circuits*, vol. 1. Cambridge university press, 2004.

[116] P. Haslinger, M. Jaffe, V. Xu, O. Schwartz, M. Sonnleitner, M. Ritsch-Marte, H. Ritsch, and H. Müller, "Attractive force on atoms due to blackbody radiation," *Nature physics*, vol. 14, no. 3, pp. 257–260, 2018.

[117] D. A. Hill, K. H. Cavcey, and R. T. Johnk, "Crosstalk between microstrip transmission lines," *IEEE Transactions on Electromagnetic Compatibility*, vol. 36, no. 4, pp. 314–321, 2002.

[118] A. Sain and K. L. Melde, "Impact of ground via placement in grounded coplanar waveguide interconnects," *IEEE Transactions on Components, Packaging and Manufacturing Technology*, vol. 6, no. 1, pp. 136–144, 2015.

[119] A. Suntives, A. Khajooeizadeh, and R. Abhari, "Using via fences for crosstalk reduction in pcb circuits," in *2006 IEEE International Symposium on Electromagnetic Compatibility, 2006. EMC 2006.*, vol. 1, pp. 34–37, IEEE, 2006.

[120] D. J. Griffiths, *Introduction to electrodynamics*. Cambridge University Press, 2023.

[121] L. G. Maloratsky and M. Lines, "Reviewing the basics of microstrip," *Microwaves RF*, vol. 39, no. March, pp. 79–88, 2000.

[122] J. Shields, "Materials characterization for microwave atom chip development," bachelor's thesis, William Mary, 2023.

[123] https://www.nitrideglobal.com/e.

[124] X. Chen, Z. Zhang, S. Yu, and T.-G. Zsurzsan, "Fringing effect analysis of parallel plate capacitors for capacitive power transfer application," in *2019 IEEE 4th International Future Energy Electronics Conference (IFEEC)*, pp. 1–5, IEEE, 2019.

[125] S. Rosene, "Progress towards electromagnetig manipulation and trapping of microparticles," bachelor's thesis, William Mary, 2022.

[126] S. Shanmugadas, "Measuring the magnetic and electric fields of a microwave lattice for atom chip development," bachelor's thesis, William Mary, 2021.

[127] R. Kamback, T. Tingle, W. Miyahira, and S. Aubin, "Microwave atom chip for ultracold trapped atom interferometery," in *APS Division of Atomic, Molecular and Optical Physics Meeting*, 2025.

[128] M. Ballu, B. Mirmand, T. Badr, H. Perrin, and A. Perrin, "Fast manipulation of a quantum gas on an atom chip with a strong microwave field," *Physical Review A*, vol. 110, no. 5, p. 053312, 2024.

[129] P. Treutlein, *Coherent manipulation of ultracold atoms on atom chips*. PhD thesis, lmu, 2008.

[130] M. Kaiser, C. Glaser, L. Y. Ley, J. Grimmel, H. Hattermann, D. Bothner, D. Koelle, R. Kleiner, D. Petrosyan, A. Günther, *et al.*, "Cavity-driven rabi oscillations between rydberg states of atoms trapped on a superconducting atom chip," *Physical Review Research*, vol. 4, no. 1, p. 013207, 2022.

[131] M. Logsdon, "Co-planar waveguides for microwave atom chips," bachelor's thesis, William Mary, 2022.

[132] W. Miyahira, "How to make a coplanar waveguide in feko," Nov 2021.

[133] N. Almuqati and H. Sigmarsson, "3d microstrip line taper on ultra-low dielectric constant substrate," in *2019 IEEE 20th Wireless and Microwave Technology Conference (WAMICON)*, pp. 1–5, IEEE, 2019.

[134] M. Ammar, M. Dupont-Nivet, L. Huet, J.-P. Pocholle, P. Rosenbusch, I. Bouchoule, C. I. Westbrook, J. Estève, J. Reichel, C. Guerlin, *et al.*, "Symmetric microwave potentials for interferometry with thermal atoms on a chip," *Physical Review A*, vol. 91, no. 5, p. 053623, 2015.

[135] M. Dupont-Nivet, C. Westbrook, and S. Schwartz, "Contrast and phase-shift of a trapped atom interferometer using a thermal ensemble with internal state labelling," *New Journal of Physics*, vol. 18, no. 11, p. 113012, 2016.

[136] M. Dupont-Nivet, R. Demur, C. I. Westbrook, and S. Schwartz, "Experimental study of the role of trap symmetry in an atom-chip interferometer above the bose–einstein condensation threshold," *New Journal of Physics*, vol. 20, no. 4, p. 043051, 2018.

[137] P. Treutlein, P. Hommelhoff, T. Steinmetz, T. W. Hänsch, and J. Reichel, "Coherence in microchip traps," *Physical review letters*, vol. 92, no. 20, p. 203005, 2004.

[138] G. A. Kazakov and T. Schumm, "Magic radio-frequency dressing for trapped atomic microwave clocks," *Physical Review A*, vol. 91, no. 2, p. 023404, 2015.

[139] L. Sárkány, P. Weiss, H. Hattermann, and J. Fortágh, "Controlling the magnetic field sensitivity of atomic clock states by microwave dressing," *arXiv preprint arXiv:1410.8171*, 2014.

[140] Y. B. Ovchinnikov, F. E. Ayi-Yovo, and A. Spampinato, "Optical dipole microtrap for atoms based on crossed planar photonic waveguides," *Journal of Physics B: Atomic, Molecular and Optical Physics*, vol. 56, no. 23, p. 235002, 2023.

[141] C. Sturner, "Development of a 780 nm external cavity diode laser for rubidium spectroscopy," bachelor's thesis, William Mary, 2023.

[142] M. Bridges, "Measuring the 5d excited energy levels of rubidium atoms using laser spectroscopy," bachelor's thesis, William Mary, 2025.

[143] S. Pegahan, T. Averett, E. Mikhalov, I. Novikova, N. Destefano, S. Zhang, A. Camsonne, S. Aubin, G. Park, M. Team, *et al.*, "Development of a rydberg atom-based apparatus for tracking charged particles," in *APS Division of Atomic, Molecular and Optical Physics Meeting Abstracts*, vol. 2023, pp. F02–009, 2023.

[144] F. Becerra, R. Willis, S. Rolston, and L. Orozco, "Two-photon dichroic atomic vapor laser lock using electromagnetically induced transparency and absorption," *Journal of the Optical Society of America B*, vol. 26, no. 7, pp. 1315–1320, 2009.

[145] A. Marian, *Direct Frequency Comb Spectroscopy for Optical Frequency Metrology and Coherent Interactions*. PhD thesis, University of Colorado at Boulder, 2005.

[146] J. P. Mcgilligan, K. R. Moore, A. Dellis, G. Martinez, E. de Clercq, P. Griffin, A. Arnold, E. Riis, R. Boudot, and J. Kitching, "Laser cooling in a chip-scale platform," *Applied Physics Letters*, vol. 117, no. 5, 2020.

[147] M. Newman, "Computational physics," *(No Title)*, 2013.

VITA

William Miyahira

William Miyahira was born in the suburbs of San Francisco, CA, where he attended Aragon High School, graduating in 2015. From there, he took his talents to the Pacific Northwest, earning degrees in physics and mathematics at the University of Puget Sound. His undergraduate summers were spent participating in research in musical acoustics with Dr. Rand Worland, and theoretical particle physics with Dr. David Latimer. In 2019, he moved to Williamsburg, VA, to begin a PhD in physics at the College of William and Mary. Mesmerized early on by the ultracold atom experiment, William joined the group of Dr. Seth Aubin in the summer of 2020, working to explore the character of AC Zeeman traps and develop a novel microwave atom chip. Following his defense, he will continue his travels east to Groningen, Netherlands, to begin a postdoc with the NL-eEDM group to establish better experimental bounds on the electron's electric dipole moment.